Carborane bis-pyridylalcohols as Globular and Flexible Linkers for Coordination Polymers: From Bulk Crystals to 2D Ultrathin Nanosheets

Fangchang Tan

Universitat Autònoma de Barcelona

Carborane bis-pyridylalcohols as Globular and Flexible Linkers for Coordination Polymers: From Bulk Crystals to 2D Ultrathin Nanosheets

Fangchang Tan

DOCTORAL THESIS

Ph. D. in Chemistry

Supervisor

Dr. José Giner Planas

Tutor

Dr. Gregori Ujaque Pérez

Institut de Ciència de Materials de Barcelona (ICMAB)-CSIC

Departament de Química - Facultat de Ciències

2019

Thesis presented to aspire to the Doctorate in Chemistry degree by Fangchang Tan.

Dr. José Giner Planas
Tenured Scientist/Científico Titular
Consejo Superior de Investigaciones Científicas
INSTITUT DE CIÈNCIA DE MATERIALS DE BARCELONA-CSIC

Dr. Gregori Ujaque Pérez
Professor Agregat
Departament de Química
Universitat Autònoma de Barcelona

Bellaterra, 17 de Julio de 2019

El Doctor JOSÉ GINER PLANAS, Científico Titular del Consejo Superior de Investigaciones Científicas (CSIC) en el Instituto de Ciencia de Materiales de Barcelona (ICMAB),

CERTIFICA:

Que Fangchang Tan, licenciada en Química, ha realizado bajo su dirección la tesis doctoral titulada "**Carborane bis-pyridylalcohols as Globular and Flexible Linkers for Coordination Polymers: From Bulk Crystals to 2D Ultrathin Nanosheets**" y que se recoge en esta memoria para optar al grado de Doctora en Química por la Universitat Autònoma de Barcelona.

Y para que así conste y tenga los efectos oportunos, firmo este certificado en Bellaterra, a 17 de Julio de 2019.

Dr. José Giner Planas

ICMAB-CSIC

This work has been financed by the Comisión Interministerial de Ciencia y Tecnología CICYT by the following projects CTQ2013-44670-R y CTQ2016-75150-R, and by the Generalitat de Catalunya (project 2014/SGR/149). F. Tang acknowledges the China Scholarship Council (CSC) for her PhD grants (201506060171). Some of the experiments were performed at the XALOC and NCD beamlines of the ALBA synchrotron with the support of ALBA staff.

The dissertation defense of the present work is scheduled for 16th September 2019. The thesis Committee consists of the following members:

- President: Prof. Nuria Aliaga Alcalde, Institut de Ciència de Materials de Barcelona-CSIC.
- Secretary: Dr. Eva Carolina Sañudo Zotes, Universitat de Barcelona.
- Vocal: Dr. Guillermo Minguez Espallargas, Universidad de Valencia.

Committee substitutes:

- Substitute 1: Dr. Inmaculada Ratera Bastardas, Institut de Ciència de Materials de Barcelona-CSIC.
- Substitute 2: Dr. Anna Laromaine Sagué, Institut de Ciència de Materials de Barcelona-CSIC.

This thesis is dedicated to my parents.

Acknowledgement

The accomplishment of this thesis is attributed to many people who support and encourage me during last four years.

First and foremost, I would like to give my sincere thanks to my supervisor, Dr. José Giner Planas for bringing me into fascinating chemistry of Carborane-based Metal-Organic Framework. He gave me a lot of valuable guidance with his profound knowledge and wisdom. His enthusiasm for chemistry and optimistic character exert an important on my Ph. D life and study in the future.

I am grateful also to Prof. Francesc Teixidor, Prof. Clara Viñas and Dr. Rosario Núñez for the support during my stay in the research group, Inorganic Materials and Catalysis in ICMAB-CSIC.

I also owe my thanks to Prof. Mark E. Light and Dr. Duane Choquesillo-Lazarte for their important effort related to single crystal structure analysis. Without their help, it would be difficult to prove our research hypothesis. I would also acknowledge Prof. Eliseo Ruiz and Dr. Jordi Cirera who performed the DFT calculations. I have to thank Prof. Jordi Sort Viñas for his kindness to let me use the high vacuum equipment and helpful discussion about nanoindentation. I would like to thank Eduardo Solano for the measurement of GIWAX and Prof. Carmen Ocal and Dr. Esther Barrena for AFM measurements and discussion. I am also thankful to Prof. Daniel Maspoch, Dr. Inhar Imaz Gabilondo and Dr. Sabina Rodriguez for their help at the very beginning of my Ph. D.

Many thanks to my group members and friends: Dr. Isa Fuentes, Dr. Ines Bennour, Dr. Mahdi Chaari, Dr. Albert Ferrer-Ugalde, Dr. Zsolt Kelemen, Ana Begoña Buades, Miquel Nuez i Martínez, Joan Soldevila, Lei Gan, Arpita Saha, Abhishek Saini, Isabel Guerrero Troyano, Sohini Sinha, Zhen Li, Dr Amirali Yazdi, Pol Gimeno Forquernié and Laura Hernández López for all the friendship and help during my Ph.D.

Additionally, I would thank my country China and CSC grant to give me this opportunity to study abroad and support me financially for 4 years. I would like to thank friends who also came from China to do Ph.D in UAB: Lu Yu, Rong Zhang, Tingting Qiu, Xiaoqing Shi and Sining Zhang. Thank you for the accompany and encouragement. Also, thanks to the guys who also majored in material science: Yu Chen, Qianzhe Zhang, Zhi Li, Jike Lv and Qiaoming Zhang for those interesting discussion about everything especially about research work. Besides, I have to thank my boyfriend Dr. Fan for his accompany and all help on many aspects.

Last but not least, I would like to express my deepest gratitude to my parents especially my mother who support me whatever I decide to do. Your understanding, acceptance and emotionally encouragement give me strength to complete my Ph.D study.（谢谢亲爱的妈咪，这么多年的支持，爱与包容）. I also wish to send gratitude to my dad for his love and those precious memory which always motivate me to realize my dream.

The present PhD thesis has been carried out at the Laboratory of Inorganic Materials and Catalysis of the Materials Science Institute of Barcelona (ICMAB)-CSIC following the doctoral program in Chemistry of the Autonomous University of Barcelona. According to the decision of the PhD commission, this Thesis is presented as a compendium of publications. Additionally, and with the idea of providing a more complete Thesis, some additional results obtained before the deposit of the present work and in process of publication are also included.

The publications accepted in the compendium are listed below in order of their appearance in the Thesis:

1) Tsang, M. Y.; Rodríguez-Hermida, S.; Stylianou, K. C.; Tan, F.; Negi, D.; Teixidor, F.; Viñas, C.; Choquesillo-Lazarte, D.; Verdugo-Escamilla, C.; Guerrero, M.; Sort, J.; Juanhuix, J.; Maspoch, D.; Giner Planas, J. Carborane Bis-pyridylalcohols as Linkers for Coordination Polymers: Synthesis, Crystal Structures, and Guest-Framework Dependent Mechanical Properties. *Cryst. Growth Des.* **2017**, *17*, 846-857.

2) Tan, F.; López-Periago, A.; Light, M. E.; Cirera, J.; Ruiz, E.; Borrás, A.; Teixidor, F.; Viñas, C.; Domingo, C.; Planas, J. G. An Unprecedented Stimuli-Controlled Single-Crystal Reversible Phase Transition of a Metal–Organic Framework and Its Application to a Novel Method of Guest Encapsulation. *Advanced Materials* **2018**, *30*, 1800726.

Carborane-based ligand

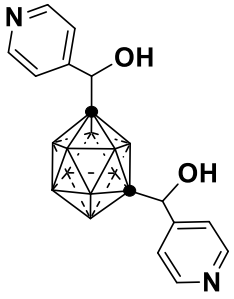

CB1

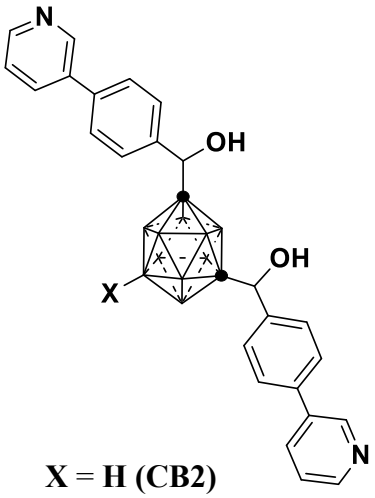

X = H (CB2)
I (I-CB2)

● = carbon; rest of vertices = BH

Carboxylic acid ligand

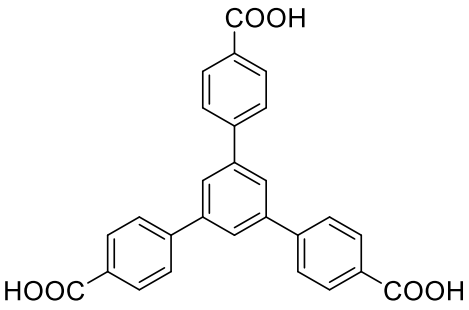

H_3BTB

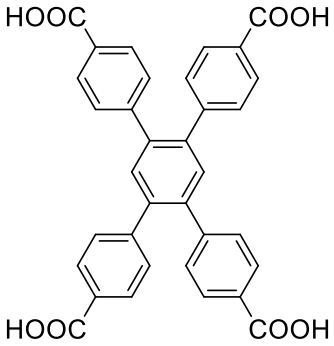

H_4TCPB

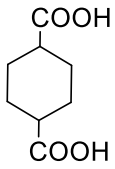

H_2CHDA

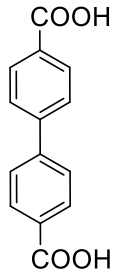

H_2BPDC

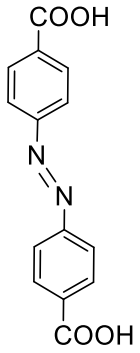

H_2ADB

Compound list

Type	Nomenclature	Formula
CPs	**CB1**MOF-1	$[Co_3(BTB)_2(CB1)_2]\cdot 4DMF$
	CB1MOF-1′	$[Co_3(BTB)_2(CB1)_2]\cdot nsolv$
	CB1MOF-1′′	$[Co_3(BTB)_2(CB1)_2]$
	CB1MOF-2	$[Zn_4(BTB)_2(CB1)(OH)_2)(H_2O)_2]\cdot 5H_2O\cdot 4DMF$
	CB1MOF-3	$[Zn_2(TCPB)(CB1)]\cdot 2DMF$
	CB1MOF-4	$[Co_2(TCPB)(CB1)(H_2O)(\mu\text{-}H_2O)(DMF)]\cdot 2.7DMF$
	CB2MOF-1	$[Co_3(BTB)_2(CB2)]\cdot nDMF$
	CB2MOF-1′	$[Co_3(BTB)_2(CB2)]\cdot nsolv$
	I-CB2MOF-1	$[Co_3(BTB)_2(I\text{-}CB2)]\cdot nDMF$
	I-CB2MOF-1′	$[Co_3(BTB)_2(I\text{-}CB2)]\cdot nsolv$
	CB2MOF-2	$[Co_2(CHDA)_2(CB2)]$
	CB2MOF-3	$[Co_2(BPDC)(CB2)_2(NO_3)_2]\cdot DMF$
	CB2MOF-4	$[Co_2(ADB)(CB2)_2(NO_3)2]\cdot DMF$
MONs	**CB1**MON-1	Nanosheet of **CB1**MOF-1′
	CB2MON-1	Nanosheet of **CB2**MOF-1
	I-CB2MON-1	Nanosheet of I-**CB2**MOF-1

Abbreviations

1 or 2 or 3D	1 or 2 or 3 dimensional
MOFs	metal-organic frameworks
MONs	metal-organic framework nanosheets
SBU	Secondary building unit
SC-SC	single crystal to single crystal
***o*-carborane or *o*CB**	*ortho*-carborane
***m*-carborane or *m*CB**	*meta*-carborane
***p*-carborane or *p*CB**	*para*-carborane
CB	carborane
Ph	phenyl
***n*-BuLi**	*n*-butyl lithium
EtOAc	ethyl acetate
EtOH	ethanol
$CHCl_3$	chloroform
CH_3CN	acetonitrile
MeOH	methanol
DMF	dimethylformamide
DMSO	dimethyl sulfoxide
THF	tetrahydrofuran
$ScCO_2$	supercritical CO_2
H_3BTB	1,3,5-tris(carboxylphenyl)benzene
H_2TCPB	1,2,4,5-tetrakis(4-carboxyphenyl) benzene
H_2BPDC	biphenyl-4,4′-dicarboxylic acid
H_2ADB	4,4′-azobenezenedicarboxylicacid
H_2CHDA	1,4-cyclohexanedicarboxylic acid
C_{60}	fullerene
AFM	atomic force microscopy

ATR-FTIR	attentuated total reflectance fourier transform infrared spectroscopy
BET	Brunauer, Emmett and Teller
DFT	density functional theory
EDX	energy-dispersive X-ray spectroscopy
EELS	electron energy loss spectroscopy
GIWAX	grazing incidence wide-angle scattering
ICP	inductively coupled plasma
NMR	nuclear magnetic resonance
PXRD	powder X-ray diffraction
SXRD	single crystal X-ray diffraction
SEM	scanning electron microscopy
TEM	transmission electron microscopy
TGA	thermalgravimetric analysis
XRD	X-ray diffraction
UV-Vis	ultra violet-visible
δ (ppm)	chemical shifts in parts per million

Abstract

The present thesis has been devoted to the synthesis of a series of novel carborane-based Coordination Polymers (CPs) or Metal Organic Frameworks (MOFs) incorporating also polycarboxylate ligands and various metals. These obtained carborane-based MOFs exhibited various architectures including 2D and 3D structures, some of them porous. Motivated by the observed weak interactions between layers in the 2D materials, the first high-aspect ratio carborane-based Metal Organic Nanosheets (MONs) were produced via exfoliation of 2D bulk crystals using top-down method.

In **chapter 1**, a brief introduction on CPs and MOFs is given, and relate this with Soft Porous Crystals (SPCs) and their Guest dependent transformations and properties. Then is briefly introduced the current methodologies and applications of Metal Organic Nanosheets (MONs) and the chapter is concluded with a short history of Carboranes, their properties and their used as linkers in CPs and MOFs.

In **chapter 2**, the general and specific objectives of this thesis are introduced.

In **chapter 3**, the synthesis and characterization of a family of carborane-based coordination polymers are described. They are constructed with cobalt or zinc metals sources, tritopic or tetratopic carboxylic acids and a bis-pyridylalcohol carborane linker. All new compounds have been fully characterized and their structures are described. One of the structures, **CB1**MOF-1 possesses large solvent accessible channels and shows a crystal sponge behavior. **CB1**MOF-1 can incorporate a variety of solvents and their structures have been determined by Single Crystal X-ray Diffraction (SXRD). A higher number of interactions could be observed between aromatic guest molecules and the **CB1**MOF-1 framework and a correlation has been found between such host-guest intermolecular interactions and the mechanical properties of **CB1**MOF-1 ⊃ **Guest** by nanoindentation experiments.

In **chapter 4**, a reversible single-crystal to single-crystal transformation of **CB1**MOF-1 is introduced. This 3D porous MOF could be transformed into 2D non-porous

structure through replacement of initial solvent (DMF) by poor hydrogen acceptor molecules following thermal vacuum treatment. In the final 2D structure **CB1**MOF-1′, the carborane linker coordinate to Co atoms in the same layer instead of in different layers like in **CB1**MOF-1. Notably, this transformation is reversible via simply heating the 2D phase in DMF solution. By taking advantage of this unprecedented reversible transformation, encapsulation of a large molecule such as fullerene was achieved.

In **chapter 5**, a disubstituted 3-pyridylphenylalcohol carborane ligand (**CB2**) and a B-iodinated bis-pyridylphenylalcohol carborane ligand (**I-CB2**) were synthesized and characterized. Solvothermal reactions of **CB2** with $Co(NO_3)_2$ and tri- and di-topic carboxylic acid afford four new carborane-based MOFs **CB2**MOF-1 to **CB2**MOF-4. Substitution of **CB2** with **I-CB2**, an iodo-functionalized compound **I-CB2**MOF-1 was obtained, which is isostructural with **CB2**MOF-1. The structures of those new MOFs were solved by SXRD and fully characterized. A fast reversible solid to solid transformation was observed for both materials 2D **CB2**MOF-1 and **I-CB2**MOF-1. When the DMF solvent molecules in the channel were exchanged by poor polar solvents or evacuated, a sliding of layers is observed affording **CB2**MOF-1′ and **I-CB2**MOF-1′. The initial framework could be recovered simply by immersing the crystals in DMF solution at room temperature for 30 min. **CB2**MOF-1′ and **I-CB2**MOF-1′ are non-porous to N_2 but porous to CO_2.

In **chapter 6**, we extend the investigation from the bulk carborane-based MOFs to high aspect ratio metal-organic framework nanosheets. Considering the brittle interaction involved in the 2D carborane based MOFs, they are adopted to exfoliate into ultrathin nanosheets. **CB1**MON-1 was obtained by exfoliation or delamination of **CB1**MOF-1′ by fast sonication. Similarly, **CB2**MOF-1 and **I-CB2**MOF-1 could also be delaminated into atomic thickness **CB2**MON-1 and **I-CB2**MON-1 respectively. The high-resolution images of SEM and TEM give information on their flat and large particle size distribution. The detected height profiles from AFM show a few layers thickness thus identifying its high surface to volume atom ratio. Tyndall light scattering effects

demonstrates the existence of nanosheets in solution. More specifically, the GIWAX spectra indicating the nanosheets are highly oriented deposited on the substrate.

x

Resumen

Este trabajo de Tesis está dedicado a la síntesis de una nueva familia de Polímeros de Coordinación (CPs) o Redes Metalorgánicas (MOFs) basados en la unidad carborano y que incorporan además ligandos policarboxílicos y diversos metales. Los MOFs obtenidos muestran diversas arquitecturas con estructuras 2D y 3D, algunas de ellas porosas. Motivados por la presencia de interacciones débiles entre capas en los materiales 2D, se ha realizado la exfoliación de dichos materiales usando un método descendente (tow-down). De esta manera se han obtenido las primeras Nanocapas (MONs) ultrafinas decoradas con carborano y con elevadas dimensiones laterales.

En el **Capítulo 1**, se hace una breve introducción sobre los CPs y MOFs, para pasar a describir los Cristales Porosos Blandos (SPCs) y las transformaciones y propiedades relacionadas con los huéspedes en este tipo de materiales. A continuación se introduce brevemente el concepto de Nanocapas Metalorgánicas (MONs), así como los métodos de preparación y aplicaciones de las mismas. Finalmente se describe brevemente la historia y propiedades de los carboranos, así como su empleo como ligandos en CPs y MOFs.

En el **Capítulo 2**, se introducen los objetivos generales y específicos de la presente tesis.

En el **Capítulo 3**, se describe la síntesis y caracterización de una familia de polímeros de coordinación basados en carborano. Estos materiales se construyen con cobalto o zinc, ácidos tri- o tetra-carboxílicos y un ligando carborano funcionalizado con bis-piridilalcoholes (**CB1**). Los nuevos compuestos se han caracterizado completamente y se describen las estructuras cristalinas. Una de dichas estructuras, **CB1**MOF-1 se comporta como una esponja cristalina, ya que presenta canales grandes en los que se alojan una variedad de disolventes. Se han determinado las estructuras cristalinas para los diversos materiales **CB1**MOF-1 ⊃ **Guest** mediante Cristalografía de Rayos X de cristal único (SXRD). Se ha observado un mayor número de interacciones intermoleculares con el material en aquellos casos en que el disolvente es aromático y

se ha establecido una relación directa entre esto y las propiedades mecánicas de material mediante experimentos de nanoindentación.

En el **Capítulo 4**, se describe una transformación reversible de cristal-único a cristal-único en **CB1**MOF-1. Este MOF 3D y poroso es capaz de transformarse en una estructura 2D y no porosa al intercambiar el disolvente en los canales (DMF) por otros disolventes que se comportan como malos aceptores de enlaces por puente de hidrógeno, y tras ser sometido posteriormente a un tratamiento de calentamiento y vacío. En la estructura final 2D **CB1**MOF-1′, el ligando carborano se coordina a átomos de Co en la misma capa, a diferencia de en **CB1**MOF-1, que se coordina entre capas. Cabe destacar además que dicha transformación es reversible y requiere tan solo calentar la fase 2D en DMF. Usando esta transformación reversible, se ha podido encapsular una molécula grande como es el fulereno.

En el **Capítulo 5**, se describe la síntesis y caracterización de un nuevo ligando carborano que contiene los fragmentos bis-piridilfenilalcohol (**CB2**) y el análogo correspondiente en el que uno de los boros del clúster ha sido iodado (I-**CB2**). Las reacciones solvotermales de **CB2** con $Co(NO_3)_2$ y tri- o di-carboxilatos han dado lugar a cuatro nuevos CPs basados en el carborano **CB2**MOF-1 a **CB2**MOF-4. El compuesto iodado I-**CB2**MOF-1, análogo a **CB2**MOF-1, se ha obtenido mediante el empleo de I-**CB2** en lugar de **CB2** en la síntesis. Las estructuras de los nuevos compuestos se han resuelto mediante SCXRD en la mayoría de los casos. Se describe además en este capítulo, una transformación de fase sólido-sólido en ambos materiales 2D **CB2**MOF-1 y **I-CB2**MOF-1. La transformación parece ser debida al desplazamiento lateral de las capas en la estructura masiva, al intercambiar el disolvente inicial (DMF) por disolventes poco polares y dando lugar a dos nuevas fases **CB2**MOF-1′ y **I-CB2**MOF-1′. Las estructuras iniciales se recuperan fácilmente mediante la inmersión de las últimas en DMF a temperatura ambiente y en 30 minutos. Se ha encontrado además que **CB2**MOF-1′ y **I-CB2**MOF-1′ no son porosos a N_2 pero sí lo son a CO_2.

En el **Capítulo 6**, se expande la investigación de los MOF basados en carborano

masivos (bulk) a la formación de nanocapas metalorgánicas. Las débiles interacciones entre capas de los materiales masivos 2D basados en carborano permiten exfoliarlos para dar lugar a nanocapas ultrafinas. Así, **CB1**MON-1 se ha obtenido mediante exfoliación o delaminación de **CB1**MOF-1´ mediante sonicación rápida. De la misma manera **CB2**MON-1 y **I-CB2**MON-1 se han obtenido mediante delaminación de **CB2**MOF-1 y **I-CB2**MOF-1, respectivamente. Se han realizado imágenes de alta resolución mediante espectroscopias SEM y TEM de las nanocapas, y que muestran la naturaleza plana y la distribución y gran tamaño de partículas. Los perfiles de altura medidos mediante AFM muestran un grosor de pocas capas y por tanto demuestran un elevado ratio de superficie a volumen atómico. El efecto Tyndall demuestra la existencia de nanocapas en disolución. Más específicamente, los espectros de GIWAX indican que las nanocapas presentan una alta orientación cuando son depositadas sobre un substrato.

Table of Content

Chapter 1

Introduction

1.1 Metal-organic frameworks (MOFs)

1.1.1 From Coordination Polymers to MOFs

Coordination polymers (CPs) belong to the extensive family of Coordination Compounds (CCs), where materials are built by joining metal-containing units with organic linkers through coordination bonds. Therefore, they are considered the natural extension of CCs towards polymerization. The dimensionality and architecture of these hybrid compounds are principally defined by the coordinative geometry of these two components, making possible to extend their structures in one, two or three dimensions leading to chains, layers and three-dimensional frameworks, respectively (Figure 1-1). It is well known that, due to the large number of available metal ions and organic ligands, as well as the different geometries of the coordinated nodes, the variety of the potential CP structures is almost unlimited.[1]

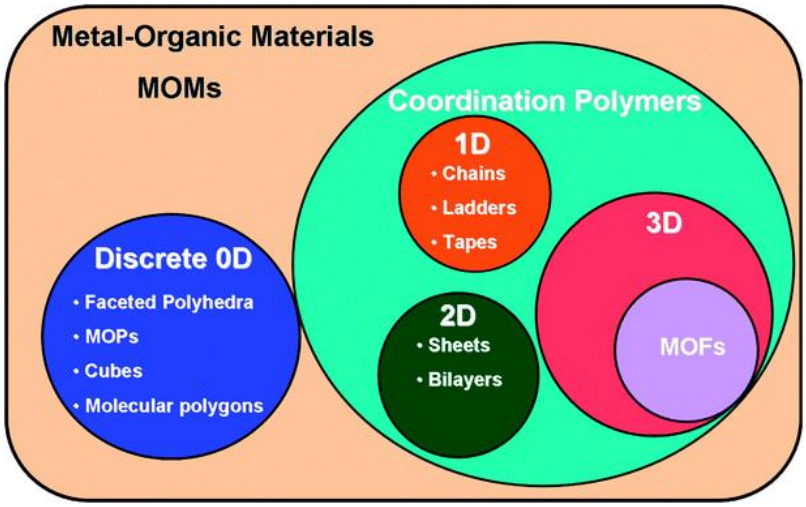

Figure 1-1. Metal–organic materials encompass discrete as well as extended structures with periodicity in one, two, or three dimensions. The latter have also been referred to as coordination polymers, metal–organic frameworks, and hybrid inorganic–organic materials.[2]

Metal-organic Frameworks (MOFs) are a class of porous crystalline materials based on the assembly of organic ligands and metal centers or metal-containing units. IUPAC (The International Union for Pure and Applied Chemistry) has recommended to define MOFs as "a coordination compound continuously extending in 1, 2 or 3 dimensions through coordination bonds (coordination polymer or alternatively coordination

network) with an open framework containing potential voids"[3]. The first MOF was born in Yaghi's group in 1995[4]. They synthesized an extended crystalline open framework $Cu(4,4'\text{-bpy})_{1.5}\cdot NO_3(H_2O)_{1.25}$ through hydrothermal reaction. This MOF possessed large rectangular channels filled with nitrate ions which could be exchanged by other anions, indicating the accessibility to channel of crystalline zeolite-like coordination polymers. Since Yaghi introduced the term of "MOF", the related publications in this field sprung up over the scientific community which is illustrated with an huge number of ca. 70 000 MOFs collected in Cambridge Structural Database (CSD) during last 20 years (Figure 1-2)[5]. This trend is still increasing as the building-block approach to MOFs synthesis provides more possibility to create new materials.

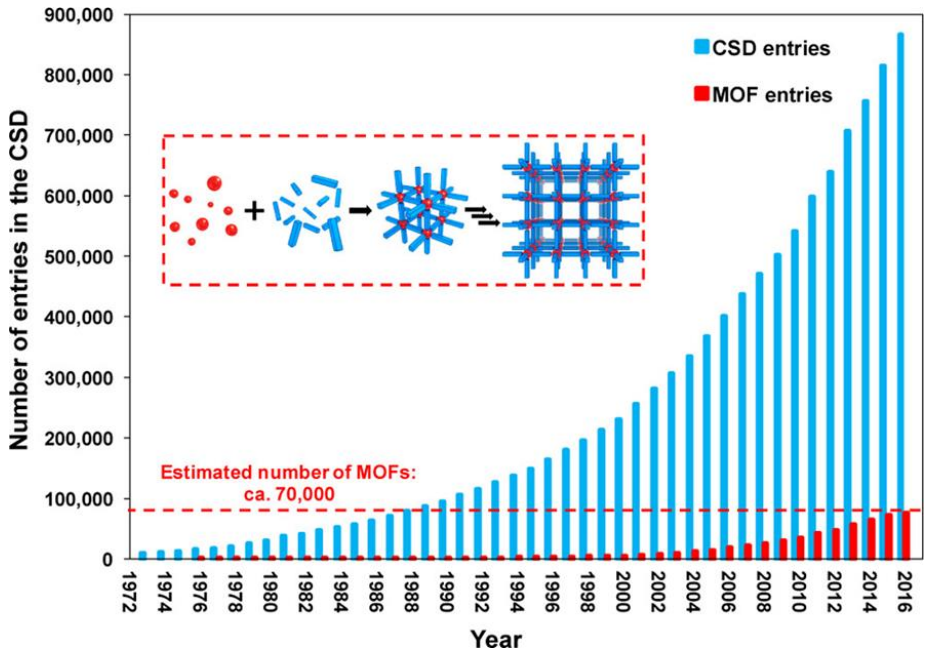

Figure 1-2. Growth of the CSD and MOF entries since 1972. The inset shows the MOF self-assembly process from building blocks: metals (red spheres) and organic ligands (blue struts)[5].

The immense interest in MOFs is due to their unprecedented properties[6–13]. Once the solvents, unreacted ligands and counterions in the frameworks are evacuated, their structures can be porous. Interestingly, the crystallinity of these compounds allows their characterization by X-ray diffraction, considerably simplifying efforts to use computational modelling in order to predict or justify their unique physical and chemical properties[14]. Apart from the purely metal ligand coordination bond, weak non-covalent interactions are of great importance because they can be responsible of

the final dimensionality, by packing one-dimensional chains or two-dimensional layers. The hybrid nature of CPs and MOFs is translated in a synergic effect between the metal containing sub-unit and the bridging ligands, where the characteristic properties of the building blocks are transferred to the final extended structure. The extraordinary variability for both, the organic and the inorganic components, provides endless possibilities and make CPs/MOFs to be strongly interesting for many potential applications[15]. The wide range of properties and potential applications that these promising materials offer goes from gas storage[7,16], chemical separations[17], chemical sensing[18], drug delivery to catalysis[19], light harvesting[13], proton conductivity[20] and magnetism[21] among others. In addition, the chemical functionality of the final materials can be tuned by modifying the functional groups of the organic ligands[22].

However, other porous materials such as aluminosilicates or zeolites have been preferentially utilized and the market has been totally dominated by them because MOFs family still present a number of limitations, such as the scale-up synthesis, production cost and chemical or mechanical stability, that do not allow them to be fully introduced in the industry yet. Specifically, these stabilities are determined by some well-known factors. On one hand, their lack of chemical stability is largely determined by the presence of environmental humidity that causes the cleavage of coordination bonding between metal nodes and organic ligands[23] (Figure 1-3). For this reason, researchers have recently begun to investigate hydrophobic and superhydrophobic MOFs to enhance their aqueous stability and enable new applications (*e.g.* self-cleaning)[24]. Some advances have been made to this end. The most common strategy to synthesize these hydrophobic MOFs is via introduction of hydrophobic molecules as linkers (*e.g.* trifluoromethyl group[25,26], carboranes[27], and alkyl chains[24,28]).

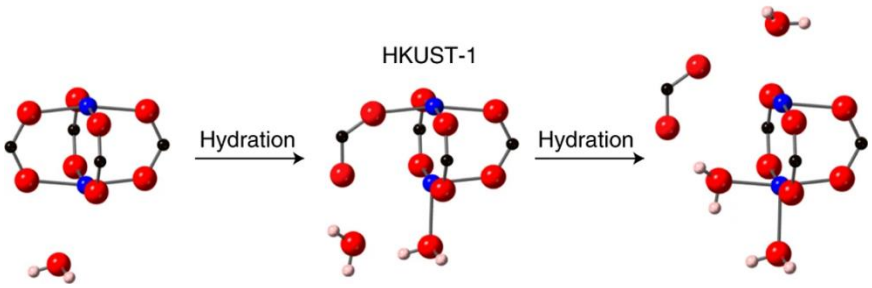

Figure 1-3. Mechanism of paddlewheel breakdown in HKUST-1 where the adsorption of water onto the open metal sites in HKUST-1 can release energy that can then be used to break metal–carboxylate oxygen bonds in the paddlewheel, opening up further sites for more water adsorption, leading to the breaking of another metal–carboxylate oxygen bond and eventual breakdown of the HKUST-1 structure. Blue spheres, Cu; red, O; black, C; pink, H[29,30].

Due to their hybrid inorganic–organic nature, MOFs possess attractive characteristics that are absent from purely inorganic or organic systems. MOFs can exhibit, for instance, higher thermal stabilities than organic polymers while maintaining a degree of mechanical flexibility that is largely inaccessible to inorganic materials[31]. By conventional mechanical property metrics such as the Young's modulus and hardness, MOFs also bridge a design space that spans those of both traditional "soft" and "hard" materials[32]. However, it is this hybrid nature combined with their permanent porosity that leads to some of their most attractive characteristics from an applications standpoint. For example, dynamic behaviors under applied stress are observed that make these "soft-porous"[33] network structures flexible or stimuli-responsive[34]. Although many phenomena fall within the realm of flexible materials, such as gate-opening[35], or breathing[36], all involve some degree of structural change, which will lead not only to a variation in porosity but also in mechanical properties[37]. However, flexibility often comes with the penalty of reduced stability, which limits their applications. Thus, the development of flexible yet stable MOFs depends on a better fundamental understanding of the conformational changes or phase transitions associated with such flexibility, opening the way to the rational design of novel "smart" or stimuli-responsive materials[38].

1.1.2 Soft porous crystals (SPCs): a subclass of MOFs

In 1998, porous coordination polymers were divided into three categories as shown in

figure 1-4[39]. The initial generation of materials exhibited fragile porosity which will collapse irreversibly after removing the guest molecules from channels or caves in the frameworks. Afterwards, a class of stable and robust frameworks have been produced that could maintain the structure after thermal activation and be considered as high porous zeolites. More recently, the third generation, soft porous crystals, have been introduced by Kitagawa that exhibited both a highly ordered network as well as a flexible and dynamic behavior of frameworks responding to chemical or physical external stimuli[33]. Its rigid regular porous structure is beneficial for molecular sieving and storage for guest species avoiding structural collapse under severe conditions similar to zeolites and aluminophosphates. Unlike the first two generation materials, soft porous crystals displayed a reversible transformability between different states, at least accessible to guest molecules in one crystal phase thus reflecting a reproducible guest adsorption. During the single crystal to single crystal transformation, the imperfect crystallinity of MOFs could be produced as a consequence of partially loss of long-range order of frameworks instead of whole structure collapsing.

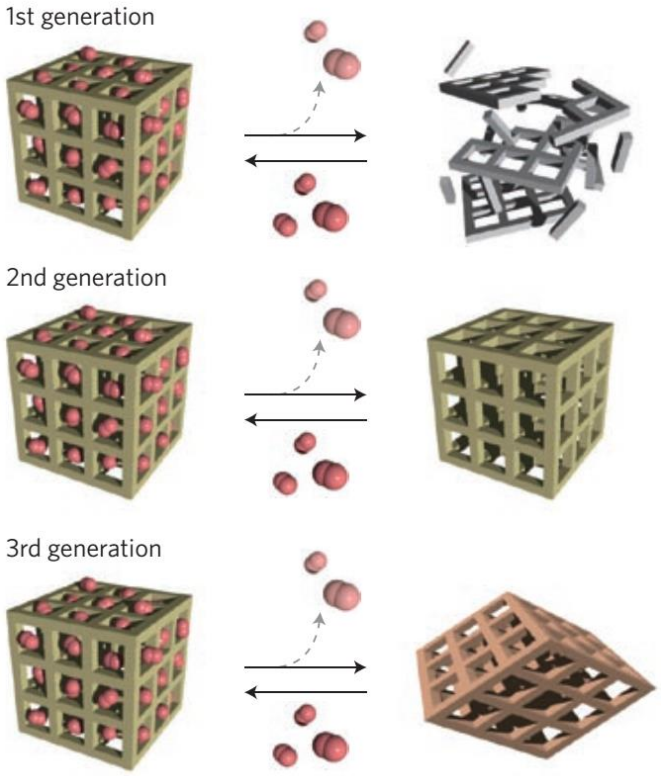

Figure 1-4. Classification of porous coordination polymers into three categories[33].

1.1.2.1 Guest dependent properties of SPCs

The flexible and responsive SPCs could act as the crystal sponge for guest molecules via a number of variable host-guest interactions between the frameworks and adsorbed molecules, which bring various interesting properties for materials. In 2002, Fujita reported a springlike 3D-coordination networks that transform in a crystal-to-crystal mode depending on guest removal and readsorption without impact in its framework or crystallinity (Figure 1-5)[40]. This structure is capable of exchanging initial guest molecules for a variety other guest molecule whose structure is able to be detected by single-crystal diffraction even after guest replacement.

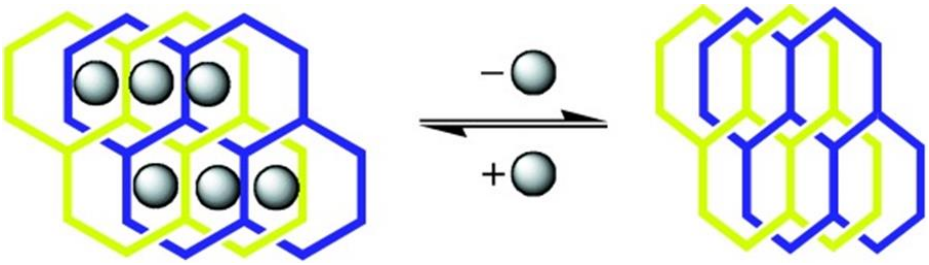

Figure 1-5. Schematic representation of the contraction or expansion of the 3D network on the removal or addition of guest molecules, respectively[40].

Mechanical properties are of great importance for materials applying in industry. However, research related to mechanical behavior of SPCs has been rarely reported[41]. Currently, Cheetham and coworkers firstly disclosed the exceptional anisotropic mechanical behavior of a series of pillared-layered SPCs of $[M_2L_2P]_n$ frameworks by single crystal nanoindentation measurements[42]. The nanomechanical properties were controlled by simple adsorption of diverse guest molecules. Immersing as-synthesized $[Zn_2(NO_2\text{-bdc})_2(dabco)]_n$ (**1**, NO_2-bdc=2-nitro-1,4-benzenedicarboxylate) into an excess of organic solvents, such as dimethyl sulfoxide (DMSO), mesitylene or toluene to exchange DMF molecules in the structure **1**, tetragonal structures with different framework geometry either bent (**1**⊃dmso) or straight NO_2-bdc linkers (**1**⊃mesitylene, **1**⊃toluene) (Figure 1-6) were obtained. Among them, **1**⊃dmso shows the largest anisotropy and the largest elastic anisotropy measured experimentally in the MOF area. This exceptional mechanical anisotropy is of major importance for variable applications such as sensitive pressure sensor or artificial skin[42].

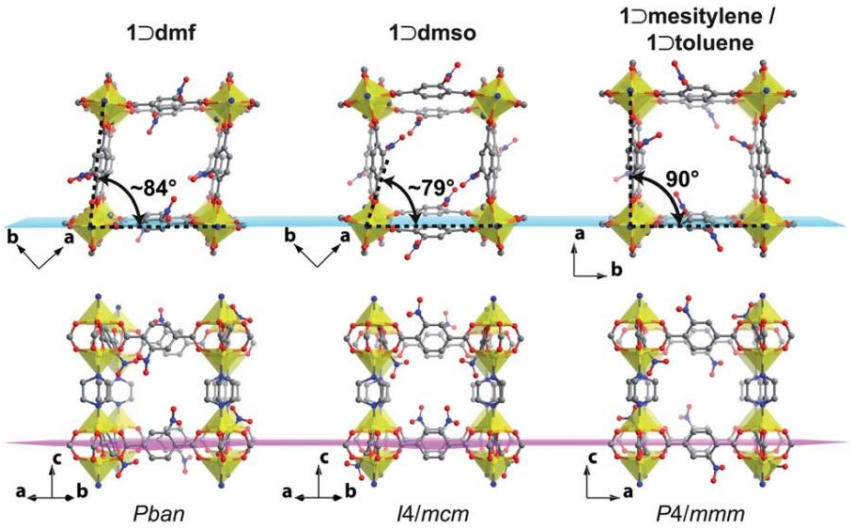

Figure 1-6. Representation of the crystal structures of different guest containing forms of $[Zn_2(NO_2\text{-}bdc)_2(dabco)]_n$ (1) viewed along the dabco axes (top) and the linker axes (bottom). Zn polyhedra, O, N and C atoms are shown in yellow, red, blue and grey. Disordered groups, H atoms and guest molecules are not shown. The dabco-linker plane ({110} for 1⊃dmf and 1⊃dmso; {100} for 1⊃mesitylene and 1⊃toluene) is shown in cyan and the plane orthogonal to the dabco axis ({001} for all compounds) is highlighted in pink. The dihedral angles between the {110}/ {100} plane and the carboxylate groups of adjacent linkers are shown in the upper panel[43].

In 2016, a novel series of 2D MOF of general formula $[Co(bpeb)_2(NCS)_2]\cdot nG$, where G stands for the ortho-dichlorobenzene (DCB@1 with n = 7), thianthrene (TAN@1 with n = 4), toluene (TOL@1 with n = 6), and pyrrole (PYR@1 with n = 8) guest molecules was synthesized with cobalt(II) single-ion magnets (SIMs) and long rod-like aromatic bipyridine ligands, possessing large square channels to accommodate different guest molecules. Based on the single crystal X-ray diffraction, the encapsulated solvent guest molecules induced non-negligible distortions on the ligand conformation thus, endowing a "fingerprint" on the cobalt environments and tune the slow magnetic relaxation effects of the SIM nodes. These results expand scope of guest-dependent SIM-MOFs[44].

1.1.2.2 Properties from transformations of SPCs

In general, the bond energies of coordination and hydrogen bonding from metal-ligand typically range from 10 to 200 kJ/mol, certainly lower than the covalent or ionic bonding with energies distributing typically between 200 and 1000 kJ/mol[45]. This

allows the realization of reversible bonding cleavage and regeneration in coordination frameworks that contributes the design and application of flexible MOFs. Such transformation often involves geometry deformation or topology change of framework, such as "breathing" behavior responding to external stimuli, reconstruction associated with secondary building units (SBUs) and photo-tuning transformation.

Inspired by the classic philosophy paradox, "ship of Theseus", Hupp and Farha developed a sequential building block replacement (BBR) method to endow specific properties for daughter porous MOFs via substitution of organic ligand and node transmetalation based on the affinity and strength of coordination bond to retain original network topology as exhibited in figure 1-7. The mother MOF $Zn_2(tmbdc)_2(bpy)$ has a non-catenated pillared-paddlewheel structure, whose exchange of two ligands was accomplished by soaking in an access of concentrated new ligand solution. In essence, the solvent assisted ligand exchange (SALE) could be achieved because the incoming linker shows higher affinity for node-based metals than the linker being replaced. Similarly, considering the relative strength of coordination bonding increase as: $Cu^{2+} > Ni^{2+} > Co^{2+} \approx Zn^{2+}$, Ni (II) was chose to substitute the Zn (II) by iterative immersion (three times) of $Zn_2(ndc)_2(dabco)$ to a concentrated solution of $Ni(NO_3)_2 \cdot 6H_2O$. The progressive transformation was proved by NMR of digested crystals in D_2SO_4 and $[D_6]$DMSO and the obtained isostructural MOF $Ni_{1.5}Zn_{0.5}(ndc)_2(dabco)$ exhibited higher BET surface areas owing to boosted structural stability resulting from stronger coordination connection of Ni atoms comparing with Zn atoms[46].

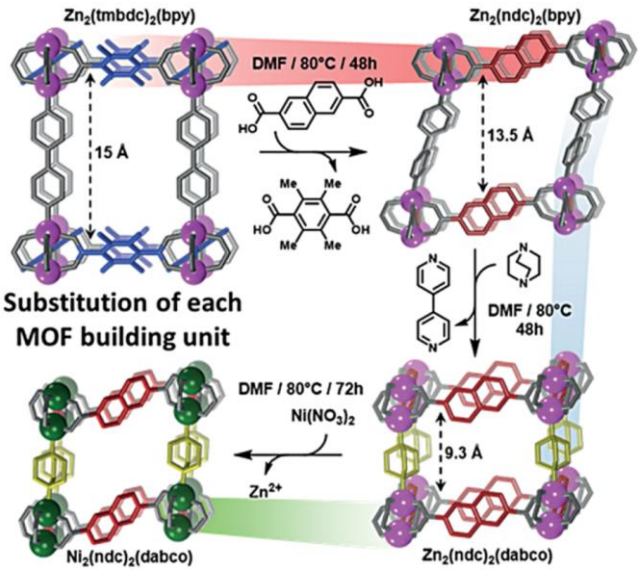

Figure 1-7. Representation of the parent framework with all of its original components replaced completely with other new ones via SALE and transmetalation to give the daughter framework[46].

Among numerous SPCs, the potential instability of SBUs could be taken advantage to build flexible frameworks. For instance, controlling the existence of coordinated solvents molecules in metal units sometimes leads to variation of coordination numbers and geometry of metal nucleus introducing favorable properties rather than collapsing the structure. Bu's group presented a reversible single-crystal to single-crystal structural transformation of a Co (II) -based framework which is the first example of self-penetrating to interpenetrating topology transformation in a 3D MOF (Figure 1-8). When the $[Co_{1.5}(tipb)(SO_4)(pta)_{0.5}]\cdot(DMF)_{1.75}$ (BP⊃DMF) was exposed to air, the coordinating configuration of Co(II) ions altered from tetrahedral to octahedral that was indicated by the color changed of crystal from blue to red (Figure 1-8). Particularly, such transformation is reversible and rapid thus creating a switchable "gate" effect where the pta^{2-} ligands act as gates distributing in the channels. This character allows it to be suitable platform for sensing and monitoring for coordinative molecules. [47]

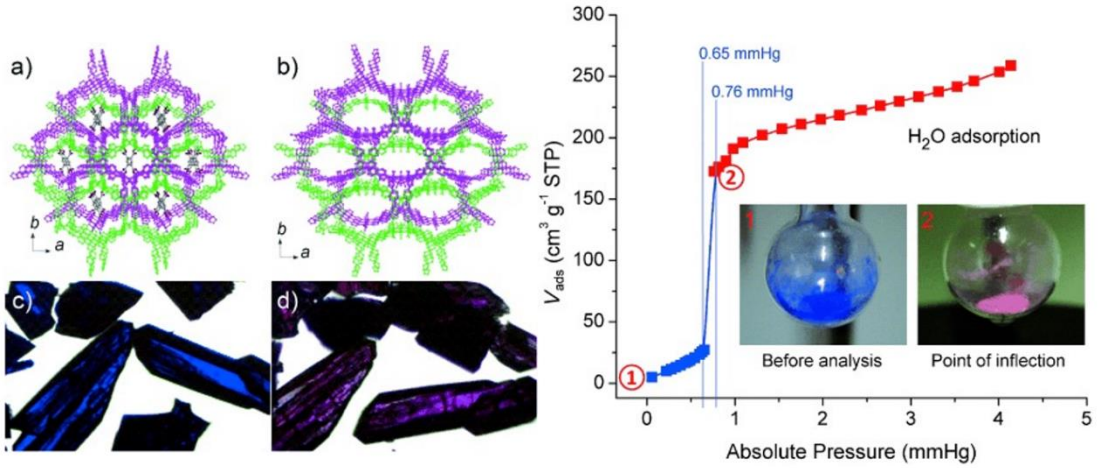

Figure 1-8. (a) Self-penetrating framework of BP. (b) Twofold interpenetrating framework of RP. Microscope image of (c) BP⊃DMF (blue) and (d) RP-H_2O (red) crystals. (e) The SC-SC transformation during H_2O adsorption[47].

Broadly speaking, the comprehensive investigation of structural transformation is still rare, especially continuous reversible behavior of flexible MOFs. In 2017, Lee Brammer and coauthor reported a diamondoid metal–organic framework $(Me_2NH_2)[In(ABDC)_2]$ (ABDC, 2-aminobenzene-1,4-dicarboxylate) whose structure shows a solvent-switchable continuous-breathing behavior reflected by its selectivity of CO_2 versus CH_4[48]. Apart from these conventional stimuli, broad wavelength of light has apparent advantage due to driving photoreactive processes without the generation of any byproducts. Utilizing photo-sensitive organic ligand is recognized as a proper route to design a light responsive MOF[49,50].

Despite the exciting application opportunities of these SPCs, to date, there is no reported fully rational method for designing a breathing MOF. As mentioned above, flexibility often comes with the penalty of reduced stability, which limits their applications. Collapsing of the structures is generally the rule, and reversible flexibility mostly a question of serendipity. Thus, the development of flexible yet stable third-generation MOFs depends on a better fundamental understanding of the conformational changes or phase transitions associated with such flexibility, opening the way to the rational design of novel “smart” or stimuli-responsive materials.

1.2 From bulk crystals to nanosheets: Metal-organic frameworks nanosheets (MONs)

Among the large number of MOFs structures, 2D layered structures take a large proportion[5]. Recently, inspired by the favorable properties of single-layer-graphene and other functional inorganic nanolayers, 2D-MOFs tend to be fabricated into high aspect ratio metal organic frameworks nanosheets (MONs) isostructural to bulk crystals[51] (Figure 1-9). Accordingly, MONs can be defined as materials that possess the following: "1) organic ligands coordinated to metal ions or clusters with continuous connectivity in two-dimensions, but only non-covalent interactions in the third dimension; 2) highly anisotropic materials with one dimension approaching monolayer thickness and the others being at least an order of magnitude larger and approximately equal in size; 3) materials which can be isolated in a form with the dimensions outlined above as free standing sheets, not attached to a surface or other scaffold or as layers in a bulk material "[52].

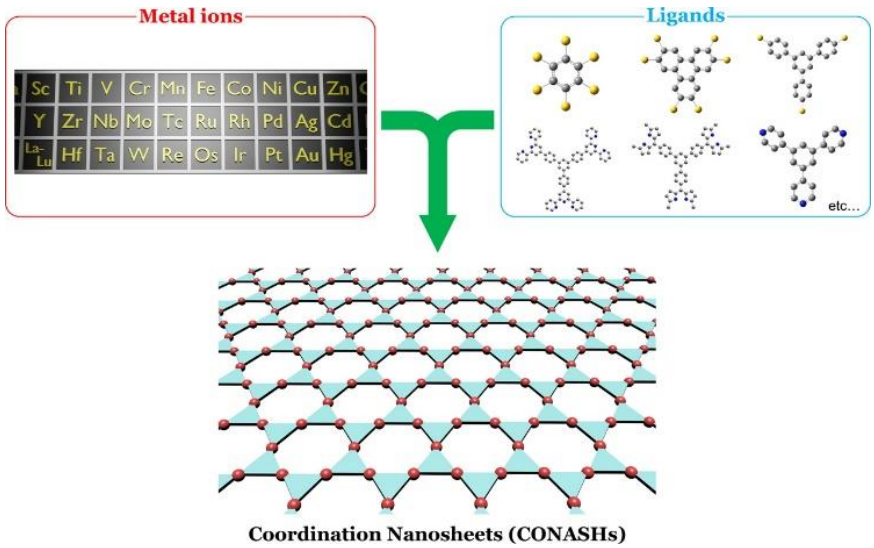

Figure 1-9. Concept of the coordination nanosheets (CONASHs). Various combinations of metal ions and ligands produce a range of functionalized CONASHs[53].

However, synthesizing high surface-to-volume atom ratios MONs is still difficult since growing 2D frameworks to the microscale and at the same time maintaining crystal stacking in the few or mono-layer often leads to fragile nanosheets lacking long-range order. Moreover, in terms of characterization, owing to specific structure of MONs, sets

of specific of proper techniques are required to identify its structures and explore properties. For instance, synchrotron grazing incidence X-ray diffraction (GIXRD), which is sensitive to lattice parameters parallel to horizon direction, can be used as an ideal technique for detecting the in-plane peaks of MONs[54–56]. Grazing incidence wide-angle X-ray scattering (GIWAX) and grazing incidence small-angle X-ray scattering (GISAX) are also powerful and versatile structural measurement techniques to probe nanoscale objects deposited on surfaces[57,58]. Solid state nuclear magnetic resonance spectroscopy (NMR), pair distribution function (PDF) data, X-ray photo spectroscopy (XPS), selected area electron diffraction (SAED) and Raman spectroscopy are also adopted to probe the structure and composition information of nanosheets. In addition to the structural analysis, the nanoscopic characteristics must also be investigated. Atomic force microscope (AFM) is used to determine the thickness of nanosheets. Scanning electron microscopy (SEM) and transmission electron microscopy (TEM) provide information about morphology with high resolution images. Energy dispersive X-ray spectroscopy (EDX) and electron energy-loss spectroscopy (EELS) were utilized to analyze the elemental distribution of nanosheets.

1.2.1 Synthesis of MONs

Different from preparation of MOFs materials, the synthesis of MONs is not restricted to self-assembly of organic linkers and metal ions or clusters, but also include delicate exfoliation from stacked bulk crystals to provide highly anisotropy 2D freestanding nanosheets (Figure 1-10). However, it remains challenging to fabricate high quality MONs with high aspect-ratio in high yield because the breaking off 2D layers and structural collapse needs to be prevented during the process. Furthermore, it is very important to control the thickness of the lamellar to avoid aggregation. To address these challenges, researchers have developed two main approaches, top-down and bottom-up methods related to a variety of nanosheets which have yielded promising applications. Top-down methods are mostly used for the 2D MOFs which are formed by layers stacking perpendicular to horizon direction with weak interactions, such as van der

waals forces, hydrogen bonding, π-π interaction, *etc*. The non-covalent bonding between layers allows the exfoliation without disturbing the coordination within layers. At present, the reported top-down approach includes liquid sonication exfoliation[59], Scotch tape method (mechanical exfoliation)[60], chemical exfoliation[61], Li-intercalation[62] and freeze–thaw method[63], to name a few. Although the top-down method is simple and efficient, the exfoliation rate and yield are generally too low for further application. Another important approach is bottom-up, which controls the growth of crystals within only two dimensions resulting in fewer layers or even monolayers without the need of further modification. Additionally, there are some researchers which successfully achieved the stacking of the layers via bottom-up method including interfacial synthesis[56], three-layer synthesis[64], modulated synthesis[65] and directly sonication synthesis[66] *etc*. In fact, the combination of solvents influenced the morphology and crystallinity of nanosheets *via* modulation of MOF growth kinetics. Although the research in MONs has developed with unexpectedly fast space, there are still some problems to solve such as chemical and mechanical stability or flexibility.

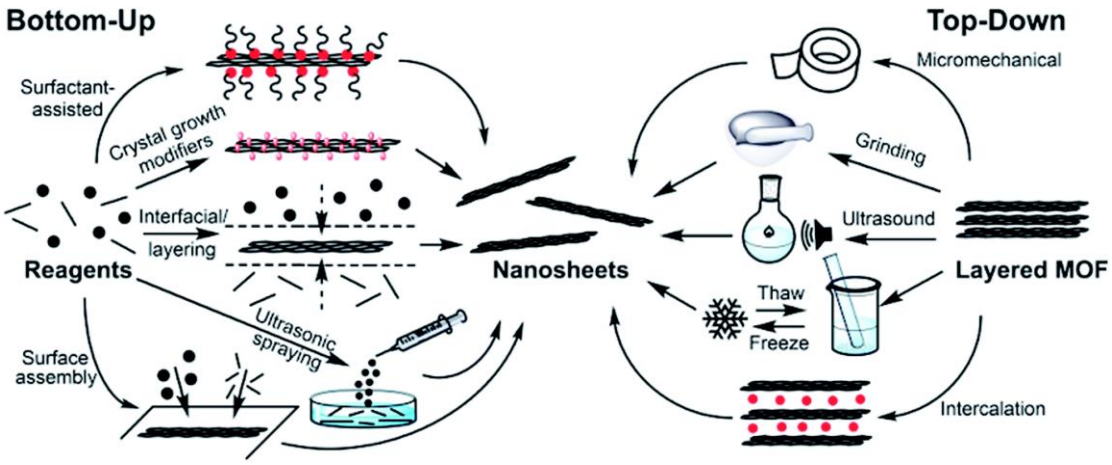

Figure 1-10. Schematic illustration of the bottom-up and top-down methodologies for producing MONs.[52]

1.2.2 Properties of MONs

In the past several years, MONs showed excellent performance in wide range of applications such as energy storage, biology, medicine and sensing[59,64,67–69]. This is

due to its unique properties stemming from distinct ultrathin 2D structures. They do not only share the advantages of other bulk 2D MOFs, such as chemical tunability and dynamic behavior, but also overcome the shortcomings from stacked layers and buried active sites.

MONs, due to the large number of exposed active sites and short diffusion distance for the regents during reaction, have attracted more and more attention as electrochemistry catalysis. Oxygen evolution reaction (OER), a reaction related to metal–air batteries, and water splitting technologies—typically require expensive noble metal or metal oxides. MONs showed high potential to improve this situation. Recently, Huang *et. al.*[70] used electrochemical exfoliation of a pillared-layer metal–organic framework to obtain a 2D ultrathin nanosheet which boost the oxygen evolution reaction. It is an efficient catalyst with overpotentials as low as 211 mV at 10 mA/cm^2 and a turnover frequency as high as 30 s^{-1} at an overpotential of 300 mV. After exfoliation, the concentration of active sites increased 4 times than 3D bulk crystals which is important for the significant improvements of the OER performances (Figure 1-11a). In 2014, Gascon *et. al.* prepared high aspect ratio and high quality Cu(BDC) MOF nanosheets using a bottom-up strategy depending on diffusion-mediated modulation of the MOF growth kinetics. The two-dimensional nanosheets could be incorporated into polymer matrices to obtain ultrathin MOF–polymer composites with outstanding CO_2 separation performance from CO_2/CH_4 gas mixtures, together with an unusual and highly desired increase in the separation selectivity with pressure. This is mainly due to superior occupation of membranes cross-section by nanosheets fillers distributing uniformly at different depth thus effectively eliminates the undesired plasticization effect and repeats gas discrimination to improve separation selectivity[64] (Figure 1-11b). Additionally, the suppressed fluorescence of materials could be turned on via solvent-mediated exfoliation which is beneficial for biology sensing platforms[71]. Zhang's group adopted 2D M-TCPP M = Zn, Cu, Cd or Co, TCPP = tetrakis(4-carboxyphenyl)porphyrin) nanosheets as fluorescent sensing platforms for DNA detection. The 2D Cu-TCPP nanosheet exhibits the best performance for sensing DNA with detection limit of 20 ×

10^{-12} M, which is much lower than the previously reported MOF particle-based fluorescent assays[72] (Figure 1-11c).

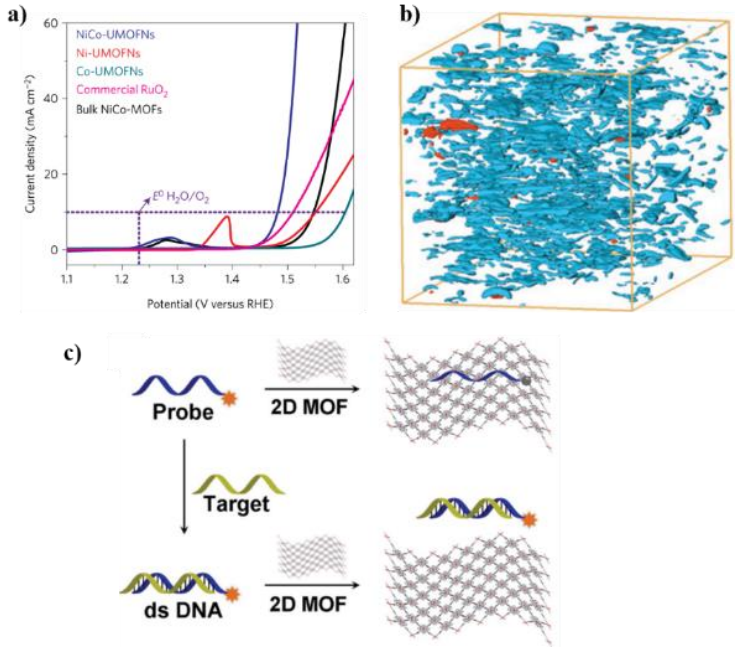

Figure 1-11. (a) Polarization curves of NiCo-UMOFNs, Ni-UMOFNs, Co-UMOFNs, RuO_2 and bulk NiCo-MOFs in O_2-saturated 1 M KOH solution at a scan rate of 5 mV/s. The dotted horizontal line is a guide to the eye showing a current density of 10 mA/cm^2[73]; (b) FEB-SEM of nanosheets dispersed in a polymer membrane[64]; (c) Schematic illustration of 2D MOF nanosheet-based fluorescent DNA assay[72].

1.3 Carborane-based MOFs

As described above, MOFs are usually constructed by the assembly of organic ligands and metal centers or metal-containing clusters. In the last decade, a few groups initiated utilization of the icosahedral boron cluster or carboranes as building blocks for ligands in metal-organic frameworks. Similar to carbon-rich organic linkers, carboranes can be functionalized, expanding the ligand pool, as well as topology of MOFs. The introduction of boranes and carboranes have a beneficial impact in the stability and properties of MOFs. In the following, I will make a brief introduction on carboranes and the more relevant studies on the MOF area.

1.3.1 Properties of Carboranes

Carboranes ("carbaboranes" in the formal nomenclature) are polyhedral boron-carbon molecular clusters that are stabilized by electron-delocalized covalent bonding in the

skeletal framework. Carboranes have been known for more than half a century, but for much of that time they were of interest primarily to boron chemists, theoreticians interested in their structures and bonding, and small groups of industrial researchers, whore cognized their potential for creating extremely heat-stable polymers. In recent years, the picture has dramatically changed. Carborane chemistry is experiencing a major surge in interest across a wide spectrum of technologies, fueled by developing applications in medicine, nanoscale engineering, catalysis, metal recovery from radioactive waste, and a number of other areas, documented in thousands of publications and patents[74–77]. This resurgence has been ignited by a wide (if belated) recognition of the unique electronic properties, geometry, and extraordinary versatility of carboranes, and a growing recognition that carborane chemistry affords a whole new realm of possibilities that transcends conventional organic, organometallic or coordination chemistry.

Carboranes had been envisioned by William Lipscomb, Roald Hoffmann, and others from theoretical considerations[78,79] before reports of the synthesis of any such compounds appeared (although it is entirely possible that they may have been present in some CxByHz products generated by experimentalists as far back as Alfred Stock, the great pioneer of boron hydride chemistry[80,81]. As icosahedral B_{12} clusters are present in all known forms of elemental boron and in some metal borides, and several boron hydrides have boron frameworks that are fragments of an icosahedron (e.g., $B_{10}H_{14}$), it was conjectured that an icosahedral $B_{12}H_{12}$ hydride might exist. However, in a classic 1955 paper, Longuet-Higgins and Roberts calculated that two additional electrons would be required, stabilizing the icosahedron as a $B_{12}H_{12}^{2-}$ dianion [82]. Shortly thereafter, $B_{12}H_{12}^{2-}$ salts were isolated by Pitochelli and Hawthorne[83] and found to be incredibly robust, withstanding temperatures above 800ºC and exhibiting inertness toward most reagents. Its discovery strongly implied the viability of neutral $C_2B_{10}H_{12}$ clusters, isoelectronic analogues of $B_{12}H_{12}^{2-}$ in which two BH units are formally replaced by CH groups whose carbon atoms would be six-coordinate (a fairly startling idea at the time)[75] Subsequently, the synthesis of polyhedral boron-rich

compounds and their various derivatives containing heteroatoms (such as carboranes, metallaboranes, and main-group heteroboranes) all have profoundly exerted influence on the area of inorganic and organic chemistry (Figure 1-12). For the 10-vertex neutral carborane cluster ($C_2B_8H_{10}$), analogues of 12-vertex carborane compound, it received less attention in spite of the fact that their unique electronic structure induces more interaction with π-substituents[84,85]. In 1965, metallacarboranes containing one or more transition metal or main group metal atoms in the cage framework were discovered by degradation of carborane with base to obtain anionic *nido* derivatives that then reacted with transition metals[85]. Those boron clusters own a number of unique properties, such as high thermal and chemical stability, ease of functionalization, three-dimensional structure, aromaticity and special electronic properties that have major importance for their use in materials science[74,86–89]. In this thesis, as only dicarba-*closo*-dodecaborane ($C_2B_{10}H_{12}$) clusters were utilized, the introduction mainly describes this carborane compound in detail.

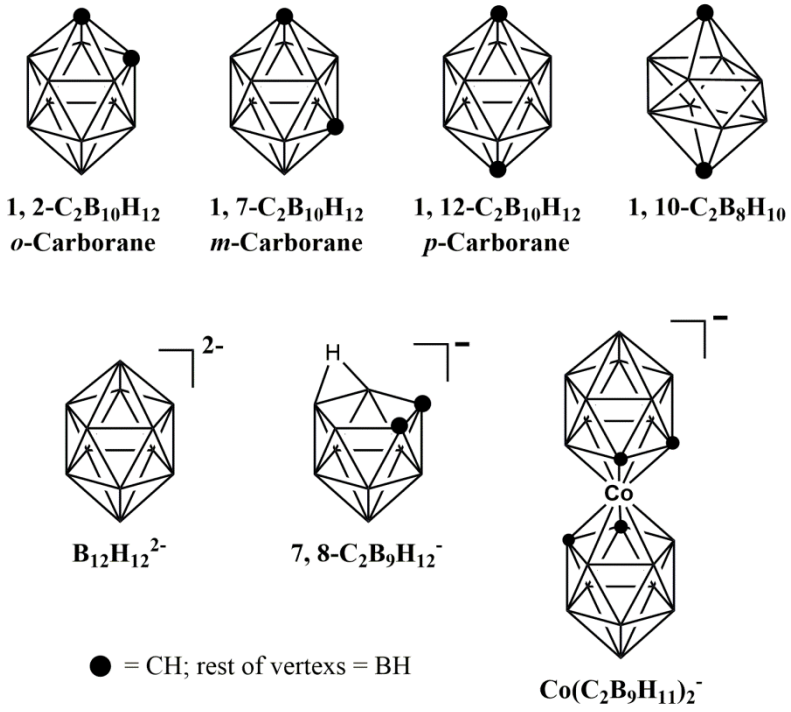

Figure 1-12. Structures of some commonly used boron clusters.

According to the position of carbon atoms in the cluster, it occurs three isomers: 1,n-

$C_2B_{10}H_{12}$ (n = 2, *ortho*; 7, *meta*; 12, *para*), as illustrated in figure 1-12. The van der Waals volume (V_{vdW}) of the cluster based on crystal structures for *ortho*-, *meta*- and *para*-carborane are 148, 143 and 141Å respectively. The cluster volume decreased slightly with the increased distance between two carbon atoms, generating a greater extent of derivation from ideal icosahedral geometry in *para*-carborane. Although carborane was called as 'benzene analogues' in the literature, it is worth noting that volume of carborane cluster is almost twice that of benzene and also slightly higher than adamantane. Even if taking into account of rotation of benzene, the volume of carborane cluster is still approximately 40% larger (Figure 1-13)[90].

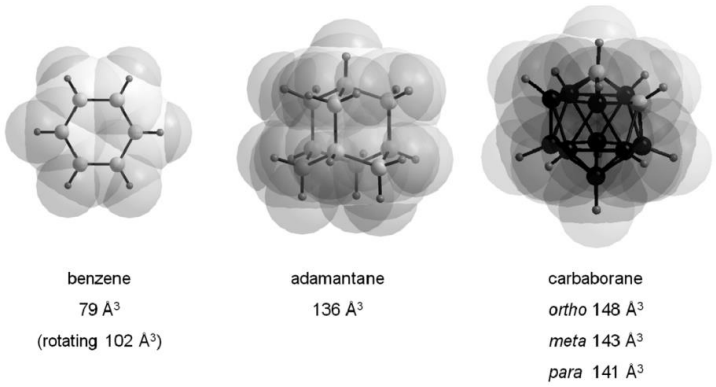

Figure 1-13. Graphical visualization of the van der Waals volumes of benzene, adamantane, and ortho-carbaborane based on the program DIAMOND (C and H = gray, B = black). Calculations are based on the program PLATON with the use of deposited crystal structure data[90].

There are 26 electrons for 12 vertices in the *closo* carborane cluster. The carbon atom is slightly more electronegative comparing with boron thus leading to hydrogen atoms at carbon vertices far more acidic than those at boron atoms. On account that the electrons distribute non uniformly at various vertex, substitutes attached at different vertex possess different inductive effects. According to studies on carborane isomers, all the cluster carbon atoms have electron withdraw inductive effect on the attached substituents (Figure 1-14)[91], while the effects exerted to substitutes at boron atoms depends on the isomer and position within the icosahedron. Boron atoms which are antipodal to carbon atoms could be electron-donating as in *ortho*- and *meta*-carborane. If substituted at boron atoms with one or two adjacent carbon atoms, it could reflect

electron-withdrawing effects. This concept has been identified by Teixidor and Viñas, who first succeed to proof the existence of electron-withdrawing methyl groups bonded to boron atoms of permethylated *o*-carborane[92].

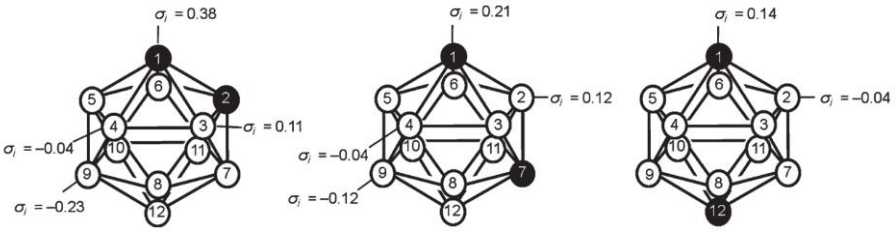

Figure 1-14. Inductive effect (σi) of the carbaborane isomers[93].

As we mentioned above, the protons at carbon atoms are relatively acidic (pKa: 23-30)[94]. An organometallic base such as *n*-BuLi, can be used to deprotonate the cluster carbon atoms obtaining a carbaboranyl nucleophile, that can further react with electrophiles for functionalization of the cluster. Carborane functionalization will be described in section 1.3.2.

In general, due to the existence of 10 rather hydride-like hydrogen at boron atoms, carborane clusters are extraordinary hydrophobic[95]. For example, Fauchére and co-workers created carborane cluster functionalized with amino groups, which is by far the most hydrophobic artificial amino acid[96]. The substitution at different vertex position of icosahedral would determine hydrophobicity of final carborane compounds. If substituting at carbon atoms, its hydrophobicity is higher than attaching at boron vertex because the acidity of free CH groups will lower hydrophobicity.

Carboranes show a rich supramolecular chemistry (Figure 1-15). When carborane moieties are employed in molecular structures, they are often involved in a number of intermolecular interactions. Two different sets of hydrogen groups are involved: acidic CH groups and hydridic BH groups creating C-H···X (X = O, N, S, F, π system)[97,98] hydrogen bonds (ca. 8~96 kJ/mol) and B-H···H-X interactions[99] (ca. 4~28 kJ/mol; electronegativity X > H > B) respectively. The existence of a S−H···H−B dihydrogen bond and its combination with a C−H···S hydrogen bond in an unusual cooperative

effect was first reported by Planas, indicating that substituted carboranes has potential to act as building blocks for assembling complex structures[100].

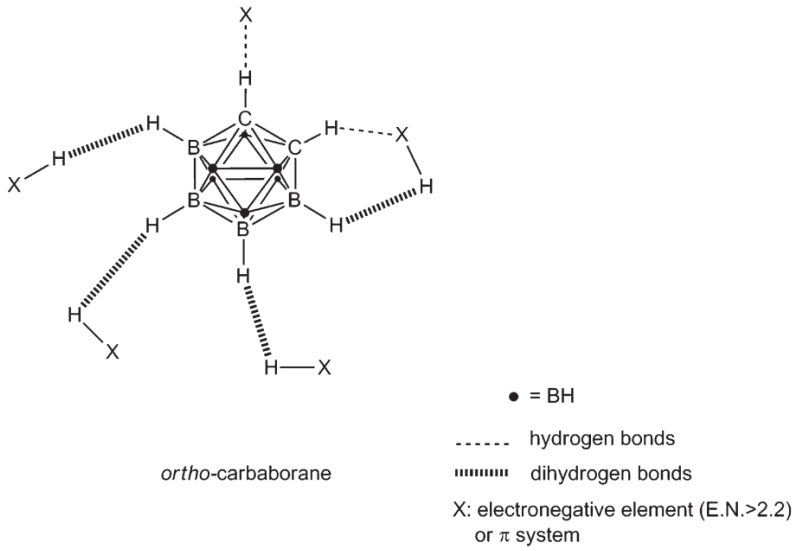

Figure 1-15. Two-dimensional illustration of intermolecular interactions of *ortho*-carbaborane, representatively for all carbaboranes. BH vertices (b) are also capable of forming dihydrogen bonds[76].

1.3.2 Carborane functionalization

Carborane chemistry is constantly expanding, however, a comprehensive review is out of scope here. Herein, only the functionalization routes related to this thesis is introduced. Due to the different nature of the vertexs, carboranes can be functionalized at carbon or at boron, without the need to use protecting and deprotecting routes. C-functionalization of carboranes *via* nucleophilic substitution is the most widespread method to substitute the carborane cluster. As previously explained, the acidic CH protons can be easily removed by a strong base (such as e.g., *n*-BuLi), resulting in a carboranyl nucleophile. The later can react with various electrophiles to obtain the desired substituted clusters. Symmetrical disubstituted carboranes could be simply formed by dilithiation of the cluster and reaction with the appropriate amount of electrophile (scheme 1-1). This reaction is conducted under relatively mild conditions and high yields. Comparing with nucleophilic substitution at carbon atoms, the electrophilic substitution at boron vertex is more challenging, because the B-H bonds

are less polar and also due to the difficulty for selective modification of one out of ten B-H vertices. Specifically, halides and AlX_3 are utilized to replace hydrogens atoms at selective boron position (B9) of *ortho*- or *meta*- carboranes. Then the boron halides can be substituted by cross-coupling reaction with a palladium catalyst (scheme 1-2). In 2013, Teixidor, Viñas and Núñez published a comprehensive review which summarized a variety of methods to generate B–C, B–P, B–N and B–S bonds in boron clusters[101].

Scheme 1-1: General synthetic procedure for C-disubstitution.

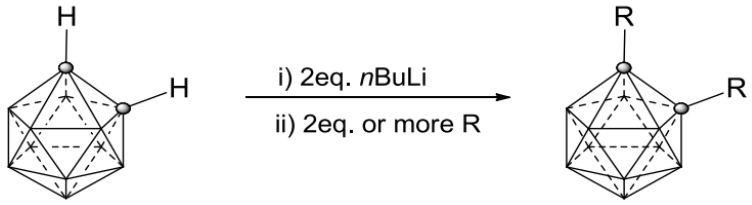

$C_2B_{10}H_{10}$; ○ = CH; rest of vertexs = BH; R = electrophile

Scheme 1-2: One of the common synthetic procedures for B9-substitution.

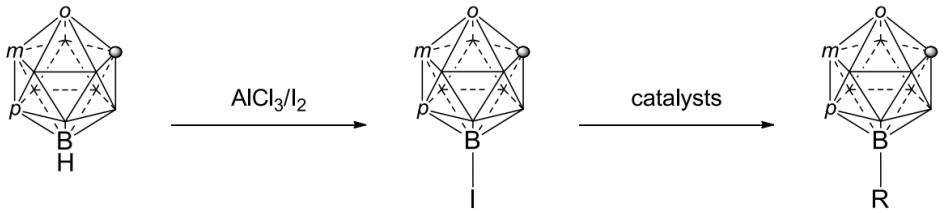

$C_2B_{10}H_{10}$; ○ = CH; rest of vertexs = BH; R = nucleophile

1.3.3 Synthesis of carborane-based MOFs

As we introduced before, carboranes exhibit various desirable properties. Scientists start to incorporate carborane cluster into coordination polymers one decade ago. However, carborane based MOFs are not yet a widespread area and less than 30 papers has been published so far[102–119]. The carboranes employed in the construction of linkers for MOFs could be categorized into two types: neutral clusters ($C_2B_{10}H_{12}$ or $C_2B_8H_{10}$),[107–109,111,120–124] which are the most widely used in design of carborane based coordination polymers (Figure 1-16); anionic boron clusters including $[B_{12}H_{12}]^{2-}$ (Figure 1-12) and metallacarborane $[Co(C_2B_9H_{11})_2]^-$ based ligand (Figure 1-

16e)[106,125,126].

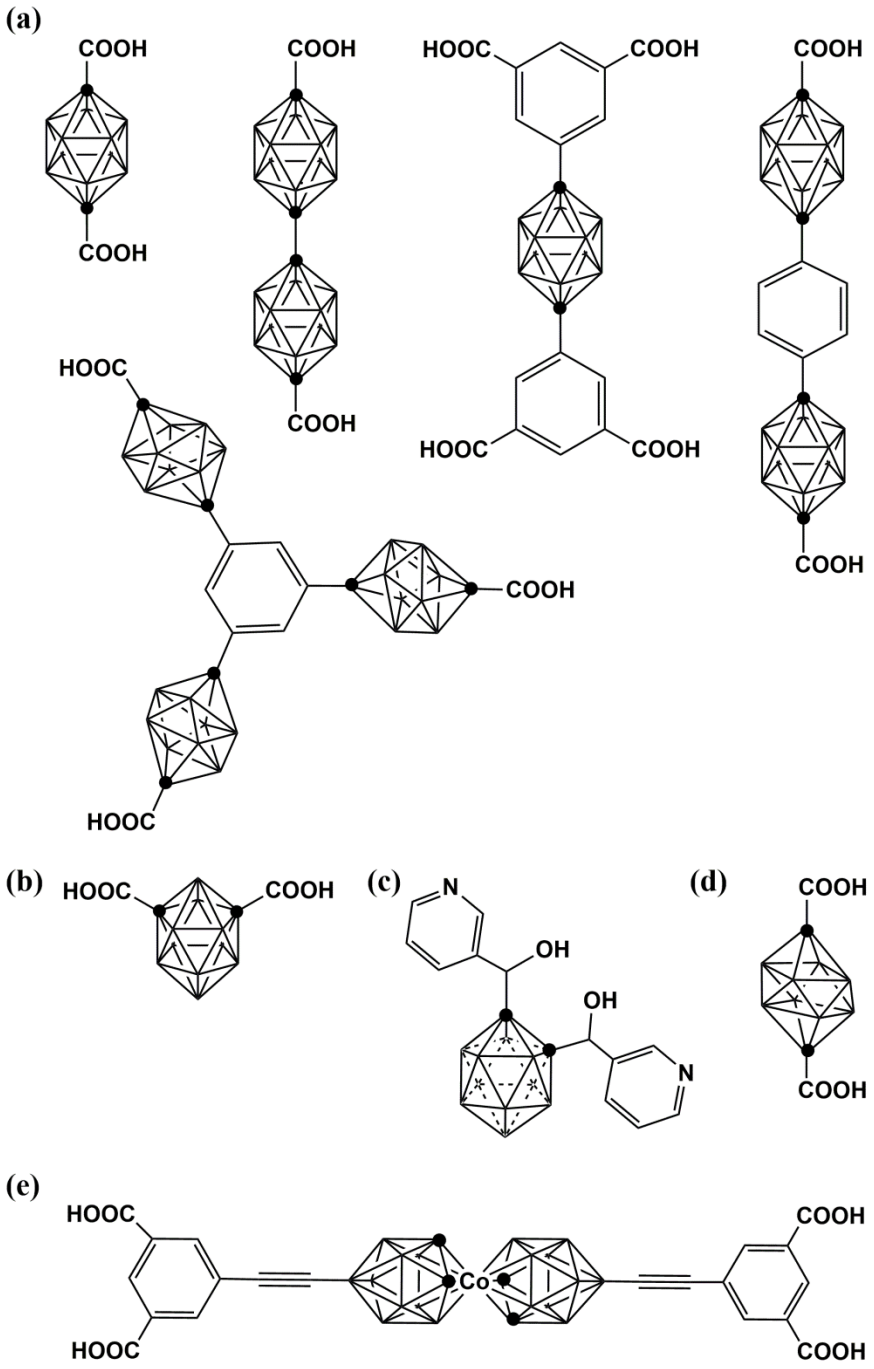

Figure 1-16. Illustration of ligands utilized for MOFs synthesis that incorporate carborane moieties[108–111,116,117,121,127]

In 2007, the first carborane-based MOF was born in Mirkin and Hupp's group who utilized 1,12-dihydroxycarbonyl-*para*-carborane (*p*-$CDCH_2$) coordinating with zinc ions to obtain a porous compound displaying hydrogen sorption[111]. Consecutively, their group reported a series of novel MOF structures constructed by the same carborane

ligand (*p*-$CDCH_2$) combining with zinc or cobalt ions under different solvothermal conditions. Owing to the structures, the materials exhibited potential for separation for CO_2/CH_4, O_2/N_2, CO_2/N_2 benefiting from molecular sieve and uncoordinated metal sites which is predicted via experimental pure isotherms using ideal adsorbed solution theory (IAST)[107,120,122]. Later, the same group synthesized a variety of carboxylic linkers incorporating the *p*-carborane or *p*-$C_2B_8H_{10}$ (Figure 1-16a) or cosane (Figure 1-16e) moieties and the corresponding porous MOFs[125]. Remarkably, among those structures, NU-135 is by far the most highly porous carborane-based MOF (Figure 1-17). Its excellent deliverable methane capacity indicated that it is a promising porous material for driving a natural gas vehicle (NGV). This is benefit from well balance between pore volume, pore size and surface area of the structure, resulting from the icosahedral carborane units and their hydride-like hydrogen atoms at boron vertex. The latter is a unique property of carboranes and inaccessible from hydrocarbon organic linkers[109]. Furthermore, the presence of carborane ligands in the frameworks allowed activation of NU-700, which retained its porosity, whereas that was not possible with the analogue structure having phenyl rings (MOF-143) instead of carboranes[121].

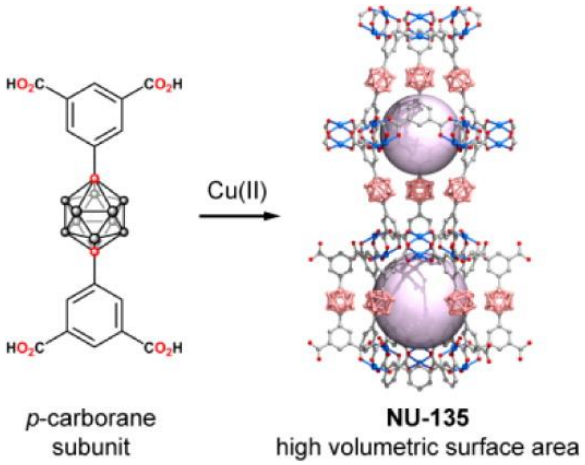

Figure 1-17. Structures of NU-135 (left) and experimental (blue) and simulated (red) high-pressure absolute gas adsorption isotherms for NU-135 at several temperatures (right)[109].

In the meantime, Jin' s group extended the carborane based MOFs by taking advantage of lanthanide contraction to improve selective CO_2 adsorption[105]. This group also employed the dicarboxylic acid of the *p*-carborane as the linker. It is important to note

that all above results deal with the use of *para*-carborane based linkers for MOFs or CPs. One of the major drawbacks of using this particular isomer of carborane is the high price of the starting compound, compared to the other two isomers: Price for 1 g: *o*-carborane: 122 EUR (Sigma-Aldrich); *m*-carborane: 176 (Sigma-Aldrich), *p*-carborane: 1963 EUR (Carbosynth US LLC). It is evident that the high price of the *p*-carborane isomer limits its practical use in industry. From this point of view, the cheaper *o*- and *m*-carborane are a more reasonable choice for designing coordination polymers (Figure 1-16b-c). A few examples have been published. For example, Jin and coauthors investigated a series of isostructural metal–organic frameworks based on the dicarboxylic acid of the *m*-carborane clusters and $Cu_2(CO_2)_4$ units[108]. Furthermore, in 2016, Planas and co-workers reported a novel highly hydrophobic *o*-carborane porous material (Figure 1-18)[27]. This material is stable in water and shows a reversible switch of the hydrophobic/hydrophilic properties. Apart from 12-vertex *closo*-carboranes, 10-vertex *closo*-carboranes were also introduced into porous frameworks, reported by Boldog (Figure 1-16d)[110,124].

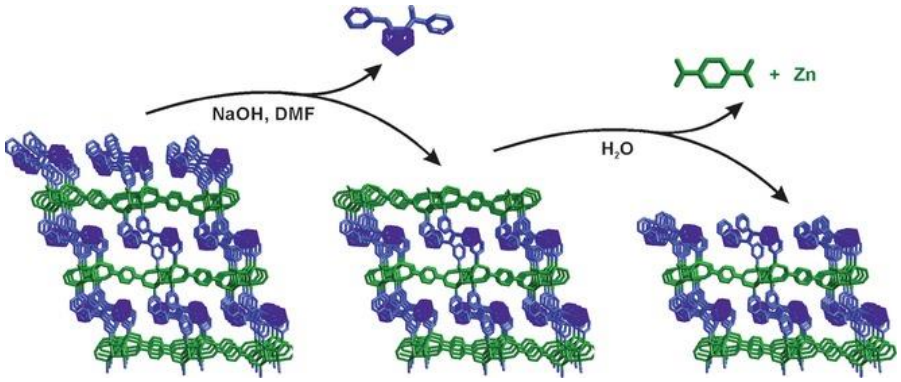

Figure 1-18. Ideal mechanism proposed for the switchable surface hydrophobicity–hydrophilicity of oCB-MOF-1. Pillaring oCB-L linkers are represented in blue and $Zn_4(bdc)_2$ layers in green[27].

Recently, a microporous 3D MOF consisting of 1,2-bis(4-pyridyl)acetylene (bpa) and copper (II) dodecaborate ($B_{12}H_{12}^{2-}$) dianion was reported. In this supramolecular MOF, the dodecaborate dianion not only serves as counter anions but also pillars to support layers (Figure 1-19)[128]. The authors also prove that this MOF is water stable and therefore a good choice for potential applications.

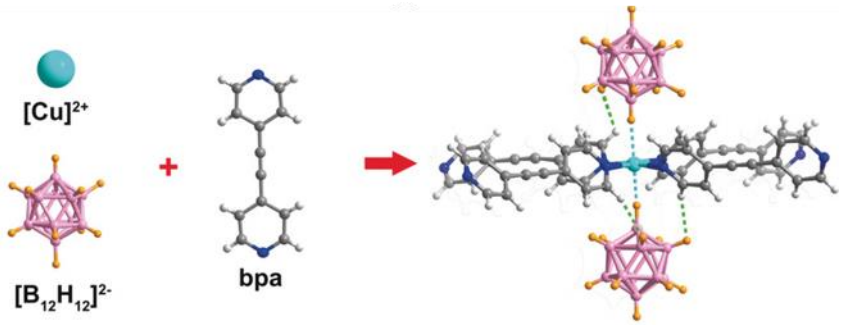

Figure 1-19 starting materials used for the synthesis of BSF-1 (left) and interactions between Cu(II), $[B_{12}H_{12}]^{2-}$ and bpa, (right), the blue dashed line representing the B–H···M interactions and the green dashed lines representing the B–$H^{\delta-}$···$H^{\delta+}$-C interactions (defined by $H^{\delta-}$ ···$H^{\delta+}$ distance shorter than 2.4 Å)[128].

The introduction of carborane based MOFs have advanced during the last 12 years. As it has been summarized above, most of the carborane linkers used in the preparation of MOFs are derivatives of *para*-carborane. A few examples from *meta*-carborane derived linkers have been also reported, but in all the cases, the choice for functionalization was the carboxylic groups (Figures 1-16). The first example of a non carboxylic carborane derivative was reported in our group, by Planas and coworkers. Overall, all these materials show a variety of promising and unprecedented properties, some derived from the carborane moieties. Some include structural robustness, exceptional hydrophobicity and porosity that are beneficial for gas separation, catalysis, medicinal chemistry etc. Herein, this thesis will try to expand this area and introduce investigation of carborane based coordination polymers and their interesting properties.

1.4 References

[1] C. Janiak, *Dalt. Trans.* **2003**, 2781.
[2] J. J. Perry IV, J. A. Perman, M. J. Zaworotko, *Chem. Soc. Rev.* **2009**, *38*, 1400.
[3] X.-M. Chen, J. Reedijk, M. Paik Suh, S. Kitagawa, N. R. Champness, M. O'Keeffe, L. Öhrström, J. Garcia-Martinez, S. R. Batten, *Pure Appl. Chem.* **2013**, *85*, 1715.
[4] O. M. Yaghi, H. Li, *J. Am. Chem. Soc.* **1995**, *117*, 10401.
[5] P. Z. Moghadam, A. Li, S. B. Wiggin, A. Tao, A. G. P. Maloney, P. A. Wood, S. C. Ward, D. Fairen-Jimenez, *Chem. Mater.* **2017**, *29*, 2618.
[6] S. Dhaka, R. Kumar, A. Deep, M. B. Kurade, S.-W. Ji, B.-H. Jeon, *Coord. Chem. Rev.* **2019**, *380*, 330.
[7] K. V. Kumar, K. Preuss, M.-M. Titirici, F. Rodríguez-Reinoso, *Chem. Rev.* **2017**, *117*, 1796.
[8] A. G. Slater, A. I. Cooper, *Science.* **2015**, *348*, aaa8075.

[9] Y. Cui, B. Li, H. He, W. Zhou, B. Chen, G. Qian, *Acc. Chem. Res.* **2016**, *49*, 483.
[10] L. Zhu, X.-Q. Liu, H.-L. Jiang, L.-B. Sun, *Chem. Rev.* **2017**, *117*, 8129.
[11] R.-B. Lin, Y. He, P. Li, H. Wang, W. Zhou, B. Chen, *Chem. Soc. Rev.* **2019**, *48*, 1362.
[12] M. Ding, R. W. Flaig, H.-L. Jiang, O. M. Yaghi, *Chem. Soc. Rev.* **2019**, *48*, 2783.
[13] H. Wang, Q.-L. Zhu, R. Zou, Q. Xu, *Chem* **2017**, *2*, 52.
[14] O. K. Farha, I. Eryazici, N. C. Jeong, B. G. Hauser, C. E. Wilmer, A. A. Sarjeant, R. Q. Snurr, S. T. Nguyen, A. Ö. Yazaydın, J. T. Hupp, *J. Am. Chem. Soc.* **2012**, *134*, 15016.
[15] H. Furukawa, K. E. Cordova, M. O'Keeffe, O. M. Yaghi, *Science.* **2013**, *341*, 1230444.
[16] R.-B. Lin, S. Xiang, H. Xing, W. Zhou, B. Chen, *Coord. Chem. Rev.* **2019**, *378*, 87.
[17] B. R. Barnett, M. I. Gonzalez, J. R. Long, *Trends Chem.* **2019**, *1*, 159.
[18] P. Kumar, K.-H. Kim, P. K. Mehta, L. Ge, G. Lisak, *Crit. Rev. Environ. Sci. Technol.* **2019**, 1.
[19] J. Liu, L. Chen, H. Cui, J. Zhang, L. Zhang, C.-Y. Su, *Chem. Soc. Rev.* **2014**, *43*, 6011.
[20] J. Escorihuela, R. Narducci, V. Compañ, F. Costantino, *Adv. Mater. Interfaces* **2018**, *6*, 1801146.
[21] G. Mínguez Espallargas, E. Coronado, *Chem. Soc. Rev.* **2018**, *47*, 533.
[22] W. Lu, Z. Wei, Z.-Y. Gu, T.-F. Liu, J. Park, J. Park, J. Tian, M. Zhang, Q. Zhang, T. Gentle III, M. Bosch, H.-C. Zhou, *Chem. Soc. Rev.* **2014**, *43*, 5561.
[23] M. De Toni, R. Jonchiere, P. Pullumbi, F.-X. Coudert, A. H. Fuchs, *ChemPhysChem* **2012**, *13*, 3497.
[24] S. Roy, V. M. Suresh, T. K. Maji, *Chem. Sci.* **2016**, *7*, 2251.
[25] T.-H. Chen, I. Popov, O. Zenasni, O. Daugulis, O. Š. Miljanić, *Chem. Commun.* **2013**, *49*, 6846.
[26] N. M. Padial, E. Quartapelle Procopio, C. Montoro, E. López, J. E. Oltra, V. Colombo, A. Maspero, N. Masciocchi, S. Galli, I. Senkovska, S. Kaskel, E. Barea, J. A. R. Navarro, *Angew. Chemie Int. Ed.* **2013**, *52*, 8290.
[27] S. Rodríguez-Hermida, M. Y. Tsang, C. Vignatti, K. C. Stylianou, V. Guillerm, J. Pérez-Carvajal, F. Teixidor, C. Viñas, D. Choquesillo-Lazarte, C. Verdugo-Escamilla, I. Peral, J. Juanhuix, A. Verdaguer, I. Imaz, D. Maspoch, J. Giner Planas, *Angew. Chemie Int. Ed.* **2016**, *55*, 16049.
[28] J. G. Nguyen, S. M. Cohen, *J. Am. Chem. Soc.* **2010**, *132*, 4560.
[29] V. Nicolosi, M. Chhowalla, M. G. Kanatzidis, M. S. Strano, J. N. Coleman, *Science.* **2013**, *340*, 1226419.
[30] N. Nijem, K. Fürsich, H. Bluhm, S. R. Leone, M. K. Gilles, *J. Phys. Chem. C* **2015**, *119*, 24781.
[31] A. J. Howarth, Y. Liu, P. Li, Z. Li, T. C. Wang, J. T. Hupp, O. K. Farha, *Nat. Rev. Mater.* **2016**, *1*, 15018.
[32] J. C. Tan, A. K. Cheetham, *Chem. Soc. Rev.* **2011**, *40*, 1059.
[33] S. Horike, S. Shimomura, S. Kitagawa, *Nat. Chem.* **2009**, *1*, 695.
[34] F.-X. Coudert, *Chem. Mater.* **2015**, *27*, 1905.
[35] Y. Sakata, S. Furukawa, M. Kondo, K. Hirai, N. Horike, Y. Takashima, H. Uehara, N. Louvain, M. Meilikhov, T. Tsuruoka, S. Isoda, W. Kosaka, O. Sakata, S. Kitagawa, *Science.* **2013**, *339*, 193.
[36] C. Serre, F. Millange, C. Thouvenot, M. Noguès, G. Marsolier, D. Louër, G. G. Férey, *J.*

Am. Chem. Soc. **2002**, *124*, 13519.
[37] T. D. Bennett, A. K. Cheetham, A. H. Fuchs, F.-X. Coudert, *Nat. Chem.* **2017**, *9*, 11.
[38] R. E. Morris, L. Brammer, *Chem. Soc. Rev.* **2017**, *46*, 5444.
[39] S. Kitagawa, M. Kondo, *Bull. Chem. Soc. Jpn.* **1998**, *71*, 1739.
[40] K. Biradha, M. Fujita, *Angew. Chemie Int. Ed.* **2002**, *41*, 3392.
[41] N. C. Burtch, J. Heinen, T. D. Bennett, D. Dubbeldam, M. D. Allendorf, *Adv. Mater.* **2018**, *30*, 1704124.
[42] S. Henke, W. Li, A. K. Cheetham, *Chem. Sci.* **2014**, *5*, 2392.
[43] S. Henke, W. Li, A. K. Cheetham, *Chem. Sci.* **2014**, *5*, 2392.
[44] J. Vallejo, F. R. Fortea-Pérez, E. Pardo, S. Benmansour, I. Castro, J. Krzystek, D. Armentano, J. Cano, *Chem. Sci.* **2016**, *7*, 2286.
[45] P. W. Shriver, Duward F.and Atkins, *Inorganic Chemistry*, Oxford University Press, **2006**.
[46] Y. Xu, N. A. Vermeulen, Y. Liu, J. T. Hupp, O. K. Farha, *Eur. J. Inorg. Chem.* **2016**, *2016*, 4345.
[47] Q. Chen, Z. Chang, W. C. Song, H. Song, H. Bin Song, T. L. Hu, X. H. Bu, *Angew. Chemie - Int. Ed.* **2013**, *52*, 11550.
[48] E. J. Carrington, C. A. McAnally, A. J. Fletcher, S. P. Thompson, M. Warren, L. Brammer, *Nat. Chem.* **2017**, *9*, 882.
[49] S.-L. Huang, T. S. A. Hor, G.-X. Jin, *Coord. Chem. Rev.* **2017**, *346*, 112.
[50] E. R. Draper, D. J. Adams, *Chem. Commun.* **2016**, *52*, 8196.
[51] R. Sakamoto, K. Takada, X. Sun, T. Pal, T. Tsukamoto, E. J. H. Phua, A. Rapakousiou, K. Hoshiko, H. Nishihara, *Coord. Chem. Rev.* **2016**, *320–321*, 118.
[52] D. J. Ashworth, J. A. Foster, *J. Mater. Chem. A* **2018**, *6*, 16292.
[53] H. Maeda, R. Sakamoto, H. Nishihara, *Langmuir* **2016**, *32*, 2527.
[54] T. Haraguchi, O. Sakata, H. Kitagawa, K. Otsubo, A. Fujiwara, *J. Am. Chem. Soc.* **2012**, *134*, 9605.
[55] H. Kitagawa, K. Otsubo, S. Sakaida, G. Xu, T. Yamada, *J. Am. Chem. Soc.* **2012**, *134*, 16524.
[56] S. Motoyama, R. Makiura, O. Sakata, H. Kitagawa, *J. Am. Chem. Soc.* **2011**, *133*, 5640.
[57] Y. Honma, K. Itoh, H. Masunaga, A. Fujiwara, T. Nishizaki, S. Iguchi, T. Sasaki, *Adv. Electron. Mater.* **2018**, *4*, 1700490.
[58] G. Renaud, *Science.* **2003**, *300*, 1416.
[59] L. J. Han, D. Zheng, S. G. Chen, H. G. Zheng, J. Ma, *Small* **2018**, *14*, 1.
[60] D. Davidovikj, B. J. C. Vieira, G. Mínguez Espallargas, I. J. Vitórica-Yrezábal, P. J. Bereciartua, H. S. J. van der Zant, E. Coronado, S. Mañas-Valero, P. G. Steeneken, J. López-Cabrelles, J. C. Waerenborgh, J. A. Rodríguez-Velamazán, *Nat. Chem.* **2018**, *10*, 1001.
[61] Y. Ding, Y.-P. P. Chen, X. Zhang, L. Chen, Z. Dong, H.-L. L. Jiang, H. Xu, H.-C. C. Zhou, *J. Am. Chem. Soc.* **2017**, *139*, 9136.
[62] H. S. Wang, J. Li, J. Y. Li, K. Wang, Y. Ding, X. H. Xia, *NPG Asia Mater.* **2017**, *9*, 1.
[63] X. Wang, C. Chi, K. Zhang, Y. Qian, K. M. Gupta, Z. Kang, J. Jiang, D. Zhao, *Nat. Commun.* **2017**, *8*, 1.
[64] H. Miro, B. Seoane, F. Kapteijn, I. Luz, F. X. Llabrés i Xamena, J. Gascon, A. Corma, T. Rodenas, G. Prieto, *Nat. Mater.* **2014**, *14*, 48.

[65] K. Sakata, S. Kashiyama, G. Matsuo, S. Uemura, N. Kimizuka, M. Kunitake, *ChemNanoMat* **2015**, *1*, 259.

[66] K. Rui, G. Zhao, Y. Chen, Y. Lin, Q. Zhou, J. Chen, J. Zhu, W. Sun, W. Huang, S. X. Dou, *Adv. Funct. Mater.* **2018**, *28*, 1801554.

[67] J. Dong, X. Li, K. Zhang, Y. Di Yuan, Y. Wang, L. Zhai, G. Liu, D. Yuan, J. Jiang, D. Zhao, K. Zhang, L. Zhai, G. Liu, J. Jiang, Y. Di Yuan, X. Li, D. Zhao, J. Dong, Y. Wang, *J. Am. Chem. Soc.* **2018**, *140*, 4035.

[68] Y. Peng, Y. Li, Y. Ban, H. Jin, W. Jiao, X. Liu, W. Yang, *Science.* **2014**, *346*, 1356.

[69] C. Tan, H. Zhang, *J. Am. Chem. Soc.* **2015**, *137*, 12162.

[70] J. Huang, Y. Li, R. K. Huang, C. T. He, L. Gong, Q. Hu, L. Wang, Y. T. Xu, X. Y. Tian, S. Y. Liu, Z. M. Ye, F. Wang, D. D. Zhou, W. X. Zhang, J. P. Zhang, *Angew. Chemie - Int. Ed.* **2018**, *57*, 4632.

[71] P. Chandrasekhar, A. Mukhopadhyay, G. Savitha, J. N. Moorthy, *J. Mater. Chem. A* **2017**, *5*, 5402.

[72] J. Ping, Q. Ma, Z. Zhang, H. Xu, Q. Lu, Y. Zhao, Y. Huang, Y. Yu, H. Zhang, M. Zhao, Y. Wang, X. Zhang, *Adv. Mater.* **2015**, *27*, 7372.

[73] S. Zhao, Y. Wang, J. Dong, C. T. He, H. Yin, P. An, K. Zhao, X. Zhang, C. Gao, L. Zhang, J. Lv, J. Wang, J. J. Zhang, A. M. Khattak, N. A. Khan, Z. Wei, J. J. Zhang, S. Liu, H. Zhao, Z. Tang, *Nat. Energy* **2016**, *1*, 1.

[74] Kaufmann, Matteson, Schaumann, Regitz, Eds. , in *Categ. 1, Organometallics*, Georg Thieme Verlag, Stuttgart, **2005**.

[75] R. N. Grimes, *Carboranes* **2011**.

[76] M. Scholz, E. Hey-Hawkins, *Chem. Rev.* **2011**, *111*, 7035.

[77] R. Núñez, I. Romero, F. Teixidor, C. Viñas, *Chem. Soc. Rev.* **2016**, *45*, 5147.

[78] R. Hoffmann, W. N. Lipscomb, *J. Chem. Phys.* **1962**, *36*, 2179.

[79] W. N. Lipscomb, *Proc. Natl. Acad. Sci.* **1961**, *47*, 1791.

[80] R. Schwarz, *Angew. Chemie* **1934**, *47*, 170.

[81] E. B. Stock, A.; Kuss, **1923**, *56*, 789.

[82] *Proc. R. Soc. London. Ser. A. Math. Phys. Sci.* **1955**, *230*, 1180.

[83] A. R. Pitochelli, F. M. Hawthorne, *J. Am. Chem. Soc.* **1960**, *82*, 3228.

[84] S. Pakhomov, P. Kaszynski, V. G. Young, *Inorg. Chem.* **2000**, *39*, 2243.

[85] M. F. Hawthorne, D. C. Young, P. A. Wegner, *J. Am. Chem. Soc.* **1965**, *87*, 1818.

[86] J. Poater, M. Solà, C. Viñas, F. Teixidor, *Chem. - A Eur. J.* **2016**, *22*, 7437.

[87] J. Poater, M. Solà, C. Viñas, F. Teixidor, *Angew. Chemie Int. Ed.* **2014**, *53*, 12191.

[88] R. N. Grimes, *Dalt. Trans.* **2015**, *44*, 5939.

[89] M. Scholz, E. Hey-Hawkins, *Chem. Rev.* **2011**, *111*, 7035.

[90] *Data Taken from CCDC Entries TOKGIJ, TOKGOP, TOKGUV, ADAMAN08, and ABELUO and Determined with the PLATON Program***.**

[91] M. F. Hawthorne, T. E. Berry, P. A. Wegner, *J. Am. Chem. Soc.* **1965**, *87*, 4746.

[92] F. Teixidor, G. Barberà, A. Vaca, R. Kivekäs, R. Sillanpää, J. Oliva, C. Viñas, *J. Am. Chem. Soc.* **2005**, *127*, 10158.

[93] I. E. Kareev, V. P. Bubnov, E. B. Yagubskii, *Russ. Chem. Bull.* **2008**, *57*, 1486.

[94] K. Hermansson, M. Wójcik, S. Sjöberg, *Inorg. Chem.* **1999**, *38*, 6039.

[95] Z. J. Lesnikowski, *Collect. Czechoslov. Chem. Commun.* **2007**, *72*, 1646.

[96] J. L. Fauchère, K. Q. Do, P. Y. C. Jow, C. Hansch, *Experientia* **1980**, *36*, 1203.
[97] M. Fox, *Coord. Chem. Rev.* **2004**, *248*, 457.
[98] X. Zhang, H. Dai, H. Yan, W. Zou, D. Cremer, *J. Am. Chem. Soc.* **2016**, *138*, 4334.
[99] J. Echeverría, G. Aullón, S. Alvarez, *Dalt. Trans.* **2017**, *46*, 2844.
[100] J. G. Planas, C. Viñas, F. Teixidor, A. Comas-Vives, G. Ujaque, A. Lledós, M. E. Light, M. B. Hursthouse, *J. Am. Chem. Soc.* **2005**, *127*, 15976.
[101] D. Olid, R. Núñez, C. Viñas, F. Teixidor, *Chem. Soc. Rev.* **2013**, *42*, 3318.
[102] A. M. Spokoyny, *Pure Appl. Chem.* **2013**, *85*, 903.
[103] A. K. Singh, A. Sadrzadeh, B. I. Yakobson, *J. Am. Chem. Soc.* **2010**, *132*, 14126.
[104] I. Boldog, M. Dušek, T. Jelínek, P. Švec, F. S. de O. Ramos, A. Růžička, R. Bulánek, *Microporous Mesoporous Mater.* **2018**, *271*, 284.
[105] S. L. Huang, Y. J. Lin, W. Bin Yu, G. X. Jin, *Chempluschem* **2012**, *77*, 141.
[106] L. Cunha-Silva, M. J. Carr, J. D. Kennedy, M. J. Hardie, *Cryst. Growth Des.* **2013**, *13*, 3162.
[107] Y.-S. S. Bae, A. M. Spokoyny, O. K. Farha, R. Q. Snurr, J. T. Hupp, C. A. Mirkin, *Chem. Commun.* **2010**, *46*, 3478.
[108] S.-L. Huang, L.-H. Weng, G.-X. Jin, *Dalt. Trans.* **2012**, *41*, 11657.
[109] R. D. Kennedy, V. Krungleviciute, D. J. Clingerman, J. E. Mondloch, Y. Peng, C. E. Wilmer, A. A. Sarjeant, R. Q. Snurr, J. T. Hupp, T. Yildirim, O. K. Farha, C. A. Mirkin, *Chem. Mater.* **2013**, *25*, 3539.
[110] I. Boldog, P. J. Bereciartua, R. Bulánek, M. Kučeráková, M. Tomandlová, M. Dušek, J. Macháček, D. De Vos, T. Baše, *CrystEngComm* **2016**, *18*, 2036.
[111] O. K. Farha, A. M. Spokoyny, K. L. Mulfort, M. F. Hawthorne, C. A. Mirkin, J. T. Hupp, *J. Am. Chem. Soc.* **2007**, *129*, 12680.
[112] K. Gopalsamy, M. Prakash, R. Mahesh Kumar, V. Subramanian, *Int. J. Hydrogen Energy* **2012**, *37*, 9730.
[113] B. P. Dash, R. Satapathy, J. A. Maguire, N. S. Hosmane, *New J. Chem.* **2011**, *35*, 1955.
[114] Y.-S. Bae, O. K. Farha, A. M. Spokoyny, C. A. Mirkin, J. T. Hupp, R. Q. Snurr, *Chem. Commun.* **2008**, 4135.
[115] D. J. Clingerman, W. Morris, J. E. Mondloch, R. D. Kennedy, A. A. Sarjeant, C. Stern, J. T. Hupp, O. K. Farha, C. A. Mirkin, *Chem. Commun.* **2015**, *51*, 6521.
[116] R. D. Kennedy, D. J. Clingerman, W. Morris, C. E. Wilmer, A. A. Sarjeant, C. L. Stern, M. O'Keeffe, R. Q. Snurr, J. T. Hupp, O. K. Farha, C. A. Mirkin, *Cryst. Growth Des.* **2014**, *14*, 1324.
[117] A. M. Spokoyny, O. K. Farha, K. L. Mulfort, J. T. Hupp, C. A. Mirkin, *Inorganica Chim. Acta* **2010**, *364*, 266.
[118] O. K. Farha, A. M. Spokoyny, K. L. Mulfort, S. Galli, J. T. Hupp, C. A. Mirkin, *Small* **2009**, *5*, 1727.
[119] C. W. Kung, K. Otake, C. T. Buru, S. Goswami, Y. Cui, J. T. Hupp, A. M. Spokoyny, O. K. Farha, *J. Am. Chem. Soc.* **2018**, *140*, 3871.
[120] O. K. Farha, A. M. Spokoyny, K. L. Mulfort, S. Galli, J. T. Hupp, C. A. Mirkin, *Small* **2009**, *5*, 1727.
[121] D. J. Clingerman, W. Morris, J. E. Mondloch, R. D. Kennedy, A. A. Sarjeant, C. Stern, J. T. Hupp, O. K. Farha, C. A. Mirkin, *Chem. Commun.* **2015**, *51*, 6521.

[122] Y. S. Bae, O. K. Farha, A. M. Spokoyny, C. A. Mirkin, J. T. Hupp, R. Q. Snurr, *Chem. Commun.* **2008**, *0*, 4135.

[123] A. M. Spokoyny, O. K. Farha, K. L. Mulfort, J. T. Hupp, C. A. Mirkin, *Inorganica Chim. Acta* **2010**, *364*, 266.

[124] I. Boldog, M. Dušek, T. Jelínek, P. Švec, F. S. de O. Ramos, A. Růžička, R. Bulánek, *Microporous Mesoporous Mater.* **2018**, *271*, 284.

[125] R. D. Kennedy, D. J. Clingerman, W. Morris, C. E. Wilmer, A. A. Sarjeant, C. L. Stern, M. O'Keeffe, R. Q. Snurr, J. T. Hupp, O. K. Farha, C. A. Mirkin, *Cryst. Growth Des.* **2014**, *14*, 1324.

[126] A. K. Singh, A. Sadrzadeh, B. I. Yakobson, *J. Am. Chem. Soc.* **2010**, *132*, 14126.

[127] S. Rodríguez-Hermida, M. Y. Tsang, C. Vignatti, K. C. Stylianou, V. Guillerm, J. Pérez-Carvajal, F. Teixidor, C. Viñas, D. Choquesillo-Lazarte, C. Verdugo-Escamilla, I. Peral, J. Juanhuix, A. Verdaguer, I. Imaz, D. Maspoch, J. Giner Planas, *Angew. Chemie Int. Ed.* **2016**, *55*, 16049.

[128] Y. Zhang, L. Yang, L. Wang, S. Duttwyler, H. Xing, *Angew. Chemie Int. Ed.* **2019**, *58*, 8145.

Chapter 2

Objectives

Objectives

As illustrated in chapter 1, the unique properties of MOFs have sparked immense attention among material researchers during last two decades. Its potential highly-developed porosity, diverse topology, controllable active sites and infinite frameworks enable it to be utilized in a variety of applications. However, to some degree, their weak structural stability restricts its extensive industrial application. Their instability toward humidity is also a major drawback that needs to be resolved. The introduction of carboranes into these potential porous materials is quite limited and most of examples are devoted to polycarboxylates of the highly expensive *para*-carborane compound. Thus, the major objective of the present Thesis was the study of N-disubstituted *meta*-carborane linkers for Coordination Polymers (CPs) or Metal-Organic Frameworks (MOFs) and study their properties. More specifically, the objectives of the present work were:

- Explore the preparation of CPs or MOFs with flexible *meta*-carborane bis-pyridylalcohols in combination with neutral polycarboxylic acids and different transition metals. It was planned to follow solvothermal reaction conditions and study the properties of the obtained materials.

- Develop new and longer derivatives of the previous carborane ligand by synthetic chemistry and further explore the formation of CPs or MOFs, following the same reasoning than above. It was interesting to investigate the influence of the length of these ligands into the final polymeric structures and their possible properties.

Demonstrate the introduction of flexibility into CPs or MOFs by using the synthesized flexible *meta*-carborane linkers. It was particularly interesting to demonstrate whether the flexibility of the ligand could be transferred to the MOFs and, in that case, if the spherical carborane moiety played any role in the stability of the final products. Owing to the hydrophobicity of the carboranes, it was also interesting to study the water stability of the new compounds.

Chapter 3

Carborane bis-pyridylalcohols as linkers for Coordination Polymers: Synthesis, Crystal Structures and Guest-Framework dependent Mechanical Properties

3. Carborane bis-pyridylalcohols as linkers for Coordination Polymers: Synthesis, Crystal Structures and Guest-Framework dependent Mechanical Properties

3.1 Introduction

Porous Coordination Polymers (CPs) or Metal-Organic Frameworks (MOFs) are a class of porous crystalline materials formed by the assembly of metal ions or metal clusters with different types of bridging organic linkers[1–4]. Multiple network structures with various topologies can be prepared by the appropriate choice of metal ion geometry and the binding mode of the bridging ligand. The primary choice of the organic part has been polycarboxylates, polypyridines, and organic ligands that possess both carboxylate groups and N donor atoms. Thus, the chemistry of CPs has been dominated by these ligands. Sometimes, the above-mentioned ligands are simultaneously used to generate mixed-ligand three-dimensional (3D) CPs[5]. The majority of these CPs are formed by connecting metal-polycarboxylate layers through pyridyl-based ligands. This approach allows higher flexibility in terms of pore size and introduction of functional groups. In this regard, MOFs can be easily tuned and are amenable to a wide variety of guest compounds, through host-guest interactions[6-8]. Preferential arrangement of guest molecules within CPs has enabled the structural determination of molecules that did not crystallize otherwise. The latter method, known as the *crystalline sponge method*[6], relies on specific host-guest interactions that renders the guest molecules regularly ordered[7]. Such host-guest interactions are being explored for a variety of applications[8]. In light of the imminence of these materials applications, mechanical properties, which are critical to the industrial manufacturing and processing, need to be taken into account[9,10].

Scheme 3-1. Graphical representation of the carborane isomers (*closo*-$C_2B_{10}H_{12}$) and their derivatives used as linkers to form CPs.

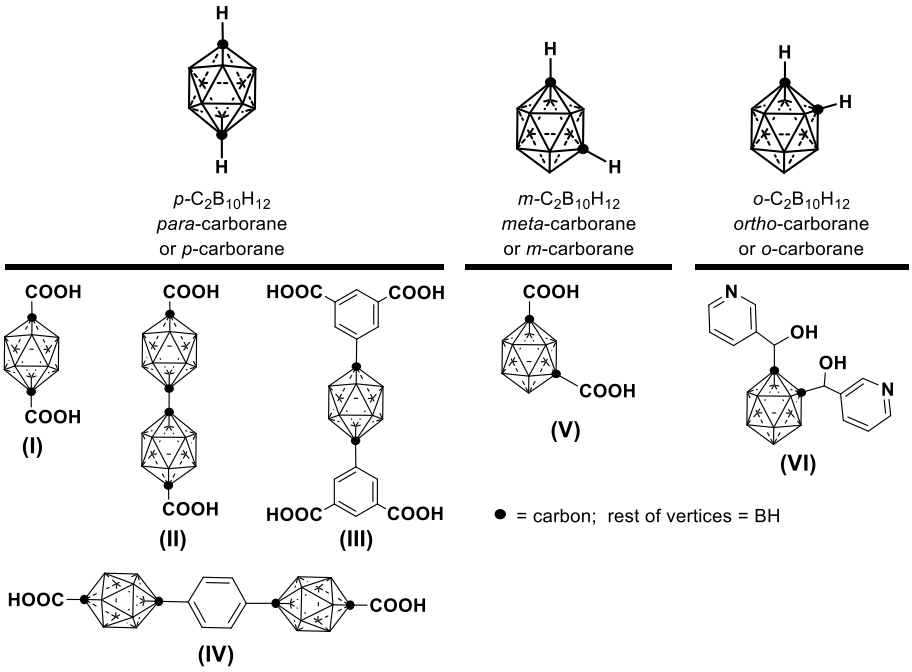

The icosahedral *closo*-carboranes (dicarba-*closo*-dodecaboranes; $C_2B_{10}H_{12}$) are an interesting class of exceptionally stable boron-rich clusters that can be prepared on the kilogram scale, and that can be modified at different vertices *via* chemical reactions[11–16]. Three isomeric forms are known: *ortho*, *meta* and *para*, which are differentiated by the position of the carbons in the cluster (Scheme 3-1). The average size of the carboranes (141-148 $Å^3$) is comparable to that of adamantane (136 $Å^3$) and is significantly larger (40%) than the phenyl ring rotation envelope (102 $Å^3$). The spherical feature of these molecules, with slightly polarized hydrogen atoms, and the presence of the hydride-like hydrogens at the B-H vertexes make the carboranes very hydrophobic. In addition to that, the high thermal and chemical stability, acceptor character and 3D aromatic nature of the icosahedral carborane clusters make them valuable ligands in coordination chemistry[17–24]. For example, some of us have reported the synthesis and electronic and magnetic properties of purely inorganic CPs based on the dicarboxylic acid of *ortho*-carborane[25–27]. Mirkin and co-workers explored the use of di-, tri- and tetra-carboxylic acid derivatives of *para*-carborane (**I** to **IV** in Scheme 1) for CPs synthesis, providing a series of CPs exhibiting unprecedented stabilities with

respect to thermal degradation, inherited from the carborane moiety[28–34]. Some of the CPs including these polycarboxylato *p*-carborane-based linkers showed gas uptake properties and excellent selectivity for CO_2/CH_4 mixtures. Jin and co-workers also constructed CPs based on the dicarboxylic acid derivatives of *para*- but also of *meta*-carborane linker (**V** in Scheme 3-1), and studied their adsorption and luminescence properties[35,36]. More recently, dicarboxylic and tricarboxylic derivatives of the smaller carborane *closo*-1,10-$C_2B_8H_{10}$ were also incorporated into porous CPs[30,37].

The hydrophobic properties of carboranes, exploited in a number of medical applications, can potentially enhance the hydrolytic stability of CPs. In fact, we have recently communicated the first example that uses a non-carboxylic derivative of *o*-carborane (**VI** in Scheme 3-1) as a linker to form a Zn(II)-based CP[38]. In this CP, the *o*-carborane based ligand **VI** acts as a bridging linker to connect Zn(II)-1,4-benzenedicarboxylate layers, giving a porous hydrophobic and water stable 3D framework. In our continuing exploration of the synthetic and structural chemistry of these carborane-based molecules, we have now synthesized a new disubstituted *m*-carboranylpyridylalcohols (**CB1** in Scheme 3-2). It is readily envisaged that these carborane based N-donor ditopic ligands are able to display various ligating topologies depending on the relative orientation of the pyridyl rings with respect to the carboranyldiol spacer. Consequently, the resulting CP architectures should be dependent on the ligand conformation and the relative position of nitrogen in the aromatic ring. The ligand flexibility is expected to be higher in the case of the *m*-carborane derivatives as the substituted carbons are farther away than in the *o*-carborane ones (**VI** in Scheme 3-1). We are particularly interested in the effect that the flexibility of these N-donor ditopic ligands may have on the crystal structures and networks but also in the potential use of these disubstituted carboranes as linkers in CPs. Herein, we report the synthesis of a novel carboranylalcohol 1,7-bis{(piridin-*n'*-yl)methanol}-1,7-dicarba-*closo*-dodecaboranes (*n'* = 4, **L2**) ligands, and their reaction with different tri- and tetratopic carboxylic acids and metal salts to form six new extended CPs (Scheme 3-2). We present the syntheses, crystal structures, thermal properties and water stability

of the new CPs. In addition, we show the crystal sponge behavior and guest dependent mechanical properties of one of these CPs.

Scheme 3-2. Representation of the new ligands (**CB1**) employed in this work and of the synthesis of CPs **CB1**MOF-**1** to **CB1**MOF-**4**.

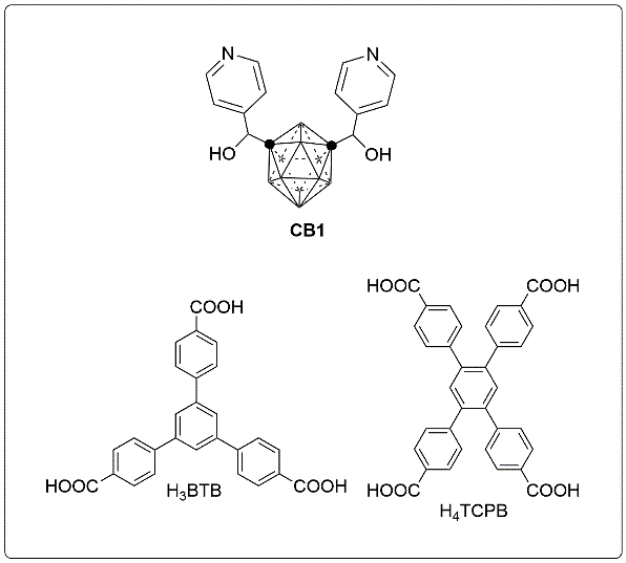

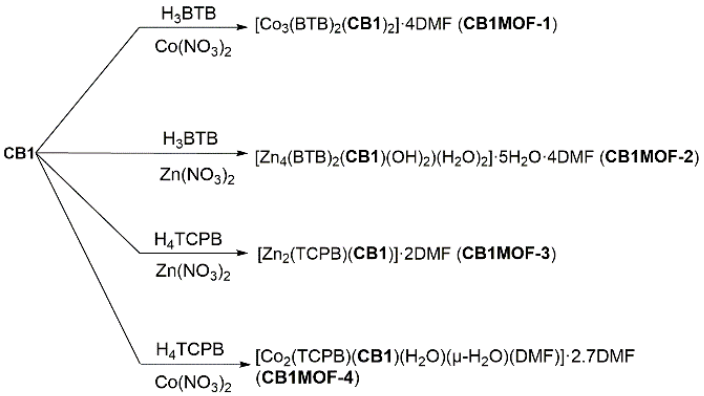

3.2 Results and discussion

Following our previous reports[19,39], a new bis-pyridylmethyl alcohols derived from the *m*-carborane cluster, **CB1** (Scheme 3-2), was prepared by the reaction of dilithiated *m*-carborane with the corresponding aromatic aldehydes at low temperature and isolated in high yields(92%). The alcohol was fully characterized by standard spectroscopic and analytical techniques[19]. The molecular structure of **CB1** was unequivocally established

by single crystal X-ray diffraction (SCXRD) (Figures 3-1), which was in agreement with the NMR data.

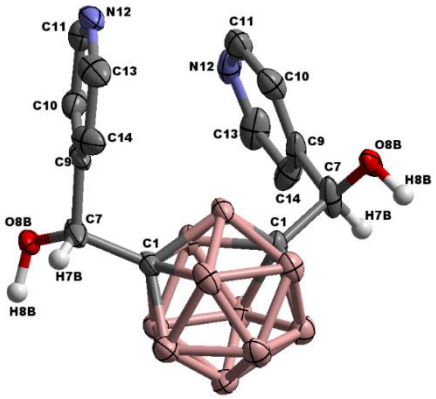

Figure 3-1. Molecular structure of **CB1**; thermal ellipsoids set at 50% probability (B-H and pyridine hydrogen atoms are omitted for clarity). Selected distances (Å) and angles (º): C1-C7, 1.558(3); C7-O8B, 1.270(4); C7-C9, 1.519(3); C1C7O8B, 116.3(2); C1C7C9, 111.8(2).

Solvothermal reactions (DMF/EtOH or DMF/EtOH/H_2O mixtures at 85 °C or 100 °C) of these *m*-carborane ligands with 1,3,5-benzenetribenzoic acid (H_3BTB) or 1,2,4,5-benzenetetrabenzoic acid (H_4TCPB) in the presence of $M(NO_3)_2$ (M = Co and Zn) provided crystalline CPs **CB1**MOF-**1** to **CB1**MOF-**4** in good yields and as pure phases (Scheme 3-2). IR spectra showed the characteristic broad B-H stretching bands from the carborane (in the range 2617 to 2531cm^{-1}), and the C=O vibration of the carboxylate groups and the DMF solvent molecules (Figure 3-2). Crystal structures of these CPs were determined by SCXRD (vide infra), and their simulated powder X-ray diffraction (PXRD) patterns compared with their experimental ones, confirming their phase purity (Figures 3-3 to 3-6). SEM and optical images of these CPs also showed the formation of homogeneous crystalline samples (Figure 3-7). TGA data for **CB1**MOF-**1** to **CB1**MOF-**4** (Figures 3-8 to 3-11) showed a first weight loss (13-20%) in the range of 95-350 ºC, which corresponds to the release of solvent molecules, followed by their decomposition starting at 350 ºC. Gas sorption measurements showed that all these CPs are non-porous to gases. Water stability of **CB1**MOF-**1** to **CB1**MOF-**4** was studied by immersing them in liquid H_2O overnight at room temperature. Analysis of the recovered crystalline solids by PXRD revealed that only **CB1**MOF-1 and **CB1**MOF-2 retained

their structure after this incubation time, as no change in their PXRD patterns were observed (Figures 3-12).

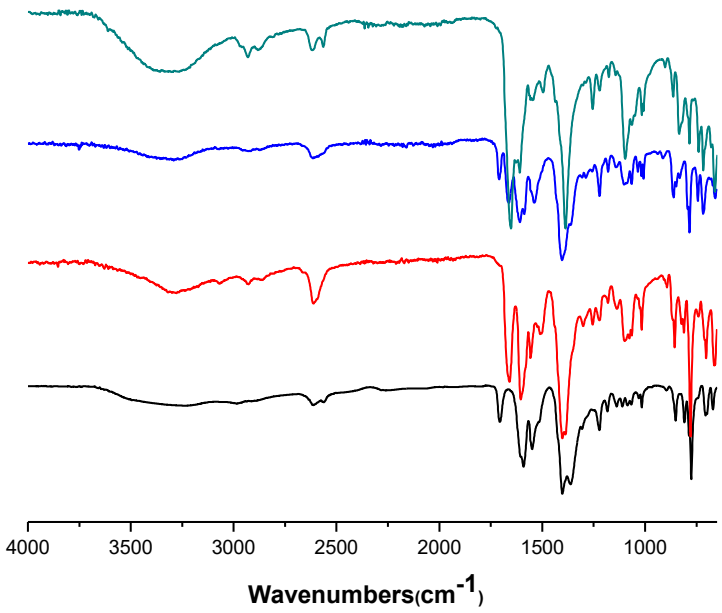

Figure 3-2. IR-ATR spectra of **CB1**MOF-2 (black)**, CB1**MOF-1 (red)**, CB1**MOF-3 (blue) and **CB1**MOF-4 (green).

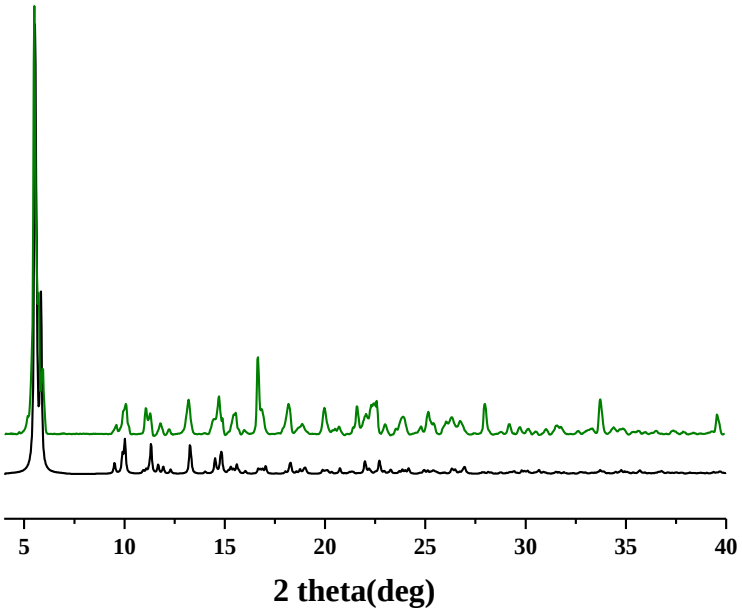

Figure 3-3. Simulated (black) and experimental (green) PXRD patterns of **CB1**MOF-1.

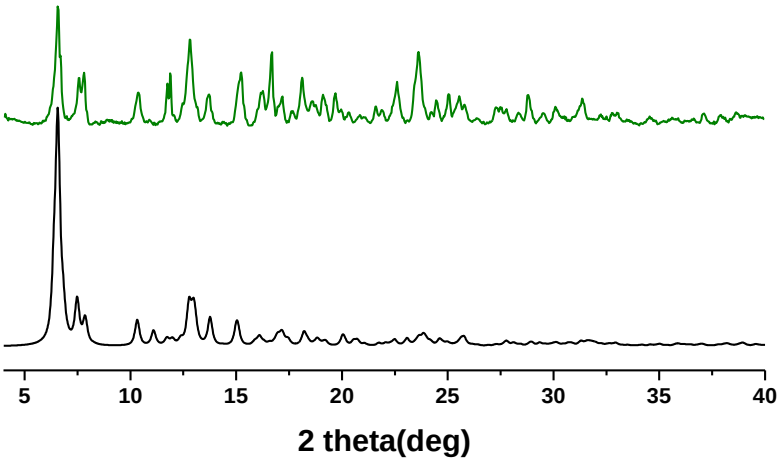

Figure 3-4. Simulated (black) and experimental (green) PXRD patterns of **CB1**MOF-1.

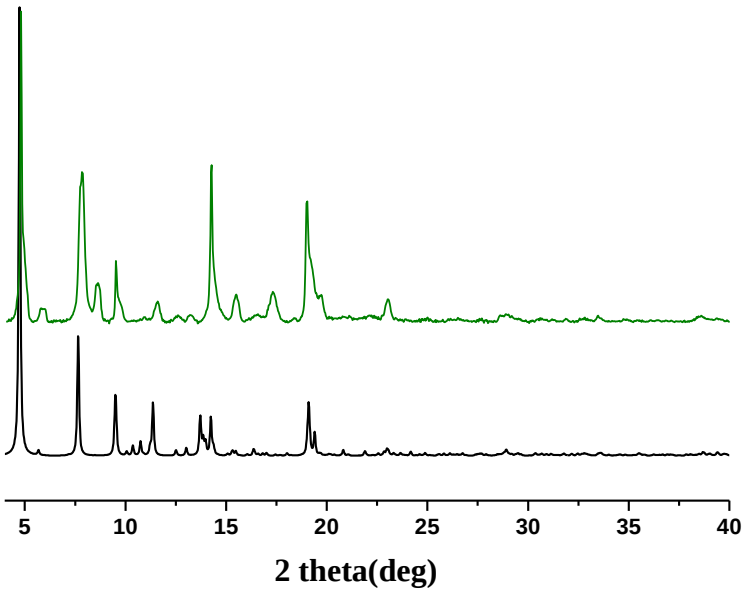

Figure 3-5. Simulated (black) and experimental (green) PXRD patterns of **CB1**MOF-3.

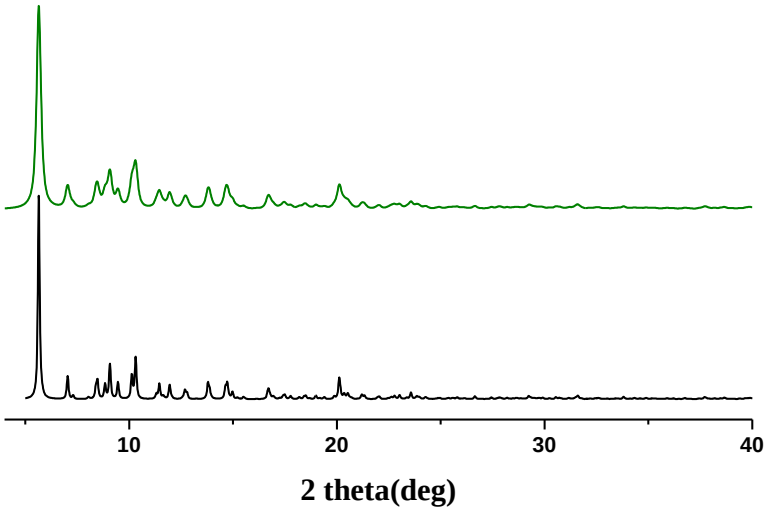

Figure 3-6. Simulated (black) and experimental (green) PXRD patterns of **CB1**MOF-4.

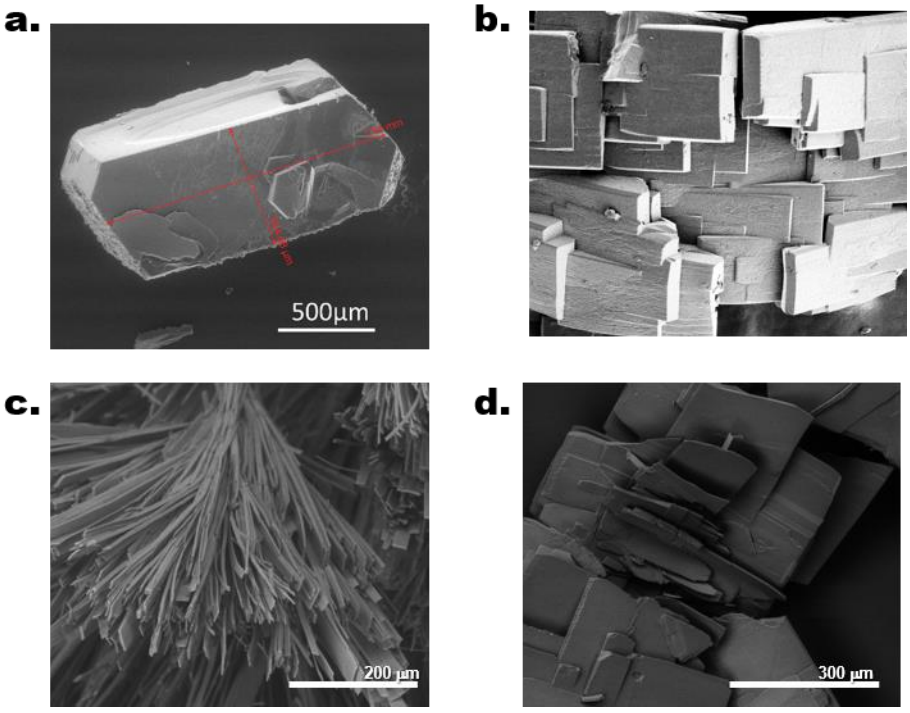

Figure 3-7. SEM images of (a) **CB1**MOF-1, (b) **CB1**MOF-2, (c) **CB1**MOF-3 and (d) **CB1**MOF-4 showing crystals morphology and confirming the homogeneity of the samples.

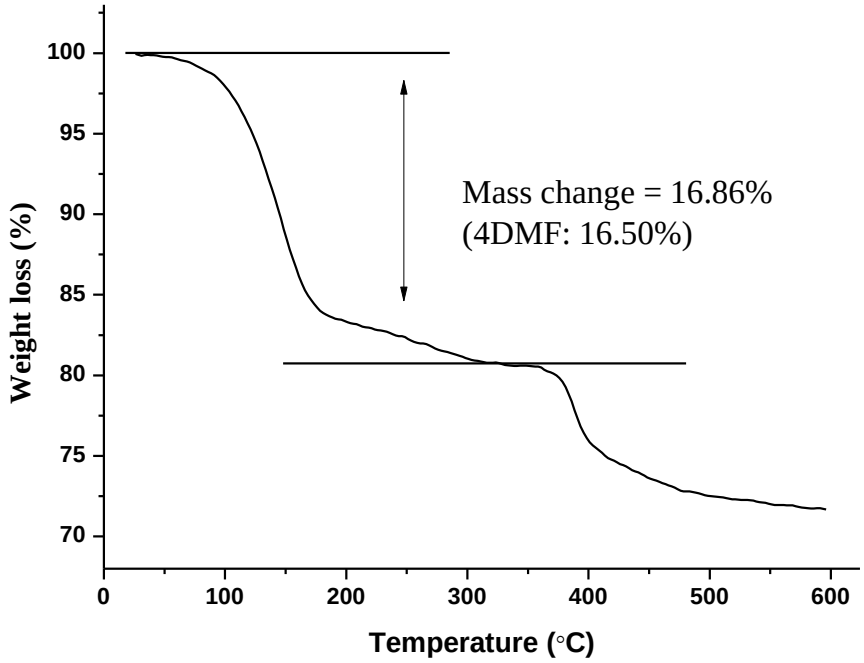

Figure 3-8. TGA diagram of **CB1**MOF-1.

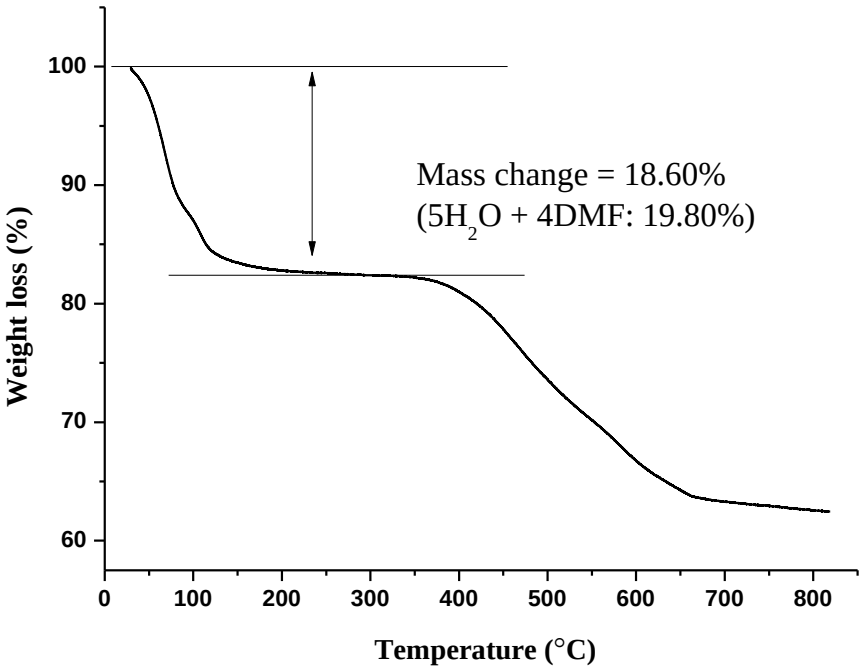

Figure 3-9. TGA diagram of **CB1**MOF-2.

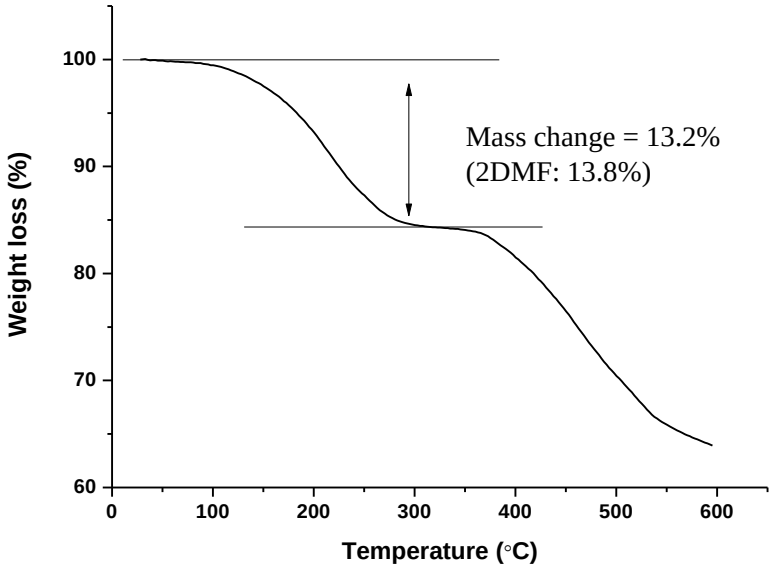

Figure 3-10. TGA diagram of **CB1**MOF-3.

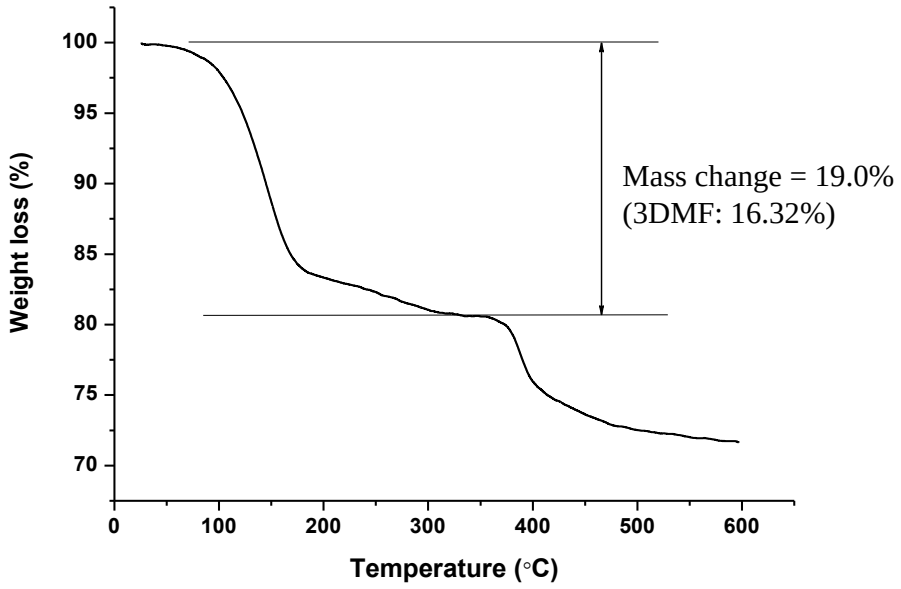

Figure 3-11. TGA diagram of **CB1**MOF-4.

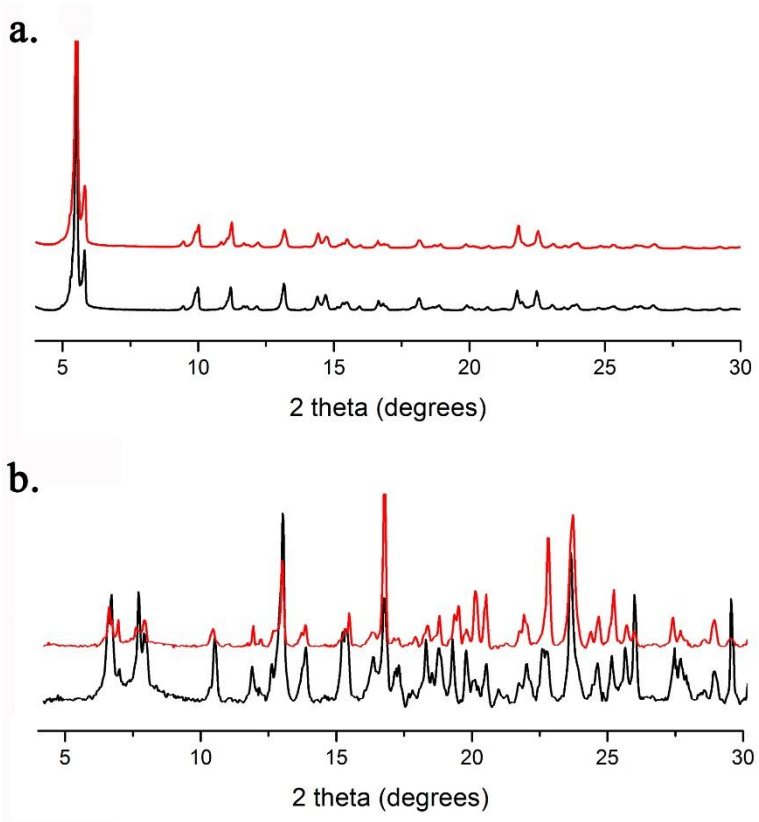

Figure 3-12. Powder patterns of the as made compounds (black) and after water treatment (red) for (a) **CB1**MOF-3 and (b) **CB1**MOF-4.

3.2.1 Crystal structures of carborane-based MOFs

Suitable crystals for SCXRD were obtained for **CB1**MOF-**1** to **CB1**MOF-4 (Table S3-1). **CB1**MOF-**1** and **CB1**MOF-3 crystallized in the triclinic *P*-1 space group. **CB1**MOF-**2** crystallized in the monoclinic *Pn* space group and **CB1**MOF-**4** in the monoclinic $P2_1/c$ one. In these structures (Figure 3-13), the carborane-based ligand **CB1** ligands showed two major roles: (i) acting as pillars, being involved in the dimensionality of the final CP structure; and (ii) acting as decorative ligands in order to complete the coordination sphere of the metal centers (Figures 3-14 to 3-17).

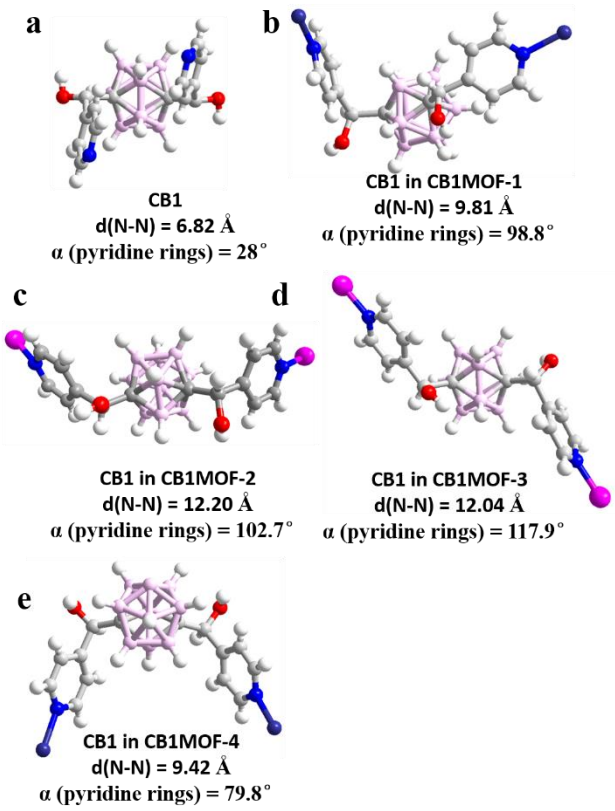

Figure 3-13. Molecular conformation of (a) free **CB1**, and **CB1** in (b) CB1MOF-1, (c) **CB1**MOF-2, (d) **CB1**MOF-3 and (e) **CB1**MOF-4 showing selected structural parameters.

*$[Co_3(BTB)_2(CB1)_2]\cdot 4DMF$ (**CB1**MOF-1).* As shown in Figure 3-14a, the basic building unit of **CB1**MOF-1 consists of a trinuclear $[Co_3(COO)_6N_4]$ unit. This unit is similar to that found in **CB1**MOF-1, except that the terminal DMF molecules are here exchanged by two **CB1** ligands. Each BTB ligand adopts the bridge bidentate (μ-κO:κO′) and the bridge bidentate chelate (μ-κ^2O,O′:κO′) coordination modes, connecting a total of six Co(II) centers. In **CB1**MOF-1, each trinuclear Co(II) unit is coordinated to six different BTB ligands, thus creating six-pointed star fashion layers running along the *bc* plane (Figure 3-14b). Then, these layers are pillared by **CB1** ligands resulting in a 3D framework that exhibits 1D channels along the *b* axis (Figure 3-14d). These channels are occupied by highly disordered DMF molecules that were masked by Olex2[40]. The total solvent-accessible volume in the channels account for approximately 35.7% of the whole crystal volume, as estimated by PLATON[41]. The flexibility of these carborane ligands was evident as the association of layers is carried out by two carborane ligands that adopt an almost L-shape (Figure 3-14c).

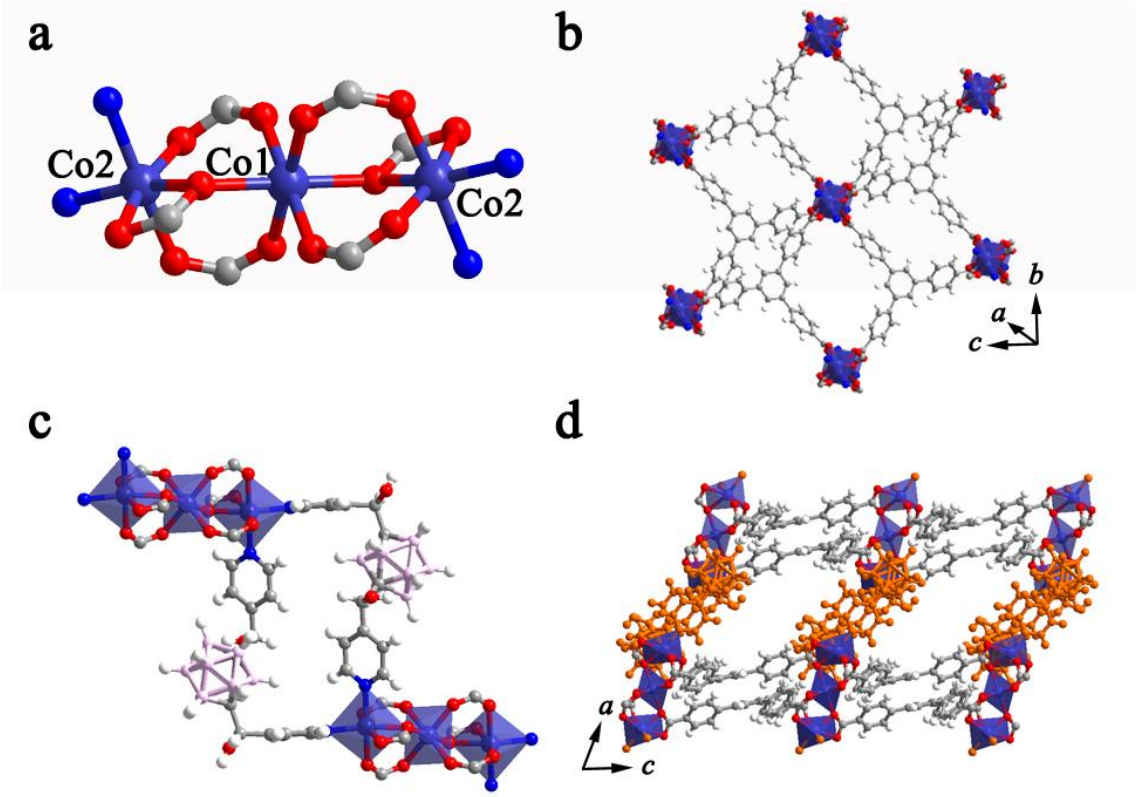

Figure 3-14. Crystal structure of **CB1**MOF-1: (a) view of the trinuclear Co(II) unit and coordination environment of the Co(II) ions; (b) six-pointed star fashion layer; (c) view of two trinuclear Co(II) units interlinked by two **CB1** ligand adopting a L-shape; and (d) 3D pillaring framework (**CB1** is represented in orange).

*$[Zn_4(BTB)_2(CB1)(OH)_2(H_2O)_2]\cdot 5H_2O\cdot 4DMF$ (**CB1**MOF-2).* The fundamental building unit of **CB1**MOF-2 is a tetranuclear ($[Zn_4O_2(COO)_6N_2]$ cluster, in which the four Zn(II) ions are connected through six BTB and two **CB1** ligands (Figure 3-15a). Zn(1) and Zn(2) are hexacoordinated with $\{O_6\}$ and $\{NO_5\}$ environments, respectively. Zn(1) is coordinated to four O atoms of three different BTB ligands and to two O atoms of two OH groups. Zn(2) is coordinated to one **CB1** ligand, to three O atoms of three BTB ligands, to one OH group and to one water molecule. Zn(3) and Zn(4) are $\{NO_3\}$- and $\{O_4\}$-tetracoordinated. These metal centers are coordinated to two O atoms of two BTB ligands, to one OH group and to one **CB1** ligand for Zn(3) or to one water molecule for Zn(4). The BTB ligands exhibit three different coordination modes: monodentate (κO), bridge bidentate (μ-κO:κO′) and bridge bidentate chelate (μ-κ^2O,O′:κO′) modes. In **CB1**MOF-2, the connection of the tetranuclear Zn(II) units through the BTB linkers creates a 3D honeycomb-like network (Figure 3-15c). In this network, **CB1** ligands

bridge two tetranuclear Zn(II) units with a N-N distance of 12.20 Å, creating zig-zag chains that run along the *ac* plane (Figure 3-15d). Overall, this framework exhibits 1D-channels running along the *b* axis, which are occupied by highly disordered DMF molecules that were masked by Olex2[40]. The total solvent-accessible volume of **CB1**MOF-2 accounts for approximately 33.3% of the whole crystal volume, as estimated by PLATON[41]. Hydroxyl groups of the carborane moiety are pointing to the interior of the honeycomb pores, and they are likely establishing H-bonds with the squeezed solvent molecules.

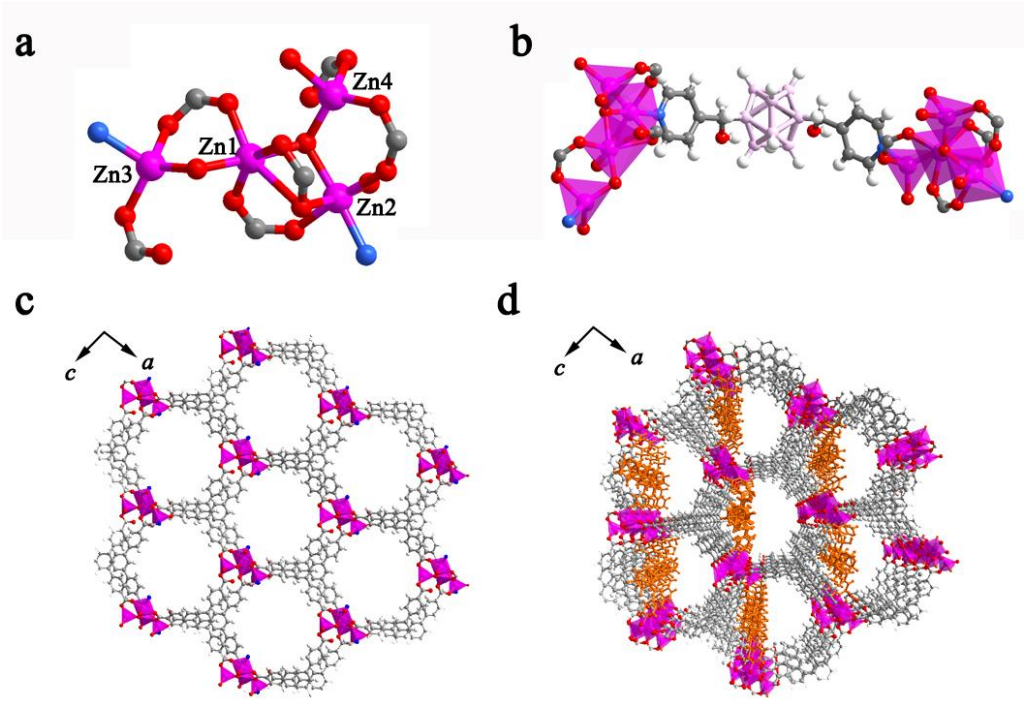

Figure 3-15. Crystal structure of **CB1**MOF-2: (a) view of the tetranuclear Zn(II) unit and coordination environment of the Zn(II) metal centers; (b) view of two tetranuclear Zn(II) units interlinked by a **CB1** ligand; and (c-d) 3D-honeycomb net (**CB1** is omitted in c and is represented in orange in d).

*[Zn_2(TCPB)(CB1)]·2DMF (**CB1**MOF-3).* The building unit of **CB1** is a paddle-wheel [$Zn_2(COO)_4N_2$] cluster (Figure 3-16a). In this unit, the Zn(II) ions are {NO_4}-pentacoordinated. The values of the Addison parameter τ[42] indicates that both Zn(II) centers adopt a square pyramidal geometry (0.054 for Zn1 and 0.059 for Zn2) coordinated to four O atoms of four different TCPB linkers occupying the basal position and to one N atom of the **CB1** in the apex position with a Zn-N distance of 2.030(4) Å.

In this structure, each TCPB ligand is fully deprotonated and coordinates four paddle-wheel units in a bridge bidentate mode (μ-κO:κO′), creating 2D layers in the *ab* plane (Figure 3-16b). These layers are further pillared by **CB1** linkers with a N-N distance of 12.04 Å (Figure 3-16c), resulting in a 3D 2-fold interpenetrated framework (Figure 3-16d)[43].

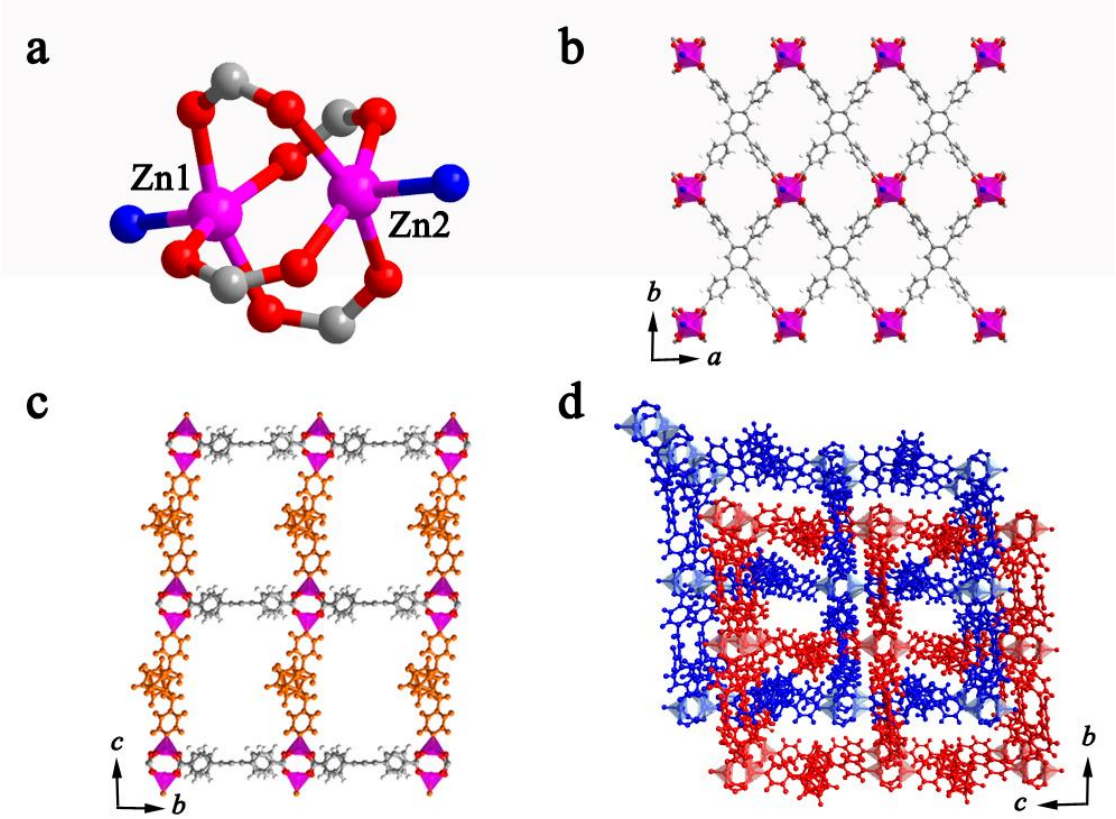

Figure 3-16. Crystal structure of **CB1**MOF-3: (a) view of the Zn(II) paddle-wheel unit; (b) 2D layer; (c) 3D pillaring structure (**CB1** is represented in orange); and (d) two-fold interpenetrated framework, highlighting each one of the pillaring structures in red and blue.

*[Co_2(TCPB)(CB1)(H_2O)(μ-H_2O)(DMF)]·2.7DMF (**CB1**MOF-4).* As shown in Figure 3-17a, the building unit of **CB1**MOF-4 is a dinuclear [$Co_2(COO)_4N_2$] cluster, in which both Co(II) centers are {NO_5}-hexacoordinated. Co(1) is coordinated to two O atoms from two TCPB ligands, to one DMF molecule, to one bridge and one terminal water molecule and to one N atom from one **CB1** linker, whereas Co(2) is coordinated to four O atoms from four different TCPB ligands, to the bridge water molecule and to the N atom of one **CB1** linker. The TCPB ligands coordinate the dinuclear Co(II) units in a bridge bidentate (μ-κO:κO′) and a monodentate (κO) coordination mode (Figure 3-17b).

The structure of **CB1**MOF-4 consists on bidimensional square grid layers built up from connecting each dinuclear Co(II) unit to four TCPB ligands and each TCPB ligand to four Co(II) units (Figure 3-17b). In this structure, **CB1** ligands are not involved in increasing the structural dimensionality of **CB1**MOF-4. Instead, the U-shape orientation of **CB1** bridges two Co(II) atoms of the same layer with a Co-Co distance of *ca.* 11 Å (Figure 3-17b and 3-17c). These layers are packed through several O-H···O H-bonds involving the coordinated water molecule and the O atom of a carboxylate group (Figure 3-17d).

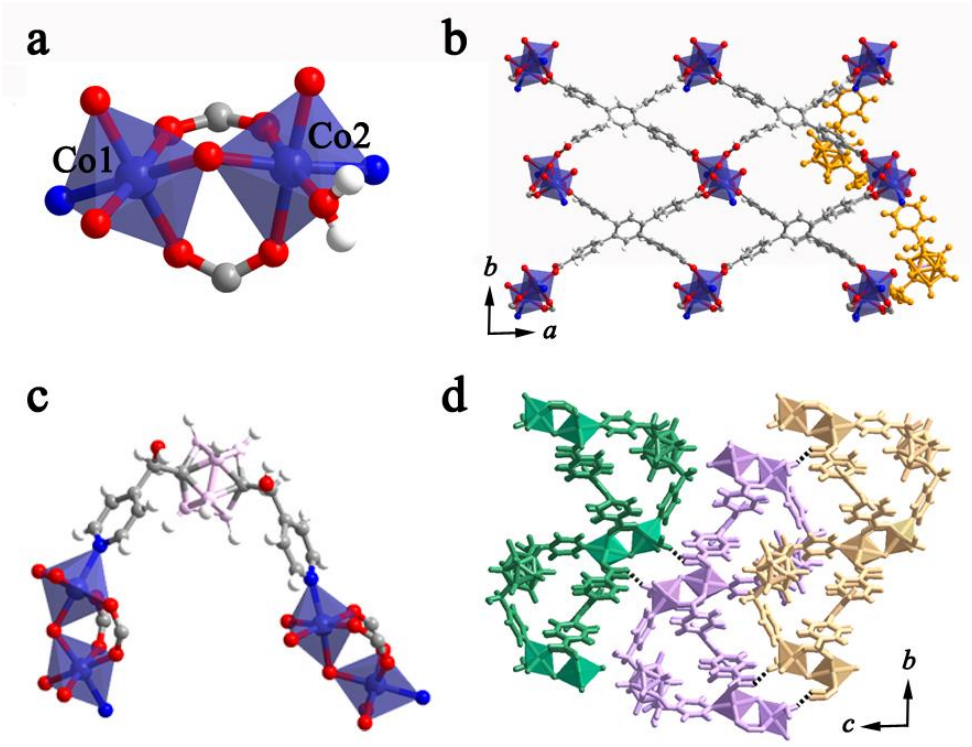

Figure 3-17. Crystal structure of **CB1**MOF-4: (a) view of the dinuclear Co(II) unit; (b) square grid layer extended along the *ab* plane (**CB1** connecting two Co(II) centers in the same layer is represented in orange); (c) view of two dinuclear Co(II) units bridged through one **CB1** ligand; and (d) 3D packing of the coordination layers through Ow-H···O H-bond interactions (represented as black dotted lines).

3.2.4 Guest encapsulation and nanomechanical properties of CB1MOF-1

Motivated by the relatively large solvent accessible volume of **CB1**MOF-1 (~36%) and the large size and morphology of the crystals (Figure 3-7a), we decided to study whether this CP could act as a crystalline sponge for guest molecules and whether some specific

host-guest interactions could be observed[6,7]. As mentioned above, the as-prepared **CB1**MOF-1 contains DMF molecules as guest; so, hereafter it will be named as **CB1**MOF-1 ⊃ **DMF**. To study its guest-exchange capabilities, the as-prepared crystals of **CB1**MOF-1 ⊃ **DMF** were immersed in an excess of several selected organic solvents for 24-48 h, and the exchange was monitored by IR-ATR following the changes in the C=O stretching band of DMF. Remarkably, complete post-synthetic exchange of DMF guest molecules was achieved in methanol, chloroform, benzene, toluene, nitrobenzene and 1-nitropropane, but no significant exchange was observed for cyclohexane, hexane and carbon tetrachloride. The different nature of the solvents that replaced the DMF in **CB1**MOF-1 ⊃ **DMF** prompted us to study more in detail the sponge behavior of this particular CP. Structural characterization using SCXRD showed that guest exchange processes resulted in six new structures, including **CB1**MOF-1 ⊃ **MeOH** (methanol), **CB1**MOF-1 ⊃ **$CHCl_3$** (chloroform), **CB1**MOF-1 ⊃ **NP** (1-nitropropane), **CB1**MOF-1 ⊃ **NBz** (nitrobenzene), **CB1**MOF-1 ⊃ **Bz** (benzene) and **CB1**MOF-1 ⊃ **Tol** (toluene). Crystal and data collection details can be found in table S3-2. All guest-containing structures **CB1**MOF-1 ⊃ **Guest** were found to crystallize in the same centrosymmetric space group *P*-1, showing an expansion (Bz < NP < Tol < NBz), a contraction (MeOH) and almost no change ($CHCl_3$) of the unit cell parameters when compared with the as-prepared **CB1**MOF-1 ⊃ **DMF**. The higher expansion of the unit cell was found in **CB1**MOF-1 ⊃ **NBz** and **CB1**MOF-1 ⊃ **Tol** with a volume increase of 140 $Å^3$ and 71 $Å^3$, respectively. DMF and MeOH molecules in **CB1**MOF-1 ⊃ **Guest** structures were highly disordered, so that the solvent masking procedure implemented in Olex2[40] was used to remove the electronic contribution of solvent molecules from the refinement. $CHCl_3$ and NP were partially masked, but aromatic solvents (benzene, toluene and nitrobenzene) were clearly located and refined (Table S3-2 and Figure 3-18).

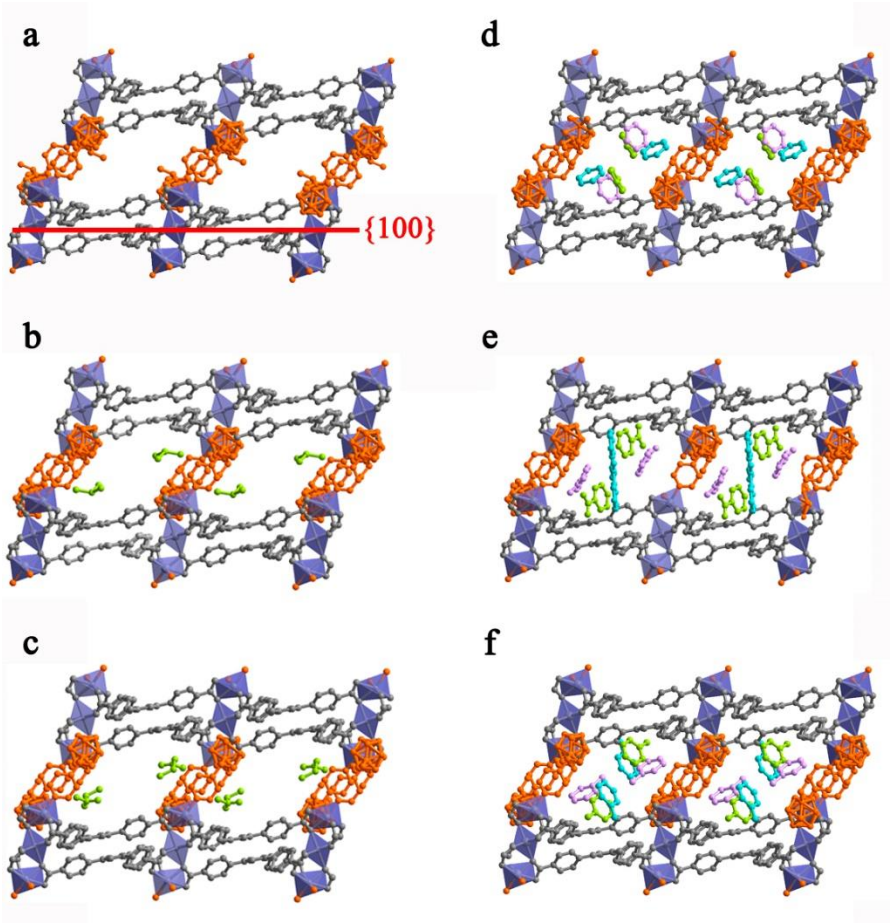

Figure 3-18. Plots of the SCXRD crystal structures for **CB1**MOF-1 ⊃ **Guest**, viewed along the *b* axis: (a) DMF, (b) chloroform, (c) 1-nitropropane, (d) benzene, (e) nitrobenzene and f) toluene. Guest molecules are shown with colors corresponding to equivalent sites. The framework is shown in grey, except for **CB1**, that are represented in orange. H atoms are omitted for clarity. The plane orthogonal to the **CB1** linkers {100} is highlighted in red.

The possibility to solve the X-ray crystal structures of the different **CB1**MOF-1 ⊃ **Guest** (Figure 3-17) allowed us to further analyze the nature of the host-guest interactions (Tables 3-1 to 3-2 and Figures S3-1 to S3-5). In the case of **CB1**MOF-1 ⊃ **$CHCl_3$** and **CB1**MOF-1 ⊃ **NPr**, one guest molecule was found in the asymmetric unit (Figures 3-18b and 3-18c). Here, whereas the nonpolar $CHCl_3$ molecule interacts with the aromatic rings of the BTB molecules by C–H···π interactions, the polar aprotic NP mainly establishes H-bond interactions with the OH groups of **CB1**. For **CB1**MOF-1 ⊃ **NBz**, **CB1**MOF-1 ⊃ **Bz** and **CB1**MOF-1 ⊃ **Tol**, it was possible to precisely refine all aromatic guest molecules inside the framework (Figure 3-18d to 3-18f), probably due to the large number of host-guest interactions present in these solvates/structures

(Tables 3-2 and Figures S3-3 to S3-5). Hydroxyl groups of **CB1** establish classical H-bond interactions with NBz molecules in **CB1** ⊃ **NBz** (Figure S3-4a), whereas O-H···π interactions are observed in **CB1**MOF-1 ⊃ **Bz** and **CB1**MOF-1 ⊃ **Tol** (Figures S3-3, S3-5). The aromatic nature of these guest molecules allows establishing C–H···π and π···π interactions with BTB and **CB1** linkers. Interestingly, the carborane core also participates in host-guest interactions *via* weak C–H···H–B interactions, as observed in **CB1**MOF-1 ⊃ **Bz** and **CB1**MOF-1 ⊃ **Tol**[44–46].

Table 3-1. Geometrical parameters of host-guest contacts (Å, º), involved in **CB1**MOF-1 ⊃ **Guest** structures[a].

Guest	D–H···A[b]	*d*(H···A)	<(DHA)	<(HHB)
$CHCl_3$	**Host-Guest**			
	($CHCl_3$) C(62)–H···M	2.367	171.86	-
	Guest-Guest			
	-	-	-	-
NPr	**Host-Guest**			
	(**L2**) O(22B)–H···O(62)	2.451	156.0	-
	(**L2**) O(22B)–H···O(64)	1.809	125.8	-
	(NPr) C(65)–H(A)···M	2.476	143.3	-
	Guest-Guest			
	-	-	-	-
NBz	**Host-Guest**			
	(**L2**) O(22A)–H···O(82)	2.368	143.9	-
	(**L2**) C(19)–H···O(92)	2.651	122.4	-
	(**L2**) C(20)–H···O(92)	2.577	124.4	-
	(BTB) C(54)–H··· O(93)^{i}	2.633	160.6	-
	(**L2**) C(17)–H···M	2.820	145.3	-
	(NBz) C(99)–H···M	2.660	153.6	-
	Guest-Guest			
	C(97)–H··· O(72)	2.483	132.9	-
Bz	**Host-Guest**			
	(**L2**) O(01M)–H··· C(95)	2.648	165.3	-
	(**L2**) O(01M)–H··· C(90)	2.702	150.6	-
	(BTB) C(45)–H··· C(90)	2.640	159.5	-
	(BTB) C(43)–H···M	2.943	139.8	-
	(Bz)C(82)–H···M^{i}	2.704	155.2	-
	(Bz) C(80)–H···H–B(2)	2.246	130.4	157.7
	Guest-Guest			
	C(96)–H···M	2.969	121.0	-

	Host-Guest			
	(**L2**)O(022A)–H⋯ C(84)	2.648	154.7	-
	(**L2**) O(022A)–H⋯ C(85)	2.654	156.1	-
Tol	(Tol) C(73)–H⋯M	2.692	147.6	-
	(Tol) C(71A)–H⋯H–C(37)	2.313	129.4	131.3
	Guest-Guest			
	C(71B)–H⋯ M	2.949	130.0	

[a]For C–H⋯π contacts, geometries are given with respect to the aromatic centroid M. See figures S3-1 to S3-5 for XRD representations of the contacts. [b] O–H bond lengths are not normalized to neutron distances. Symmetry codes (i) -x,1-y,1-z.

Table 3-2. Arene–arene packing geometries (Å, º), involved in **CB1**MOF-1 ⊃ **Bz** and **CB1**MOF-1 ⊃ **Tol**.[a]

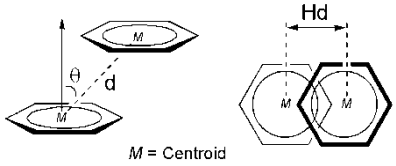

	Interplanar				
Guest	**distance**	**angle**	**d**[b]	**Hd**[b]	**θ**[c]
Bz	3.396[d]	11.39	3.890	1.897	29.2
	3.082[e]	22.53	3.988	2.531	39.4
Tol	3.397[f]	10.11	3.848	1.808	28.0

[a] See embedded Chart at the top for nomenclature and Figures S3-2 and S3-4. [b] Ring centroid to ring centroid distance. [c] Ring normal to vector between the ring centroids. [d] Shortest carbon-carbon distance (C24–C92). [e] Shortest carbon-carbon distance (C36–C98). [f] Shortest carbon-carbon distance (C24–C82)

3.2.5 Nanomechanical Properties of CB1MOF-1 ⊃ Guest.

Mechanical tunability of CPs/MOFs as a result of strong host–guest interactions represent nowadays a challenging approach for the development of novel applications[9,10] (Figure 3-19). The mechanical properties of a number of CPs/MOFs, such as MOF-5[47,48], ZIFs[49] and soft porous crystals of the type $[Zn_2(L_2)(dabco)]_n$ (L = 1,4-benzenedicarboxylate derivatives, dabco = 1,4-diazabicyclo[2.2.2]octane), have been investigated experimentally[50]. The latter is an interesting example that is closely related to our findings. It was found that the mechanical properties of $[Zn_2(L_2)(dabco)]_n$ are primarily dependent on the detailed network geometry and the precise orientation

of the molecular building blocks within the porous framework, but not to specific guest-framework interactions. However, in this study, the authors demonstrated that guest molecules influence the framework geometry (*e.g.* tilt angle and bending of linkers) of this family of CPs and, therefore, their mechanical properties. On another study, effects of pore occupancy on elasticity were proved on ZIF-8 single-crystals, where a decrease (to 7%) in elasticity (*E*) was observed on desolvation[49].

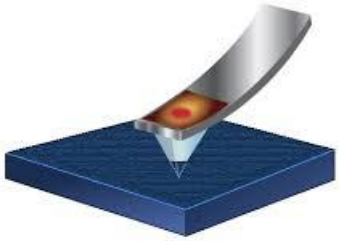

Figure 3-19. Simplified image of nanoindentation technique

The series of guest-containing structures **CB1**MOF-1 ⊃ **Guest** in this work represents an ideal platform for studying the mechanical properties of such porous materials. Indeed, as shown in the previous section, the guest molecules affect the volume of the structures but not the symmetry of the framework (neither tilt angle nor bending of linkers was observed). Thus, we hypothesized that any variation on the mechanical properties for the **CB1**MOF-1 ⊃ **Guest** structures should be related to the nature of the guest molecules and/or the specific host-guest interactions.

Single-crystal nanoindentation experiments were performed under conventional quasi-static stiffness using Berkovich pyramidal-shaped diamond tip operating in the load control mode. Crystals of **CB1**MOF-1 ⊃ **Guest** (Guest = DMF, $CHCl_3$, NPr, NBz, Bz, Tol and MeOH) were carefully selected, for the indentation measurements and the {100}-oriented facets were oriented normal to the indenter axis. Note here that the anisotropic shape of the plate-like crystals of **CB1**MOF-1 ⊃ **Guest** enabled indexing their plate face, which was identified as the {100} plane (Figure 3-18a and 3-20). Measurements were done after taking the crystals from the appropriate solvents (within

5 h) and crystallinity of the measured samples was confirmed *a posteriori* by PXRD and optical microscope. Solvent loss and amorphization were observed in crystals being in air for over 24 h in all cases, except for $CHCl_3$ and MeOH that occurred after 10 h (Figure 3-21). Averaged data is listed in Table 3-3. The nanoindentation results on **CB1**MOF-1 ⊃ **Guest** revealed significant variations in the reduced Young's modulus (E_r) depending on the guest.

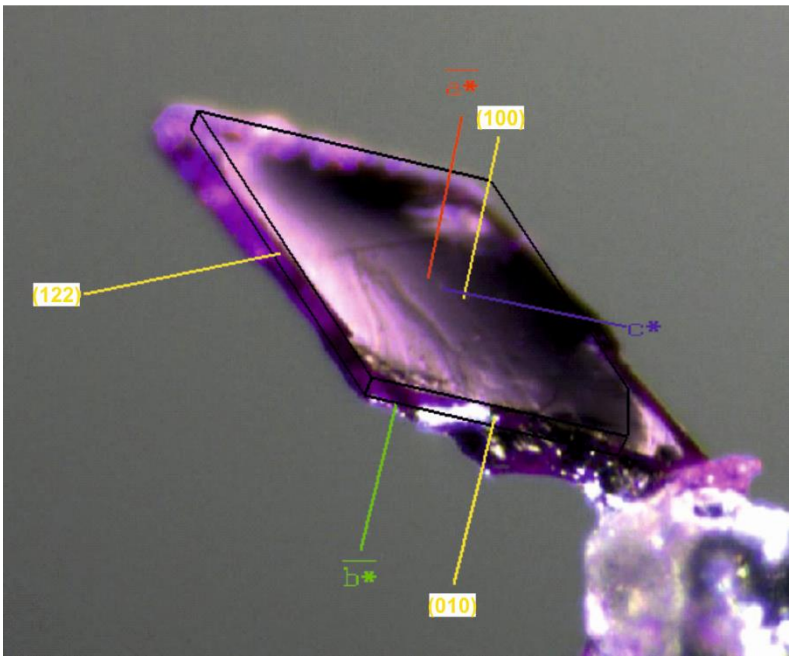

Figure 3-20. Photograph of representative example of face-indexed single crystals for **CB1**MOF-1 ⊃ **$CHCl_3$**.

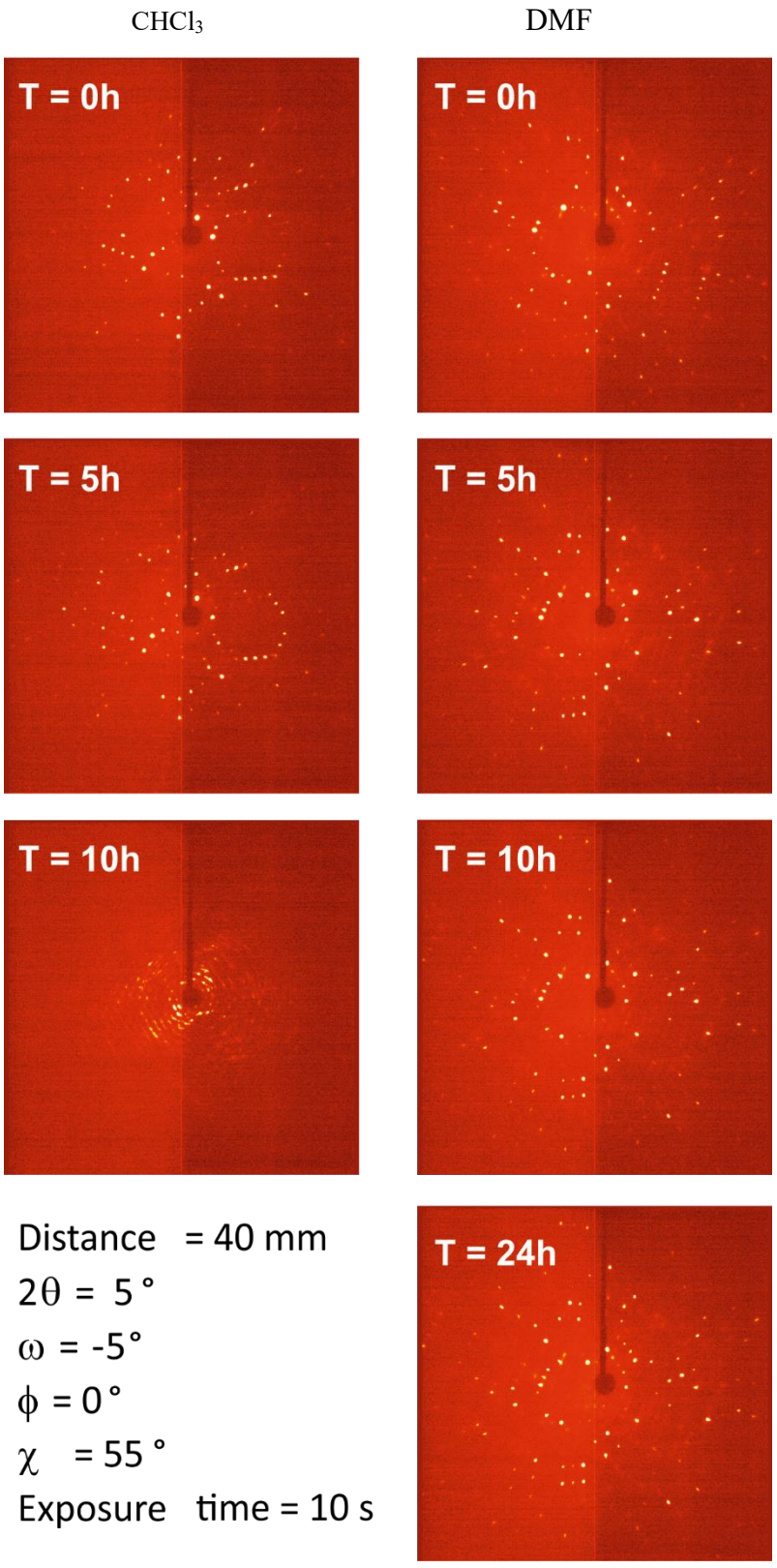

Figure 3-21. Representative diffraction images of **CB1**MOF-1 ⊃ **$CHCl_3$** (left column) and **CB1**MOF-1 ⊃ **DMF** (right column) at different times. First measurement of crystals right after being taken from the solvents is taken as T = 0h.

Table 3-3. Mechanical properties of different **CB1**MOF-1 ⊃ **Guest** on the {100}-oriented facets determined by nanoindentation experiments. E_r is the reduced elastic modulus and H the hardness. All samples were measured right after taking them out of the solvents and slightly dried on a filter paper.

Guest	E_r/GPa	H/GPa
$CHCl_3$	0.556(36)	0.078(8)
NPr	1.20(13)	0.203(28)
MeOH	1.367(65)	0.272(18)
DMF	1.71(17)	0.197(27)
Toluene	1.75(15)	0.250(28)
NBz	1.83(13)	0.471(43)
Bz	2.67(28)	0.322(56)

The elastic modulus of **CB1**MOF-1 can vary by a factor of nearly 5 for the {100} crystallographic orientation by simply exchanging the guest molecules. The average moduli $E_{\{100\}}$ are in the range from 0.6 to 2.7 GPa. These values are comparable to other porous MOFs[49,50]. It is however interesting that higher elastic modulus values of **CB1**MOF-1 were observed when aromatic solvent molecules or DMF were occupying the voids (1.71-2.67 GPa). On the other hand, sensibly smaller elastic modulus values were observed when non aromatic polar solvent molecules (MeOH, 1.37 GPa; NPr, 1.20 GPa) or the non-polar $CHCl_3$ (0.56 GPa) were filling the pores of **CB1**MOF-1. The hardness along the same {100} crystallographic orientation also revealed an increase, although not as pronounced, depending on the adsorbed guest. $H_{\{100\}}$ values are in the range 0.20-0.47 GPa, except that for the $CHCl_3$ guest structure, that gives a sensibly lower value (0.08 GPa).

As hypothesized above, any variation on the mechanical properties for **CB1**MOF-1 ⊃ **Guest** structures should be related to the nature of the guest molecules and/or the specific host-guest interactions. The mechanical response of the {100}-oriented facets is mainly dominated by the **CB1**-pillars, which interconnect the 2D {Co-BTB} layers

(Figures 3-14 and 3-18). In all **CB1**MOF-1 ⊃ **Guest** structures, the **CB1**-pillars are at the same angle with respect to the {100} crystals facets, so that comparable E_r and H values should be obtained based on the network geometries[50]. This suggests that the observed specific host-guest interactions have an impact in the mechanical properties of **CB1**MOF-1. Solvates with higher number of host-guest interactions lead to higher Young's moduli and higher hardness (Young´s moduli is 5 times higher in **CB1**MOF-1 ⊃ **Bz** than in **CB1**MOF-1 ⊃ **$CHCl_3$**). In contrast, lower elastic modulus and hardness was found in **CB1**MOF-1 ⊃ **$CHCl_3$**, in **CB1**MOF-1 ⊃ **NPr** and in **CB1**MOF-1 ⊃ **DMF**, where the guest molecules are highly or partially disordered, which suggests that very weak or non-specific host-guest interactions are taking place in these cases. On the contrary, aromatic solvents show a high number of specific interactions with the framework of **CB1**MOF-1, and consequently, lead for high elastic modulus and hardness values.

3.3 Conclusions

In conclusion, we have reported the synthesis and characterization of four new CPs obtained from the reaction between a novel *m*-carborane bispyridylalcohol ligand and tri- and tetracarboxylic linkers with $M(NO_3)_2$ salts (M = Zn and Co). The flexibility of the carborane moieties is reflected in the structural diversity of the generated coordination networks, showing in most of the cases their ability to increase the dimensionality of the final framework by acting as pillar ligands. Complete post-synthetic exchange of DMF guest molecules by a variety of organic solvents was achieved in one of these CPs. This CP (named as **CB1**MOF-1) acts as a crystalline sponge showing a higher affinity for aromatic guest molecules due to the presence of a large number of host-guest interactions (O–H···π, C–H···π, π···π and weak C–H···H–B). This high number of interactions is probably the reason to render the aromatic guest molecules regularly ordered in the X-ray structures, unlike other non-aromatic molecules. The nanoindentation experiments on **CB1**MOF-1 ⊃ **Guest** suggest that a higher number of host-guest contacts has also an effect on the hardness and Young's

moduli values, which can vary by a factor of five (*e.g.* **CB1**MOF-1 ⊃ **Bz** *versus* **CB1**MOF-1 ⊃ **$CHCl_3$**).

3.4 Experimental section

3.4.1 Materials and methods

Syntheses for the carboranylalcohol ligands were carried out under nitrogen atmosphere in round-bottomed flasks equipped with a magnetic stirring bar, capped with a septum. Tetrahydrofuran (THF) was distilled from Na/benzophenone. CPs syntheses were done in air. All chemicals were commercially available and used as received. IR ATR spectra were recorded on a Perkin–Elmer Spectrum One spectrometer. ^{1}H, ^{13}C and ^{11}B NMR spectra were recorded respectively at 300, 75 and 96 MHz with a Bruker Advance-300 spectrometer in deuterated dimethylsulfoxide, unless denoted, and referenced to the residual solvent peak for ^{1}H and ^{13}C NMR or to $BF_3 \cdot OEt_2$ as an external standard for ^{11}B NMR. Chemical shifts are reported in ppm and coupling constants in Hertz. Multiplets nomenclature is as follows: s, singlet; d, doublet; t, triplet; br, broad; m, multiplet. Elemental analyses were obtained by a CarboErba EA1108 microanalyzer. The mass spectra were recorded in the negative ion mode using a Bruker Biflex MALDI-TOF-MS [N_2 laser; λ_{exc} 337 nm (0.5 ns pulses); voltage ion source 20.00 kV (Uis1) and 17.50 kV (Uis2)] with 3,5-dimethoxy-4-hydroxycinnamic acid as the matrix. TGA-DSC from NETZSCH (heating rate: 10 ºC/min; temperature range: 25 to 800 ºC). Gas sorption (CO_2/195 K and N_2/77 K) measurements for **CB1**MOF-2 were performed using an AutosorbIQ (Quantachrome Instruments). Field-Emission Scanning Electron Microscopy (FE-SEM) images were collected using a Quanta 650F Environmental Scanning Electron Microscopy (Field Emission Inc, USA). Powder X-ray Diffraction (PXRD) patterns were recorded at room temperature on an X'Pert PRO MPD diffractometer (Panalytical) using Cu Kα (λ = 1.5405 Å) radiation.

3.4.2 Synthesis of carborane substitute ligands

1,2-bis{(pyridin-4´-yl)methanol}-1,7-dicarba-closo-dodecaborane (CB1). *n*-BuLi (4.49 mL, 1.55 M in hexane, 7.0 mmol) was added dropwise to a solution of

m-carborane (502.4 mg, 3.5 mmol) in THF (25 mL) at 0 °C (ice/water bath) under nitrogen atmosphere. The mixture was stirred at 0 °C for 30 min and at room temperature for 1h to give a pale-yellow suspension. The flask was then cooled to -41 °C (acetonitrile /liquid N_2), whereupon a solution of 4-pyridinecarboxaldehyde (0.7 mL, 7.0 mmol) in THF (1 mL) was added. The resulting solution was stirred at -41 °C for 4 h. Then, a saturated aqueous solution of NH_4Cl (10 mL) was added at -41 °C. The resulting mixture was taken out of the cooling bath and allowed to warm naturally to room temperature while stirring. Afterwards, Et_2O (15 mL) was added while stirring. A white solid precipitated after to 20-25 min, which was filtrated, washed with water and Et_2O, and dried under vacuum affording pure **CB1** (1.16 g, 3.23 mmol, 92.3 %). ^{1}H NMR 8.53 (d, J = 6.0 Hz, 4H, C_5H_4N), 7.23 (d, J = 6.0 Hz, 4H, C_5H_4N), 6.64 (d, J = 5.1 Hz, 2H, OH), 4.83 (d, J = 5.1, 2H, CHOH). ^{11}B NMR: -11.36 (br, 10B). ^{13}C NMR: 149.9 (C_5H_4N), 149.3 (C_5H_4N), 127.8 (C_5H_4N), 81.0 ($C_{cluster}$), 72.2 (CHOH). IR (ATR; selected bands; cm^{-1}): ν 3093 (OH), 2590 (BH). MALDI-TOF, m/z: M: 359.4 $[M+H]^+$. Elemental analysis (%) calculated for $B_{10}C_{14}O_2N_2H_{22}$: C 46.9, H 6.2, N 7.8; found C 46.5, H 6.2, N 7.6.

3.4.3 Synthesis and characterizations of carborane-based MOFs CB1MOF-1 to CB1MOF-4

$[Co_3(BTB)_2(CB1)_2]\cdot 4DMF$ (CB1MOF-1). $Co(NO_3)_2\cdot 6H_2O$ (31.43 mg, 0.108 mmol) was mixed with **CB1** (10 mg, 0.027 mmol) and H_3BTB (23.6 mg, 0.054 mmol) in 2 mL of DMF/ethanol/H_2O (2:1:1). This mixture was sonicated until all solids were uniformly dispersed, followed by heating at 100 °C for 48 h. Red-violet crystals of **CB1**MOF-1 were collected and washed with DMF (28 mg, 81.7%). IR (ATR; selected bands; cm^{-1}): ν 3298 (OH); 2931, 2829 (CH); 2607 (BH); 1662 (C=O from DMF); 1602 (C=O from carboxylate). Elemental analysis (%) calculated for $Co_3C_{94}H_{102}B_{20}N_8O_{20}$: C 53.4, H 5.0, N 5.2; Found: C 53.2, H 5.1, N 5.3.

[$Zn_4(BTB)_2(CB1)(OH)_2(H_2O)_2$]·$5H_2O$·4DMF (CB1MOF-2**).** **CB1**MOF-2 was obtained by mixing $Zn(NO_3)_2·6H_2O$ (33.2 mg, 0.112 mmol), **CB1** (10 mg, 0.027 mmol) and H_3BTB (23.6 mg, 0.054 mmol) in 2 mL of DMF/ethanol/H_2O (2:1:1). This mixture was sonicated until all solids were uniformly dissolved, followed by heating at 85 ºC for 48 h. Colorless block crystals of **CB1**MOF-2 were collected and washed with DMF (48.5 mg, 89%). IR (ATR; selected bands; cm^{-1}): ν 3350 (OH); 2933, 2964, 2865 (CH); 2617, 2554 (BH); 1660 (C=O from DMF); 1610, 1585 (C=O from carboxylate). Elemental analysis (%) calculated for $Zn_4C_{80}H_{88}O_{23}B_{10}N_6$: C 49.5, H 4.9, N 4.3; Found: C 50.0, H 4.7, N 4.7.

[Zn_2(TCPB)(CB1)]·2DMF (CB1MOF-3**).** **CB1**MOF-3 was obtained by mixing $Zn(NO_3)_2·6H_2O$ (11.06 mg, 0.037 mmol), **CB1** (20 mg, 0.054 mmol) and H_4TCPB (20.8 mg, 0.037 mmol) in 2 mL of DMF/ethanol/H_2O (2:1:1), and one drop of concentrated HCl. This mixture was sonicated until all solids were uniformly dissolved, followed by heating at 80 ºC for 48 h. Pale yellow crystals of **CB1** were filtered and washed with DMF (14.9 mg, 67.4%). IR (ATR; selected bands; cm^{-1}): ν 3434 (OH); 2927, 2859 (CH); 2604(BH); 1653 (C=O from DMF); 1609 (C=O from carboxylate). Elemental analysis (%) calculated for $C_{54}H_{54}B_{10}N_4O_{12}Zn_2$: C 54.51, H 4.57, N 4.71; Found: C 54.70, H 4.58, N 4.70.

[Co_2(TCPB)(CB1)(H_2O)(H_2O)(DMF)]·2.7DMF (CB1MOF-4**).** **CB1**MOF-4 was obtained by mixing $Co(NO_3)_2·6H_2O$ (16.3 mg, 0.056 mmol), **CB1** (10 mg, 0.027 mmol) and H_4TCPB (15.6 mg, 0.027 mmol) in 2 mL of DMF/ethanol/H_2O (2:1:1). This mixture was sonicated until all solids were uniformly dissolved, followed by heating at 80 ºC for 48 h. Violet crystals of **CB1**MOF-4 were collected and washed with DMF (29.73 mg, 79.8%). IR (ATR; selected bands; cm^{-1}): ν 3374 (OH); 2925, 2872 (CH); 2616 (BH); 1647 (C=O from DMF); 1608 (C=O from carboxylate). Elemental analysis (%) calculated for $C_{60}H_{72}B_{10}Co_2N_6O_{16}$: C 53.02, H 5.34, N 6.18; Found: C 51.50, H 5.20, N 6.05.

3.5 References

[1] S. Kitagawa, R. Kitaura, S. I. Noro, *Angew. Chemie - Int. Ed.* **2004**, *43*, 2334.

[2] Z. J. Lin, J. Lü, M. Hong, R. Cao, *Chem. Soc. Rev.* **2014**, *43*, 5867.

[3] S. L. James, *Chem. Soc. Rev.* **2003**, *32*, 276.

[4] H. Li, M. Eddaoudi, M. O'Keeffe, O. M. Yaghi, *Nature* **1999**, *402*, 276.

[5] R. Haldar, T. K. Maji, *CrystEngComm* **2013**, *15*, 9276.

[6] Y. Inokuma, S. Yoshioka, J. Ariyoshi, T. Arai, Y. Hitora, K. Takada, S. Matsunaga, K. Rissanen, M. Fujita, *Nature* **2013**, *495*, 461.

[7] L. M. Hayes, C. E. Knapp, K. Y. Nathoo, N. J. Press, D. A. Tocher, C. J. Carmalt, *Cryst. Growth Des.* **2016**, *16*, 3465.

[8] A. M. Ullman, J. W. Brown, M. E. Foster, F. Léonard, K. Leong, V. Stavila, M. D. Allendorf, *Inorg. Chem.* **2016**, *55*, 7233.

[9] W. Li, S. Henke, A. K. Cheetham, *APL Mater.* **2014**, *2*, 123902.

[10] J. C. Tan, A. K. Cheetham, *Chem. Soc. Rev.* **2011**, *40*, 1059.

[11] Grimes, R. N., Carboranes (Second Edition). ed.; Academic Press: Oxford, 2011.

[12] M. Scholz, E. Hey-Hawkins, *Chem. Rev.* **2011**, *111*, 7035.

[13] D. Olid, R. Núñez, C. Viñas, F. Teixidor, *Chem. Soc. Rev.* **2013**, *42*, 3318.

[14] R. N. Grimes, *Dalt. Trans.* **2015**, *44*, 5939.

[15] A. M. Spokoyny, *Pure Appl. Chem.* **2013**, *85*, 903.

[16] F. Teixidor, *Sci. Synth.* **2005**, *6*, 1275.

[17] M. Y. Tsang, F. Teixidor, C. Viñas, D. Choquesillo-Lazarte, N. Aliaga-Alcalde, J. G. Planas, *Inorganica Chim. Acta* **2016**, *448*, 97.

[18] J. Planas, F. Teixidor, C. Viñas, *Crystals* **2016**, *6*, 50.

[19] M. Y. Tsang, C. Viñas, F. Teixidor, J. G. Planas, N. Conde, R. Sanmartin, M. T. Herrero, E. Domínguez, A. Lledós, P. Vidossich, D. Choquesillo-Lazarte, *Inorg. Chem.* **2014**, *53*, 9284.

[20] F. Di Salvo, M. Y. Tsang, F. Teixidor, C. Viñas, J. G. Planas, J. Crassous, N. Vanthuyne, N. Aliaga-Alcalde, E. Ruiz, G. Coquerel, S. Clevers, V. Dupray, D. Choquesillo-Lazarte, M. E. Light, M. B. Hursthouse, *Chem. - A Eur. J.* **2014**, *20*, 1081.

[21] F. Di Salvo, F. Teixidor, C. Viñas, J. Giner Planas, *Zeitschrift fur Anorg. und Allg. Chemie* **2013**, *639*, 1194.

[22] F. Di Salvo, F. Teixidor, C. Viñas, J. G. Planas, M. E. Light, M. B. Hursthouse, N. Aliaga-Alcalde, *Cryst. Growth Des.* **2012**, *12*, 5720.

[23] F. Teixidor, G. Barberà, A. Vaca, R. Kivekäs, R. Sillanpää, J. Oliva, C. Viñas, *J. Am. Chem. Soc.* **2005**, *127*, 10158.

[24] J. Poater, M. Solà, C. Viñas, F. Teixidor, *Angew. Chemie - Int. Ed.* **2014**, *53*, 12191.

[25] M. Fontanet, A.-R. Popescu, X. Fontrodona, M. Rodríguez, I. Romero, F. Teixidor, C. Viñas, N. Aliaga-Alcalde, E. Ruiz, *Chem. - A Eur. J.* **2011**, *17*, 13217.

[26] M. Fontanet, M. Rodríguez, I. Romero, X. Fontrodona, F. Teixidor, C. Viñas, N. Aliaga-Alcalde, P. Matějíček, *Dalt. Trans.* **2013**, *42*, 7838.

[27] M. Fontanet, M. Rodríguez, X. Fontrodona, I. Romero, F. Teixidor, C. Viñas, N. Aliaga-Alcalde, P. Matějíček, *Chem. - A Eur. J.* **2014**, *20*, 13993.

[28] Y.-S. Bae, A. M. Spokoyny, O. K. Farha, R. Q. Snurr, J. T. Hupp, C. A. Mirkin, *Chem.*

Commun. **2010**, *46*, 3478.

[29] Y.-S. Bae, O. K. Farha, A. M. Spokoyny, C. A. Mirkin, J. T. Hupp, R. Q. Snurr, *Chem. Commun.* **2008**, 4135.

[30] D. J. Clingerman, W. Morris, J. E. Mondloch, R. D. Kennedy, A. A. Sarjeant, C. Stern, J. T. Hupp, O. K. Farha, C. A. Mirkin, *Chem. Commun.* **2015**, *51*, 6521.

[31] R. D. Kennedy, V. Krungleviciute, D. J. Clingerman, J. E. Mondloch, Y. Peng, C. E. Wilmer, A. A. Sarjeant, R. Q. Snurr, J. T. Hupp, T. Yildirim, O. K. Farha, C. A. Mirkin, *Chem. Mater.* **2013**, *25*, 3539.

[32] A. M. Spokoyny, O. K. Farha, K. L. Mulfort, J. T. Hupp, C. A. Mirkin, *Inorganica Chim. Acta* **2010**, *364*, 266.

[33] O. K. Farha, A. M. Spokoyny, K. L. Mulfort, M. F. Hawthorne, C. A. Mirkin, J. T. Hupp, *J. Am. Chem. Soc.* **2007**, *129*, 12680.

[34] O. K. Farha, A. M. Spokoyny, K. L. Mulfort, S. Galli, J. T. Hupp, C. A. Mirkin, *Small* **2009**, *5*, 1727.

[35] S.-L. Huang, Y.-J. Lin, W.-B. Yu, G.-X. Jin, *Chempluschem* **2012**, *77*, 141.

[36] S.-L. Huang, L.-H. Weng, G.-X. Jin, *Dalt. Trans.* **2012**, *41*, 11657.

[37] I. Boldog, P. J. Bereciartua, R. Bulánek, M. Kučeráková, M. Tomandlová, M. Dušek, J. Macháček, D. De Vos, T. Baše, *CrystEngComm* **2016**, *18*, 2036.

[38] S. Rodríguez-Hermida, M. Y. Tsang, C. Vignatti, K. C. Stylianou, V. Guillerm, J. Pérez-Carvajal, F. Teixidor, C. Viñas, D. Choquesillo-Lazarte, C. Verdugo-Escamilla, I. Peral, J. Juanhuix, A. Verdaguer, I. Imaz, D. Maspoch, J. Giner Planas, *Angew. Chemie - Int. Ed.* **2016**, *55*, 16049.

[39] F. Di Salvo, C. Paterakis, M. Y. Tsang, Y. García, C. Viñas, F. Teixidor, J. Giner Planas, M. E. Light, M. B. Hursthouse, D. Choquesillo-Lazarte, *Cryst. Growth Des.* **2013**, *13*, 1473.

[40] O. V Dolomanov, L. J. Bourhis, R. J. Gildea, J. A. K. Howard, H. Puschmann, *J. Appl. Crystallogr.* **2009**, *42*, 339.

[41] A. L. Spek, *J. Appl. Crystallogr.* **2003**, *36*, 7.

[42] A. W. Addison, T. N. Rao, J. Reedijk, J. Van Rijn, G. C. Verschoor, *J. Chem. Soc. Dalt. Trans.* **1984**, 1349.

[43] O. K. Farha, C. D. Malliakas, M. G. Kanatzidis, J. T. Hupp, *J. Am. Chem. Soc.* **2010**, *132*, 950.

[44] M. A. Fox, A. K. Hughes, *Coord. Chem. Rev.* **2004**, *248*, 457.

[45] J. G. Planas, C. Viñas, F. Teixidor, M. E. Light, M. B. Hursthouse, *CrystEngComm* **2007**, *9*, 888.

[46] F. Di Salvo, B. Camargo, Y. García, F. Teixidor, C. Viñas, J. G. Planas, M. E. Light, M. B. Hursthouse, *CrystEngComm* **2011**, *13*, 5788.

[47] D. F. Bahr, J. A. Reid, W. M. Mook, C. A. Bauer, R. Stumpf, A. J. Skulan, N. R. Moody, B. A. Simmons, M. M. Shindel, M. D. Allendorf, *Phys. Rev. B* **2007**, *76*, 184106.

[48] A. J. Graham, D. R. Allan, A. Muszkiewicz, C. A. Morrison, S. A. Moggach, *Angew. Chemie - Int. Ed.* **2011**, *50*, 11138.

[49] J. C. Tan, T. D. Bennett, A. K. Cheetham, *Proc. Natl. Acad. Sci. U. S. A.* **2010**, *107*, 9938.

[50] S. Henke, W. Li, A. K. Cheetham, *Chem. Sci.* **2014**, *5*, 2392.

Chapter 4

An Unprecedented Stimuli Controlled Single-crystal Reversible Phase Transition of a Metal-Organic Framework and its Application to a Novel Method of Guest Encapsulation

4. An Unprecedented Stimuli Controlled Single-crystal Reversible Phase Transition of a Metal-Organic Framework and its Application to a Novel Method of Guest Encapsulation

4.1 Introduction

So called "stimuli-responsive" or "smart" materials have the ability to go through conformational changes or phase transitions as a result of external chemical or physical stimuli[1–6]. Such responsiveness to specific stimuli or local environment is typical for biomolecules in nature but it is particularly difficult to achieve artificially. Such materials form the corner stone of developing intelligent technologies and are at the forefront of strategies addressing a number of global challenges[7]. Porous Coordination Polymers (CPs) or Metal-Organic Frameworks (MOFs) are a class of porous crystalline materials formed by the assembly of metal ions or metal clusters with different types of bridging organic linkers or ligands[8–11]. Third-generation MOFs, also known as "soft porous crystals" (SPCs) are defined as "porous solids that possess both a highly ordered network and structural transformability. They are bistable or multistable crystalline materials with long range structural ordering, a reversible transformability between states, and permanent porosity, at least in one crystal phase"[12]. These latter materials undergo a structural change, known as a "breathing" phenomenon, whereby the framework flexes in a reversible fashion in response to the changing nature and quantity of the adsorbed guest. However, flexibility often comes with the penalty of reduced stability, which limits their applications. Thus, the development of flexible yet stable third-generation MOFs depends on a better fundamental understanding of the conformational changes or phase transitions associated with such flexibility, opening the way to the rational design of novel "smart" or stimuli-responsive materials[13–17]. Despite the exciting application opportunities of these SPCs, e.g. in selective gas adsorption, chemical sensing or hazardous waste adsorption[18–20], to date, there is no reported fully rational method for designing a breathing MOF. Framework flexibility is usually associated with flexible ligands, bond cleavage and regeneration, metal-metal interactions, supramolecular host-guest interactions, or a combination of a number of

these[12,14–17,21,22]. Ligands in MOFs or CPs are usually built from aromatic fragments with planar structures (e.g, phenyl, pyridyl, porphirinyl)[17,23,24]. Some degree of flexibility can be easily introduced by using flexible ligands, e.g., by adding aliphatic chains to the ligand structures or by substituting the planar systems by non-planar ones[25]. However, as mentioned above, flexibility often comes with the penalty of reduced stability. Collapsing of the structures is generally the rule, and reversible flexibility mostly a question of serendipity. In this investigation, we argue that with an appropriate design, the substitution of planar by spherical systems could influence the dynamic behavior of MOFs in the sense of avoiding or limiting the collapse of the structure. Spherical shaped linkers in 3D MOFs could help in stabilizing flexible structures. Different from classical rigid flat aromatic ligands-based MOFs, spherical based linkers can access to extensive conformational space by a combination of low-energy torsion of the substituents (e.g., aliphatic) and by the spherical core of the linker. Thus, a spherical ligand shape could diminish or even prevent the structure collapse simply by its globular nature or multiple supramolecular contacts, as opposed to the conventional planar nature of the ligands commonly employed. The idea of spherically shaped linkers avoiding collapse of the structure can also be understood like this: two layers will roll over each other if separated by spheres; whereas they will collapse if non-spherical columns are used (like in classical aromatic linkers). Suitable spherical systems for ligand syntheses are represented by C_{60} or dodecahedrane ($C_{20}H_{20}$). These carbon-based molecules can be envisioned with various heteroatoms incorporated, but their synthesis is a challenging task[26–28]. In comparison, icosahedral boranes and carboranes ($[B_{12}H_{12}]^{2-}$, 1,n-$C_2B_{10}H_{12}$ (n = 2, 7 or 12)) are an interesting class of commercially available and exceptionally stable 3D-aromatic[29,30] boron-rich clusters that possess material-favorable properties such as thermal and chemical stability and hydrophobicity[31–33]. Interestingly, such molecules can be easily functionalized by a wide range of known chemical transformations[34,35]. These icosahedral boron-based molecules can be visualized as hollow spheres. This fact has previously been exploited to provide carborane capped gold nanoparticles that exhibit redox-dependent solubility

and phase transfer between water and nonpolar solvents[36] and also carborane linked quantum dots with unprecedented Kinetic Fluorescence Switching[37]. The packing of the spherical carborane moieties creates openings or channels that are crucial for such unprecedented properties. Herein we report a SPC containing a flexible carborane linker that reversibly responds to guest exchange through multi-step SCSC transformations, in which the synthesis of a crystalline 2D material is attained from a 3D framework and vice versa.

4.2 Results and discussions

4.2.1 Reversible single-crystal to single-crystal transformation

In pursuit of synthesizing water resistant architectures in general, and dynamic MOFs in particular, we have recently initiated the design of flexible carborane based ligands[38,39]. In this endeavor, we have recently reported a water stable SPC that behaves as a crystalline sponge for a variety of guests $[Co_3(BTB)_2(CB1)_2]\cdot$Guest (**1** ⊃ **Guest**; BTB: 1,3,5-benzenetricarboxylate, **CB1**: 1,7-bis{(piridin-4-yl)methanol}-1,7-dicarba-closo-dodecaborane; in figure 4-1 and left column figure 4-2 [39] (see also chapter 3). The available open space of this SPCs is not just a container for guest accommodation, but it demonstrates host-guest interactions between the framework and the guest molecules. Hence, either a contraction (in methanol (MeOH) or chloroform ($CHCl_3$)) or an expansion (in benzene, nitropropane, toluene or nitrobenzene) of the unit cell parameters of **CB1**MOF-1 were observed upon solvent exchange when compared with the as-prepared **CB1**MOF-1 ⊃ **DMF** (dimethylformamide); this is in agreement with a lower or higher number of intermolecular contacts, respectively. Flexibility of **CB1**MOF-1⊃ **Guest** is related to the flexible *m*-carborane bispyridylalcohol ligand (**CB1**) and to the supramolecular host-guest interactions, as demonstrated by the mechanical properties and crystalline sponge behavior of **CB1**MOF-1 ⊃ **Guest**[39] (as introduced in chapter 3). In this chapter, we show that this SPC/MOF (**CB1**MOF-1) shows an unprecedented reversible multi-step SCSC

transformation from a 3D to a 2D framework through partial metal-linker bond cleavage/formation, rather than through the conventional metal-linker bond deformation[4]. This reversible transformation is achieved by solvent-guest exchange under ambient conditions in one direction (3D to 2D) and in DMF solutions at 100 ºC in the other (2D to 3D). A combination of single-crystal (SCXRD), powder (PXRD) X-ray diffraction and DFT calculations provided an unusually detailed structural insight into the observed reversible dynamic behavior. Moreover, it is demonstrated that such reversible transformation can be used for entrapping molecular guests that are too large to diffuse into the initial 3D structure, disclosing a new approach for exploring encapsulation in other flexible MOFs.

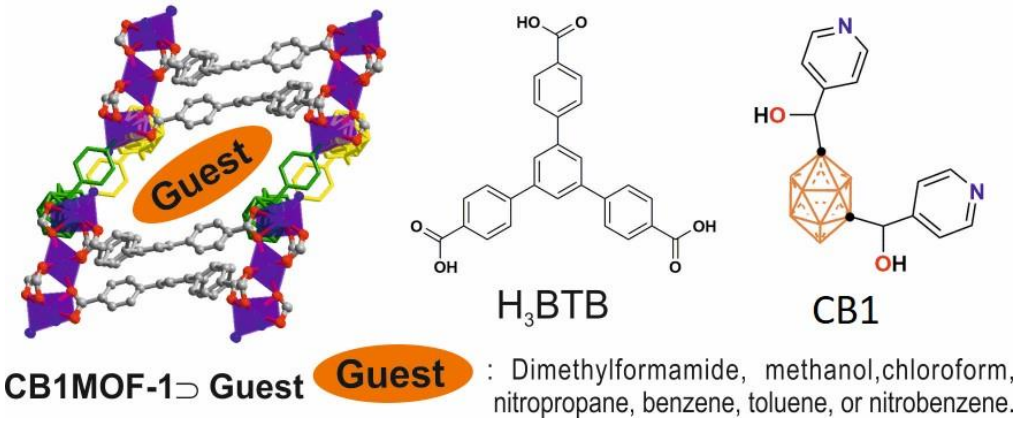

Figure 4-1. Plot of the SCXRD crystal structure of **CB1**MOF-1 ⊃ Guest and ligands employed in this work. (a), Perspective view along the *b* crystallographic axis of the crystal structure of **CB1**MOF-1, showing the channels where various guests can be encapsulated. (b), H_3BTB is 1,3,5-tris(4-carboxyphenyl)benzene. (c), 1,7-dicarba-*closo*-dodecaborane or *m*eta-carborane fragment, $C_2B_{10}H_{10}$ is depicted as an orange icosahedra with two black dots, the latter representing the carbon atoms.

The previously reported SPC $[Co_3(BTB)_2(CB1)_2]\cdot x$DMF (**CB1**MOF-1 ⊃ **DMF** or just **CB1**MOF-1) can be seen as a 2D rigid system composed of flat layers that can be opened and closed via flexible carborane linkers connecting the layers. **CB1**MOF-1 consists of trinuclear $[Co_3(COO)_6N_4]$ units (left of Figure 4-2b), each coordinated to six different BTB ligands, thus creating six-pointed star motif Co/BTB rigid layers extending in the *bc* plane (left of Figure 4-2c). These layers are pillared by **CB1** ligands resulting in a 3D framework that exhibits 1D channels along the *b* axis (Figure 4-1 and Figure 4-2d)[39]. The flexibility of the carborane ligands was evident by nanoindentation

experiments, as the association of layers occurs through two carborane ligands that adopt an almost L-shape (left of Figures 4-2a and 4-2d). Thus, **CB1**MOF-1 can be seen as a model SPC with flexibility along one dimension, through the flexible ligand 3D aromatic based carborane system.

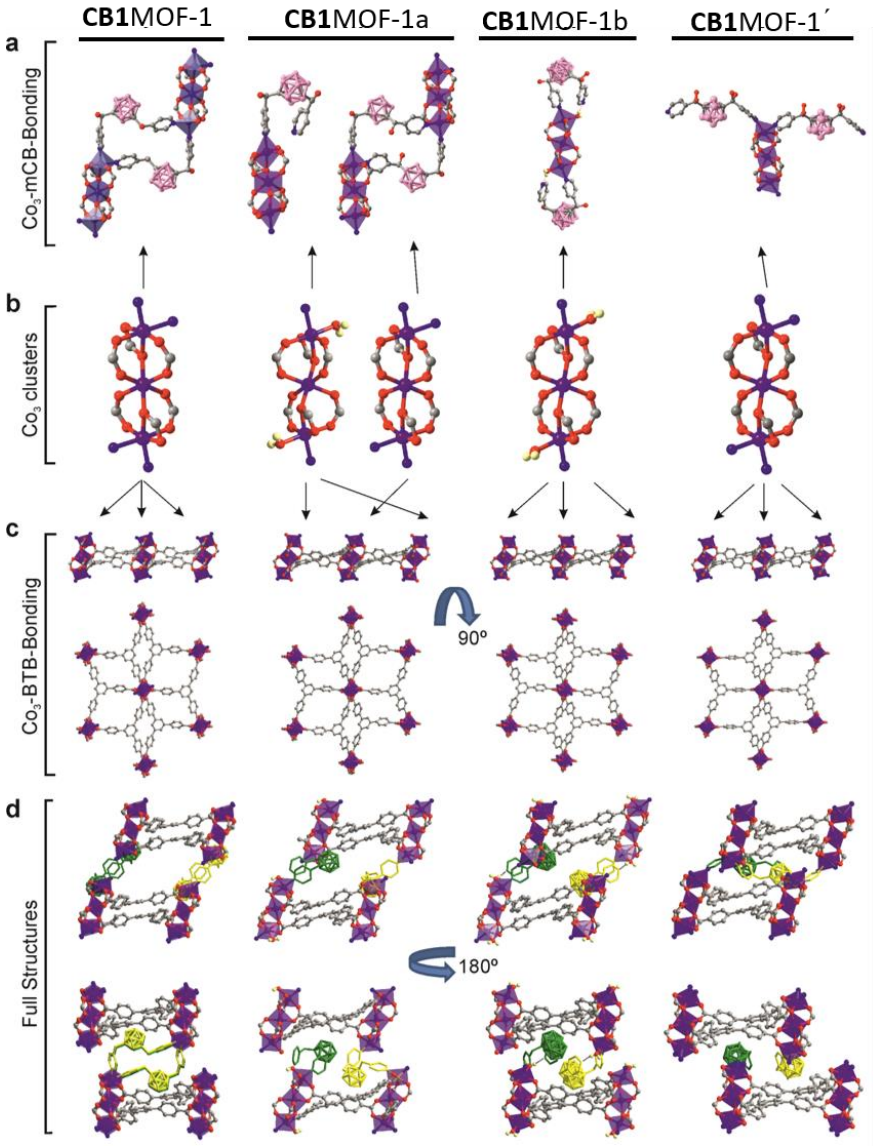

Figure 4-2. Crystal structures of **CB1**MOF-1, **CB1**MOF-1**a**, **CB1**MOF-1**b** and **CB1**MOF-1´. (a) View of the trinuclear Co(II) units (as blue-violet polyhedrons) with CB1 coordination. (b) View of the trinuclear Co(II) unit and coordination environment of the Co(II) ions. (c) Six-pointed star motif trinuclear Co(II)/BTB layers. (d) A comparative view of the structures represented in three dimensions along two perpendicular directions; for clarity carborane linkers are here colored green or yellow and the OH groups are omitted. H atoms (except that for H_2O) are omitted for clarity. Color code: H yellow; B pink; C grey; O red; N blue, Co violet.

Immersion of crystals of **CB1**MOF-1 ⊃ **DMF** in methanol (MeOH) for 1-2 days under ambient conditions showed a clear macroscopic transformation in the morphology of the crystals, from large rhombohedral crystals to thin plates (Figure 4-3). Such a macroscopic change in the habit was also observed after a similar treatment in $CHCl_3$ or by processing the crystals under a continuous flow of supercritical CO_2 ($scCO_2$) at 45 ºC and 20 MPa. No such changes were observed by immersion of **CB1**MOF-1 ⊃ **DMF** crystals in benzene, nitropropane, toluene or nitrobenzene or even in water for 2 days. Crystals of $[Co_3(BTB)_2(CB1)_2(H_2O)]\cdot H_2O$ (**CB1**MOF-1a), $[Co_3(BTB)_2(CB1)_2(H_2O)_2]\cdot xDMF$ (**CB1**MOF-1b) and $[Co_3(BTB)_2(CB1)_2]\cdot 4H_2O$ (**CB1**MOF-1´), were recovered at different times of the solvent exchange process and their structures were solved by SCXRD. A full comparison of the structure of **CB1**MOF-1 with those obtained for **CB1**MOF-1a, **CB1**MOF-1b and **CB1**MOF-1´ is shown in figure 4-2. Structural details are provided in the Annex 1 (Table 4-1). The basic unit of **CB1**MOF-1, **CB1**MOF-1a, **CB1**MOF-1b and **CB1**MOF-1´ is a trinuclear $Co_3(COO)_6$ cluster in which the central Co atoms adopt an octahedral geometry $\{O_6\}$-coordinated to six neighboring BTB ligands (Figure 4-4). The terminal Co atoms of the trinuclear $Co_3(COO)_6$ clusters also adopt an octahedral geometry; however, they differ in the nature of their terminal ligands and this has a pronounced effect on their 3D structures as explained below. In **CB1**MOF-1 and **CB1**MOF-1´ both terminal Co atoms are $\{N_2O_4\}$-octahedrally coordinated to two CB1 ligands and to four O atoms of three BTB ligands (Figure 4-4 and Figure 4-5). In contrast, both terminal Co atoms in **CB1**MOF-1b are $\{NO_5\}$-octahedrally coordinated to one **CB1** ligand, four O atoms of three BTB ligands and one O atom from a coordinated H_2O molecule (Figure 4-2a to 4-2b). Interestingly, an uncoordinated pyridine moiety from the **CB1**ligand is O–H···N hydrogen bonded to the coordinated H_2O molecule in **CB1**MOF-1b (H···N, 1.83(3) Å; OHN, 172(4)°; Figure 4-2a and Figure 4-6). The situation is more complex in the case of **CB1**MOF-1a as the terminal Co atoms alternate throughout the structure, either $\{N_2O_4\}$- or $\{NO_5\}$-octahedral coordination (Figures 4-2a to 4-2b). As mentioned above, the Co/BTB layers are pillared by **CB1** ligands resulting in a 3D framework that

exhibits 1D channels along the *b* axis in **CB1**MOF-1 (Figure 4-1 and Figure 4-2d)[39]. That is, each pyridine moiety of one **CB1** ligand is coordinated to a terminal Co atom of contiguous Co/BTB layers. In **CB1**MOF-1a and **CB1**MOF-1b, some or all of the **CB1** ligands are not acting as pillars (Figure 4-2a) since one of the two pyridyl moieties per **CB1** linker is no longer directly bonded to a Co atom. The Co-N bond cleavage generates unsaturated vacant sites at the metals that has been occupied by an H_2O molecule, as exhibited in the crystal structures **CB1**MOF-1a and **CB1**MOF-1b (Figure 4-2). The consequence of such partial (**CB1**MOF-1a) or total (**CB1**MOF-1b) Co-N bond cleavage of one of the pyridyl moieties per **CB1** linker is the transformation of a 3D structure (**CB1**MOF-1a) into a 2D structure (**CB1**MOF-1b) with an associated loss of porosity (Figure 4-2d). Such a 2D structure is also observed in **CB1**MOF-1´, however the uncoordinated pyridine moieties in **CB1**MOF-1b are now again coordinated to Co atoms (e.g. displacing the Co-coordinated H_2O molecules in **CB1**MOF-1b), but now to a contiguous trinuclear $Co_3(COO)_6$ cluster in the same layer (Figures 4-2a and 4-2d). Figures 4-4 and 4-5 show a schematic representation of the transformation. The SCXRD data confirms that a 3D (**CB1**MOF-1, **CB1**MOF-1a) to 2D (**CB1**MOF-1b and **CB1**MOF-1´) transformation is feasible by solvent exchange in MeOH, $CHCl_3$ and by desolvation aided by $scCO_2$ (Crystallography and structural details in supporting information S4.1 and table S4-1).

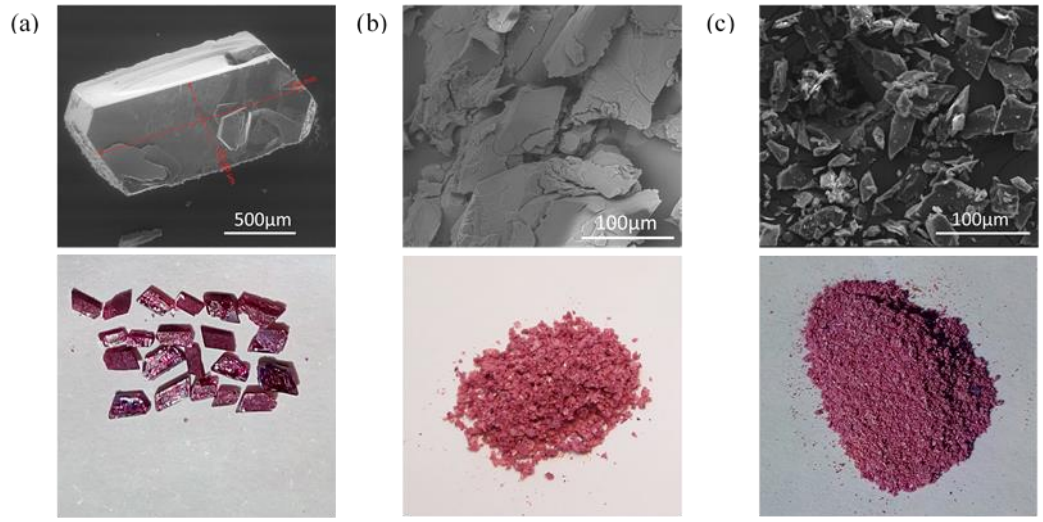

Figure 4-3. SEM (Top) and low-resolution images (Bottom) showing crystals morphology of: (a) as made **CB1**MOF-1, (b) **CB1**MOF-1 after 5 days in methanol, and (c) **CB1**MOF-1´.

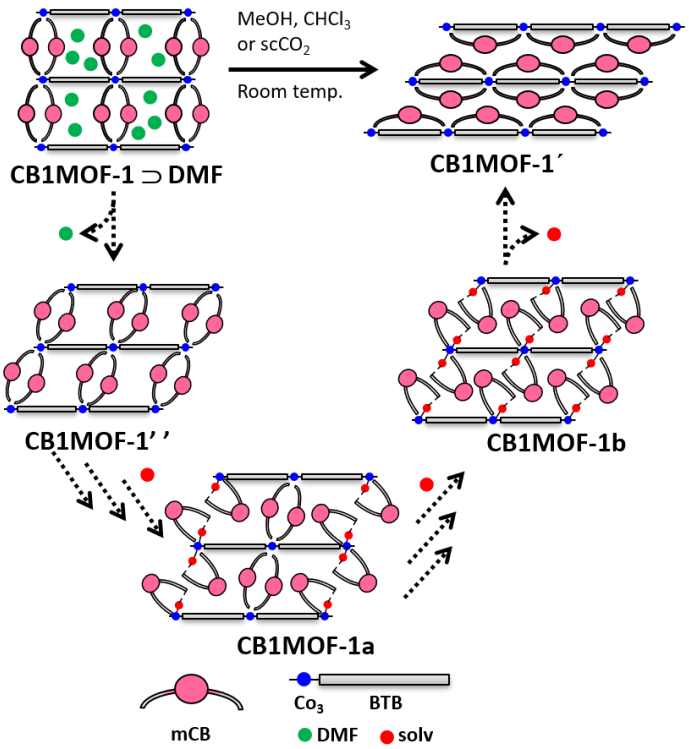

Figure 4-4. Schematic illustration of the multi-step SCSC transformations from **CB1**MOF-1 to **CB1**MOF-1´. Proposed mechanism for the 3D to 2D transformation based on the SCXRD analysis.

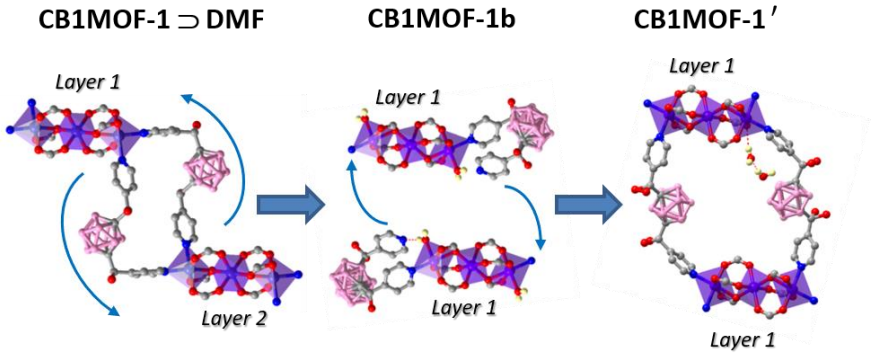

Figure 4-5. Schematic illustration of the multi-step SCSC transformations from **CB1**MOF-1 to **CB1**MOF-1´. View of the trinuclear Co(II) units (as blue-violet polyhedrons) with **CB1** linker coordination; narrow blue arrows represent the movement of pyridine moieties during the process. Note the interlayer linker coordination in **CB1**MOF-1 and intralayer hydrogen bonded or coordination in **CB1**MOF-1b or **CB1**MOF-1´, respectively.

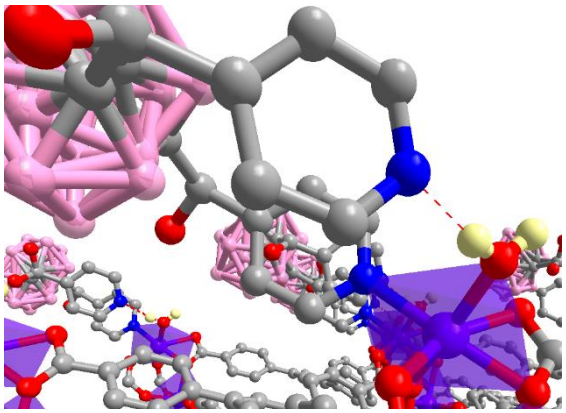

Figure 4-6. Representation of the O–H···N hydrogen bonded to the coordinated H_2O molecule in **CB1**MOF-1b.

The observed arrangement of the **CB1** ligand during the transformation is certainly unusual: one of the pyridine moieties of each ligand uncoordinated from a Co center and coordinates to another Co in the same layer in a sort of inter-layer to intra-layer arrangement or folding of the **CB1** linkers (Figure 4-4). Such folding of the carborane linkers causes the "disconnection" of the Co/BTB layer and therefore the 3D to 2D transformation (Figures 4-4 and 4-5). Structural conversion of compound **CB1**MOF-1 occurs when DMF guest molecules are exchanged with poor hydrogen bonding acceptors such as MeOH, $CHCl_3$ or $scCO_2$ (vide infra). With the solvent-synthesis molecules gradually escaping, the unit cell parameters dramatically change while the space group symmetry is retained. Phase **CB1**MOF-1´ was indexed with a cell similar to that of phase **CB1**MOF-1, except for a radically contracted *c* axis (reduction of 38 %). In the absence of weak or specific host-guest interactions, the network contracts to fill the void space created by the displacement of DMF. The deformation of the network then provokes a displacement of the pyridyl ligands bound to the Co/BTB layers through a multi-step SCSC transformation to yield **CB1**MOF-1´ (Figure 4-4). The process can be observed macroscopically as a change in the morphology and size of the crystals (Figure 4-3). **CB1**MOF-1a to CB1MOF-1b are presumably not the only transition points between **CB1**MOF-1 and **CB1**MOF-1´, but simply the ones that were characterized in this work, although other successive intermediates should be formed in a continuous structural transformation. Note that the single crystals used to elucidate **CB1**MOF-1a and **CB1**MOF-1´ were obtained from the same sample, thus showing that

the bulk crystals of **CB1**MOF-1 were not all transformed into **CB1**MOF-1´ under the exchange conditions used. The isolation and characterization of these structural intermediates was crucial in proposing the mechanism for the dynamic transformation, since they provide convenient snapshots during the dynamic transformation.

Motivated by the above SCXRD results, we followed the transformation of **CB1**MOF-1 ⊃ **DMF** crystals exposed to MeOH by powder X-ray diffraction (PXRD). Here, we have focused on the low angle peaks, from 2θ 5 to 12º as our similarity markers, since powder diffraction patterns of low symmetry flexible structures can become quite dissimilar at higher 2θ angles as a result of only very minor structural changes. In addition, the transformation of 3D crystals into 2D crystals involves crack or crumble as a result of the long-range strain introduced when the internal periodicity is disrupted (Figure 4-3). The transformation thus involves concomitant degradation of crystal singularity and the forming multiple domains, which results in diffraction peak broadening. Another possible source of peak broadening is the reduction of order along the *c* direction –perpendicular to the Co/BTB layers– in the 2D phases **CB1**MOF-1b and **CB1**MOF-1´[40]. Considering this, the SCSC transformation from **CB1**MOF-1 to **CB1**MOF-1´ could also be identified by PXRD (Figure 4-7). Recorded profiles obtained by treating **CB1**MOF-1 in MeOH at different immersion times were compared with the calculated PXRDs patterns from single crystal data of structure **CB1**MOF-1. The analysis of data reveals that **CB1**MOF-1 gradually transforms into **CB1**MOF-1´ and other intermediate phases when exposed to MeOH for 2-5 days (Figure 4-7b to 4-7d). Crystals were then further treated at 40 ºC under vacuum for 20 h (Figure 4-7e); however, complete transformation to phase **CB1**MOF-1´ was only achieved after heating at 80 ºC (Figure 4-7f). The heating step is fully consistent with the above SCXRD results (Figure 4-3), as uncoordination of water (or any other solvent) from the cobalt centers in intermediate stages, such as e.g. **CB1**MOF-1b**,** is required in order to obtain **CB1**MOF-1´. Hydration/dehydration of the Co(II) centers with displacement/coordination, respectively, of a 4,4'-bipyridine has been previously observed. In addition to the PXRD data, unit cell determination by SCXRD of up to

sixteen crystals of the transformed phase provides further support for the conversion of **CB1**MOF-1 to **CB1**MOF-1´ (Table S4-2). Furthermore, optimization of the framework transformation from **CB1**MOF-1 to **CB1**MOF-1´ is achieved by solvent exchange of **CB1**MOF-1 ⊃ **DMF** with MeOH or $CHCl_3$ under ambient conditions for 5 days followed by heating at 80 ºC under vacuum for 20 h; or by straight treatment in a flow of $scCO_2$ at 20 MPa and 45 ºC (Figure 4-8 and Table 4-2). FT-IR, thermogravimetric analysis (TGA), elemental analysis and nitrogen sorption measurements (Figures 4-9 and 4-10) of **CB1**MOF-1´ confirms the non-porous nature of this phase, only containing residual water (<5%).

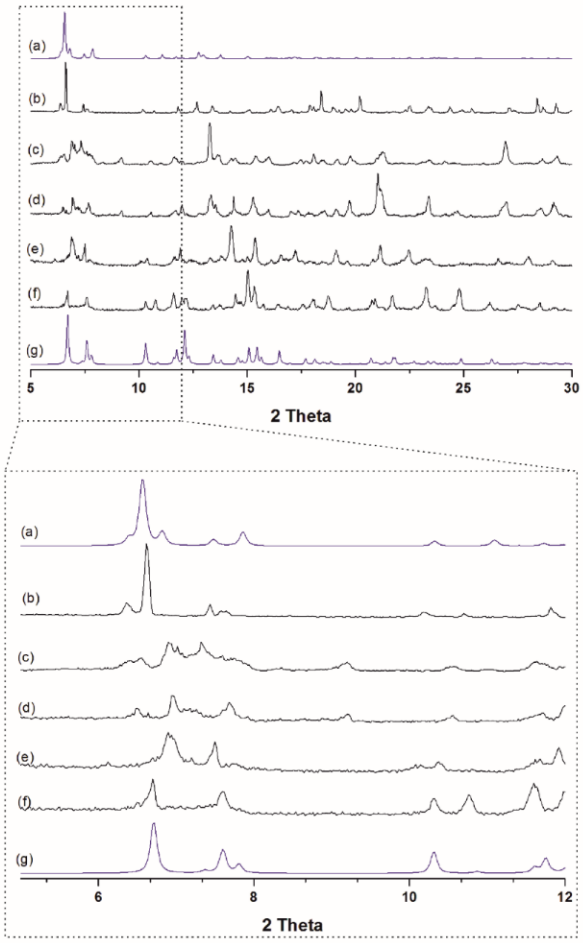

Figure 4-7. PXRD of **CB1**MOF-1 ⊃ **DMF** (2θ 5 to 30º and 5 to 12º) on methanol exchange experiments and further vacuum treatment. (a) Calculated PXRD of **CB1**MOF-1 from single crystal data. (b) as synthesized **CB1**MOF-1 ⊃ **DMF**. (c) 2 days immersion in MeOH under ambient conditions. (d) 5 days immersion in MeOH under ambient conditions. (e) heating at 40 ºC under vacuum for 20 h. (f), heating at 80 ºC under vacuum for 20 h. (g) Calculated PXRD of **CB1**MOF-1´ from single crystal data.

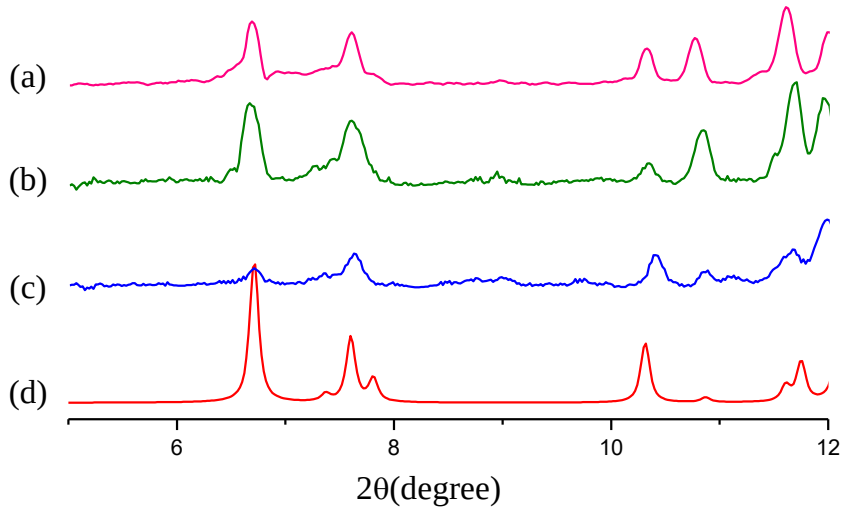

Figure 4-8. PXRD spectra of **CB1**MOF-1´ obtained from: (a) MeOH. (b) $CHCl_3$. (c) $scCO_2$. (d) calculated.

Table 4-2. Elemental analysis of as made **CB1**MOF-1´, after vacuum for 12-48 h.

	%C	**%N**	**%H**
CB1MOF-1´ as made from MeOH (exp. wt%)	51.49	2.45	4.31
Calcd. wt% $[Co_3(BTB)_2(CB1)_2]\cdot 7H_2O$	52.09	2.96	4.69
CB1MOF-1´ as made from CHCl3 (exp. wt%)	53.35	3.36	4.47
Calcd. wt% $[Co_3(BTB)_2(CB1)_2]\cdot 6H_2O$	52.60	2.99	4.63
CB1MOF-1´ as made from scCO2 (exp. wt%)	53.63	3.05	4.50
Calcd. wt% $[Co_3(BTB)_2(CB1)_2]\cdot 4H_2O$	53.70	3.46	4.36

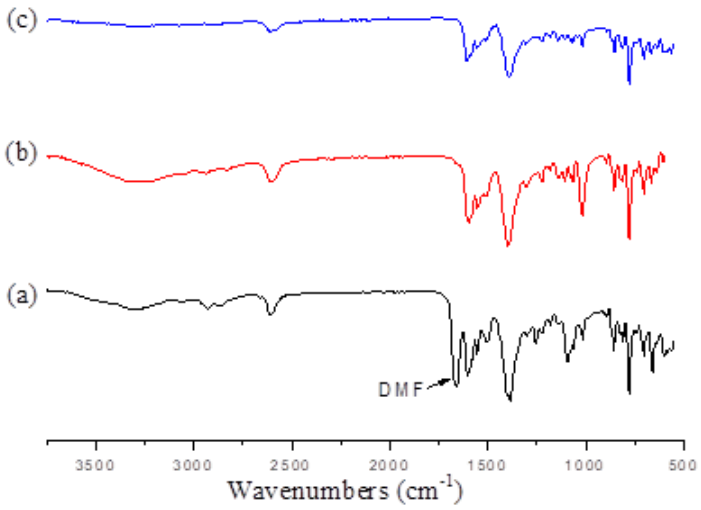

Figure 4-9. IR-ATR spectra of (a) **CB1**MOF-1⊃ **DMF**, (b) **CB1**MOF-1 after 5 days immersion in MeOH under ambient conditions, and (c) **CB1**MOF-1´.

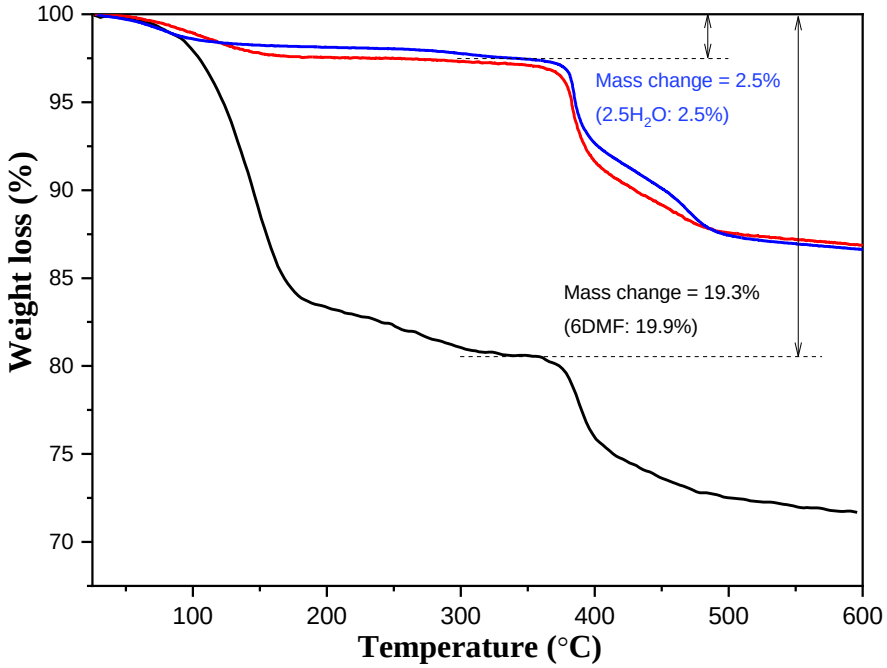

Figure 4-10. TGA diagram of as made **CB1**MOF-1 ⊃ **DMF** (black), after immersion in MeOH for 5 days (red), and **CB1**MOF-1´ (blue).

Density Functional Theory (DFT) calculations were performed to analyze the energy contributions involved in the MOF transformation described in Figure 4-4. The structures of the systems **CB1**MOF-1 ⊃ **DMF**, **CB1**MOF-1´´ (**CB1**MOF-1 with empty channels), **CB1**MOF-1b and **CB1**MOF-1´ were thus optimized using the FHI-aims code (PBE exchange correlation functional including dispersion energies, see

supporting information S4.2 for details). Compound **CB1**MOF-1a was not considered due to its large unit cell. Energy comparison between **CB1**MOF-1 ⊃ **DMF** and **CB1**MOF-1´´ clearly shows the large tendency to fill the channels of the latter with DMF molecules. The inclusion of DMF molecules in the **CB1**MOF-1´´ channels is strongly favored due to an interaction of 23.3 kcal/mol per solvent molecule while the reorganization energy of the host structure is only 10.0 kcal/mol. The latter is the result of the presence of a large number of host-guest interactions (O–H···O, C–H···O and C–H···π). As previously reported, inclusion of DMF over MeOH is favored. The interaction of MeOH molecules with **CB1**MOF-1´´ is weaker than that for the DMF molecules, with an interaction energy of 9.1 kcal/mol per MeOH molecule and with a host reorganization energy of only 4.3 kcal/mol. These results confirm the selectivity of the host structure towards DMF solvent. More importantly, an energy comparison between **CB1**MOF-1´´ (3D) and **CB1**MOF-1´ (2D) reveals that the latter is 25.7 kcal/mol more stable than **CB1**MOF-1´´. It is worth noting that without dispersion contributions, **CB1**MOF-1´´ is 34.6 kcal/mol more stable than **CB1**MOF-1´, showing the key role that inclusion of this term has in stabilizing **CB1**MOF-1´ due to its compact structure. Finally, the optimized structure for the intermediate **CB1**MOF-1b, containing four water and two DMF solvent molecules, shows relatively high stability. It is around 110.1 kcal/mol more stable than the **CB1**MOF-1´´ structure and a system containing six isolated solvent molecules (with the same structure as **CB1**MOF-1b). Due to the presence of the host-solvent interaction in **CB1**MOF-1b, such a system is also more stable than **CB1**MOF-1´ (84.3 kcal/mol, taking into account the energy of **CB1**MOF-1´ plus the energy of the 4 water and 2 DMF solvent molecules set). In this case, the equilibrium is shifted towards the free solvent structure of **CB1**MOF-1´ because the reaction is performed under vacuum and high temperature to facilitate the elimination of the solvent molecules as explained above.

The observed transformation involves the partial uncoordination of the **CB1** ligands and their re-coordination (*folding* linker) with simultaneous shifting of the Co/BTB layers in a very slow and concerted way, that maintains a significant degree of

crystallinity for all intermediate phases involved in the transformation. Even if the crystallinity is not perfect, that just means that some long range order in the framework is lost, but without the collapse of the network[12]. Such a slow process could be due to the presence of the carborane moieties. The 3D globular shape of the carborane moieties could conceivably minimize the collapse of the structure when DMF is removed from the channels of **CB1**MOF-1 ⊃ **DMF**. For example, in the event of a porous pillared 3D structure collapse, the globular shaped pillars will help to maintain porosity as compared with the case of flat pillars. Another point to consider in the present transformation is the possible effect of water, as molecules of this solvent were positively identified in the solved structures of **CB1**MOF-1a, **CB1**MOF-1b and **CB1**MOF-1´. However, the water present in the structure, from the synthesis or adsorbed from atmosphere during manipulation, does not seem to initiate the transformation, since the rate of the 3D to 2D transformation was not affected by the addition of water (up to 20 v%) to the MeOH suspension. Combined TGA, IR and elemental analysis confirms the presence of <3% water in the as made **CB1**MOF-1. More importantly, **CB1**MOF-1 remains stable in water for weeks. The latter certainly indicates that water is not promoting the phase transformation. Thus, we believe that the displacement of DMF by poorer hydrogen bonding acceptor molecules (e.g., MeOH, $CHCl_3$ or $scCO_2$) is the driving force for the transformation and this conclusion is clearly supported by the DFT calculations. A detailed explanation of the procedure followed for the energy calculations can be found in the Supporting Information S4.2.

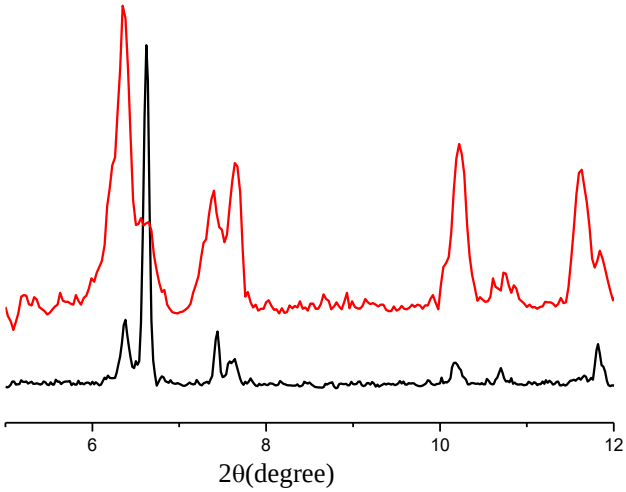

Figure 4-11. PXRD patterns of as-synthesized **CB1**MOF-1 ⊃ **DMF** (black), and **CB1**MOF-1-made from **CB1**MOF-1´ (red).

Formally, **CB1**MOF-1 and **CB1**MOF-1´ are polymeric compounds with the same molecular formula. However, the **CB1** linkers are *folded* into the Co/BTB layers in **CB1**MOF-1´, but are *unfolded* in **CB1**MOF-1 (Figure 4-4). The higher calculated stability of **CB1**MOF-1 ⊃ **DMF** as compared to **CB1**MOF-1´ prompted us to consider whether the transformation could be reversible, that is, whether the folded **CB1** linkers in **CB1**MOF-1´ can be unfolded to provide **CB1**MOF-1. Remarkably, this transformation of **CB1**MOF-1 into **CB1**MOF-1´ is indeed reversible (Top of Figure 4-12). Crystals from **CB1**MOF-1´ were converted into **CB1**MOF-1 by heating at 100 ºC in DMF for 48h and the transformation was confirmed by a combination of SCXRD and PXRD analysis. PXRD shows that the transformation of phase **CB1**MOF-1´ into **CB1**MOF-1 took place under the above conditions, as indicated by the diffraction peak at 2θ 6.4 º in the diffractogram, which only occurs for phase **CB1**MOF-1 (Figure 4-11). Further confirmation for the reversibility of this process was obtained from SCXRD performed on ten crystals of the bulk material recovered after the transformation (Supplementary Table S4-3). Such a flexible behavior, in which metal-linker bonds undergo cleavage in a reversible manner and without loss of the linkers, has not been previously described. There are only a few examples of metal-dipyridine bond cleavage, but with complete loss of the linkers, and therefore providing non reversible transformations[40,41]. In the present case, flexibility of the **CB1** ligand facilitates its

partial decoordination (*folding/unfolding*) during the process and therefore reversibility is simply achieved by heating in DMF. This solvent is crucial for the reversibility process as no transformation was observed when using other poorly coordinating solvents such as acetonitrile or dichlorobenzene.

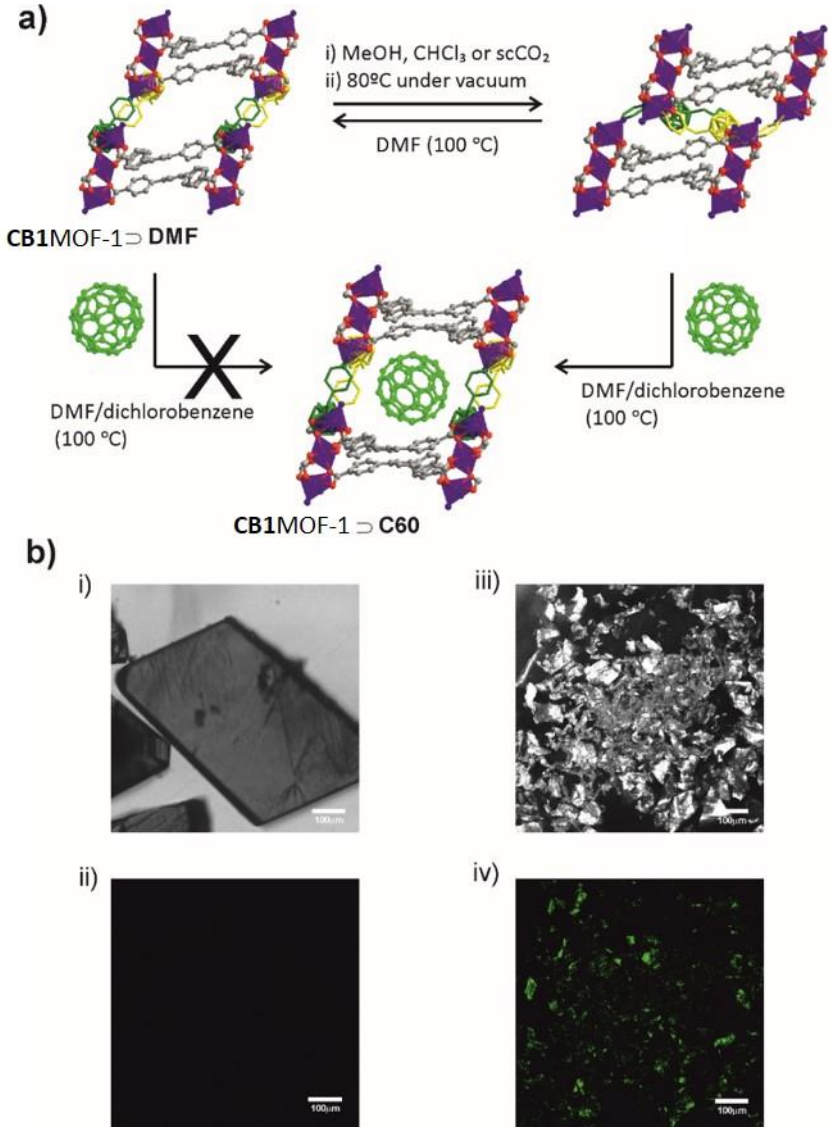

Figure 4-12 (a) Optimized conditions for the bulk reversible **CB1**MOF-1 to **CB1**MOF-1´ transformation and C_{60} encapsulation. **CB1**MOF-1 ⊃ **DMF** and **CB1**MOF-1´ are drawn from their crystal structures. **CB1**MOF-1 ⊃ $\mathbf{C_{60}}$ is drawn from the DFT optimization. (b) White light (top) and fluorescence images (bottom) for **CB1**MOF-1 and **CB1**MOF-1 ⊃ $\mathbf{C_{60}}$ composites. i, white light transmission of **CB1**MOF-1. ii, fluorescence image of **CB1**MOF-1. iii, white light reflexion of **CB1**MOF-1 ⊃ $\mathbf{C_{60}}$. iv, fluorescence image of **CB1**MOF-1 ⊃ $\mathbf{C_{60}}$.

4.2.2 Encapsulation of fullerene

The reversibility of the **CB1**MOF-1 to **CB1**MOF-1´ transformation opens a new way to encapsulate different guests. As previously mentioned, **CB1**MOF-1 behaves as a crystalline sponge for a variety of guests, mainly small organic compounds that stablish a large number of intermolecular interactions with the channel walls[38]. Large channel dimensions of **CB1**MOF-1 (~11 x 13 Å in **CB1**MOF-1 ⊃ **DMF**) are, in principle, suitable to accommodate bulky molecular compounds, such as e.g., [60]Fullerene (C_{60})[42]. This is supported by DFT calculations (**CB1**MOF-1 ⊃ **C_{60}** in Figure 4-9a and calculation details in S4.2 of annex 1), which indicate that C_{60} inclusion energy on **CB1**MOF-1´´ is 60.0 kcal/mol. This value can be split in two contributions, the host-guest interaction energy (86.2 kcal/mol), and a much smaller reorganization energy of the host contribution (22.2 kcal/mol). Conventional immersion experiments performed in concentrated C_{60} toluene solutions at 100 ºC for one week or even direct synthesis of **CB1**MOF-1 in the presence of C_{60} proved ineffectual. Contrarily, C_{60} was trapped in **CB1**MOF-1 when the phase transformation **CB1**MOF-1´ → **CB1**MOF-1 was performed in the presence of this fullerene (in a DMF/dichlorobenzene mixture, v/v = 3/1). PXRD characterization of the **CB1**MOF-1 ⊃ **C_{60}** composite confirmed that the structure of phase **CB1**MOF-1 was essentially recovered upon **C_{60}** incorporation, since the signal at 6.4 º is clearly visible in the diffractogram (Figure 4-11). Proof for the formation of the **CB1**MOF-1 ⊃ **C_{60}** composite was obtained by the combination of confocal fluorescence images, TGA and FT-Raman analysis (Figures 4-12 to 4-15). A bright green fluorescence was observed in **CB1**MOF-1 ⊃ **C_{60}** crystals, from top surface downward to the median cross-section in every 1.5 µm depth (Figure 4-12b and Figure 4-13), evidencing that C_{60} was homogeneously distributed throughout the MOF matrix[43]. In contrast, no fluorescence was observed in **CB1**MOF-1 ⊃ **DMF** or after incubating **CB1**MOF-1 in C_{60} DMF/dichlorobenzene solutions at 100 ºC in DMF for 48h. A small broad band centered at 1461 cm^{-1} in the FT-Raman spectrum of **CB1**MOF-1 ⊃ C_{60} composites, corresponding to the $A_g(2)$ mode of **CB1**MOF-1-trapped C_{60}, add

further evidence for its incorporation within **CB1**MOF-1 (Figure 4-15). The C_{60} content in **CB1**MOF-1 ⊃ **C_{60}** composite was estimated by TGA as about 2 wt.% (Figure 4-14).

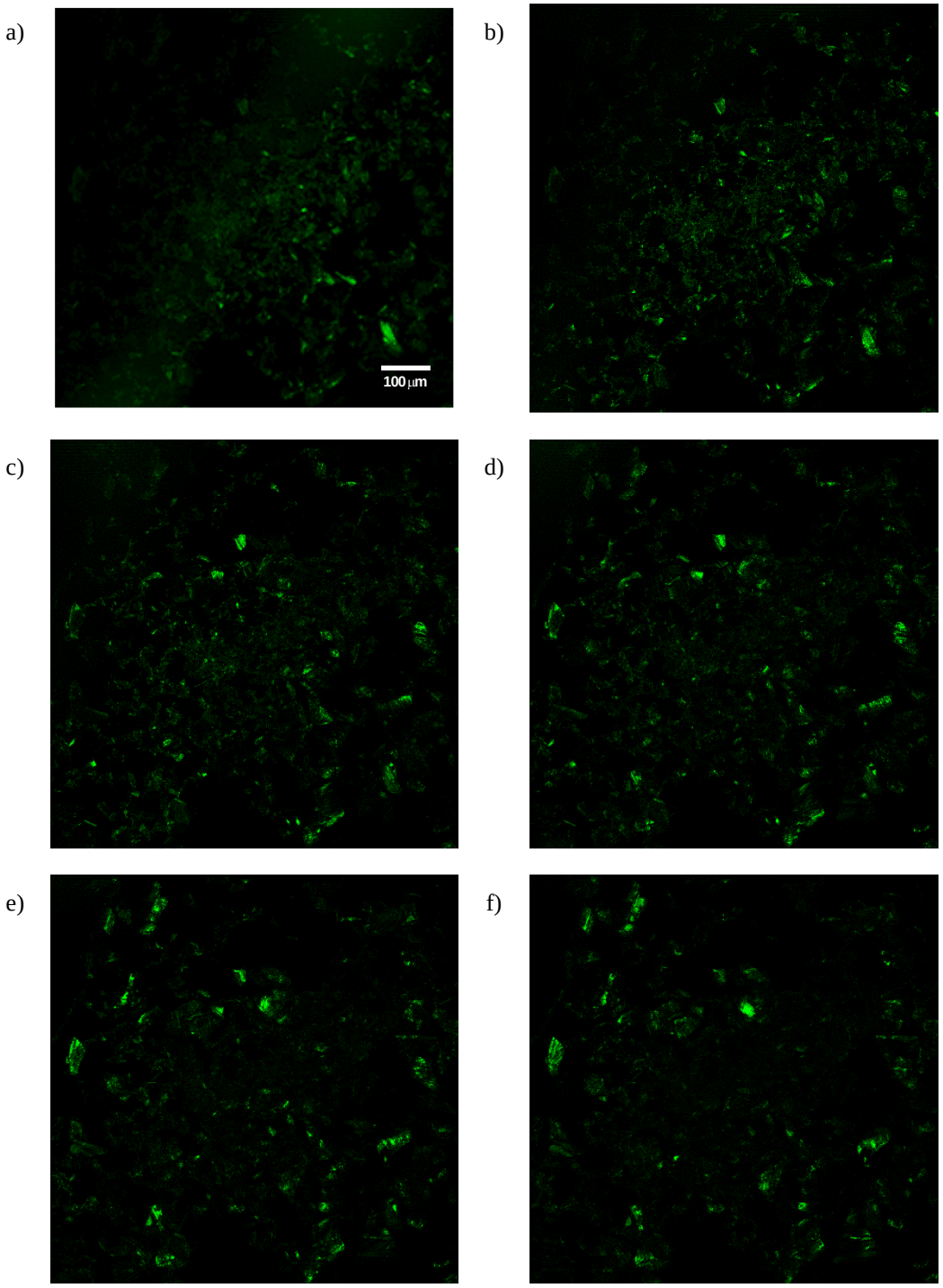

Figure 4-13. Fluorescent confocal images of cross-sections of **CB1**MOF-1 ⊃ **C_{60}** obtained by scanning the crystals from top surface downward to the median cross-section by 1.5 µm of depth (a-f).

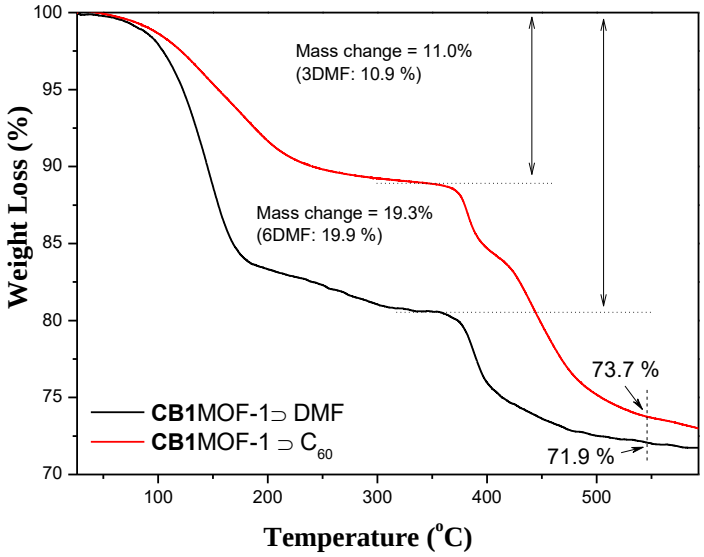

Figure 4-14 TGA diagram of as made **CB1**MOF-1 ⊃ **DMF** (black), and **CB1**MOF-1 ⊃ **C60** (red). Pure C_{60} is stable up to 550 ºC under nitrogen. However, **CB1**MOF-1 ⊃ **DMF** (black), and **CB1**MOF-1 ⊃ **C60** loose DMF between 120-150 ºC, followed by decomposition at 383 ºC. Therefore, we assume that the difference in % of weight loss of the residues at 550ºC should correspond to the amount of C_{60} (~2 wt.%).

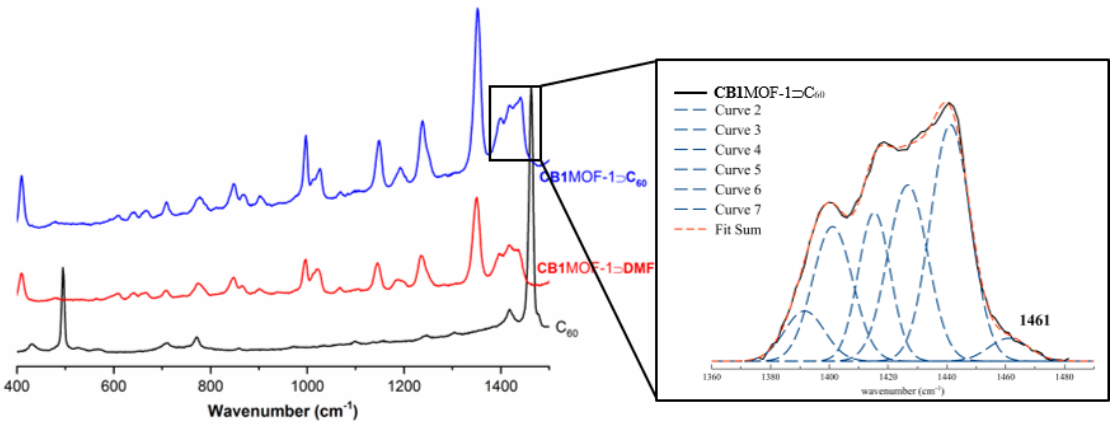

Figure 4-15 FT-Raman spectra of the pristine C_{60} (black), **CB1**MOF-1 ⊃ **DMF** (red) and **CB1**MOF-1 ⊃ **C60** (blue). The insert is the Raman spectrum bands in the >1400 cm^{-1} region for **CB1**MOF-1 ⊃ **C60** fitted by Gaussian.

4.3 Conclusions

In conclusion, a flexible carborane based dipyridine ligand (**CB1**) was employed as the linker in **CB1**MOF-1 to explore the framework flexibility and possible influence of the icosahedral core of the ligand on the stability of **CB1**MOF-1. We report that the 3D MOF $[Co_3(BTB)_2(CB1)_2]\cdot xDMF$ (**CB1**MOF-1 ⊃ **DMF**) shows a flexible and reversible dynamic behavior distinct from that previously reported for other porous materials. A solid phase transition can be induced in **CB1**MOF-1 to generate a new non

porous 2D structure $[Co_3(BTB)_2(CB1)_2]\cdot$xsolv (**CB1**MOF-1´) without loss of the carborane linkers, that are now coordinated to Co atoms in the same layer (linker *folding*). The structural transformation was visualized by snapshots of the multi-step SCSC transformations by single and powder XRD. Poor hydrogen bond acceptors such as MeOH, $CHCl_3$ or $scCO_2$ induce such 3D to 2D transformation by exchange of the DMF in the channels of **CB1**MOF-1. In the absence of stabilizing DMF, the structure of **CB1**MOF-1 is not stable and suffers a solid phase transition leading to **CB1**MOF-1´ as the most stable product. Gas phase calculation provides full support for the observed transformations. Remarkably, the transformation is reversible and **CB1**MOF-1´ can be further converted back into **CB1**MOF-1 by just heating in DMF. Intra-layer Co-N bond cleavage (linker *unfolding*) and inter-layer Co-N formation occur under such conditions, with the recovery of the initial porous 3D structure. As a proof of concept for potential applications, encapsulation of C_{60} has been achieved by trapping during the 2D to 3D phase transition, whereas no adsorption was observed by diffusion on the pores of the 3D phase **CB1**MOF-1. The observed process constitutes a new way to encapsulate large molecules that cannot easily diffuse into the porous material.

Given the versatile composition of MOFs, and the fact that they can be fabricated by design, we believe our work here will facilitate development of flexible MOFs with reversible breathing or phase transitions triggered by stimuli such as guest exchange or temperature. Other spherical and flexible ligands can be envisaged as key players to increase the stability of further flexible porous materials. Such materials would ultimately provide very exciting pathways for obtaining smart porous materials with application opportunities in, e.g. selective gas adsorption, chemical sensing or hazardous waste adsorption.

4.4 Experimental section

4.4.1 Characterization and methods

Attenuated total reflection Fourier transformed infra-red (ATR-FTIR) spectra were recorded using a PerkinElmer Spectrum One spectrometer equipped with a Universal ATR sampling accessory. Spectra were collected with 2 cm^{-1} spectral resolution in the 4000-650 cm^{-1} range. Elemental analyses were obtained by using a Thermo (Carlo Erba) Flash 2000 Elemental Analyser, configured for wt.%CHN. Thermogravimetric Analysis (TGA) was performed in N_2, on an nSTA 449 F1 Jupiter-Simultaneous TGA-DSC or SDT Q600 V8.3 Build 101 instruments (heating rate: 10 ^oC/min; temperature range: 25 ^oC to 600 ^oC). The textural properties were determined by N_2 adsorption at -196 °C applying the BET method, using an ASAP 2000 Micromeritics Inc. Samples were first degassed at 60 °C for 20 h. Powder X-ray Diffraction (PXRD) was recorded at room temperature on PANalytical X'Pert PRO MPDθ/θ powder diffractometer with a goniometer radius of 240 mm and equipped with automatic divergence slits. Bragg-Brentano geometry was used with Cu Kα radiation (λ = 1.5418 Å). Morphological features were examined first by optical microscopy and next by scanning electron microscopy (SEM) with a QUANTA FEI 200 FEGESEM microscope. Fluorescent confocal images were taken by Confocal TCS SP5 (Leica) Microscope. The specimens (crystals dispersed on slides) were imaged under the same instrumental conditions. Raman spectra were determined on micro-Raman equipped a dispersive spectrometer Jobin-Yvon LabRam HR 800 and coupled to an optical microscope Olympus BXFM. The CCD detector was cooled at -70^oC. The compounds were transformed in a high vacuum furnace (10^{-4} Pa).

Materials. All chemicals were of reagent-grade quality. They were purchased from commercial sources and used as received. **CB1**MOF-1 ⊃ **DMF** was prepared as previously reported.[39]

4.4.2 Synthesis of CB1MOF-1´, CB1MOF-1 from CB1MOF-1´ and CB1MOF-1 ⊃ C_{60} composites

Bulk synthesis of CB1MOF-1´. As-synthesized crystals of **CB1**MOF-1 (200 mg) were immersed in methanol or chloroform (4 mL) for 5 days with the solvent being exchanged once a day. Large crystals of **CB1**MOF-1 gradually broke into smaller crystals during this time. The resultant small crystals were dried on filter paper and then heated to 80 ºC for 24 h under high vacuum to form **CB1**MOF-1´. Crystals for **CB1**MOF-1 can be alternatively obtained from as-synthesized **CB1**MOF-1 by $scCO_2$ treatment in a continuous mode in a high-pressure equipment (bellow).

Bulk synthesis of CB1MOF-1´ by the $scCO_2$ procedure. Sample transformation from **CB1**MOF-1 to phase **CB1**MOF-1´ was carried out in $scCO_2$ in a continuous mode in a high pressure equipment described elsewhere.[2] In this approach, 200 mg of sample **CB1**MOF-1 was filtered off from DMF, the collected solid was enclosed in a 0.45 µm pore filter paper cartridge, and introduced in a 100 mL autoclave. The reactor was heated at 45 ºC and pressurized to 20 MPa using a pump (Isco Teledyne). The system was kept running at a constant delivery flow of 1 mL/min during 8 h. Finally, the $scCO_2$ flow was stopped, the pressure was slowly released and the reactor cooled down to room temperature.

Bulk synthesis of CB1MOF-1 from CB1MOF-1´. Crystals for **CB1**MOF-1´ (20 mg) were suspended in DMF (2 mL) in a capped glass vial and heated in an oven at 100 ºC for 48 h. No dissolution of the crystals was observed during this time. Crystals for **CB1**MOF-1 were then filtered, washed with DMF and stored in the same solvent.

Synthesis of CB1MOF-1 ⊃ C_{60} composites. Crystals for **CB1**MOF-1´ (20 mg) were added into a glass vial containing a 6.75 mM of C_{60} solution in a mix solvent of DMF and dichlorobenzene (v/v = 3/1). The resulting mixture was heated at 100ºC for 48h. After thorough rinsing with dichlorobenzene and DMF, crystals for **CB1**MOF-1 ⊃ **C_{60}** composite were obtained.

4.5 References

[1] X. Wang, C. Chi, K. Zhang, Y. Qian, K. M. Gupta, Z. Kang, J. Jiang, D. Zhao, *Nat. Commun.* **2017**, *8*, 14460.

[2] E. J. Carrington, C. A. McAnally, A. J. Fletcher, S. P. Thompson, M. Warren, L. Brammer, *Nat. Chem.* **2017**, *9*, 882.

[3] W. Cai, A. Gładysiak, M. Anioła, V. J. Smith, L. J. Barbour, A. Katrusiak, *J. Am. Chem. Soc.* **2015**, *137*, 9296.

[4] A. B. Cairns, J. Catafesta, C. Levelut, J. Rouquette, A. Van Der Lee, L. Peters, A. L. Thompson, V. Dmitriev, J. Haines, A. L. Goodwin, *Nat. Mater.* **2013**, *12*, 212.

[5] G. K. Kole, J. J. Vittal, *Chem. Soc. Rev.* **2013**, *42*, 1755.

[6] J. Rabone, Y. F. Yue, S. Y. Chong, K. C. Stylianou, J. Bacsa, D. Bradshaw, G. R. Darling, N. G. Berry, Y. Z. Khimyak, A. Y. Ganin, P. Wiper, J. B. Claridge, M. J. Rosseinsky, *Science.* **2010**, *329*, 1053.

[7] S. S. Nagarkar, A. V. Desai, S. K. Ghosh, *Chem. - An Asian J.* **2014**, *9*, 2358.

[8] J. R. Long, O. M. Yaghi, *Chem. Soc. Rev.* **2009**, *38*, 1213.

[9] S. Kitagawa, R. Kitaura, S. I. Noro, *Angew. Chemie - Int. Ed.* **2004**, *43*, 2334.

[10] S. L. James, *Chem. Soc. Rev.* **2003**, *32*, 276.

[11] H. Li, M. Eddaoudi, M. O'Keeffe, O. M. Yaghi, *Nature* **1999**, *402*, 276.

[12] S. Horike, S. Shimomura, S. Kitagawa, *Nat. Chem.* **2009**, *1*, 695.

[13] R. E. Morris, L. Brammer, *Chem. Soc. Rev.* **2017**, *46*, 5444.

[14] G. Férey, *New J. Chem.* **2016**, *40*, 3950.

[15] C. R. Murdock, B. C. Hughes, Z. Lu, D. M. Jenkins, *Coord. Chem. Rev.* **2014**, *258–259*, 119.

[16] A. Schneemann, V. Bon, I. Schwedler, I. Senkovska, S. Kaskel, R. A. Fischer, *Chem. Soc. Rev.* **2014**, *43*, 6062.

[17] Z. J. Lin, J. Lü, M. Hong, R. Cao, *Chem. Soc. Rev.* **2014**, *43*, 5867.

[18] N. A. Khan, Z. Hasan, S. H. Jhung, *J. Hazard. Mater.* **2013**, *244–245*, 444.

[19] R. J. Kuppler, D. J. Timmons, Q. R. Fang, J. R. Li, T. A. Makal, M. D. Young, D. Yuan, D. Zhao, W. Zhuang, H. C. Zhou, *Coord. Chem. Rev.* **2009**, *253*, 3042.

[20] J. R. Li, R. J. Kuppler, H. C. Zhou, *Chem. Soc. Rev.* **2009**, *38*, 1477.

[21] G. Férey, *Dalt. Trans.* **2016**, *45*, 4073.

[22] B. Manna, A. V Desai, S. K. Ghosh, *Dalt. Trans.* **2016**, *45*, 4060.

[23] F. A. Almeida Paz, J. Klinowski, S. M. F. Vilela, J. P. C. Tomé, J. A. S. Cavaleiro, J. Rocha, *Chem. Soc. Rev.* **2012**, *41*, 1088.

[24] A. Y. Robin, K. M. Fromm, *Coord. Chem. Rev.* **2006**, *250*, 2127.

[25] C. Martí-Gastaldo, D. Antypov, J. E. Warren, M. E. Briggs, P. A. Chater, P. V Wiper, G. J. Miller, Y. Z. Khimyak, G. R. Darling, N. G. Berry, M. J. Rosseinsky, *Nat. Chem.* **2014**, *6*, 343.

[26] Y. Li, L. Gan, *Chem. Eur. J.* **2017**, *23*, 10485.

[27] H. Prinzbach, F. Wahl, A. Weiler, P. Landenberger, J. Wörth, L. T. Scott, M. Gelmont, D. Olevano, F. Sommer, B. Von Issendorff, *Chem. - A Eur. J.* **2006**, *12*, 6268.

[28] R. J. Ternansky, D. W. Balogh, L. A. Paquette, *J. Am. Chem. Soc.* **1982**, *104*, 4503.

[29] J. Poater, M. Solà, C. Viñas, F. Teixidor, *Chem. - A Eur. J.* **2016**, *22*, 7437.

[30] J. Poater, M. Solà, C. Viñas, F. Teixidor, *Angew. Chemie - Int. Ed.* **2014**, *53*, 12191.
[31] R. N. Grimes, in Carboranes (Third Edition), Academic Press, Oxford, 2016.
[32] M. Scholz, E. Hey-Hawkins, *Chem. Rev.* **2011**, *111*, 7035.
[33] F. Teixidor, C. Viñas, *Sci. Synth.* **2005**, *6*.
[34] R. N. Grimes, *Dalt. Trans.* **2015**, *44*, 5939.
[35] D. Olid, R. Núñez, C. Viñas, F. Teixidor, *Chem. Soc. Rev.* **2013**, *42*, 3318.
[36] A. M. Cioran, A. D. Musteti, F. Teixidor, Z. Krpetić, I. A. Prior, Q. He, C. J. Kiely, M. Brust, C. Viñas, *J. Am. Chem. Soc.* **2012**, *134*, 212.
[37] A. Saha, E. Oleshkevich, C. Vinas, F. Teixidor, *Adv. Mater.* **2017**, *29*, 1704238.
[38] K. C. Stylianou, J. Pérez-Carvajal, M. Y. Tsang, C. Viñas, S. Rodríguez-Hermida, J. Juanhuix, D. Maspoch, C. Verdugo-Escamilla, C. Vignatti, F. Teixidor, I. Imaz, V. Guillerm, D. Choquesillo-Lazarte, A. Verdaguer, I. Peral, J. Giner Planas, *Angew. Chemie Int. Ed.* **2016**, *55*, 16049.
[39] M. Y. Tsang, S. Rodríguez-Hermida, K. C. Stylianou, F. Tan, D. Negi, F. Teixidor, C. Viñas, D. Choquesillo-Lazarte, C. Verdugo-Escamilla, M. Guerrero, J. Sort, J. Juanhuix, D. Maspoch, J. G. Planas, *Cryst. Growth Des.* **2017**, *17*, 846.
[40] M. J. Cliffe, E. Castillo-Martínez, Y. Wu, J. Lee, A. C. Forse, F. C. N. Firth, P. Z. Moghadam, D. Fairen-Jimenez, M. W. Gaultois, J. A. Hill, O. V Magdysyuk, B. Slater, A. L. Goodwin, C. P. Grey, *J. Am. Chem. Soc.* **2017**, *139*, 5397.
[41] Z. Chen, S. Xiang, D. Zhao, B. Chen, *Cryst. Growth Des.* **2009**, *9*, 5293.
[42] C.-X. Yang, X.-P. Yan, *J. Mater. Chem.* **2012**, *22*, 17833.
[43] H. Li, M. R. Hill, R. Huang, C. Doblin, S. Lim, A. J. Hill, R. Babarao, P. Falcaro, *Chem. Commun.* **2016**, *52*, 5973.

Chapter 5

Carborane bis-pyridylphenylalcohols as linkers for Coordination Polymers: Synthesis, Crystal Structures and Phase Transitions

5. Carborane bis-pyridylphenylalcohols as linkers for Coordination Polymers: Synthesis, Crystal Structures and Phase Transitions

5.1 Introduction

Porous Coordination Polymers (CPs) or Metal-Organic Frameworks (MOFs) are a class of porous crystalline materials formed by the assembly of metal ions or metal clusters with different types of bridging organic linkers[1–4]. The hybrid nature of CPs and MOFs is translated in a synergic effect between the metal containing sub-unit and the bridging ligands, where the characteristic properties of the building blocks are transferred to the final extended structure. The extraordinary variability for both, the organic and the inorganic components, provides endless possibilities and make CPs/MOFs to be strongly interesting for many potential applications[1]. Given their modular structure, their architectures and porosity can in principle be modulated by modifying the chemistry, shape and length of the ligands[5]. Particularly interesting is the design of flexible yet stable MOFs opening the way to the rational design of novel "smart" materials. This field of study has been continuously expanding and the progress has been extensively reviewed[4,6–10]. Despite the exciting application opportunities of these SPCs, e.g. in selective gas adsorption, chemical sensing or hazardous waste adsorption[2,11–16], to date, there is no reported fully rationale way to design a breathing MOF. As already described in the introduction in Chapter 4, the rationalization of available data allows for the design of ways to induce softness and, possibly, reversible structural transformation phenomena, in these porous networks[4,6–9,17,18]. Framework flexibility is usually associated with flexible ligands, bond cleavage and regeneration, metal-metal interaction, supramolecular host-guest interaction, or a combination of a number of these. However, flexibility often comes with the penalty of reduced stability, which limits their application as stimuli-responsive or smart materials. Ligands in CPs chemistry are commonly built from planar aromatic moieties which are responsible of the rigidity of the frameworks. Some degree of flexibility can be introduced by using flexible ligands[19]; however, flexibility often comes with the penalty of reduced stability. Collapsing of the structures is generally the rule, and reversible flexibility mostly a question of serendipity. We have previously proposed the substitution of planar systems by spherical moieties as a way to stabilize the flexible structure diminishing or avoiding the structure collapse thanks to the globular nature or multiple supramolecular contacts (Chapter 4)[20]. Among the suitable spherical systems for

ligand syntheses, we have been working for many years with icosahedral carboranes (1, n-$C_2B_{10}H_{12}$ (n = 2 (*ortho*-carborane), 7 (*meta*-carborane) or 12 (*para*-carborane); see also Scheme 5-1)). The latter are an interesting class of commercially available and exceptionally stable 3D-aromatic[21,22] boron-rich clusters that possess material-favorable properties such as thermal and chemical stability and hydrophobicity[23–25]. As described in the previous chapters of this Thesis, carboranes are remarkably robust boron clusters with two carbon atoms and possess 26 electrons for 12 vertices. The delocalized electron density is not uniform through the cage, giving rise to extraordinary differences in the electronic effects of the cluster[26]. This unusual electronic structure is often highlighted by regarding carboranes as inorganic three-dimensional "aromatic" analogs of arenes[22]. Such properties make icosahedral carborane clusters valuable ligands for CPs or MOFs.

Scheme 5-1. Graphical representation of the carborane isomers (*closo*-$C_2B_{10}H_{12}$) and their derivatives used as linkers to form CPs.

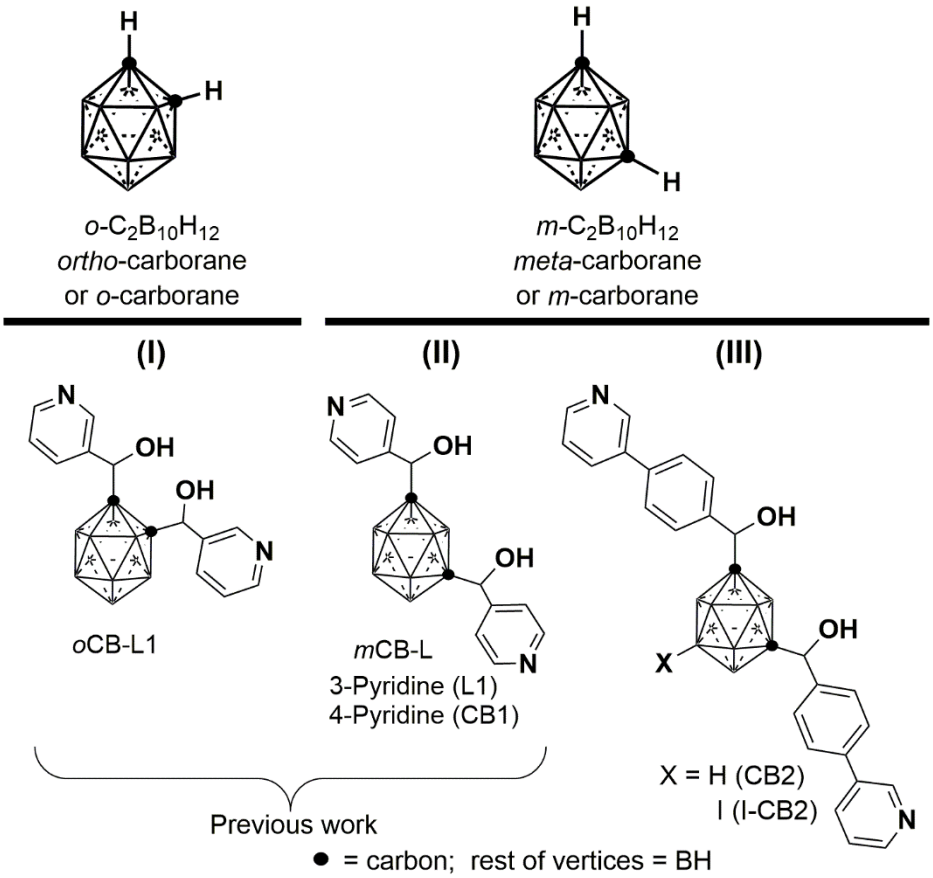

These icosahedral boron-based molecules can be visualized as hollow spheres that are capable of multiple supramolecular contacts that are of a different nature to those found in conventional planar carbon based ligands. These include B–H···A (A = H[27–29], I[30],

π[31,32]) interactions or B–H···Metal[33–40] interactions. Very recently a first example of a B–H···Cu(II) supramolecular MOF has been reported[41]. We have previously synthesized a family of disubstituted *m*-carboranylpyridylalcohols (**oCB-L1** and **mCB-L1** and **CB1** in Scheme 5-1) that proved useful N-donor ditopic ligands in CPs and MOFs[20,42–48]. Those ligands are able to display various ligating topologies depending on the relative orientation of the pyridyl rings with respect to the carboranyldiol spacer and the flexibility of the spacer. Consequently, the resulting CP architectures are dependent on the ligand conformation and the relative position of nitrogen in the aromatic ring. The ligand flexibility was found to be higher in the case of the *m*-carborane derivatives as the substituted carbons are farther away than in the *o*-carborane ones (Figure 5-1)[44]. We hypothesized that introducing a longer pyridylalcohols arms into the carborane moiety would increase the ligand flexibility and possibly provide a new family of isoreticular MOFs to those previously reported and described in Chapters 3 and 4. Herein, we report the synthesis of two novel carboranylalcohol 9-X-1,2-bis{(4-pyridin-3-yl)phenylmethanol}-1,7-dicarba-*closo*-dodecaboranes (X = H, **CB2**; X = I, **I-CB2**) ligands, and their reaction with different di- or tritopic carboxylic acids and $Co(NO_3)_2$ to form five new extended CPs (Scheme 5-2). We present the syntheses, crystal structures and full characterization of the new CPs.

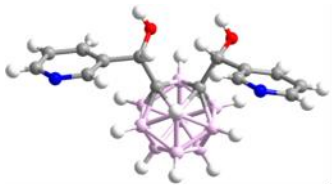

***o*CB(1,2-bis{(pyridin-3-yl)methanol}-1,2-dicarba-closo-dodecarborane)2**
d(N-N) = 8.55 Å
α (pyridine rings) = 18°

Figure 5-1. Molecular conformation of free ***o*CB(L)$_2$.**[44]

Scheme 5-2. Representation of the carboxylic ligands employed in this work and of the synthesis of CPs **CB2**MOF-1 to **CB2**MOF-4 and **I-CB2**MOF-1.

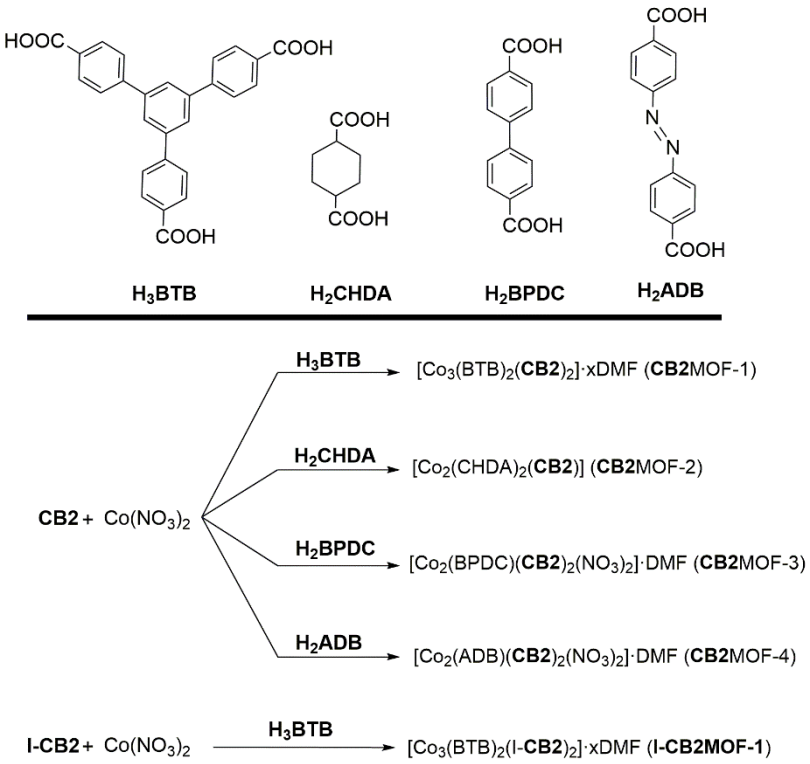

5.2 Results and discussion

5.2.1 Synthesis and Characterization

Following our previous reports[43,46,47], we have prepared two new bis-pyridylmethyl alcohols derived from the *m*-carborane cluster, **CB2** and **I-CB2** (Scheme 5-1). The new ligands were obtained by the one-pot reaction of dilithiated *m*-carborane with the corresponding aromatic aldehydes at low temperature and isolated in reasonable yields. Both ligands were fully characterized by standard spectroscopic and analytical techniques and are in agreement with previous shorter bis-pyridylmethyl alcohol derivatives of *m*-carborane[43,46]. Figure 5-2 shows a comparison of the ^{11}H and ^{11}B NMR spectra for **CB2** and **I-CB2**. The peaks assignment for the chemical shifts in these compounds has been done by comparison with the related **CB1** compound in Chapter 3. ^{11}B NMR spectra for these compounds are consistent with a *closo*-icosahedral geometry for the boron cage and show a very broad signal due to the fluxional behavior of these compounds in solution. ^{11}B NMR spectrum of **I-CB2** shows an additional and relatively sharp resonance at – 25 ppm that correspond to the B-I vertex. IR-ATR

spectra of these two compounds (Figure S5-1), show the characteristic peak corresponding to stretching bond of B-H at ca. 2600 cm^{-1}.

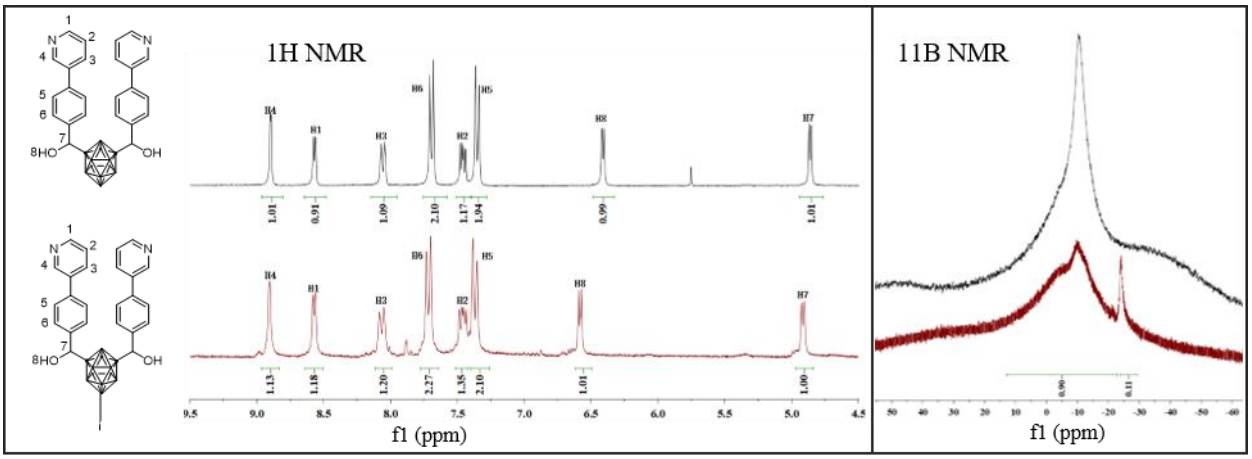

Figure 5-2 ^{1}HNMR (left) and ^{11}BNMR (right) of **CB2** (black) and **I-CB2** (red) in DMSO-D6.

Solvothermal reactions (DMF/EtOH mixtures at 100 °C) of **CB2** with 1,3,5-benzenetribenzoic acid (H_3BTB), 1,4-cyclohexanedicarboxylic acid (H_2CHDA), biphenyl-4,4′-dicarboxylic acid (H_2BPDC) or 4,4′-azobenezenedicarboxylicacid (H_2ADB) in the presence of $Co(NO_3)_2$ provided crystalline **CB2**MOF-1 to **CB2**MOF-4 in good yields and as pure phases (Scheme 5-2). **I-CB2** reacted with H_3BTB and $Co(NO_3)_2$ to form **I-CB2**MOF-1. IR spectra showed the characteristic broad B-H stretching bands from the carborane (in the range 2617~2531 cm^{-1}), and the C=O vibration of the carboxylate groups (Figure S5-2). Crystal structures of **CB2**MOF-1 to **CB2**MOF-4 were determined by SCXRD (*vide infra*), and their simulated powder X-ray diffraction (PXRD) patterns compared with their experimental ones, confirming their phase purity (Figures S5-3 to S5-6). SEM images of these CPs also showed the formation of homogeneous crystalline samples (Figure 5-3). TGA data for obtained CPs (Figures S5-7 to S5-11) showed a first weight loss (2-26%) in the range of 95-300 ºC, which corresponds to the release of solvent molecules (see SI 5 for details), followed by their decomposition starting at 400 ºC for **CB2**MOF-1 and **I-CB2**MOF-1 or 300 ºC for **CB2**MOF-2 to **CB2**MOF-4. Compounds **CB2**MOF-2 to **CB2**MOF-4 are water stable, even in basic conditions as proved by PXRD after immersing the crystals into neutral or basic (pH 13) water solutions (Figure S5-12 to Figure S5-14).

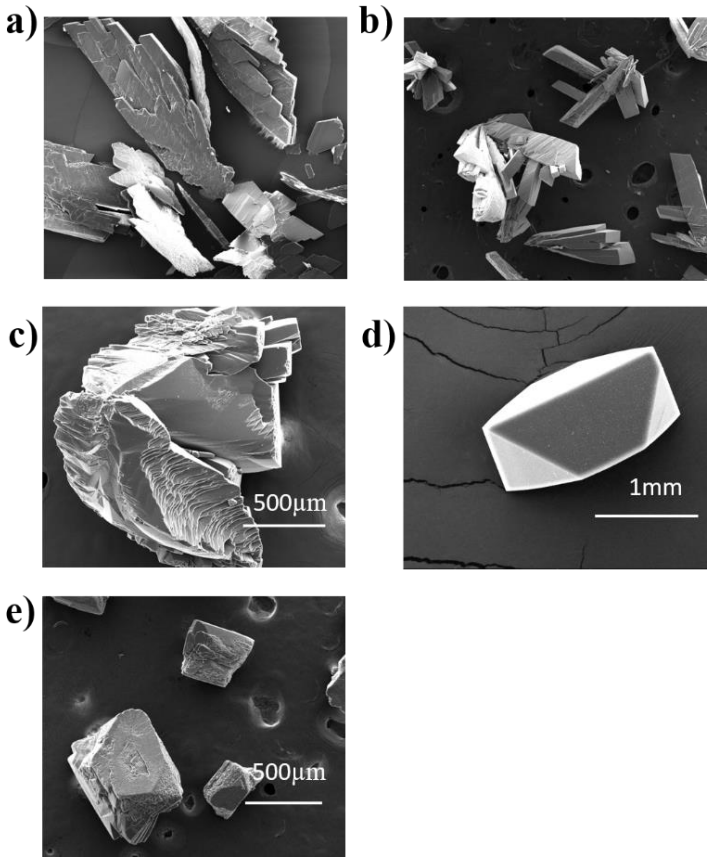

Figure 5-3. SEM images of (a) **CB2**MOF-1, (b) **I-CB2**MOF-1, (c) **CB2**MOF-2, (d) **CB2**MOF-3 and (e) **CB2**MOF-4.

5.2.2 Crystal Structures of CB2MOF-1 to CB2MOF-4 and I-CB2MOF-1

Suitable crystals for SCXRD were obtained for **CB2**MOF-1 to **CB2**MOF-4. All compounds crystallized in the monoclinic crystal system (Table 5-2). **CB2**MOF-1 crystallized in the $P2_1/n$ space group. **I-CB2**MOF-1 was identified by comparing the as-synthesized PXRD patterns resulting in lattice constants similar to that for **CB2**MOF-1. **CB2**MOF-2 crystallized in the monoclinic space group $C2/c$, whereas **CB2**MOF-3 and **CB2**MOF-4 crystallized in the monoclinic $P2_1/c$ space group.

*$[Co_3(BTB)_2(CB2)(DMF)_2]\cdot 15DMF$ (**CB2**MOF-1) and $[Co_3(BTB)_2(I\text{-}CB2)(DMF)_2]\cdot xDMF$ (**I-CB2**MOF-1).* **CB2**MOF-1 and **I-CB2**MOF-1 are two closely related isomorphous CPs. Single crystal analysis of **CB2**MOF-1 revealed the formation of a 2D framework based on pinwheel $[Co_3(COO)_6O_2N_2]$ units (Figure 5-4a and 5-4b). The Co–O bond lengths for **CB2**MOF-1 vary in the range 2.022/2.229, and the Co–N

bond lengths are 2.075/2.127, respectively, which are similar to those found in other related compounds[43,49]. The $[Co_3(COO)_6O_2N_2]$ units are linear trinuclear cobalt clusters in which the central Co atom resides at a crystallographic inversion center and adopts an octahedral geometry $\{O_6\}$-coordinated to six neighboring BTB ligands (Figure 5-4a). Both symmetry related terminal Co atoms are $\{NO_5\}$-octahedrally coordinated to one **CB2** ligand, to four O atoms of three BTB ligands and to one O atom of DMF molecules. As shown in Figure 5-4a, the BTB ligands adopt two distinct coordination modes: the bridge bidentate μ-κO:κO´ and the bridge bidentate chelate μ-κ^2O,O´:κO´ modes. In this structure, each trinuclear Co(II) cluster is connected to six BTB units, thus creating six-pointed star fashion layers running along the *ac* plane (Figure 5-4b). However, the **CB2** ligand is not acting as pillar, but coordinate contiguous trinuclear $Co_3(COO)_6$ clusters in the same layer (Figure 5-4c), and similarly to a related shorter version of **CB1**. Layers in **CB2**MOF-1 are arrange so as to generate 1D channels (51% of the unit cell) running along the *a* axis, as shown in figure 5-4d.

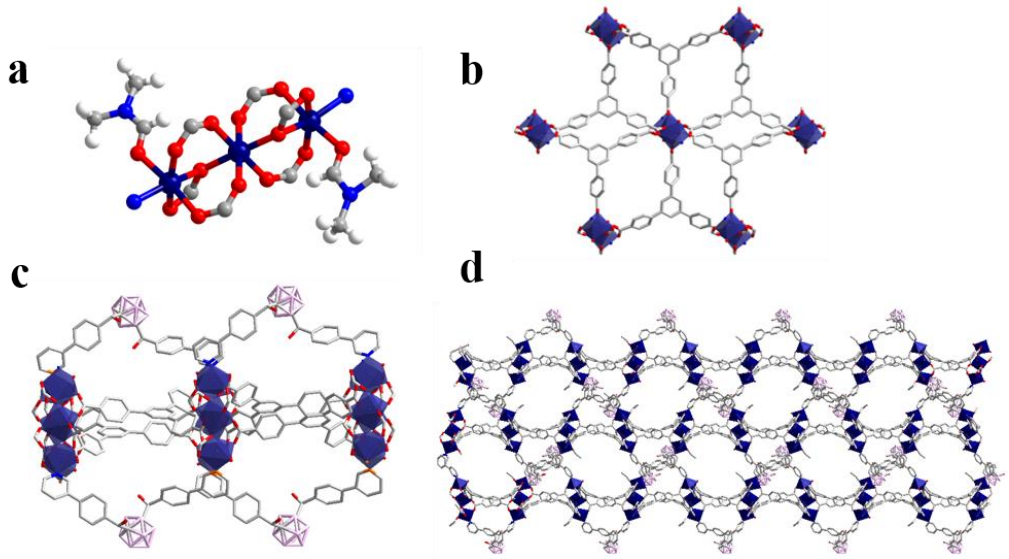

Figure 5-4. Crystal structure of **CB2**MOF-1: (a) view of the trinuclear Co(II) cluster and coordination environment; (b) 2D {Co_3-BTB} layers; (c) view of three trinuclear Co(II) cluster units interlinked by **CB2** ligands; and (d) Supramolecular 3D structure (**CB2** in cyan) showing the 1D channels.

Unfortunately, by the time we have deposited this PhD thesis, we were yet not able to provide the solved structure for **I-CB2**MOF-1. However, as mentioned above, its

experimental PXRD pattern matches quite well with that for **I-CB2**MOF-1 and therefore provides an evidence for these two CPs being isomorphous (Figure 5-5).

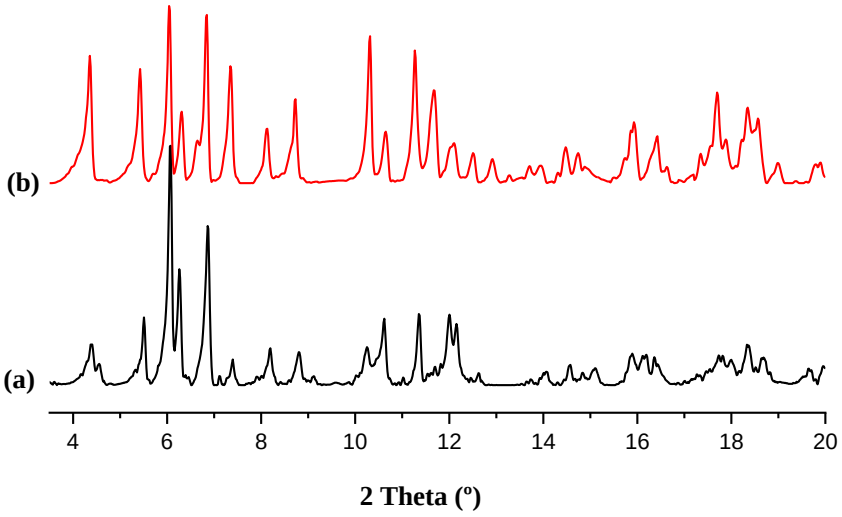

Figure 5-5. Experimental PXRD for (a) **CB2**MOF-1 and (b) **I-CB2**MOF-1.

*[Co_2(CHDA)$_2$(CB2)] (**CB2**MOF-2).* Single-crystal X-ray diffraction (Figure 5-6) revealed a three-dimensional (3D) network of formula [Co_2(CHDA)$_2$(CB2)$_2$]. The basic unit of **CB2**MOF-2 is a Co_2-paddlewheel motif of [Co_2(COO)$_4$] units (Figure 5-6a), each coordinated to four different CHDA ligands, thus creating a two-dimensional (2D) square grid (Figure 5-6b). These 2D square grids are further pillared by **CB2**, occupying the axial sites of the Co_2 paddle wheels and forming the observed 3D structure (Figure 5-6d). The Co–O and Co–N bond lengths lie in the range 2.008-2.045 Å and 2.060 Å, respectively. The Co–Co distances in the paddle-wheel unit is 2.6395(6) Å, which is in the range found for other Co_2-paddlewheel motifs[49,50]. As shown in figure 5-6b, each CHDA ligand in fully deprotonated and coordinate four different Co(II) atoms corresponding to two different paddlewheel units in a bridge bidentate mode (μ-κO:κO´), creating 2D layers in the *ab* plane. Then, these layers are further pillared by **CB2** ligands by coordination of the nitrogen atoms of the pyridyl moieties (Figure 5-6d). However, the conformation of **CB2** on coordination is rather unusual. Instead of the extended coordination, the pyridine moieties in each ligand are facing each other and show intramolecular π-π interactions (centroid to centroid distances 3.458 Å; pyridine planes at 10.85º). The later makes ligand **CB2** behave as a rather short ditopic

nitrogen ligand like e.g., dabco (diazabicyclo[2.2.2]octane)[51]. The flexibility of **CB2** make this conformation possible and provide a rather short distance between 2D layers (7.537 Å), comparable to other small dipyridine linkers. As a result, **CB2**MOF-2 is non-porous.

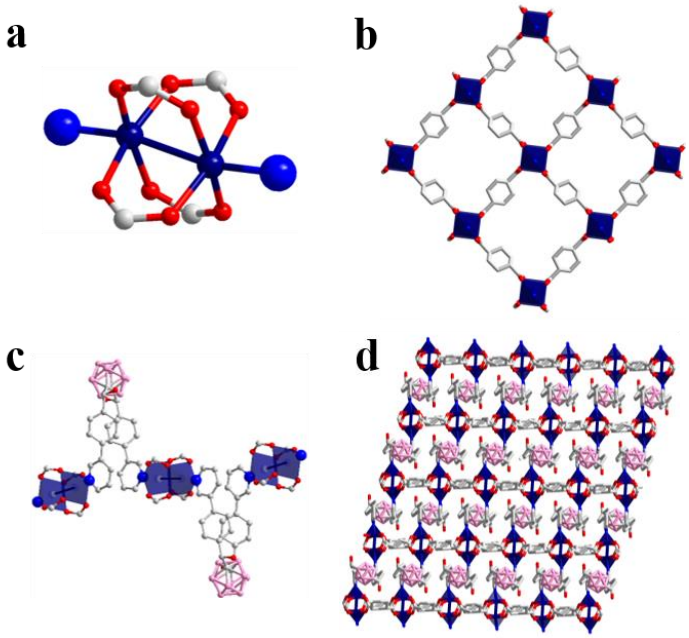

Figure 5-6. Crystal structure of **CB2**MOF-2: (a) view of the Co_2-paddlewheel cluster; (b) 2D {Co_2-CHDA} layers; (c) view of three Co_2-paddlewheel cluster units interlinked by **CB2**; and (d) 3D pillared structure.

*$[Co_2(BPDC)(CB2)_2(NO_3)_2]\cdot DMF$ (**CB2**MOF-3) and $[Co_2(ADB)(CB2)_2(NO_3)_2]\cdot DMF$ (**CB2**MOF-4)*. These two compounds are isostructural. **CB2**MOF-3 and **CB2**MOF-4 revealed 3D networks of formula $[Co_2(L_{COO})_2(CB2)_2(NO_3)_2]$ (L_{COO} = BPDC (CB2MOF-3) or ADB (**CB2**MOF-4)). The single crystal X-ray analysis for these two compounds revealed the basic building unit is formed by two Co(II) atoms that are bridged by two carboxylate groups adopting a bis-bidentate coordination mode (Figures 5-7a and 5-8a). Each Co atom exhibits a distorted octahedral geometry, the axial positions occupied by the two nitrogen atoms from two **CB2** ligands while the equatorial plane consists of four oxygen atoms, two from a NO_3^- anion and two from different dicarboxylate ligands. The Co–O bond lengths vary in the range 1.984/2.200 Å, and the Co–N bond lengths are 2.134/2.153 Å, respectively, which are similar to those found in other related compounds[52]. The dinuclear Cobalt building units show

Co···Co distance of 3.9391(7) Å for **CB2**MOF-3 and 4.0871(7) Å for **CB2**MOF-4. Each $[Co_2(L_{COO})_2]$ bridges *trans*-dicarboxylate ligands to yield 1D chains that are then connected by dipyridine **CB2** ligands to form the observed 3D network (Figure 5-7d and 5-8d). The **CB2** ligand shows the same folded conformation observed in **CB2**MOF-2, however no intramolecular π-π interactions are found in **CB2**MOF-3 or **CB2**MOF-4.

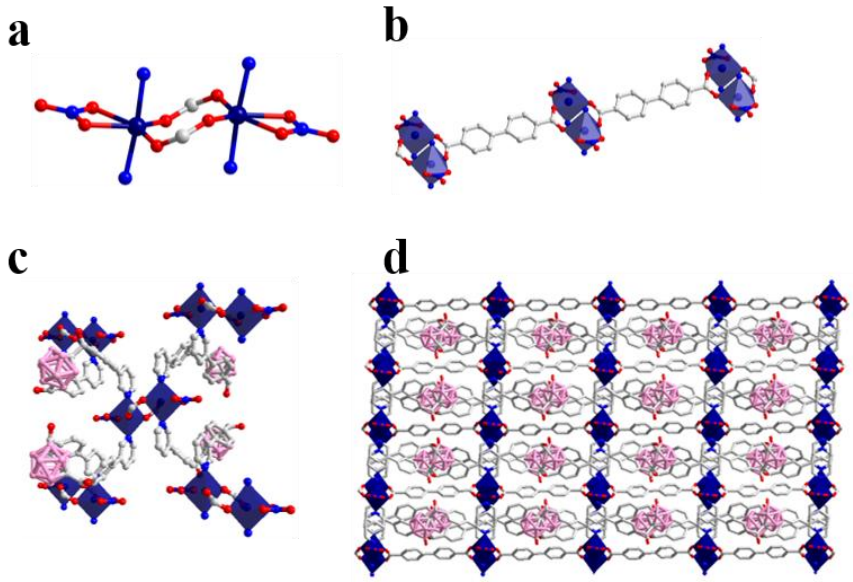

Figure 5-7. Crystal structure of **CB2**MOF-3: (a) view of the dinuclear Co(II) cluster and coordination environment; (b) a 1D {Co_2-BPDC} chain; (c) view of five Co(II) cluster units interlinked by **CB2** ligands; and (d) 3D structure.

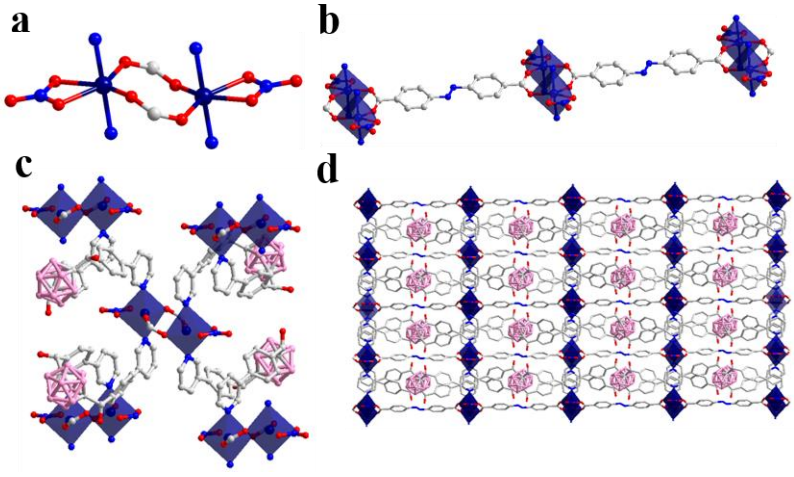

Figure 5-8. Crystal structure of **CB2**MOF-4: (a) view of the dinuclear Co(II) cluster and coordination environment; (b) a 1D {Co_2-ADB} layer; (c) view of five Co(II) cluster units interlinked by **CB2** ligands; and (d) 3D pillared structure.

A comparison of the two different ligand conformations observed in structures **CB2**MOF-1 to **CB2**MOF-4 and **I-CB2**MOF-1 is shown in Figure 5-9. As described above, **CB2** adopts a folded conformation with the pyridine moieties in each ligand facing each other in **CB2**MOF-2 to **CB2**MOF-4, resembling an ice tweezer (Figure 5-9a). Such conformation provided the shorter N···N distance and lower pyridine-pyridine angle obtained so far for these types of ligands (Figures 5-6 to 5-8). Although **CB2** is acting as a pillar ligand in **CB2**MOF-2 to **CB2**MOF-4, the short distances between the nitrogen atoms give rise to non-porous CPs. The tweezer-like angle and N···N distance for **CB2** (and most probably **I-CB2**) is however wider in **CB2**MOF-1 and **I-CB2**MOF-1 (Figure 5-9b) and provides 2D materials as previously obtained for **CB1**[20].

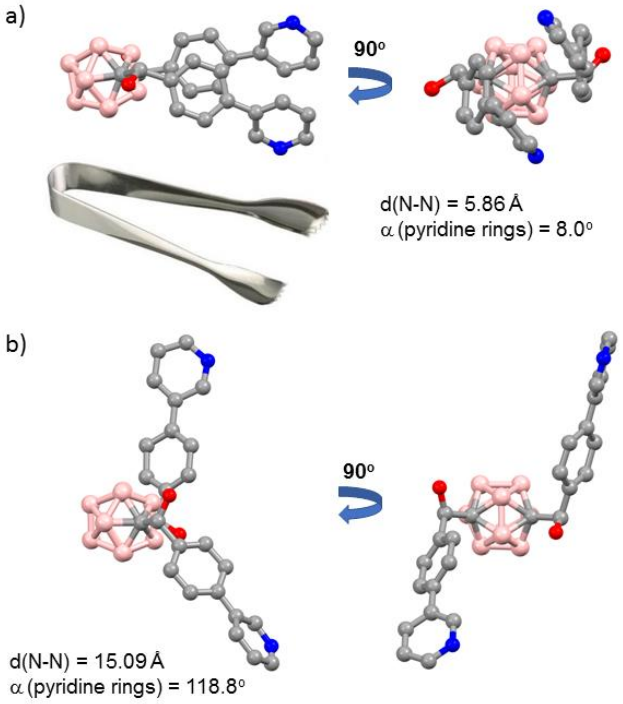

Figure 5-9. Molecular conformation of **CB2** in (a) **CB2**MOF-2 to **CB2**MOF-4 and (b) in **CB2**MOF-1 and **I-CB2**MOF-1. An image of an ice tweezer is shown.

5.2.3 Fast and reversible phase transformations of CB2MOF-1 and I-CB2MOF-1

Due to the high similarity between **CB2**MOF-1 and the related CP having the shorter **CB1** ligand $[Co_3(BTB)_2(CB1)_2]$·solv (**CB1**MOF-1´ in Chapter 4), we decided to investigate whether the previously observed 2D to 3D phase transition (Figure 4-12a in

Chapter 4) for the latter could also be observed in **CB2**MOF-1. However, heating of **CB2**MOF-1 in DMF or even in the presence of C_{60} did not provide any new phase. We did however notice that **CB2**MOF-1 suffered a phase transition when immersed in other solvents, such as, $CHCl_3$, EtOH or acetone at room temperature. Figure 5-10 shows the PXRD data for **CB2**MOF-1, and that after being immersed in $CHCl_3$ for one day. There is a clear change of the diffraction peaks toward lower angles, consistent with the shrinking of some unit cell parameters. Quite interestingly, such transformation is reversible and the new phase (**CB2**MOF-1´) converts back into **CB2**MOF-1 when immersing in DMF for 30 minutes at room temperature. Such a reversible transformation under ambient conditions indicates a rather weak interaction between layers in **CB2**MOF-1. Raman spectra were measured for **CB2**MOF-1 and **CB2**MOF-1´ (Figures S5-17) and show no significant changes, indicating that not bond breaking seems to be happening from **CB2**MOF-1 to **CB2**MOF-1´ and therefore we assume that the individual layers in these two compounds are basically identical.

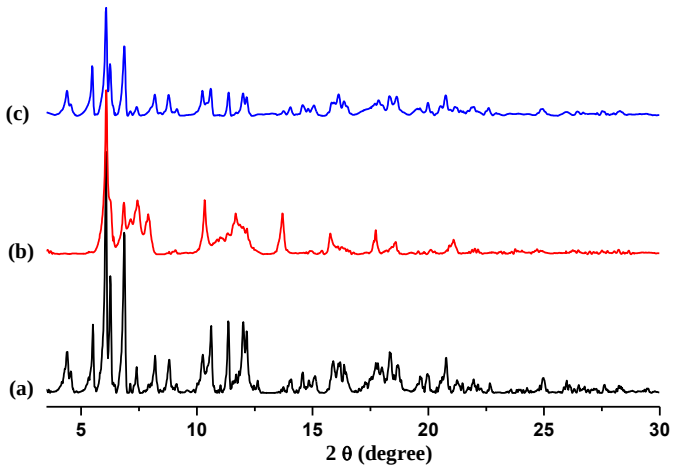

Figure 5-10. PXRD patterns showing the reversible transformation between **CB2**MOF-1 and **CB2**MOF-1´. PXRD of (a) as synthesized **CB2**MOF-1; (b) **CB2**MOF-1´, obtained after immersing **CB2**MOF-1 for one day in $CHCl_3$ under ambient conditions; (c) **CB2**MOF-1´, obtained after immersion of **CB2**MOF-1´ in DMF under ambient conditions for 30 mins.

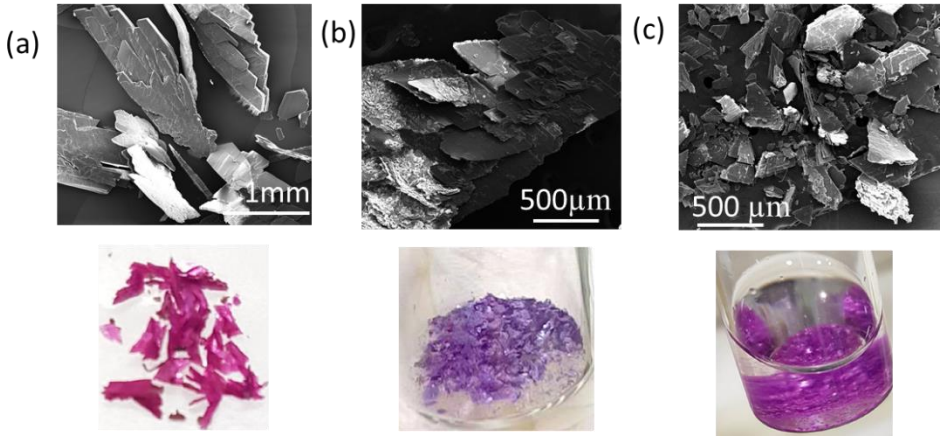

Figure 5-11. SEM (Top) and low-resolution (Bottom) images showing crystals morphology of as made **CB2**MOF-1 (a), **CB2**MOF-1′, obtained after immersing **CB2**MOF-1 for one day in $CHCl_3$ under ambient conditions; (c) **CB2**MOF-1′, obtained after immersion of **CB2**MOF-1′ in DMF under ambient conditions for 30 mins.

Phase transformation of **CB2**MOF-1 into **CB2**MOF-1' can be clearly observed in the crystals. Treatment of large **CB2**MOF-1 crystals with $CHCl_3$ showed a clear macroscopic transformation in the size and color of the crystals to give the new phase **CB2**MOF-1' (Figure 5-11). Large platelets broke into small pieces, followed with a color change from purple to violet. Immersion of **CB2**MOF-1' crystals in DMF provoked a color change back to purple but no further change of morphology or dissolution of crystals was observed (Figure 5-11c).

The iodinated compound **I-CB2**MOF-1 shows a very similar behavior as the one observed for **CB2**MOF-1. Both, a crystal color and morphology changes (Figure 5-13) and the corresponding one in the PXRD pattern (Figure 5-12) were observed when immersing crystals of **I-CB2**MOF-1 into $CHCl_3$. We also confirmed that the phase change is also reversible as shown in Figure 5-12.

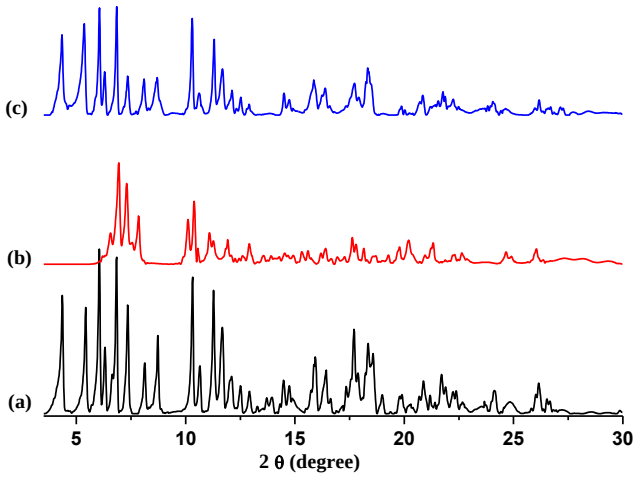

Figure 5-12. PXRD patterns showing the reversible transformation between **I-CB2**MOF-1 and **I-CB2**MOF-1′. Patterns of (a) as synthesized **I-CB2**MOF-1; (b) **I-CB2**MOF-1′, obtained after immersing **I-CB2**MOF-1 for one day in $CHCl_3$ under ambient conditions; (c) **I-CB2**MOF-1′, obtained after immersion of **I-CB2**MOF-1′ in DMF under ambient conditions for 30 mins.

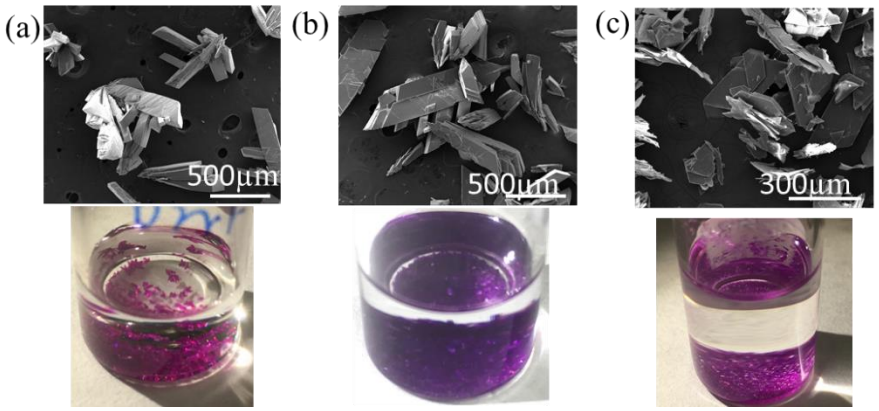

Figure 5-13. SEM (Top) and low-resolution (Bottom) images showing crystals morphology of as made **I-CB2**MOF-1 (a), **I-CB2**MOF-1′, obtained after immersing **I-CB2**MOF-1 for one day in $CHCl_3$ under ambient conditions; (c) **I-CB2**MOF-1′, obtained after immersion of **I-CB2**MOF-1′ in DMF under ambient conditions for 30 mins.

Such reversible transformations of **CB2**MOF-1 and **I-CB2**MOF-1 under ambient conditions clearly suggest that rather weak interactions are present between layers in these 2D materials. The transformations can be explained by sliding of layers generating channels as represented schematically in figure 5-14. Such interlayer displacement will open and close the observed channels in **CB2**MOF-1 (Figure 5-4d), explaining the observed displacement of the PXRD peaks (Figure 5-10 and 5-12). It is possible that DMF molecules interact with the framework and thus create the interlayer channels. When the DMF is displaced by the less polar and poor hydrogen bond donor/acceptor $CHCl_3$, weaker intermolecular interactions between the solvent and the

CP layers are disfavored, causing the layer sliding to a denser structure. The latter is however a working hypothesis that should be verified.

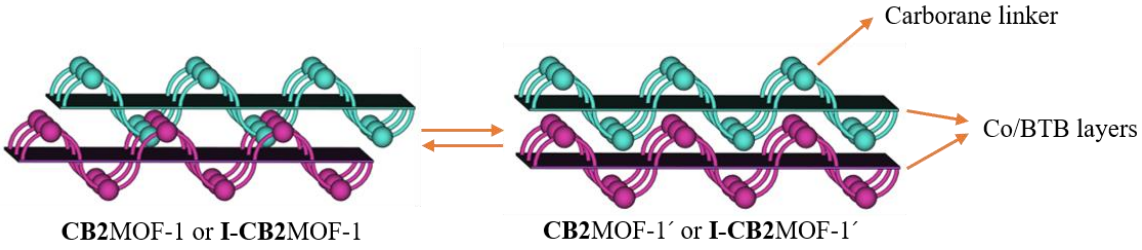

Figure 5-14. Schematic representation of a possible mechanism for the observed reversible phase transition in **CB2**MOF-1 and **I-CB2**MOF-1. Different color represents different layers in the 2D structure of the CPs.

5.2.4 CO_2 and N_2 adsorption of CB2MOF-1 and I-CB2MOF-1

As mentioned above, compounds **CB2**MOF-2 to **I-CB2**MOF-4 have no potential voids and therefore are not expected to be porous. However, **CB2**MOF-1 and **I-CB2**MOF-1 are potentially porous as the first one shows 1D channels running along the *a* axis (Figure 5-4d) and the second is isomorphous. Although we have not been able yet to obtained the crystal structure for the **CB2**MOF-1´ or **I-CB2**MOF-1´ phases, we decided to investigate the porosity of the transformed phases. Thus, **CB2**MOF-1´ or **I-CB2**MOF-1' were activated at high vacuum and 120ºC for 10 h and measured their porosity to N_2 and CO_2 (Table 5-1 and Figures 5-15 and 5-16).

Table 5-1. Summary of **CB2**MOF-1 and **I-CB2**MOF-1 surface area obtained based on N_2- and CO_2-adsorption measurements.

Compound	**N_2 surface area[a]/[b] (m^2/g)**	**CO_2 surface area[c] (m^2/g)**
CB2MOF-1	109.5/117.1	247.6
I-CB2MOF-1	12.8/40.7	248.2

[a] and [b] N_2 BET surface area and Langmuir surface area.

[c] CO_2 surface area calculated by Dubinin-Astakhov method.

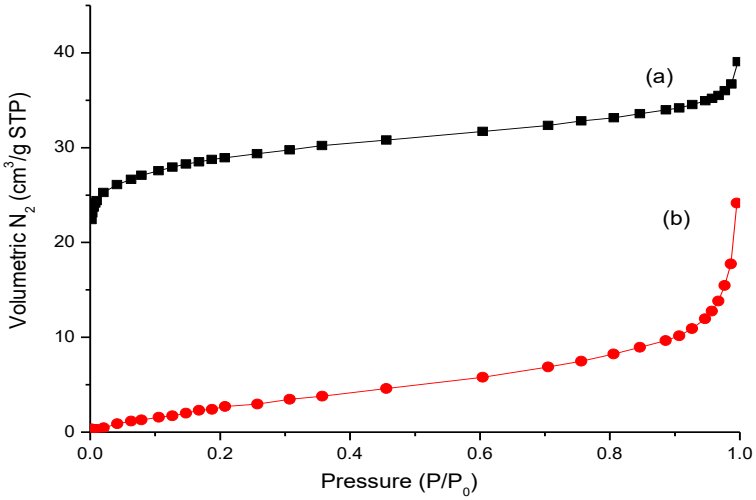

Figure 5-15. N_2 adsorption isotherms for (a) **CB2**MOF-1 and (b) **I-CB2**MOF-1 at 77 K.

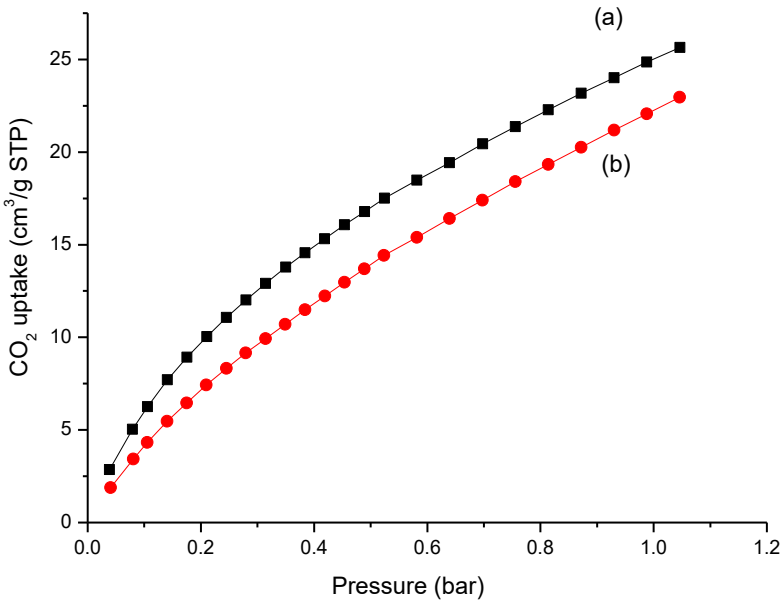

Figure 5-16. CO_2 adsorption isotherms for (a) **CB2**MOF-1 (b) and **I-CB2**MOF-1 at 273 K.

N_2 sorption isotherm of **CB2**MOF-1 exhibits a type-I isotherm typical for a microporous structure (Figure 5-15). However, **I-CB2**MOF-1 is not porous to N_2 at 77 K, possibly due to bulky iodo substituents that slightly constrict the pores. Interestingly, both compounds are porous to CO_2 at 195K and 1bar and with very similar uptakes (22-26 cm^3g^{-1} STP; Figure 5-16). The calculated accessible surface area for both materials is higher than that observed from N_2 as shown in table 5-1, which implies that CO_2 interacts stronger with **CB2**MOF-1 and **I-CB2**MOF-1 than N_2 (CO_2 quadrupole moment: 43×10^{-27} $esu^{-1}cm^{-1}$, N_2 quadrupole moment: 15.2×10^{-27} $esu^{-1}cm^{-1}$). The selectivity of **I-CB2**MOF-1 towards CO_2 could be due to the generation a unsaturated

Co(II) center on activation[53]. Another possible reason for this is the slightly smaller kinetic diameter of CO_2 molecules than N_2 This investigation proves that **CB2**MOF-1 and **I-CB2**MOF-1 possessed selectivity for CO_2 over N_2, especially for iodo-containing **I-CB2**MOF-1, which is beneficial for the capture of greenhouse gas CO_2 from flue gas emission of power plants[54].

5.3 Conclusions

In conclusion, we have synthesized two new carborane bis-pyridylphenylalcohol compounds and prepared a novel family of coordination polymers, by the reaction of the linkers with various organic di- or tricarboxylic acids and $Co(NO_3)_2$. Five coordination polymers or MOFs were obtained where the carborane linkers either adopts a folded conformation with the pyridine moieties in each ligand facing each other, resembling an ice tweezer, or in a more opened conformation providing 2D materials. The latter show a reversible phase transformation on solvent exchange from DMF to $CHCl_3$. The new phases seem to be the result of sliding of layers and are non-porous to N_2 but porous to CO_2.

5.4 Experimental section

5.4.1 Materials and Characterization

Syntheses of the carboranylalcohol ligands were carried out under nitrogen atmosphere in round-bottomed flasks equipped with a magnetic stirring bar, capped with a septum. Tetrahydrofuran (THF) was distilled from Na/benzophenone. CPs syntheses were done in air. All chemicals were commercially available and used as received. I-mCB was synthesized following the previous report[55]. IR ATR spectra were recorded on a Perkin–Elmer Spectrum One spectrometer. ^{1}H, ^{13}C and ^{11}B NMR spectra were recorded respectively at 300, 75 and 96 MHz with a Bruker Advance-300 spectrometer in deuterated dimethylsulfoxide, unless denoted, and referenced to the residual solvent peak for ^{1}H and ^{13}C NMR or to $BF_3{\cdot}OEt_2$ as an external standard for ^{11}B NMR. Chemical shifts are reported in ppm and coupling constants in Hertz. Multiplets

nomenclature is as follows: s, singlet; d, doublet; t, triplet; br, broad; m, multiplet. Elemental analyses were obtained by a CarboErba EA1108 microanalyzer. TGA-DSC from NETZSCH (heating rate: 10 ºC/min; temperature range: 25 to 600 ºC). Gas sorption (CO_2/195 K and N_2/77 K) measurements for **CB2**MOF-1 **and I-CB2**MOF-1 were performed using an AutosorbIQ (Quantachrome Instruments). Field-Emission Scanning Electron Microscopy (FE-SEM) images were collected using a Quanta 650F Environmental Scanning Electron Microscopy (Field Emission Inc, USA). Powder X-ray Diffraction (PXRD) patterns were recorded at room temperature on an X'Pert PRO MPD diffractometer (Panalytical) using Cu Kα (λ = 1.5405 Å) radiation.

5.4.2 Synthesis of the ligands and compounds

1,2-bis{(4-pyridin-3-yl)phenylmethanol}-1,7-dicarba-*closo*-dodecaborane (CB2). nBuLi (1.04 mL, 1.55 M in hexane, 1.63 mmol) was added dropwise to a solution of m-carborane (98 mg, 0.68 mmol) in THF (20 mL) at 0 ºC (ice/water bath) under nitrogen atmosphere. The mixture was stirred for 30 min at low temperature and for a further 1 h at room temperature to give a clear, pale yellow suspension. The flask was then cooled to -85 ºC (acetone/liquid N_2), whereupon a solution of the 4-pyridine-3ylbenzadehyde (314.7 mg, 1.63 mmol) in THF (2 mL) was added. The resulting pale-yellow solution was stirred at -85 ºC for 4 h. Then a saturated aqueous solution of NH_4Cl (10 mL) was added at -84 ºC and then the mixture was taken out of the cooling bath and allowed to warm naturally to room temperature while stirring. The aqueous phase was then extracted with THF (3 x 20 mL) and the organic phases were dried over $MgSO_4$, filtered, and evaporated to dryness. Then the dichloromethane (15 mL) was added while stirring. A white solid precipitated after about 25-30 min that was filtrated, washed with dichloromethane and dried under vacuum affording pure compound (126.5 mg, 0.26mmol, 38.4 %). ^{1}H NMR 8.89 (d, *J* = 2.0, 2H, C_5H_4N), 8.56 (d, *J* = 3.5, 2H, C_5H_4N), 8.04 (d, *J* = 8.0, 2H, C_5H_4N), 7.69(d, *J* = 8.2, 4H, C_6H_4), 7.45(dd, *J* = 7.9, 4.8, 2H, C_5H_4N), 7.35(d, *J* = 8.3, 4H, C_6H_4), 6.41 (d, J=4.7, 2H, CHO*H*), 4.86(d, J=4.9, 2H, C*H*OH). ^{11}B NMR: -10.57 (brs, 10B). ^{13}C NMR 150.0, 148.0, 142.5, 137.1, 135.6,

134.4, 128.1, 126.6 (C_5H_4N + C_6H_4), 124.52 (C_6H_4), 82.7 ($C_{cluster}$), 73.8 (*C*HOH). IR (ATR), υ [cm^{-1}] = 3101 (br, OH), 2596 (m, BH), (only selected peaks bands are reported).

9-iodo-1,2-bis{(4-pyridin-3-yl)phenyl)methanol}-1,7-dicarba-closo-dodecaborane (I-CB2). The synthesis procedure for **I-CB2** was adapted from the synthesis of **CB2**. 9-iodo-metacarborane (0.597 g, 2.21 mmol) was reacted with nBuLi (3.3 mL, 1.44 M in hexane, 4.48 mmol) at 0 °C (ice/water bath) in anhydrous THF under N_2 atmosphere for 30 min and 1 h at r.t. After cooling down the reaction mixture at -84 °C, 4-pyridine-3yl-benzadehyde (1.66 g, 9.7 mmol) in THF (1 mL) was added. This pale-yellow suspension was reacted 4 h. The reaction was quenched with NH4Cl (10mL) and, then the aqueous phase was extracted with THF. The organic phases were dried over MgSO4, filtered and evaporated under vacuum. The resulting yellow oil was sonicated in n-hexane and after ca. 1 h, and a light-yellow powder appeared. After removing the solvent, the yellow solid was dried under vacuum. ^{1}H NMR (400 MHz, DMSO-d^6): δ_H (ppm) = 8.91 (s, 2H, C_5H_4N), 8.58 (d, *J*= 3 Hz, 2H, C_5H_4N), 8.08 (d, *J*= 8 Hz, 2H, C_5H_4N), 7.72 (d, *J* = 8, 4H, C_6H_4), 7.45 (dd, *J* = 4, 2H, C_5H_4N), 7.37 (d, *J* = 8, 2H, C_6H_4), 7.37 (d, *J* = 4 Hz, 2H, O*H*), 4.93 (d, *J* = 4 Hz, 2H, C*H*OH); ^{11}B NMR: -10.57 (brs, 10B). IR (ATR; selected bands): v[cm^{-1}] = 3082 (OH); 2921, 2837 (CH); 2603 (BH); (only selected peaks bands are reported).

[Co_3(BTB)$_2$(CB2)(DMF)$_2$]·15DMF (CB2MOF-1**).** **CB2**MOF-1 was obtained by mixing $Co(NO_3)_2·6H_2O$ (22.8 mg, 0.078 mmol), **CB2** (10 mg, 0.019 mmol) and H_3BTB (17.5 mg, 0.039 mmol) in 2 mL of DMF/ethanol (1:1). This mixture was sonicated until all solids were uniformly dissolved, followed by heating at 100 °C for 48 h. Violet flake-like crystals of **CB2**MOF-1 were collected and washed with DMF (37.8 mg, 71.0%). IR (ATR; selected bands; cm^{-1}): ν 3350 (OH); 2925， 2851 (CH); 2588 (BH); 1660 (C=O from DMF); 1583, 1600 (C=O from carboxylate). Elemental analysis (%) calculated for $C_{80}H_{60}B_{10}Co_3N_2O_{14}·6(C_3H_7NO)$ 4(H_2O): C, 56.89; H, 5.36; N, 5.42; Found: C 55.9, H 5.11, N 5.4.

[Co_3(BTB)$_2$(I-CB2)(DMF)$_2$]·xDMF (I-CB2MOF-1**).** **I-CB2**MOF-1 was obtained by mixing $Co(NO_3)_2·6H_2O$ (22.8 mg, 0.078 mmol), **I-CB2** (12.1 mg, 0.039 mmol) and H_3BTB (17.5 mg, 0.039 mmol) in 2 mL of DMF/ethanol (1:1). This mixture was sonicated until all solids were uniformly dissolved, followed by heating at 90 ºC for 48 h. Violet flake-like crystals of **I-CB2**MOF-1 were collected and washed with DMF (14.1 mg, 24.1%). IR (ATR; selected bands; cm^{-1}): ν 3447 (OH); 3066， 2927, 2852 (CH); 2616 (BH); 1655 (C=O from DMF); 1586, 1548 (C=O from carboxylate). Elemental analysis (%) calculated for $IC_{80}H_{60}B_{10}Co_3N_2O_{14}·6(C_3H_7NO)$ $4(H_2O)$: C, 53.61; H, 5.05; N, 5.10; Found: C 53.9, H 4.7, N 5.1.

[Co_2(CHDA)$_2$(CB2)] (CB2MOF-2**).** $Co(NO_3)_2·6H_2O$ (22.8 mg, 0.078 mmol) was mixed with **CB2** (40 mg, 0.078 mmol) and H_2CHDA (6.8 mg, 0.039 mmol 1,4-Cyclohexanedicarboxylic acid) in 2 mL of DMF/ethanol (1:1). This mixture was sonicated until all solids were uniformly dissolved, followed by heating at 100 ºC for 48 h. Dark violet block crystals of **CB2**MOF-2 were collected and washed with DMF (2.9 mg, 7.7 %). IR (ATR; selected bands; cm^{-1}): ν 3377 (OH); 2925, 2857 (CH); 2595, 2570 (BH); 1662 (C=O from DMF); 1600(C=O from carboxylate). Elemental analysis (%) calculated for: $C_{21}H_{25}B_5CoNO_5·0.25(C_3H_7NO)$: C 51.9, H 5.4, N 3.5; Found: C 51.0, H 5.5, N 3.2.

[Co_2(BPDC)(CB2)$_2$(NO_3)$_2$]·DMF (CB2MOF-3**).** **CB2**MOF-3 was obtained by mixing $Co(NO_3)_2·6H_2O$ (11.4 mg, 0.039 mmol), **CB2** (20 mg, 0.039 mmol) and H_2BPDC (4.75 mg, 0.020 mmol Biphenyl-4,4′ -dicarboxylic acid) in 2 mL of DMF/ethanol (1:1). This mixture was sonicated until all solids were uniformly dissolved, followed by heating at 100 ºC for 48 h. Pink crystals of **CB2**MOF-3 were collected and washed with DMF (17.3 mg, 92.5 %). IR (ATR; selected bands; cm^{-1}): ν 3300 (OH); 3033, 2916 (CH); 2600 (BH); 1658 (C=O from DMF); 1600 (C=O from carboxylate). Elemental analysis (%) calculated for $C_{33}H_{34}B_{10}CoN_3O_7·0.5(C_3H_7NO)$: C 52.5, H 4.8, N 6.22; Found: C 52.0, H, 5.0, N 6.6.

[Co_2(ADB)(CB2)$_2$(NO_3)$_2$]·DMF (CB2MOF-4**).** **CB2**MOF-4 was obtained by mixing $Co(NO_3)_2·6H_2O$ (11.4 mg, 0.039 mmol), **CB2** (20 mg, 0.039 mmol) and H_2ADB (5.3 mg, 0.020 mmol 4,4'-Azodibenzoic acid) in 2 mL of DMF/ethanol (1:1). This mixture was sonicated until all solids were uniformly dissolved, followed by heating at 100 ºC for 48 h. Orange block crystals of **CB2**MOF-4 were collected and washed with DMF (7.7 mg, 40.5 %). IR (ATR; selected bands; cm^{-1}): ν 3350 (OH); 2936 (CH); 2619, 2592 (BH); 1660 (C=O from DMF); 1617, 1600 (C=O from carboxylate). Elemental analysis (%) calculated for $C_{33}H_{34}B_{10}CoN_4O_7·0.5(C_3H_7NO)$: C 51.6, H 4.71, N 7.86; Found: C 49.0, H 4.6, N 7.9.

Synthesis of CB2MOF-1´ and I-CB2MOF-1´. Immersing crystals of complex **CB2**MOF-1 in $CHCl_3$ at room temperature for overnight, the red crystals will turn to violet crystals of complex **CB2**MOF-1´. **I-CB2**MOF-1´ was prepared in the same method.

Synthesis of CB2MOF-1 and I-CB2MOF-1 from CB2MOF-1´ and I-CB2MOF-1´. Immersing crystals of complex **CB2**MOF-1´ in DMF at room temperature for 30 min, the violet crystals will turn into back red crystals of complex **CB2**MOF-1. **I-CB2**MOF-1 was prepared in the same method.

Crystallography. Measured crystals were prepared under inert conditions immersed in perfluoropolyether or paratone as protecting oil for manipulation. Suitable crystals were mounted on MiTeGen Micromounts™, and used for data collection. Crystallographic data for **CB2**MOF-2**,** **CB2**MOF-3 and **CB2**MOF-4 were collected at 100K at XALOC beamline at ALBA synchrotron[56] (λ = 0.82652 Å) and for **CB2**MOF-1 using a Bruker D8 Venture diffractometer. Data were processed with APEX2[57] program and corrected for absorption using SADABS[58]. The structures were solved by direct methods and subsequently refined by correction of F^2 against all reflections[59]. All non-hydrogen atoms were refined with anisotropic thermal parameters by full-matrix least-squares calculations on F^2.[60] All hydrogen atoms were located in difference Fourier maps and included as fixed contributions riding on attached atoms with isotropic

thermal displacement parameter 1.2 (C-H, B-H) or 1.5 (O-H) times those of the respective atom. In **CB2**MOF-2**, CB2**MOF-3 and **CB2**MOF-4, hydroxyl groups of the ligand are disordered over two positions in a ratio close to 0.50:0.50 (0.49:0.51 for **CB2**MOF-3 and 0.46:0.54 for **CB2**MOF-4) excepting in **CB2**MOF-1 (0.84:0.16). **CB2**MOF-3 and **CB2**MOF-4 were treated as a two component non-merohedral twin, the exact twin matrix identified by the integration program was found to be 1 0 0 0 -1 0 0 0 -1 for **CB2**MOF-3 and -1 0 0 0 -1 0 0 0 1 for **CB2**MOF-4. The structures were solved using direct methods with only the non-overlapping reflections of component 1. The structure was refined using the HKLF 5 routine with all reflections of component **CB2**MOF-2 (including the overlapping ones), resulting in BASF value of 0.47 (2) and 0.33 (3). A solvent mask was calculated for **CB2**MOF-1 and 2301.0 electrons were found in a volume of 6999.0 $Å^3$ in one void. This is consistent with the presence of 15 disordered molecules of DMF per formula unit.

Table 5-2. Crystal and Structure Refinement data for **CB2**MOF-1 to **CB2**MOF-4**.**

Compound	**CB2**MOF-1	**CB2**MOF-2	**CB2**MOF-3	**CB2**MOF-4
Empirical formula	$C_{80}H_{60}B_{10}Co_3N_2O_{14}$ ·15(C_3H_7NO)	$C_{21}H_{25}B_5CoNO_5$	$C_{36}H_{41}B_{10}$ CoN_4O_8	$C_{36}H_{41}B_{10}CoN_5O_8$
Formula weight	2800.81	484.40	824.76	838.77
Crystal system	Monoclinic	Monoclinic	Monoclinic	Monoclinic
Space group	$P2_1/n$	C2/c	$P2_1/c$	$P2_1/c$
a (Å)	17.2184(10)	15.2931(5)	14.7414(5)	16.4751(14)
b (Å)	30.7175(15)	15.4473(5)	16.3439(5)	15.2064(13)
c (Å)	25.6063(15)	20.9877(6)	16.5915(5)	16.4768(15)
α (deg)	90	90	90	90
β (deg)	92.724(4)	104.589(1)	93.520(1)	91.361(3)
γ (deg)	90	90	90	90
V ($Å^3$)	13528.0(13)	4798.2(3)	3989.9(2)	4126.7(6)
Z	4	8	4	4
F (000)	5908	2000.0	1704.0	1732.0
Max./min. transmission	0.7528/0.2512	0.018/ 0.003	0.011/0.001	0.746/0.525
Final R indices [I > 2σ(I)]	R1 = 0.1311 wR2 = 0.3507	R1 = 0.0740 wR2 = 0.2026	R1= 0.0650 wR2 = 0.1969	R1=0.0800 wR2 = 0.2365
R indices (all data)	R1 = 0.1632, wR2 = 0.3795	R1 = 0.0741, wR2 = 0.2026	R1 = 0.0666, wR2 = 0.1969	R1 = 0.0815, wR2 = 0.2365
Largest diff. peak and hole	1.481 and -1.231 $e.Å^{-3}$	1.282 and -1.626 $e.Å^{-3}$	1.489 and -0.557 $e.Å^{-3}$	0.929 and -0.421 $e.Å^{-3}$

5.5 Reference

[1] H. Li, M. Eddaoudi, M. O'Keeffe, O. M. Yaghi, *Nature* **1999**, *402*, 276.

[2] S. Kitagawa, R. Kitaura, S. Noro, *Angew. Chemie Int. Ed.* **2004**, *43*, 2334.

[3] S. L. James, *Chem. Soc. Rev.* **2003**, *32*, 276.

[4] Z.-J. Lin, J. Lü, M. Hong, R. Cao, *Chem. Soc. Rev.* **2014**, *43*, 5867.

[5] V. Colombo, C. Montoro, A. Maspero, G. Palmisano, N. Masciocchi, S. Galli, E. Barea, J. A. R. Navarro, *J. Am. Chem. Soc.* **2012**, *134*, 12830.

[6] C. R. Murdock, B. C. Hughes, Z. Lu, D. M. Jenkins, *Coord. Chem. Rev.* **2014**, *258–259*, 119.
[7] A. Schneemann, V. Bon, I. Schwedler, I. Senkovska, S. Kaskel, R. A. Fischer, *Chem. Soc. Rev.* **2014**, *43*, 6062.
[8] G. Férey, *Dalt. Trans.* **2016**, *45*, 4073.
[9] G. Férey, *New J. Chem.* **2016**, *40*, 3950
[10] R. E. Morris, L. Brammer, *Chem. Soc. Rev.* **2017**, *46*, 5444.
[11] G. Férey, *Chem. Soc. Rev.* **2008**, *37*, 191.
[12] A. J. Fletcher, K. M. Thomas, M. J. Rosseinsky, *J. Solid State Chem.* **2005**, *178*, 2491.
[13] N. A. Khan, Z. Hasan, S. H. Jhung, *J. Hazard. Mater.* **2013**, *244–245*, 444.
[14] R. J. Kuppler, D. J. Timmons, Q.-R. Fang, J.-R. Li, T. A. Makal, M. D. Young, D. Yuan, D. Zhao, W. Zhuang, H.-C. Zhou, *Coord. Chem. Rev.* **2009**, *253*, 3042.
[15] J.-R. Li, R. J. Kuppler, H.-C. Zhou, *Chem. Soc. Rev.* **2009**, *38*, 1477.
[16] K. Uemura, R. Matsuda, S. Kitagawa, *J. Solid State Chem.* **2005**, *178*, 2420.
[17] S. Horike, S. Shimomura, S. Kitagawa, *Nat. Chem.* **2009**, *1*, 695.
[18] B. Manna, A. V. Desai, S. K. Ghosh, *Dalt. Trans.* **2016**, *45*, 4060.
[19] C. Martí-Gastaldo, D. Antypov, J. E. Warren, M. E. Briggs, P. A. Chater, P. V. Wiper, G. J. Miller, Y. Z. Khimyak, G. R. Darling, N. G. Berry, M. J. Rosseinsky, *Nat. Chem.* **2014**, *6*, 343.
[20] F. Tan, A. López-Periago, M. E. Light, J. Cirera, E. Ruiz, A. Borrás, F. Teixidor, C. Viñas, C. Domingo, J. G. Planas, *Adv. Mater.* **2018**, *30*, 1800726.
[21] J. Poater, M. Solà, C. Viñas, F. Teixidor, *Chem. A Eur. J.* **2016**, *22*, 7437.
[22] J. Poater, M. Solà, C. Viñas, F. Teixidor, *Angew. Chemie Int. Ed.* **2014**, *53*, 12191.
[23] R. N. Grimes, *Carboranes* **2016**.
[24] M. Scholz, E. Hey-Hawkins, *Chem. Rev.* **2011**, *111*, 7035.
[25] C. Teixidor, F.; Viñas, *Thieme: Stuttgart* **2005**, *6*, 1325.
[26] F. Teixidor, G. Barberà, A. Vaca, R. Kivekäs, R. Sillanpää, J. Oliva, C. Viñas, *J. Am. Chem. Soc.* **2005**, *127*, 10158.
[27] F. Di Salvo, B. Camargo, Y. García, F. Teixidor, C. Viñas, J. G. Planas, M. E. Light, M. B. Hursthouse, *CrystEngComm* **2011**, *13*, 5788.
[28] J. G. Planas, C. Viñas, F. Teixidor, A. Comas-Vives, G. Ujaque, A. Lledós, M. E. Light, M. B. Hursthouse, *J. Am. Chem. Soc.* **2005**, *127*, 15976.
[29] M. A. Fox, A. K. Hughes, *Coord. Chem. Rev.* **2004**, *248*, 457.
[30] M. Chaari, Z. Kelemen, J. G. Planas, F. Teixidor, D. Choquesillo-Lazarte, A. Ben Salah, C. Viñas, R. Núñez, *J. Mater. Chem. C* **2018**, *6*, 11336.
[31] X. Zhang, H. Dai, H. Yan, W. Zou, D. Cremer, *J. Am. Chem. Soc.* **2016**, *138*, 4334.
[32] V. Terrasson, Y. García, P. Farràs, F. Teixidor, C. Viñas, J. G. Planas, D. Prim, M. E. Light, M. B. Hursthouse, *CrystEngComm* **2010**, *12*, 4109.
[33] B. J. Eleazer, D. V. Peryshkov, *Comments Inorg. Chem.* **2018**, *38*, 79.
[34] L. E. Riley, A. P. Y. Chan, J. Taylor, W. Y. Man, D. Ellis, G. M. Rosair, A. J. Welch, I. B. Sivaev, *Dalt. Trans.* **2016**, *45*, 1127.
[35] L. Cunha-Silva, M. J. Carr, J. D. Kennedy, M. J. Hardie, *Cryst. Growth Des.* **2013**, *13*, 3162.

[36] F. Teixidor, M. A. Flores, C. Viñas, R. Sillanpää, R. Kivekäs, *J. Am. Chem. Soc.* **2000**, *122*, 1963.

[37] P. E. Behnken, T. B. Marder, R. T. Baker, C. B. Knobler, M. R. Thompson, M. F. Hawthorne, *J. Am. Chem. Soc.* **1985**, *107*, 932.

[38] J. A. Long, T. B. Marder, P. E. Behnken, M. F. Hawthorne, *J. Am. Chem. Soc.* **1984**, *106*, 2979.

[39] C. B. Knobler, T. B. Marder, E. A. Mizusawa, R. G. Teller, J. A. Long, P. E. Behnken, M. F. Hawthorne, *J. Am. Chem. Soc.* **1984**, *106*, 2990.

[40] F. Teixidor, M. A. Flores, C. Viñas, R. Kivekäs, R. Sillanpää, *Angew. Chemie Int. Ed. English* **1996**, *35*, 2251.

[41] Y. Zhang, L. Yang, L. Wang, S. Duttwyler, H. Xing, *Angew. Chemie Int. Ed.* **2019**, *58*, 8145.

[42] M. Y. Tsang, C. Viñas, F. Teixidor, D. Choquesillo-Lazarte, J. Giner Planas, *Eur. J. Inorg. Chem.* **2017**, *2017*, 4589.

[43] M. Y. Tsang, S. Rodríguez-Hermida, K. C. Stylianou, F. Tan, D. Negi, F. Teixidor, C. Viñas, D. Choquesillo-Lazarte, C. Verdugo-Escamilla, M. Guerrero, J. Sort, J. Juanhuix, D. Maspoch, J. Giner Planas, *Cryst. Growth Des.* **2017**, *17*, 846.

[44] S. Rodríguez-Hermida, M. Y. Tsang, C. Vignatti, K. C. Stylianou, V. Guillerm, J. Pérez-Carvajal, F. Teixidor, C. Viñas, D. Choquesillo-Lazarte, C. Verdugo-Escamilla, I. Peral, J. Juanhuix, A. Verdaguer, I. Imaz, D. Maspoch, J. Giner Planas, *Angew. Chemie Int. Ed.* **2016**, *55*, 16049.

[45] J. Planas, F. Teixidor, C. Viñas, *Crystals* **2016**, *6*, 50.

[46] M. Y. Tsang, C. Viñas, F. Teixidor, J. G. Planas, N. Conde, R. SanMartin, M. T. Herrero, E. Domínguez, A. Lledós, P. Vidossich, D. Choquesillo-Lazarte, *Inorg. Chem.* **2014**, *53*, 9284.

[47] F. Di Salvo, C. Paterakis, M. Y. Tsang, Y. García, C. Viñas, F. Teixidor, J. Giner Planas, M. E. Light, M. B. Hursthouse, D. Choquesillo-Lazarte, *Cryst. Growth Des.* **2013**, *13*, 1473.

[48] F. Di Salvo, F. Teixidor, C. Viñas, J. G. Planas, M. E. Light, M. B. Hursthouse, N. Aliaga-Alcalde, *Cryst. Growth Des.* **2012**, *12*, 5720.

[49] N. Benbellat, K. S. Gavrilenko, Y. Le Gal, O. Cador, S. Golhen, A. Gouasmia, J.-M. Fabre, L. Ouahab, *Inorg. Chem.* **2006**, *45*, 10440.

[50] P. Power, *J. Am. Chem. Soc.* **2007**, *129*, 8396.

[51] S. Furukawa, K. Hirai, K. Nakagawa, Y. Takashima, R. Matsuda, T. Tsuruoka, M. Kondo, R. Haruki, D. Tanaka, H. Sakamoto, S. Shimomura, O. Sakata, S. Kitagawa, *Angew. Chemie Int. Ed.* **2009**, *48*, 1766.

[52] T. Wang, L. Qin, C. Zhang, H. Zheng, *RSC Adv.* **2015**, *5*, 64514.

[53] K. Sumida, D. L. Rogow, J. A. Mason, T. M. McDonald, E. D. Bloch, Z. R. Herm, T.-H. Bae, J. R. Long, *Chem. Rev.* **2012**, *112*, 724.

[54] Y.-S. Bae, O. K. Farha, J. T. Hupp, R. Q. Snurr, *J. Mater. Chem.* **2009**, *19*, 2131.

[55] M. A. Fox, Cosahedral Carborane Derivatives, Durham University, **1991**.

[56] J. Juanhuix, F. Gil-Ortiz, G. Cuní, C. Colldelram, J. Nicolás, J. Lidón, E. Boter, C. Ruget, S. Ferrer, J. Benach, *J. Synchrotron Radiat.* **2014**, *21*, 679.

[57] Bruker, A. S., V2012.2; Bruker AXS Inc.: Madison, WI, 2012.

[58] G. M. Sheldrick, *SADABS, Progr. Empir. Absorpt. Correct. Area Detect. Data* **2003**.
[59] G. M. Sheldrick, *Acta Crystallogr. Sect. A Found. Crystallogr.* **2008**, *64*, 112.
[60] G. M. Sheldrick, *Acta Crystallogr. Sect. C Struct. Chem.* **2015**, *71*, 3.

Chapter 6

Ultrathin 2D Carborane capped Metal-Organic Framework Nanosheets

Chapter 6 Ultrathin 2D Carborane capped Metal-Organic Framework Nanosheets

6.1 Introduction

The rational design and construction of functional layered systems on surfaces, whose structures are finely controlled at the nanoscale represent a key objective of modern materials science and is a key challenge for creating new nanodevices[1]. In the past 20 years, metal organic frameworks (MOFs) and coordination polymers (CPs) have attracted considerable attention due to their unique properties. Those include gas sorption, molecular separation, sensing or catalysis[2–6]. In order to employ MOFs or related coordination materials in nanodevices, their fabrication in the film state have been actively pursued. There are two general methods to obtain nanosheets of MOFs: top-down and bottom-up syntheses[7,8]. In the latter, direct growth on substrates or freestanding synthesis in solution is included. Materials generated by bottom-up methods benefit from their non-limited lateral dimensions, since they are not based on bulk precursors but their yields are very low. One example is the synthesis of $Cu_2(bdc)_2$ in an intermediate region between the linker and metal ion solutions, resulting in sheets with lateral dimensions of 0.5-4 μm and thickness of 5-25 nm[2]. In the top-down approach, ultrasound, shaking or ball milling are the most used methods to generate nanosheets by *delamination* from bulk materials and therefore provide those in higher yields[9–13]. In this way, e.g, Zn(bdc) (MOF-2) was successfully exfoliated to obtain nano- or even mono-layers with a thickness down to 1 nm[14]. However, the harsh conditions employed in the top-down methods cause uncontrolled structural deterioration, fragmentation and morphological damage, due to the low bulk and shear moduli of the MOFs.[15]. For these methods, MOFs or CPs consisting on 2D neutral layers are commonly used since more or less weak forces need to be applied to overcome the cohesive interactions between the layers in the bulk 2D material. Those interlayer interactions are commonly hydrogen bonding or π-π interaction holding the neutral layers together in the crystal. The challenge is therefore to delaminate the 2D

layers of the bulk material with the minimal force to avoid deterioration of the layers on delamination.

We have previously synthesized bulk 2D coordination polymers, where each layer is capped or decorated by icosahedral carborane clusters (Chapter 3 to chapter 5). Due to the presence of hydridic hydrogens from the carborane clusters, the interlayers' interactions are dominated by very weak dihydrogen bonding contacts in the bulk crystals. The latter might facilitate the delamination by top-down methods, while maintaining large lateral dimension nanosheets. We demonstrate that top-down delamination of our carboranes based 2D materials effectively achieve ultrathin nanometer scale nanosheets and lateral dimensions up to micrometers.

6.2 Results and discussion

6.2.1 Synthesis of high aspect ratio CB1MON-1 nanosheets

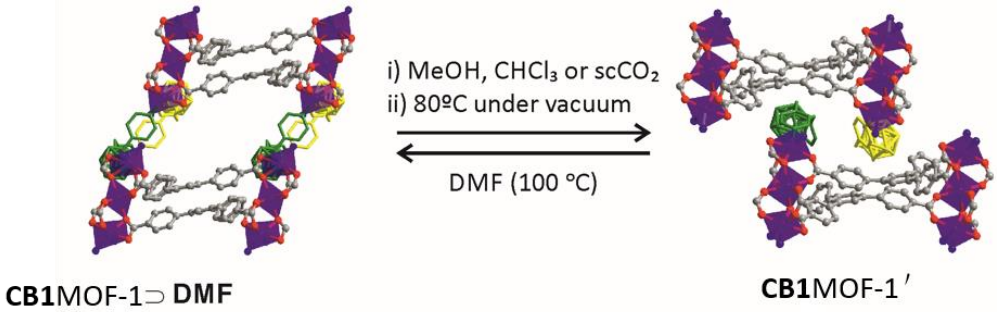

Figure 6-1. Conditions for the bulk reversible **CB1**MOF-1 to **CB1**MOF-1´ transformation.

We have previously described the synthesis of a 2D nonporous coordination polymer $[Co_3(BTB)_2(CB1)_2]$·solv (**CB1**MOF-1´), that can be reversibly transform into a porous 3D structure (**CB1**MOF-1) (Figure 6-1). **CB1**MOF-1´ was initially synthesized by a solvent mediated phase transition from a 3D $[Co_3(BTB)_2(CB1)_2]$·DMF (**CB1**MOF-1 ⊃ **DMF**) structure. Such transformation was shown to occur by immersing **CB1**MOF-1 ⊃ **DMF** in MeOH, $CHCl_3$ or $scCO_2$ for 2-5 days at room temperature and further heating under vacuum. We have now optimized the synthesis of **CB1**MOF-1´ by sonicating crystals of **CB1**MOF-1 in CH_3CN for 30 minutes. Complete transformation of **CB1**MOF-1 into **CB1**MOF-1´ was proved by PXRD (Figure S6-1). Figure 6-2a and

6-2b show scanning electron microscopy (SEM) images of the synthesized bulk material in MeOH (after several days) and acetonitrile (30 minutes). The images show irregular crystals as previously reported for **CB1**MOF-1´. Interestingly, simple shaking of the crystals in methanol induces partial exfoliation of the crystals (Figure 6-2c) and suggests that intermolecular contacts between layers in **CB1**MOF-1´ are quite weak. Thus, we decided to investigate the delamination of our compound by sonication and using either MeOH or CH_3CN as solvents.

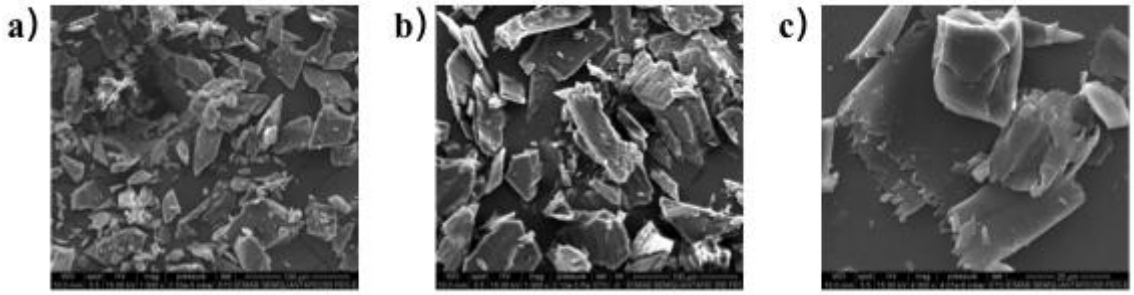

Figure 6-2. SEM pictures of: (a) **CB1**MOF-1´ synthesized from **CB1**MOF-1 by immersion in MeOH for 5 days; (b) **CB1**MOF-1´ synthesized from **CB1**MOF-1 by sonication in acetonitrile for 30 minutes and (c) crystals obtained after sonicating **CB1**MOF-1´ in MeOH for 1 min.

Comparable results on **CB1**MON-1 were obtained by either sonication (30 minutes) or ultrasonication (1min) in MeOH or acetonitrile, followed by centrifugation for 40 minutes. The UV-visible absorption of the methanol suspension of **CB1**MON-1 displayed adsorption spectra in the range 250-325 nm (λ_{max} = 269 nm; black line in figure 6-3), consistent with the presence of exfoliated 2D nanosheets[16,17]. The adsorption turns to be red shifted compared to that observed for the carborane ligand (λ_{max} = 259 nm; red line in figure 6-3) in methanol while blue shifted comparing with the adsorption observed for H_3BTB (λ_{max} = 275 nm). The supernatant suspensions also showed the Tyndall light scattering typical of colloidal suspensions of nanosheets (Inset of figure 6-3). The PXRD patterns of the restacked powder fits the reflections of **CB1**MOF-1´ indicating the sonication transformed the **CB1**MOF-1 into **CB1**MOF-1´, which is not affected by the (ultra)sonication in either solvent (Figure S6-1). The Tyndall effect, UV-visible spectrum in methanol or ethanol suspension (Figure S6-2)

of the suspension and PXRD results on the restacked powder suggest the formation of **CB1**MOF-1´ nanosheets *via* top-down delamination.

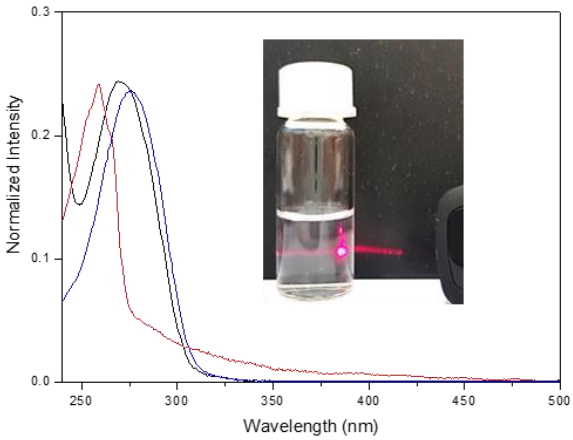

Figure 6-3. UV-vis adsorption of H_3BTB (blue line), **CB1**(red line) and **CB1**MON-1 suspension (black) in MeOH. Inset: Tyndall effect for the colloidal suspension of **CB1**MON-1.

In order to further verify the formation of nanosheets, the morphology of the delaminated **CB1**MON-1 nanosheets was examined by SEM, transmission electron microscopy (TEM) and atomic-force microscopy (AFM). Samples suitable for microscopy were prepared by dropping 1 to 2 drops of the as-prepared suspension onto an appropriate substrate. The SEM and TEM measurements revealed that the lateral dimension of the flat-layered **CB1**MON-1 nanosheets varied from 100 nm to micrometers (Figure 6-4). We observed that these nanostructures were extremely sensitive to the electron beam, and hence, it was challenging to record their energy-dispersive X-ray (EDX) spectra for boron. A similar challenge was reported earlier for other studies of boron nanoparticles with dimensions less than 45 nm[18,19]. To obtain insight into the chemical composition of these nanostructures, we performed boron electron energy-loss spectroscopy (EELS) and TEM/EDX for other elements. The representative TEM/EDX and boron EELS results of a small piece of nanosheet are shown in figure 6-4c and 6-4d, respectively. TEM/EDX analysis shows the presence of B, C, O, and Co. The boron EELS spectrum shows the presence of boron moiety from the typical boron K-edges at about 200 eV[20].

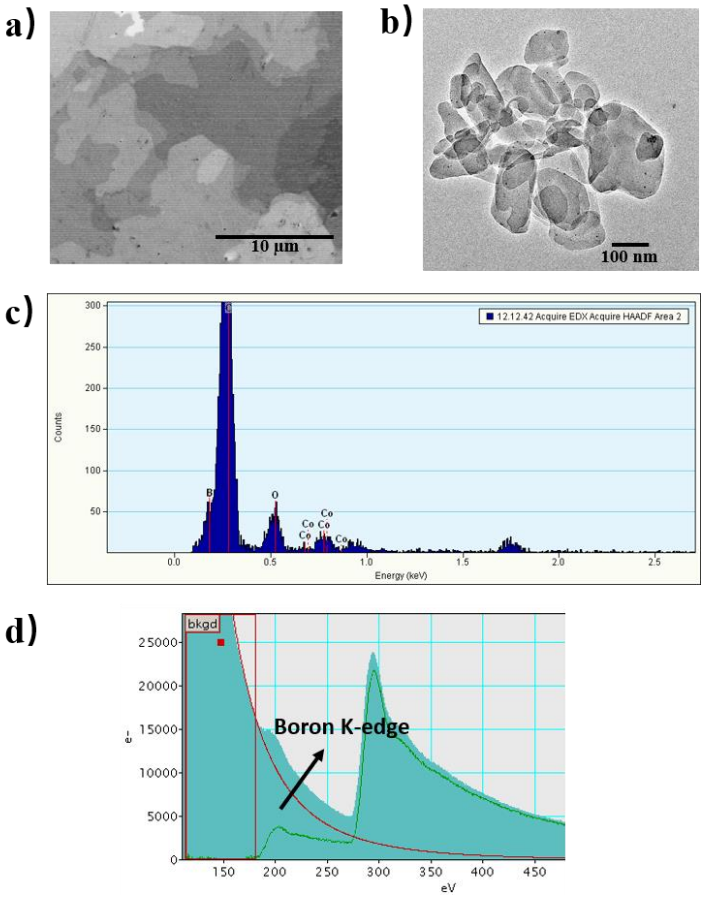

Figure 6-4. SEM (a) and TEM (b) images of **CB1**MON-1 synthesized from acetonitrile. TEM/EDX (c) and (d) boron EELS spectrum.

The tapping-mode AFM (atomic force microscopy) images of the sample deposited on a silicon substrate also revealed flat 2D objects as shown in figure 6-5. The thickness between the flaky object and the substrate surface or between two neighboring overlapped flaky objects was normally ca. 3.5 nm with lateral dimensions varying from 200 nm to 5 µm exhibiting the aspect-ratio ranges from 50 to 1400. According to the calculated thickness from crystal structure[21] of **CB1**MOF-1´ (Figure 6-6), the height profile displayed the obtained **CB1**MON-1 from different solvents are bi-layer nanosheets. Figure 6-5c shows of the nanosheets with an average thickness of approximately 2 nm, corresponding to one **CB1**MON-1 layer.

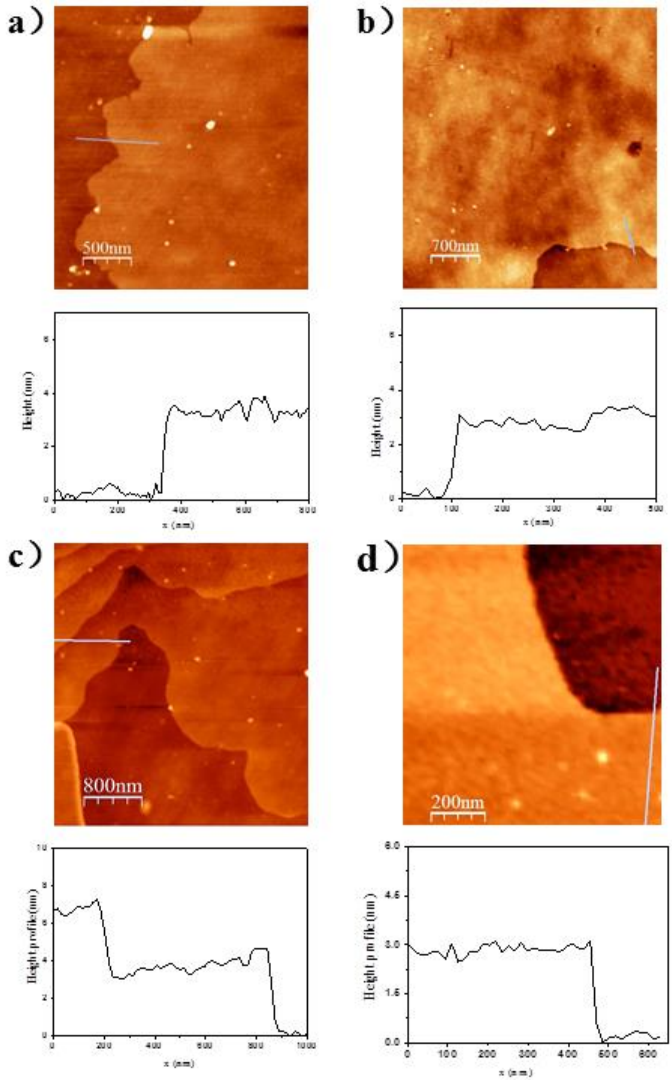

Figure 6-5. AFM images of exfoliated nanosheets synthesized from different solvents (a) CH_3CN, (b) MeOH (c) $CHCl_3$ and (d) EtOH; the corresponding height profile.

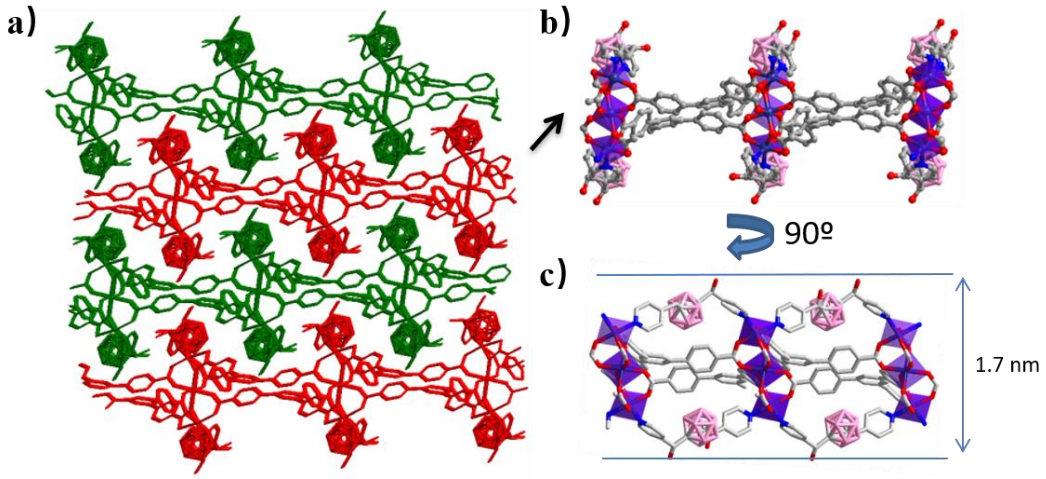

Figure 6-6. (a) 3D structure of **CB1**MON-1´, showing the stacking of 2D layers in the bulk structure (adjacent layers are colored differently for clarity). (b) and (c) Two perpendicular views of a single layer, indicating the thickness in the solid structure[21].

Two-dimensional synchrotron-based grazing-incidence wide-angle X-ray scattering (2D-GIWAXS) is an unique technique allowing us to acquire characteristics of 2D materials in molecular scales[22] which was adopted to investigate molecular ordering and possible orientation of the **CB1**MON-1 nanosheets in the substrates. Figure 6-7a shows a GIWAXS image of drop casted **CB1**MON-1 on silicon wafer. q_y and q_z are the scattering vectors representing the in-plane and out-of-plane scattering components, respectively. Four evident anisotropic scattering features are observable: moderate scattering at q_z < 6 nm^{-1}, and weak scattering at q_z = 8.8 nm^{-1}. In particular, the anisotropy of the small q scattering is quite significant. Figure 6-7b presents the out of plane q_z vertical cut, extracted from Figure 6-7a. Moderate scattering bellow 6 nm^{-1} is only observed in q_z, which exhibits peaks at 2.7, 3.5, 4.0 and 5.3 nm^{-1}. The latter clearly indicates large-scale vertical stacking, consistent with a laminated structure of **CB1**MON-1 nanosheets on the substrates, as observed in the AFM images (Figure 6-5). These findings clearly indicate that most of **CB1**MON-1 nanosheets were oriented face-on in the film.

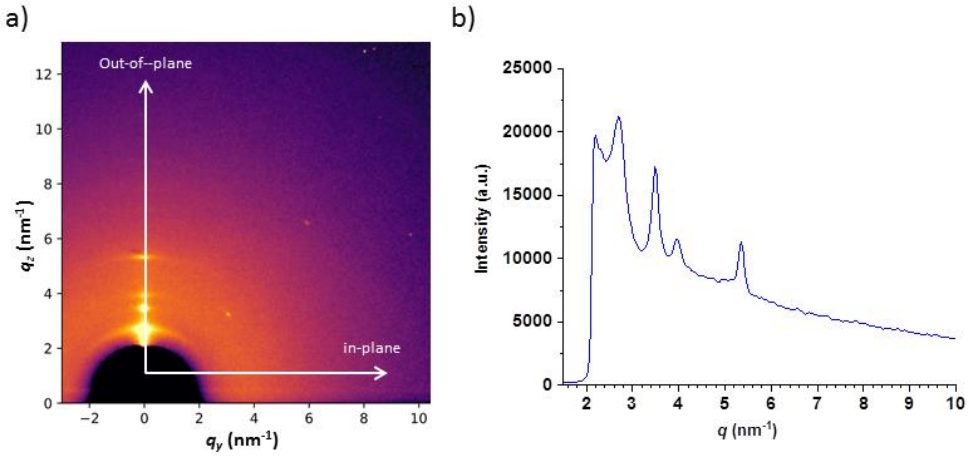

Figure 6-7. (a) GIWAXS image of **CB1**MON-1 nanosheets on a silicon wafer. (b) Scattering profile of q_z (out of plane).

6.2.2 Exfoliation of layered CB2MON-1 and I-CB2MON-1 nanosheets

The successful delamination of the 2D material **CB1**MOF-1´ prompted us to explore the exfoliation of the isostructural 2D frameworks **CB2**MOF-1 and **I-CB2**MOF-1, decorated with the longer carborane ligands **CB2** and **I-CB2**, respectively (See Chapter 5). Following the optimized exfoliation protocol described above, we sonicated **CB2**MOF-1 and **I-CB2**MOF-1 in the solvents. Ethanol provided the best results in this case. The Tyndall effect, UV-visible spectrum of the suspensions and PXRD results on the restacked powder suggested also the formation of **CB2**MON-1 and **I-CB2**MON-1 nanosheets *via* top-down delamination (Figure 6-8, Figure S6-3 and Figure S6-4). The UV-vis spectra for **CB2**MOF-1 and **I-CB2**MOF-1 show new adsorption bands at 278 and 279 nm, respectively. SEM and TEM measurements revealed the formation of ultrathin layers in the EtOH suspensions of **CB2**MOF-1 after sonication and restacked thin crystals at the bottom of the vials (Figure 6-9).

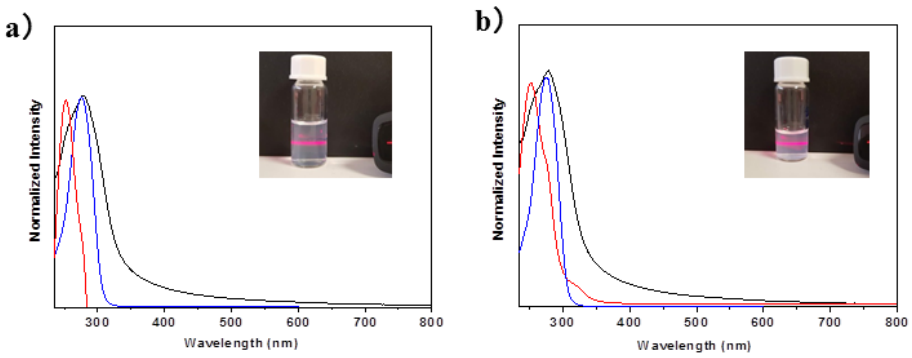

Figure 6-8. (a) UV-vis adsorption of H_3BTB (blue line), **CB2** (red line) and **CB2**MON-1 suspension (black) in EtOH. Inset: Tyndall effect for the colloidal ethanol suspension of **CB2**MON-1. (b) UV-vis adsorption of H3BTB (blue line), **I-CB2** (red line) and **I-CB2**MON-1 suspension (black) in EtOH. Inset: Tyndall effect for the colloidal ethanol suspension of **I-CB2**MON-1.

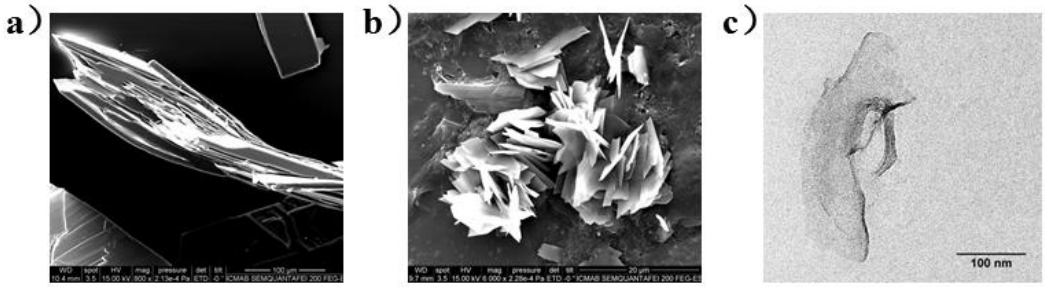

Figure 6-9. SEM images of: (a) as synthesized **CB2**MOF-1 from EtOH; (b) restacked crystals of **CB2**MON-1 after sonication in EtOH in acetonitrile. (c) TEM image of **CB2**MON-1 synthesized from EtOH.

The tapping-mode AFM images of the samples for **CB2**MON-1 and **I-CB2**MON-1 deposited on a silicon substrate also revealed flat 2D objects as shown in Figure 6-10. The thickness of the flaky objects and the substrate surface was approximately 4 and 4.5 nm for **CB2**MON-1 and **I-CB2**MON-1, respectively, with lateral dimensions varying from 200 nm to 2 μm— that is aspect-ratio varying from 50 to 500 (Figure 6-10). The resulting thickness of **CB2**MON-1 is slightly thicker than a single layer of **CB2**MOF-1 from the single crystal data (Figure 6-11). As expected, the monolayer thickness of **I-CB2**MON-1 is slightly thicker (~ 0.5 nm) than that for the non iodo derivative. Considering the Van der Waals radius of iodine atoms is 198 pm[23], the difference of thickness between these two isostructural nanosheets is reasonable.

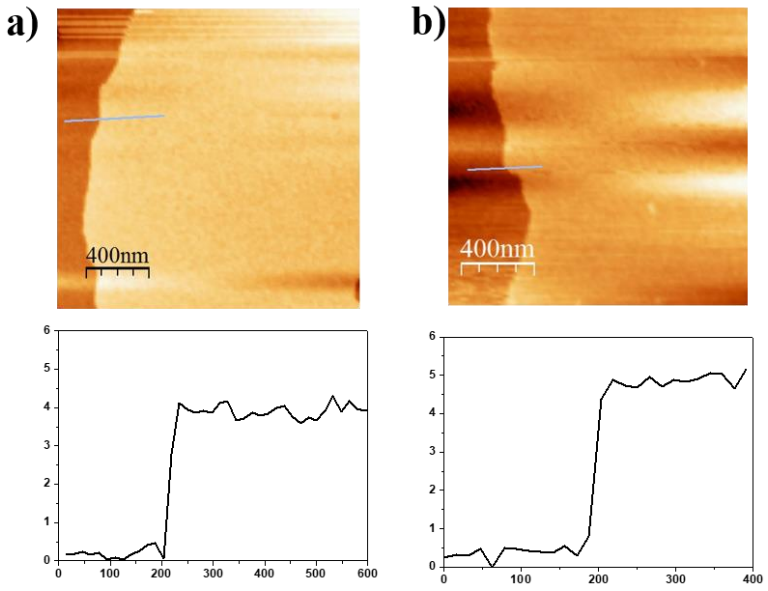

Figure 6-10. AFM images of EtOH exfoliated nanosheets for (a) **CB2**MON-1, (b) **I-CB2**MON-1 and corresponding height profile.

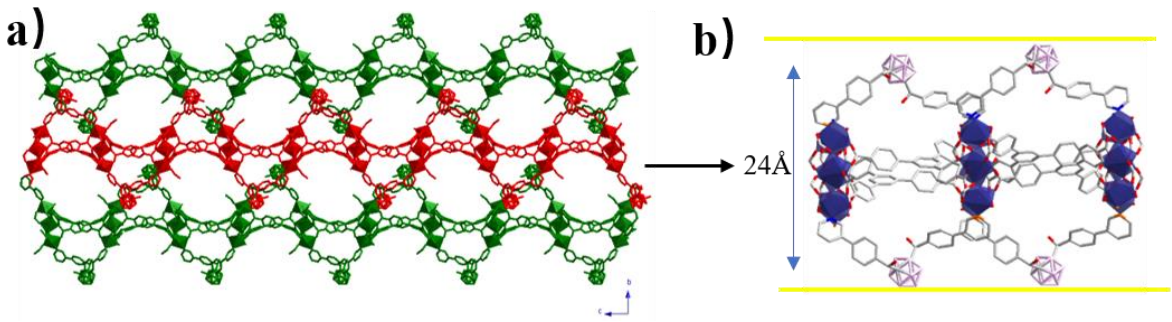

Figure 6-11. (a) 3D structure of **CB2**MON-1, showing the stacking of 2D layers in the bulk structure (adjacent layers are colored differently for clarity). (b) A view of a single layer, indicating the thickness in the solid structure.

2D-GIWAXS image of drop casted **CB2**MON-1 film on silicon wafer also shows a clear anisotropy of the small q scattering (Figure 6-12). Three evident anisotropic scattering features are observable: moderate scattering at q_z < 6 nm^{-1}, and weak scattering at q_z = 8.7 nm^{-1}. Figure 6-12b presents the scattering components q_z extracted from Figure 6-12a. As observed for the analogue **CB1**MON-1 (Figure 6-7), **CB2**MON-1 nanosheets only show moderate scattering bellow 6 nm^{-1} in q_z, which exhibits peaks at 2.2, 3.6, 5.3 and 8.7 nm^{-1}. These data clearly indicate large-scale vertical stacking, consistent with a laminated structure of **CB2**MON-1 nanosheets on the substrates, as observed in the AFM images (Figure 6-10). These findings again identified that most of **CB2**MON-1 nanosheets were oriented face-on in the film.

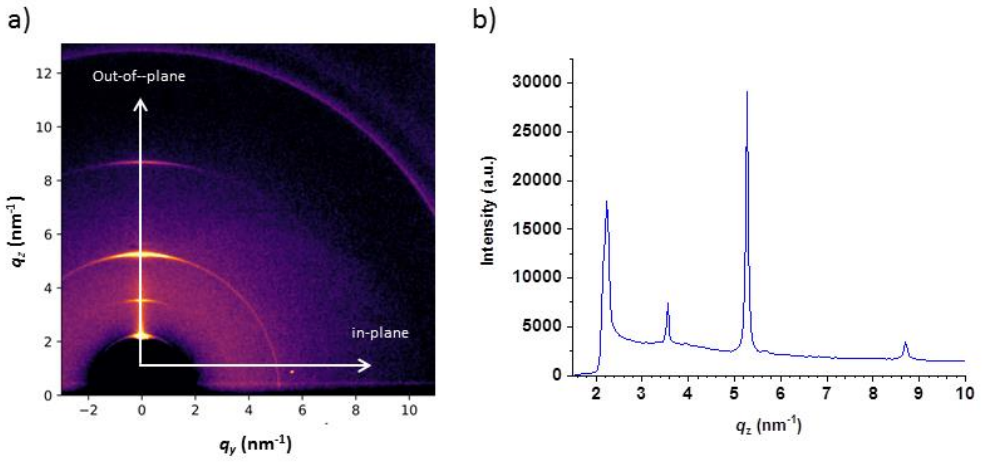

Figure 6-12. (a) GIWAXS image of **CB2**MON-1 nanosheets on silicon wafer. (b) Scattering profile of q_z (out of plane).

It is remarkable that large aspect ratio nanosheets are generated in all the above cases by sonicating the bulk structures in organic solvents for a short time. The large aspect ratio of the sheets suggests that the forces maintaining the sheets together in the 3D structure are rather weak. In deep, the intermolecular interactions between layers are dominated by dihydrogen bond contacts. The later can certainly explain the easiness for exfoliation the layers and without extensive breaking off the sheets.

6.3 Conclusions

In summary, we have demonstrated that a novel family of nano-scale crystalline films can be easily prepared by tow-down delamination of bulk 2D coordination polymers, decorated by ligands incorporating the icosahedral *meta*-carborane clusters. The formation of the metal organic nanosheets (MONs) have been evidenced by UV-vis, the phenomena of Tyndall light scattering, SEM, TEM, AFM and GIWAX. The data shows the formation of ultrathin nanosheets face-on oriented in silicon substrates and of large aspect/ratio. The latter seems to be due to the weak nature of the intermolecular interactions (mainly dihydrogen bonding) between layers in the bulk 2D material.

6.4 Experimental section

Materials: All chemicals were of reagent-grade quality. They were purchased from commercial sources and used as received. **CB1**MOF-1 ⊃DMF was prepared as previously reported.

6.4.1 Preparation of nanosheets

CB1MON-1 nanosheets were synthesized in glass vial. A 10-15mg **CB1**MOF-1 was immersed in 5mL solvents. Then sonicated the solution 30min. Then the residue was removed by centrifugation with 6000r/min for 40 min. Finally take out the decant carefully and leave it under static conditions for at least one week. Similar procedure is used to exfoliate **CB2**MOF-1 and **I-CB2**MOF-1.

6.4.2 Characterization methods

Grazing Incidence Wide Angle X-ray Scattering (GIWAXS) 2D patterns were collected in the NCD-SWEET beamline at ALBA synchrotron (Cerdanyola del Vallès, Spain). A monochromatic beam of 12.4 keV (0.998 Å) was set using a Si (111) channel cut monochromator. The scattered radiation was recorded using the Rayonix LX-255HS® area detector, which consist of a pixel array of 5760 x 1920 (V × H) area detector with a pixel size of 44 × 44 μm^2. The detector binning was set to 2 × 2. The reciprocal space, sample to detector distance, beam center and detector tilts were calculated using Cr_2O_3, a common standard used as calibrant for wide angle scattering experiments.

Powder X-ray Diffraction (PXRD) patterns were recorded at room temperature on an X'Pert PRO MPD diffractometer (PanAnalytical) using Cu Kα (λ = 1.5405 Å) radiation.

Atomic Force microscopy (AFM). The nanosheet suspension was adsorbed on a silicon wafer by drop casting and air dried. Subsequently, the morphology of the surface was analyzed by using an Asylum Research system (Model Number: AC240TS-R3, Oxford Instruments Company). The AFM images were recorded in the dynamic mode (i.e., tapping or non-contact mode) using a silicon tip (radius = 9 ± 2 nm) and a silicon cantilever (with Al (100) coating) with a resonance frequency (f) of 70 kHz and a force constant (k) of 2 N/m. The operations were carried out at room temperature under ambient air conditions. The images were processed using the WSxM 5.0 software.

UV-vis (ultra violet-visible) absorption. UV/Vis measurements were carried out by using a Hewlett Packard 8453 diode array spectrometer equipped with a Lauda RE 207 thermostat and a screw-capped quartz cuvette.

Field-Emission Scanning Electron Microscopy (FE-SEM) images were collected using the Magellan 400L Field Emission Scanning Electron Microscope equipped with a newly developed electron column with a monochromator, UC (UniColore) Technology.

Scanning Transmission Electron Microscopy (STEM) images were acquired at 200 keV on a FEI Tecnai G2 F20 microscope using a high angle annular dark field (HAADF) detector. Energy Dispersive X-Ray (EDX) spectra were obtained with an EDAX super ultra-thin window (SUTW) X-ray detector. Electron Energy-Loss Spectroscopy (EELS) and Energy Filtered TEM (EFTEM) experiments were performed using a Gatan Imaging Filter (GIF) Quantum SE 963 fitted with a 2k x 2k CCD camera.

6.5 Rererences

[1] H. Zhang, *Chem. Rev.* **2018**, *118*, 6089.

[2] H. Miro, B. Seoane, F. Kapteijn, I. Luz, F. X. Llabrés i Xamena, J. Gascon, A. Corma, T. Rodenas, G. Prieto, *Nat. Mater.* **2014**, *14*, 48.

[3] J. Huang, Y. Li, R. K. Huang, C. T. He, L. Gong, Q. Hu, L. Wang, Y. T. Xu, X. Y. Tian, S. Y. Liu, Z. M. Ye, F. Wang, D. D. Zhou, W. X. Zhang, J. P. Zhang, *Angew. Chemie - Int. Ed.* **2018**, *57*, 4632.

[4] Y. Peng, Y. Li, Y. Ban, W. Yang, **n.d.**

[5] J. Zhu, J. Hou, A. Uliana, Y. Zhang, M. Tian, B. Van Der Bruggen, *J. Mater. Chem. A* **2018**, *6*, 3773.

[6] H. S. Wang, J. Li, J. Y. Li, K. Wang, Y. Ding, X. H. Xia, *NPG Asia Mater.* **2017**, *9*, 1.

[7] D. J. Ashworth, J. A. Foster, *J. Mater. Chem. A* **2018**, *6*, 16292.

[8] M. Zhao, Y. Huang, Y. Peng, Z. Huang, Q. Ma, H. Zhang, *Chem. Soc. Rev.* **2018**, *47*, 6267.

[9] M. Zhao, Q. Zhao, B. Li, H. Xue, H. Pang, C. Chen, *Nanoscale* **2017**, *9*, 15206.

[10] K. Varoon, X. Zhang, B. Elyassi, D. D. Brewer, M. Gettel, S. Kumar, J. A. Lee, S. Maheshwari, A. Mittal, C.-Y. Sung, M. Cococcioni, L. F. Francis, A. V. McCormick, K. A. Mkhoyan, M. Tsapatsis, *Science (80-.).* **2011**, *334*, 72.

[11] C. Hermosa, B. R. Horrocks, J. I. Martínez, F. Liscio, J. Gómez-Herrero, F. Zamora, *Chem. Sci.* **2015**, *6*, 2553.

[12] T. Araki, A. Kondo, K. Maeda, *Chem. Commun.* **2013**, *49*, 552.

[13] A. Abhervé, S. Mañas-Valero, M. Clemente-León, E. Coronado, *Chem. Sci.* **2015**, *6*, 4665.

[14] P. Z. Li, Y. Maeda, Q. Xu, *Chem. Commun.* **2011**, *47*, 8436..

[15] C. Kutzscher, A. Gelbert, S. Ehrling, C. Schenk, I. Senkovska, S. Kaskel, *Dalt. Trans.* **2017**, *46*, 16480.

[16] P. Chandrasekhar, A. Mukhopadhyay, G. Savitha, J. N. Moorthy, *J. Mater. Chem. A* **2017**, *5*, 5402.

[17] H. Kitagawa, K. Otsubo, S. Sakaida, G. Xu, T. Yamada, *J. Am. Chem. Soc.* **2012**, *134*, 16524.

[18] H. Gunda, S. K. Das, K. Jasuja, *ChemPhysChem* **2018**, *19*, 880.

[19] A. L. Pickering, C. Mitterbauer, N. D. Browning, S. M. Kauzlarich, P. P. Power, *Chem. Commun.* **2007**, 580.

[20] S. Turner, Y.-G. Lu, S. D. Janssens, F. Da Pieve, D. Lamoen, J. Verbeeck, K. Haenen, P. Wagner, G. Van Tendeloo, *Nanoscale* **2012**, *4*, 5960.

[21] F. Tan, A. López-Periago, M. E. Light, J. Cirera, E. Ruiz, A. Borrás, F. Teixidor, C. Viñas, C. Domingo, J. G. Planas, *Adv. Mater.* **2018**, *30*, 1800726.

[22] L. Sanchez-Botero, A. V. Dimov, R. Li, D.-M. Smilgies, J. P. Hinestroza, *Langmuir* **2018**, *34*, 5263.

[23] S. C. Gad, in *Encycl. Toxicol. Third Ed.*, **2014**.

Supporting Information

Supporting information for Chapter 3

Table S3-1. Crystal and Structure Refinement data for **CB1**MOF-1 to **CB1**MOF-4**.**

Compound	**CB1**MOF-1	**CB1**MOF-2	**CB1**MOF-3	**CB1**MOF-4
Empirical formula	$C_{88}H_{88}B_{20}N_6O_{18}Co_3$	$C_{68}H_{45}B_{10}N_2O_{17}Zn_4$	$C_{72}H_{96}B_{10}N_{10}O_{18}Zn_2$	$C_{59.10}H_{67.90}B_{10}N_{5.70}O_{15.70}Co_2$
Formula weight	1910.63	1540.71	1628.42	1335.25
Crystal system	Triclinic	Monoclinic	Triclinic	Monoclinic
Space group	P-1	Pn	P-1	$P2_1/c$
CCDC ref	1517352	1517351	1517359	1517360
a (Å)	14.9086(4)	18.5945(10)	11.6364(5)	16.2470(9)
b (Å)	15.3237(4)	8.0800(5)	15.5850(6)	21.0403(9)
c (Å)	15.6621(5)	30.2904(19)	18.8230(8)	22.8395(11)
α (deg)	67.5200(10)	90	86.4230(18)	90
β (deg)	62.9120(10)	90.819(2)	82.8690(19)	105.811(2)
γ (deg)	69.2370(10)	90	89.7220(19)	90
V ($Å^3$)	2871.90(15)	4550.5(5)	3380.6(2)	7512.1(6)
Z	1	2	2	4
F (000)	983	1564	1704	2768
θ (range)	2.629-28.321	1.277-25.023	2.370-66.598	2.334-25.060
Max./min. transmission	0.7457/0.6447	0.7452/0.2826	0.7528/0.6338	0.7452/0.2826
Ind refln (R_{int})	14224 (0.0336)	15879 (0.1216)	11752 (0.0509)	12998 (0.1505)
Final R indices [I > 2σ(I)]	R1 = 0.0388 wR2 = 0.1142	R1 = 0.0759 wR2 = 0.1858	R1 = 0.0736 wR2 = 0.1979	R1 = 0.0678 wR2 = 0.1790
R indices (all data)	R1 = 0.0446, wR2 = 0.1169	R1 = 0.0848, wR2 = 0.1904	R1 = 0.0874, wR2 = 0.2049	R1 = 0.1055, wR2 = 0.1917
Largest diff. peak and hole	0.484 and -0.352 $e.Å^{-3}$	1.108 and -0.992 $e.Å^{-3}$	1.645 and -0.826 $e.Å^{-3}$	0.633 and -0.514 $e.Å^{-3}$

Table S3-2. Crystallographic data of the different guest-containing structures for **CB1**MOF-1⊃ **guest**.

Guest	MeOH	$CHCl_3$	NP	NBz	Bz	Tol
Empirical formula	$C_{88}H_{88}B_{20}Co_3N_6O_{18}$	$C_{88}H_{88}B_{20}Co_3N_6O_{18}$	$C_{88}H_{88}B_{20}Co_3N_6O_{18}$	$C_{88}H_{88}B_{20}Co_3N_6O_{18}$	$C_{88}H_{88}B_{20}Co_3N_6O_{18}$	$C_{88}H_{88}B_{20}Co_3N_6O_{18}$
Formula weight	1910.63	1910.63	1910.63	1910.63	1910.63	1910.63
T/*K*	100(2)	100(2)	100.0	100.0	100.0	100.0
Crystal system	Triclinic	Triclinic	Triclinic	Triclinic	Triclinic	Triclinic
Space group	P-1	P-1	P-1	P-1	P-1	P-1
CCDC	1517353	1517354	1517355	1517356	1517357	1517358
a/Å	14.6335(18)	14.7030(8)	15.0089(10)	14.9235(9)	14.7228(6)	14.7141(8)
b/Å	15.2993(14)	15.2876(7)	15.3987(12)	15.1203(9)	15.2375(5)	15.3016(7)
c/Å	15.6868(17)	15.7014(7)	15.5691(12)	15.9793(11)	15.7764(6)	15.8557(10)
α/°	66.973(4)	67.499(2)	67.873(3)	67.399(2)	67.5260(10)	67.095(2)
β/°	62.396(5)	64.547(2)	64.609(3)	68.016(2)	65.8470(10)	66.061(2)
γ/°	70.264	69.969(2)	68.959(3)	70.670(2)	70.8660(10)	70.802(3)
V/Å^3	2811.1(5)	2876.3(3)	2926.2(4)	3012.1(3)	2921.87(19)	2943.0(3)
Z	2	2	2	2	2	2
ρ_{calc}/mg mm^{-3}	1.118	1.206	1.254	1.380	1.279	1.307
F(000)	975	1061	1143	1287	1164	1203
2*θ* range for data collection	2.402 to 33.813°	2.374 to 27.162°	2.362 to 30.517°	2.344 to 27.558°	2.347 to 27.073°	2.344 to 30.085°
Reflections collected	73697	39449	181513	68700	48175	53989
Independent reflections	22487 [R(int) = 0.0372]	12708 [R(int) = 0.0437]	17862[R(int) = 0.0898]	13855[R(int) = 0.0464]	12818[R(int) = 0.0405]	17211[R(int) = 0.0477]
Goodness-of-fit on F^2	1.021	1.027	1.132	1.137	1.048	1.032
Final *R* indexes [$I \geq 2\sigma(I)$]	R1 = 0.0397, wR2 = 0.1061	R1 = 0.0544, wR2 = 0.1635	R1 = 0.0506, wR2 = 0.1464	R1 = 0.0501, wR2 = 0.1039	R1 = 0.0403, wR2 = 0.0895	R1 = 0.0579, wR2 = 0.1306
Final *R* indexes [all data]	R1 = 0.0537, wR2 = 0.1108	R1 = 0.0702, wR2 = 0.1718	R1 = 0.0684, wR2 = 0.1545	R1 = 0.0674, wR2 = 0.1156	R1 = 0.0536, wR2 = 0.0966	R1 = 0.0887, wR2 = 0.1444
Largest diff. Peak/hole / e Å^{-3}	0.559 / -0.581	0.677 / -0.640	1.045 / -0.921	0.834 /-0.557	0.623 / -0.621	0.994 / -0.628
No. guest per unit cell Refined / Masked	0 / 2	1 / 0.36	1 / 1.5	3 / 0	3 / 0	3 / 0
No. of guests by DTA[i]	8	1.5	7	3	3	3

[i] Crystals were measured after being dried under vacuum for 3h (DMF, MeOH, $CHCl_3$, NP, Bz, Tol) or 12h (NBz). 4 DMF guests were found for **CB1**MOF-1 ⊃ **DMF** by DTA.

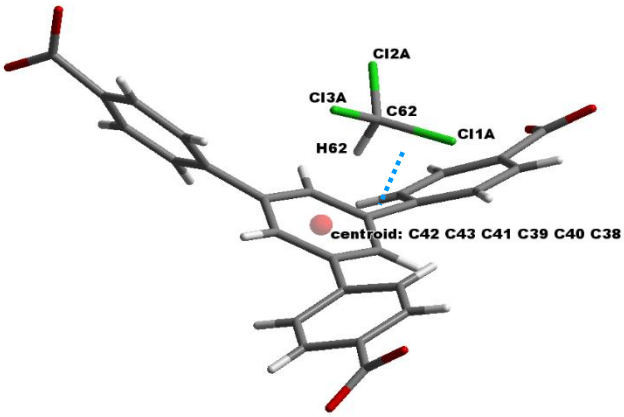

Figure S3-1. Intermolecular chloroform-framework contacts in **CB1**MOF-1 ⊃ **$CHCl_3$**. See Table S3-2 for geometrical parameters.

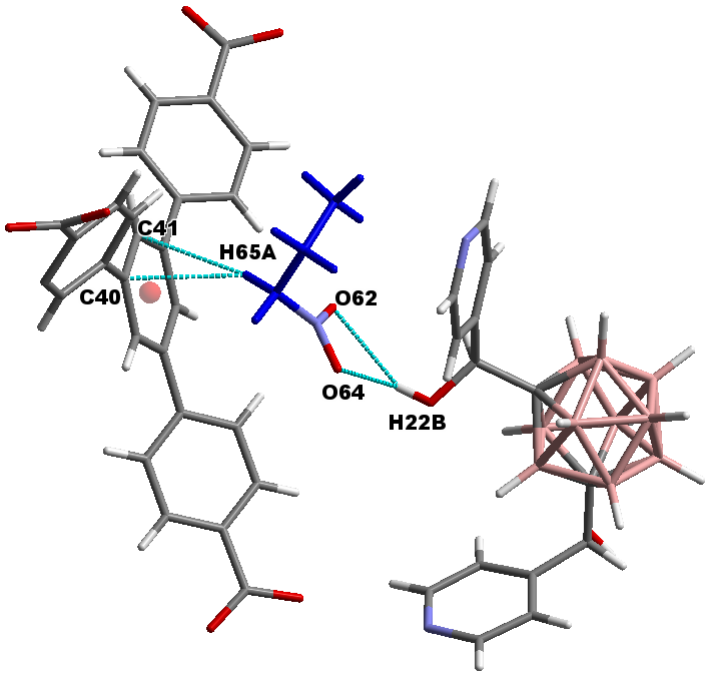

Figure S3-2. Intermolecular 1-nitropropane-framework contacts in **CB1**MOF-1 ⊃ **NPr**.
1-nitropropane molecules are colored by symmetry equivalence as implemented in mercury. See table S3-2 for geometrical parameters.

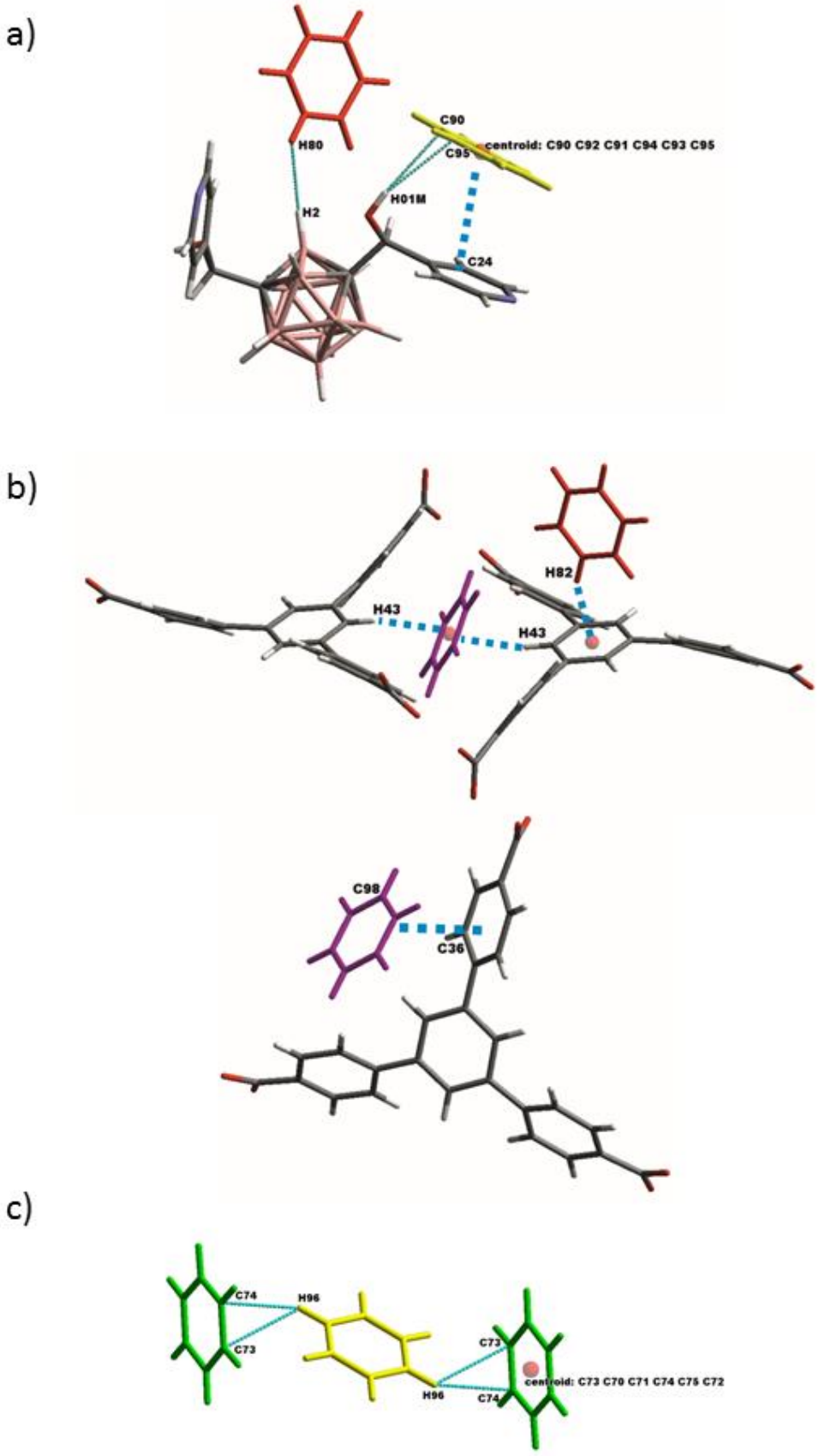

Figure S3-3. Intermolecular benzene-framework contacts in **CB1**MOF-1 ⊃ **Bz** (a) Bz-**CB1** contacts; (b) Bz-BTB contacts; (c) Bz-Bz contacts. See table S3-2 for geometrical parameters.

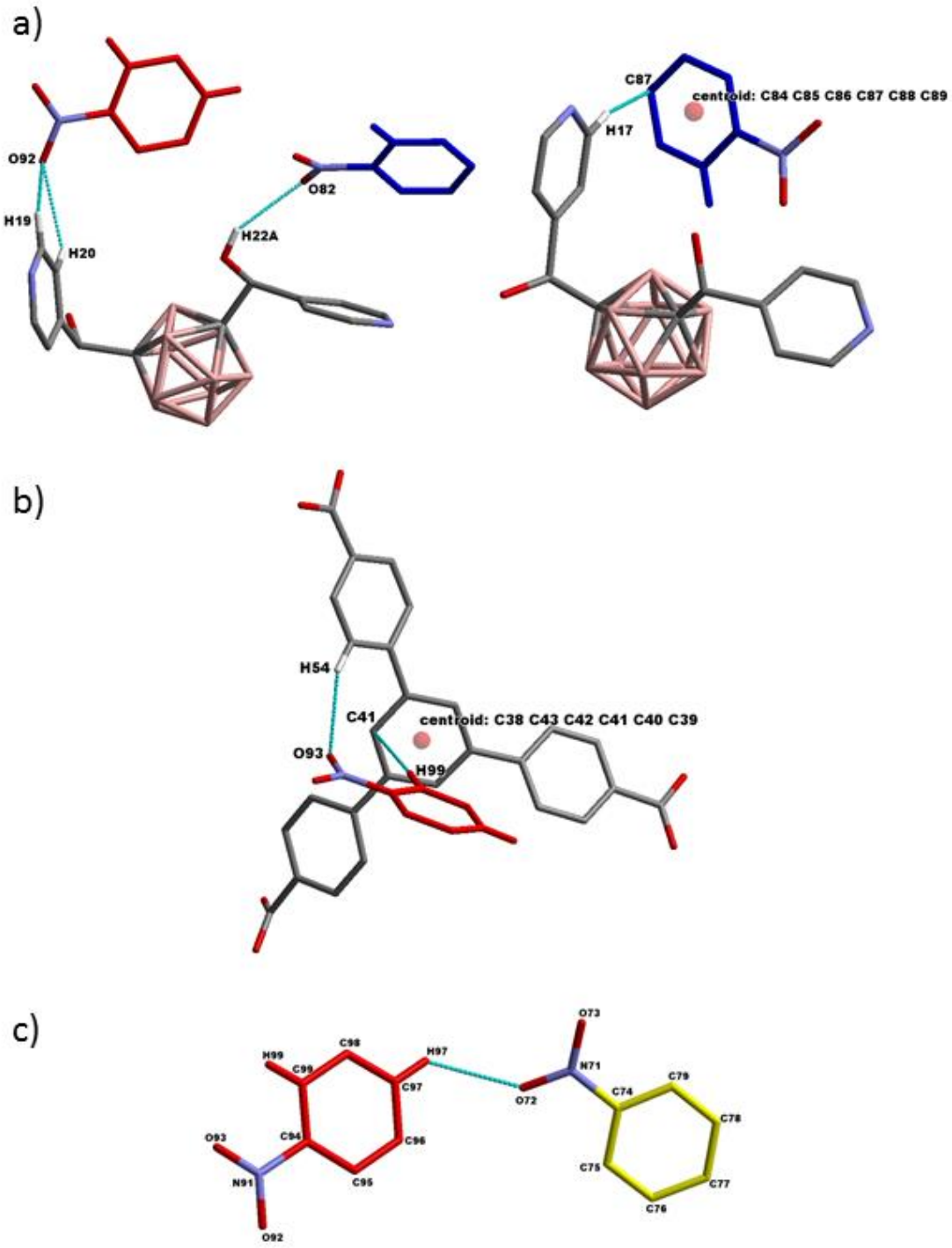

Figure S3-4. Intermolecular nitrobenzene-framework contacts in **CB1**MOF-1 ⊃ **NBz**: (a) NBz-**CB1** contacts; (b) NBz-BTB contacts; (c) NBz-NBz contacts. Nitrotoluene molecules are colored by symmetry equivalence as implemented in mercury. See table S3-2 for geometrical parameters.

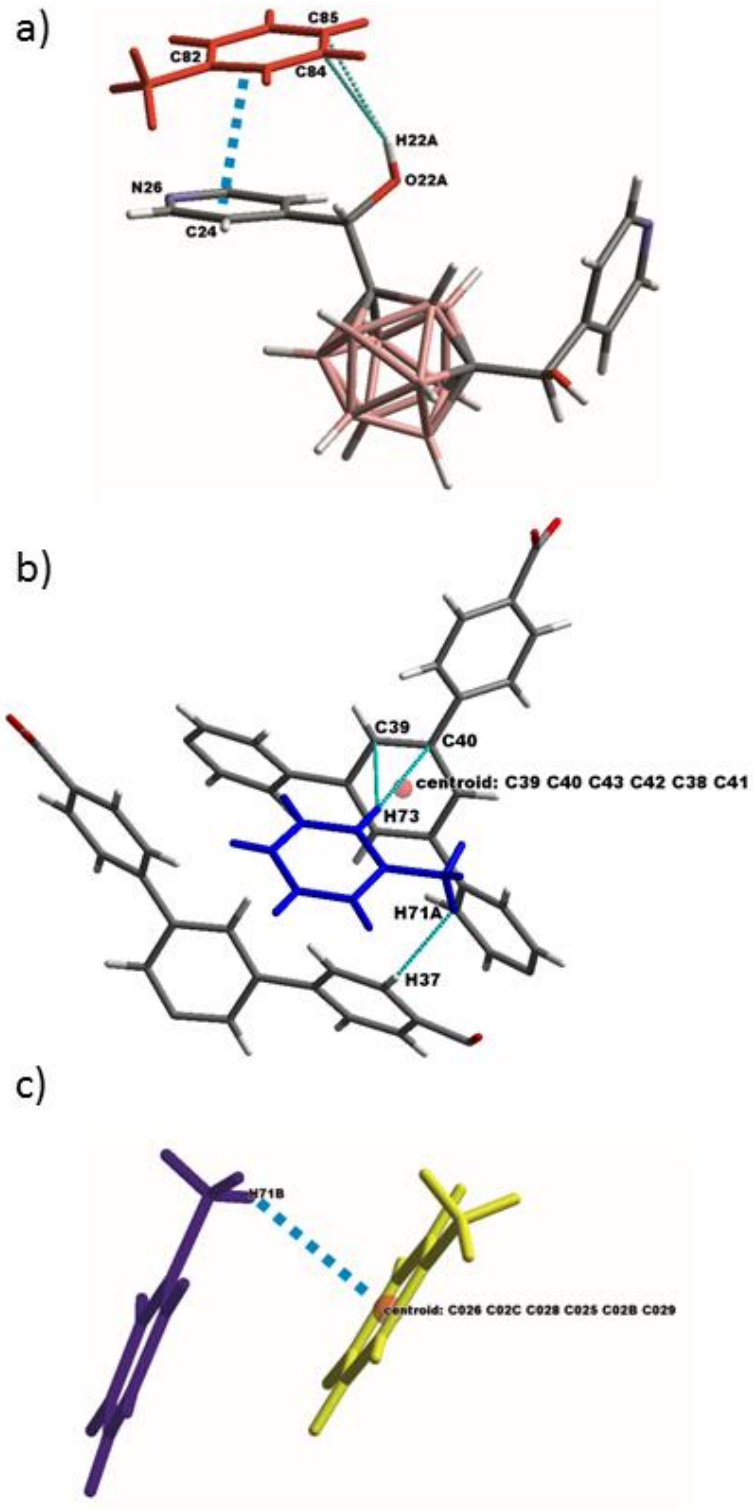

Figure S3-5. Intermolecular toluene-framework contacts in **CB1**MOF-1 ⊃ **Tol**: (a) Tol-**CB1** contacts; (b) Tol-BTB contacts; (c) Tol-Tol contacts. Toluene molecules are colored by symmetry equivalence as implemented in mercury. See table S3-2 for geometrical parameters.

Supporting information for Chapter 4

S 4.1 Crystallography

Crystals for **CB1**MOF-1a and **CB1**MOF-1´ were obtained from the mixture obtained after treating **CB1**MOF-1 ⊃ **DMF** with MeOH for 3 days. Crystals for **CB1**MOF-1b were obtained from the mixture obtained after treating **CB1**MOF-1 ⊃ **DMF** with scCO2. Data were collected on a Rigaku AFC12 4-circle goniometer equipped with an enhanced sensitivity (HG) Saturn724+ detector mounted at the window of an FR-E+ SuperBright molybdenum (Mo Ka1/Ka2 = 0.71073Å) rotating anode generator with VHF Varimax optics (70µm focus) operating at 2.475kW (45kV, 55mA). Using Olex2[1], the structure was solved with the ShelXT[2] structure solution program, using the Intrinsic Phasing solution method. The model was refined with version 2016/6 of ShelXL[2] using Least Squares minimisation. The sample **CB1**MOF-1a is obviously a mix of structures representing various stages of 'transformation'. This data set is the best of a number of attempts to measure this larger cell structure. The data are weak and the refinement has the associated problems – however, it clearly reveals the crystallographic features of this structure. The structure contains a solvent accessible void of 1059.7 angs 3, and using solvent masking 167 electrons can be assigned to this void. This improves the R1 value by ca. 3%. It is unclear what this represents. In all refinements extensive use of geometrical and thermal parameter restrains/constraints was necessary to refine against the weak data. Unit cell determinations for bulk synthesis of **CB1**MOF-1-back were measured at the XALOC beamline of the ALBA synchrotron at 100 K using a MD2M single-axis diffractometer (Maatel, France) and a Pilatus 6M detector (Dectris, Switzerland).

Table S4-1. Crystal and structural refinement data for crystal **CB1**MOF-1a, crystal **CB1**MOF-1b and crystal **CB1**MOF-1´.

Crystal Data	**CB1**MOF-1a	**CB1**MOF-1b	**CB1**MOF-1´
T/K	100	100	100
Empirical formula	$C_{82}H_{78}B_{20}Co_3N_4O_{18}$	$C_{88}H_{98}B_{22}Co_3N_6O_{22}$	$C_{82}H_{82}B_{20}Co_3N_4O_{20}$
Formula weight	1800.47	2006.33	1836.50
Crystal system	Triclinic	Triclinic	Triclinic
Space group	*P-1*	*P-1*	*P-1*
Unit-cell dimensions	a = 13.3699(14) Å	a = 13.4599(5) Å	a = 12.7760(8) Å
	b = 16.3896(11) Å	b = 14.3042(5) Å	b = 12.9917(7) Å
	c = 24.7232(13) Å	c = 15.5205(4) Å	c = 15.3607(5) Å
	α = 95.962(5)°	α = 113.653(3)°	α = 107.242(4)°
	β = 100.013(6)°	β = 92.654(3)°	β = 112.907(5)°
	γ = 110.984(8)°	γ = 111.589(4)°	γ = 96.664(5)°
Volume/ $Å^3$	4899.2(7) $Å^3$	2478.31(16) $Å^3$	2164.0(2) $Å^3$
Z	2	1	1
Density (calculated)/ $mg.\mu m^{-3}$	1.221	1.344	1.409
Absorption coefficient/ mm^{-1}	0.564	0.568	0.642
F(000)	1846	1035	943
Theta range for data collection/deg	2.925 to 25.026	2.943 to 28.699	2.930 to 25.027
Reflections collected/unique	34888/17176 [R_{int} = 0.0655]	29921/12708 [Rint = 0.0246]	15901/7554 [Rint = 0.0501]
Max. and min. transmission	1.00000 and 0.75723	1.00000 and 0.89342	1.00000 and 0.52283
Final R indices [I>2sigma(I)]	R1 = 0.1486, wR2 = 0.3603	R1 = 0.0709, wR2 = 0.2019	R1 = 0.0609, wR2 = 0.1569
R indices (all data)	R1 = 0.2258, wR2 = 0.4115	R1 = 0.0872, wR2 = 0.2172	R1 = 0.0777, wR2 = 0.1671
Largest diff. peak and hole	3.845 and -1.195 $e.Å^{-3}$	1.787 and -1.773	1.039 and -0.919 $e.Å^{-3}$

CCDC 1820704-1820706 contains the supplementary crystallographic data for this paper. These data can be obtained free of charge from The Cambridge Crystallographic Data Centre via www.ccdc.cam.ac.uk/data_request/cif.

Table S4-2. Unit cell determination for various crystals from two different batches of phase **CB1**MOF-1´ preparation.

	Measurements	*a* (Å)	*b* (Å)	*c* (Å)	α (°)	β (°)	γ (°)
Batch 1	1	13.133(16)	13.479(15)	15.227(15)	108.68(9)	110.18(10)	99.58(9)
	2	13.144(18)	13.490(20)	15.230(19)	108.87(13)	109.76(13)	99.77(12)
	3	13.11(4)	13.45(4)	15.31(4)	109.3(3)	109.1(3)	99.8(3)
	4	13.06(7)	13.25(4)	15.31(5)	109.0(3)	109.5(4)	98.7(4)
	5	13.09(2)	13.491(18)	15.233(18)	108.59(11)	109.93(14)	99.61(13)
	6	13.04(3)	13.43(3)	15.21(2)	108.86(16)	109.84(16)	99.35(17)
	7	13.176(19)	13.443(18)	15.242(17)	108.84(11)	110.28(12)	99.37(12)
	8	13.20(3)	13.51(4)	15.20(3)	108.4(2)	110.2(2)	100.0(2)
Batch 2	1	13.145(18)	13.512(17)	15.19(2)	108.67(12)	109.78(12)	99.81(11)
	2	13.12(2)	13.469(17)	15.261(16)	109.22(11)	109.86(12)	99.33(12)
	3	13.166(19)	13.427(19)	15.23(2)	108.71(13)	109.67(13)	99.92(12)
	4	13.167(19)	13.483(17)	15.195(19)	109.03(11)	109.43(12)	99.66(12)
	5	13.164(17)	13.423(18)	15.244(19)	108.90(12)	110.32(12)	99.22(11)
	6	13.081(12)	13.466(14)	15.250(14)	108.53(9)	109.84(9)	99.59(8)
	7	13.12(2)	13.455(18)	15.21(2)	108.77(13)	109.82(15)	99.61(14)
	8	13.100(12)	13.477(15)	15.223(14)	108.88(9)	109.91(8)	99.51(8)

S 4.2 Computational details

DFT calculations were performed with the all-electron FHI-aims computer code using numerical local orbital basis set[3]. This approach allows for a full-potential calculations at a low computational cost without using any a priori approximations for the potential, such as pseudopotentials or frozen cores. The calculations were performed using the generalized-gradient approximation PBE functional[4] including the dispersion effects with the Hirschfield approach[5]. In the FHI-aims code, there are three levels of accuracy in the choice of the numerical basis set ("light", "tight" and "really tight") and the "tight" level was employed[3]. The SCF parameters to reach a good convergence in the calculations were a Gaussian occupation type with a parameter of 0.01, a Pulay mixer with 10 cycles and a mixing parameter of 0.05. Due to the large size of the unit cells, only the gamma point was employed for the calculations. The structures for systems **CB1**MOF-1, **CB1**MOF-1·8DMF, **CB1**MOF-1·8MeOH, **CB1**MOF-1**b**·4H_2O·2DMF, **CB1**MOF-1´ and **CB1**MOF-1+ C_{60} were optimized by DFT calculations. In the case of the **CB1**MOF-1·8MeOH structure, we have employed a molecular dynamics

simulation of the solvent molecules in order to have a starting geometry for the DFT optimization.

Interaction energies have been calculated taking as reference the host-guest optimized structure subtracting the energies of isolated host and guest subsystems keeping the structure that they have in the whole optimized host-guest system. Inclusion energies were obtained using also as the host-guest optimized structure but performing the comparison of such energy with those of the optimized isolated host and guest subsystems. To extract the energies of some structures that correspond to chemical reactions and they have different number of solvent molecules, for instance MOFs **CB1**MOF-1´´ or **CB1**MOF-1´ (solvent free) and **CB1**MOF-1**b** (that contains 4 water + 2 DMF molecules), we have to consider the energy of MOFs **CB1**MOF-1´´ or **CB1**MOF-1´ plus the energy of four free water and two free DMF molecules to compare with the **1b** energy.

Table S4-3 Unit cell determination for ten crystals from two different batches of **CB1**MOF-1-back preparation.

Measurements	*a* (Å)	*b* (Å)	*c* (Å)	α (°)	β (°)	γ (°)
1	14.7448(4)	15.2987(6)	15.7208(5)	67.158(3)	62.875(3)	69.521(3)
2	14.7639(4)	15.2844(4)	15.7052(5)	67.146(3)	62.845(3)	69.489(2)
3	14.7693(7)	15.2952(7)	15.7180(6)	67.126(4)	62.849(4)	69.449(4)
4	14.7287(15)	15.2904(12)	15.7093(11)	67.03(7)	62.967(3)	69.701(8)
5	14.7030(13)	15.3125(8)	15.7394(14)	66.876(6)	62.560(9)	69.656(6)
6	14.523(3)	15.357(3)	15.563(3)	66.723(17)	62.026(18)	69.321(16)
7	14.7546(6)	15.2888(6)	15.7526(6)	66.857(4)	62.121(4)	69.285(4)
8	14.704(3)	15.285(18)	15.742(3)	66.735(16)	61.82(2)	69.344(16)
9	14.715(2)	15.3051(15)	15.782(3)	66.740(13)	61.983(17)	69.412(13)
10	14.8039(7)	15.2985(9)	15.7390(9)	67.026(5)	62.693(6)	69.310(5)

S4.3. References

[1] O. V Dolomanov, L. J. Bourhis, R. J. Gildea, J. A. K. Howard, H. Puschmann, *J. Appl. Crystallogr.* **2009**, *42*, 339.

[2] G. M. Sheldrick, *Acta Crystallogr. Sect. C Struct. Chem.* **2015**, *71*, 3.

[3] V. Blum, R. Gehrke, F. Hanke, P. Havu, V. Havu, X. Ren, K. Reuter, M. Scheffler, *Comput. Phys. Commun.* **2009**, *180*, 2175.

[4] J. P. Perdew, K. Burke, M. Ernzerhof, *Phys. Rev. Lett.* **1996**, *77*, 3865.

[5] A. Tkatchenko, M. Scheffler, *Phys. Rev. Lett.* **2009**, *102*, 073005.

Supporting Information for Chapter 5

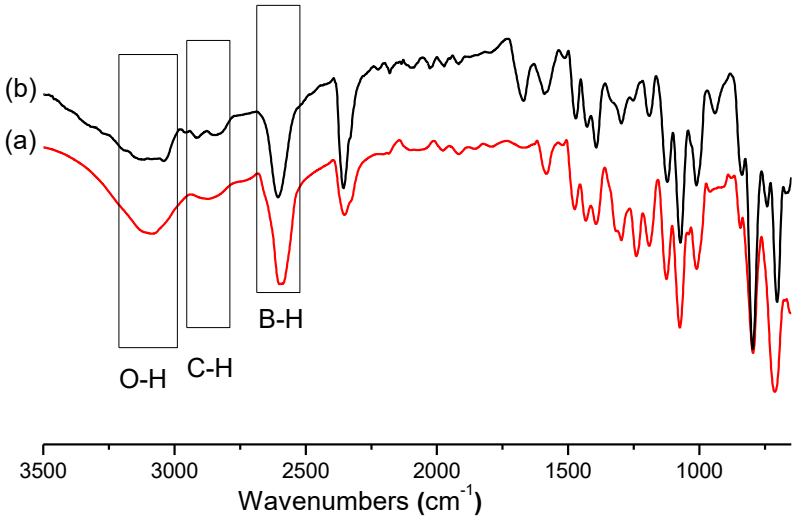

Figure S5-1. IR-ATR spectra of (a) **CB2** and (b) **I-CB2**. Characterized peak of O-H stretching, C-H stretching and the B-H stretching are indicated.

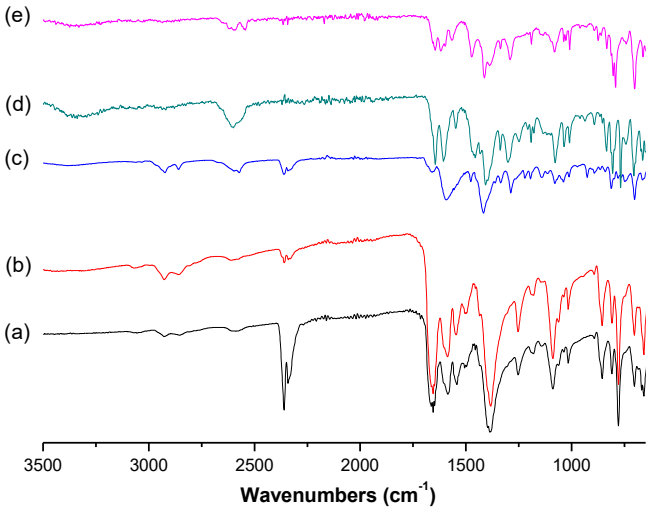

Figure S5-2. IR-ATR spectra of (a) **CB2**MOF-1, (b) **I-CB2**MOF-1, (c) **CB2**MOF-2, (d) **CB2**MOF-3, (e) **CB2**MOF-4.

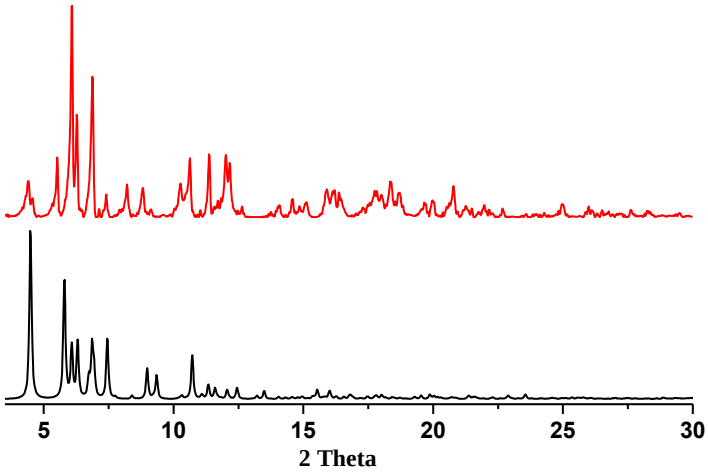

Figure S5-3 Calculated XRD (black) from model of **CB2**MOF-1 and experimental PXRD (red) of **CB2**MOF-1.

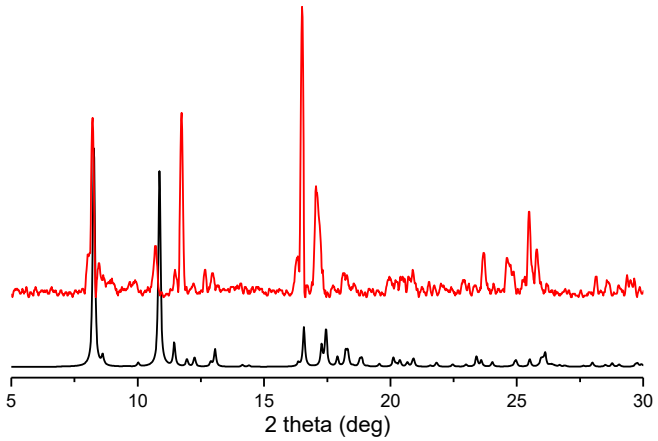

Figure S5-4. Simulated (black) and experimental (red) PXRD patterns of **CB2**MOF-2.

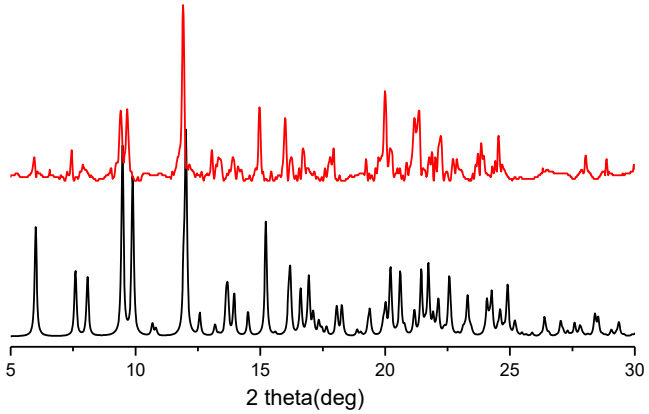

Figure S5-5. Simulated (black) and experimental (r**e**d) PXRD patterns of **CB2**MOF-3.

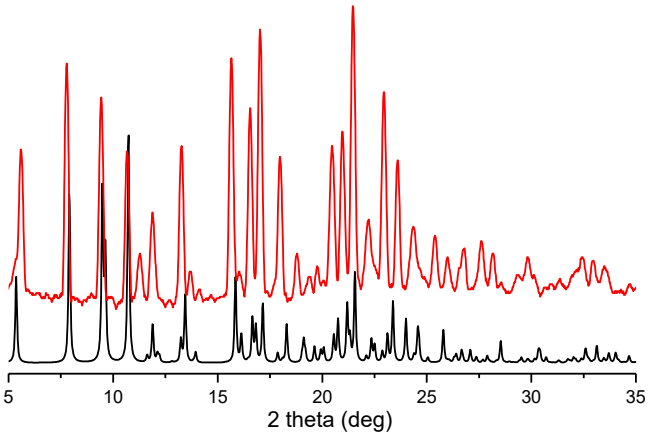

Figure S5-6. Simulated (black) and experimental (red) PXRD patterns of **CB2**MOF-4.

S2. Thermal Analysis

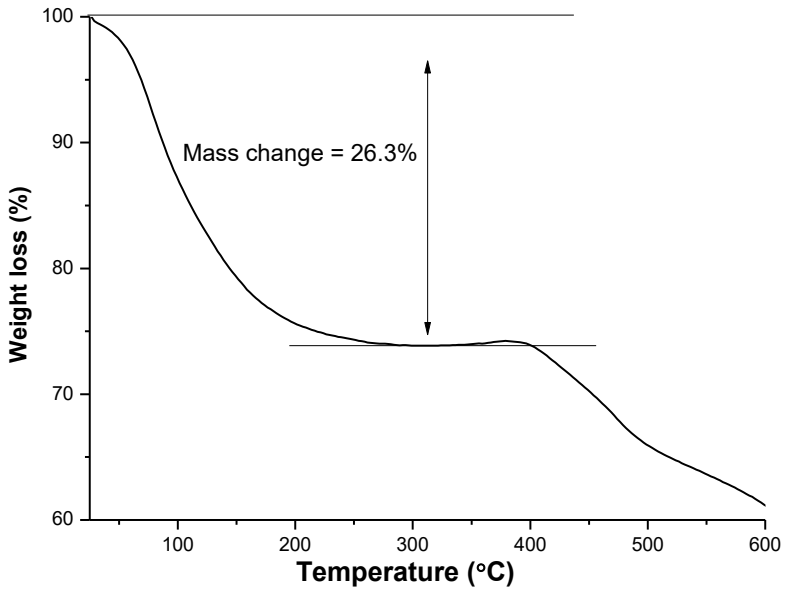

Figure S5-7. TGA diagram of **CB**2MOF-1.

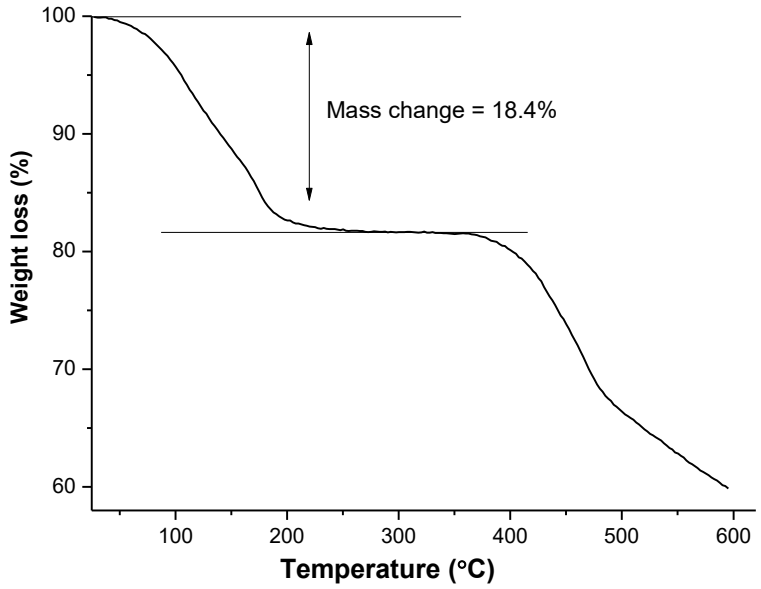

Figure S5-8. TGA diagram of **I-CB2**MOF-1.

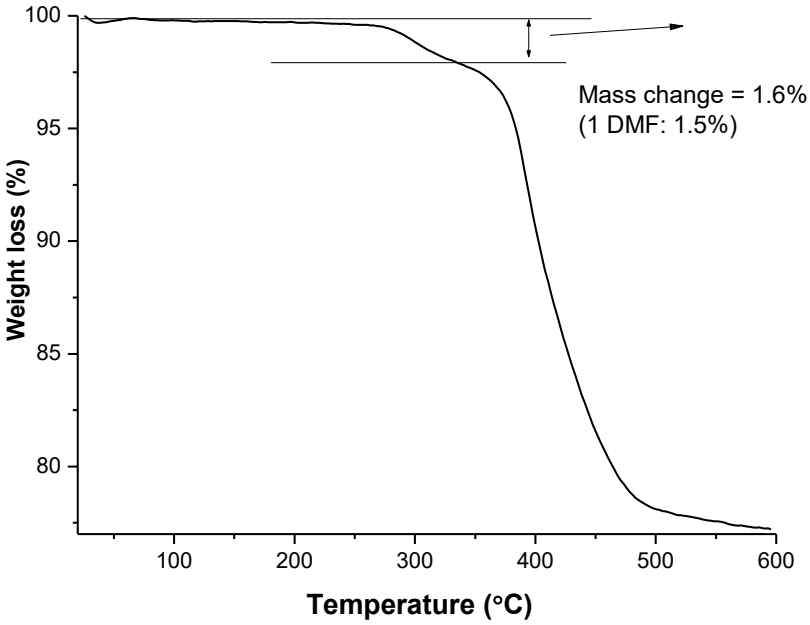

Figure S5-9. TGA diagram of **CB2**MOF-2.

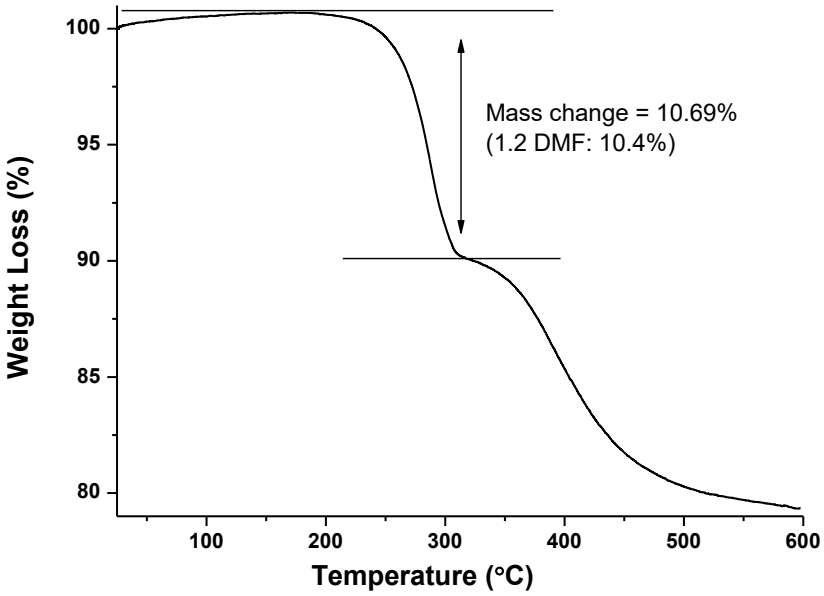

Figure S5-10. TGA diagram of **CB2**MOF-3.

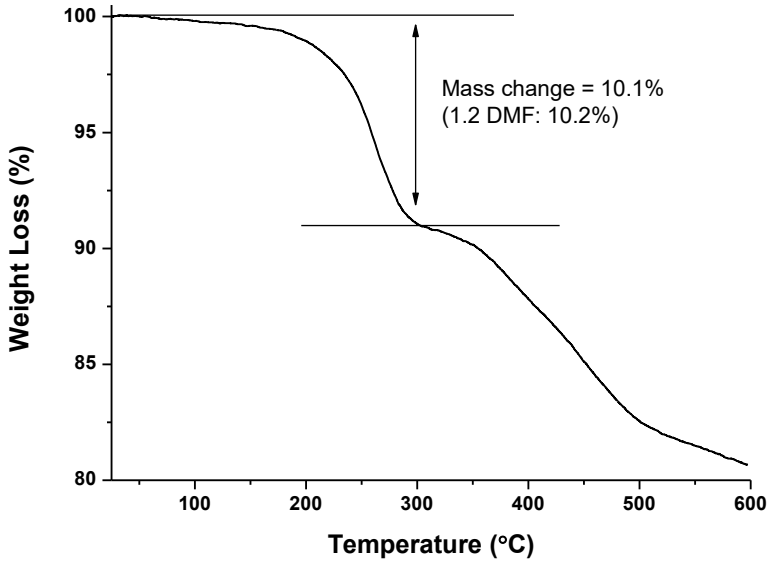

Figure S5-11. TGA diagram of **CB2**MOF-4.

S3. Stability in pH=13 aqueous solution

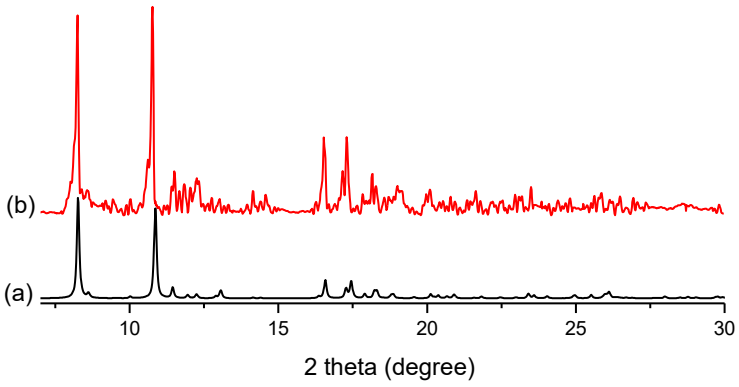

Figure S5-12. PXRD of (a) the as made compounds **CB2**MOF-2 and (b) after immersion in pH=13 aqueous solution for 48h.

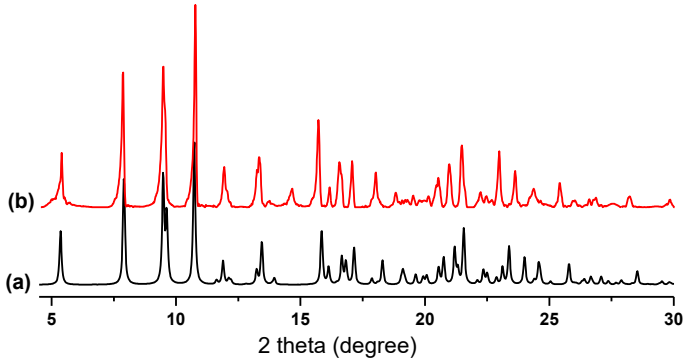

Figure S5-13. Powder patterns of (a) the as made compounds **CB2**MOF-3 and (b) after immersion in pH=13 aqueous solution for 48h.

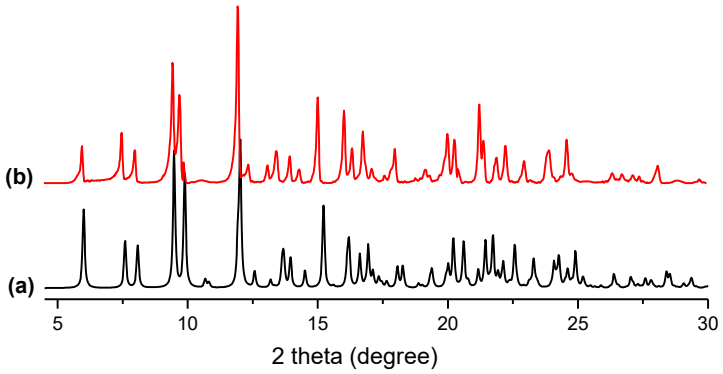

Figure S5-14. Powder patterns of (a) the as made compounds **CB2**MOF-4 and (b) after immersion in pH=13 aqueous solution for 48h.

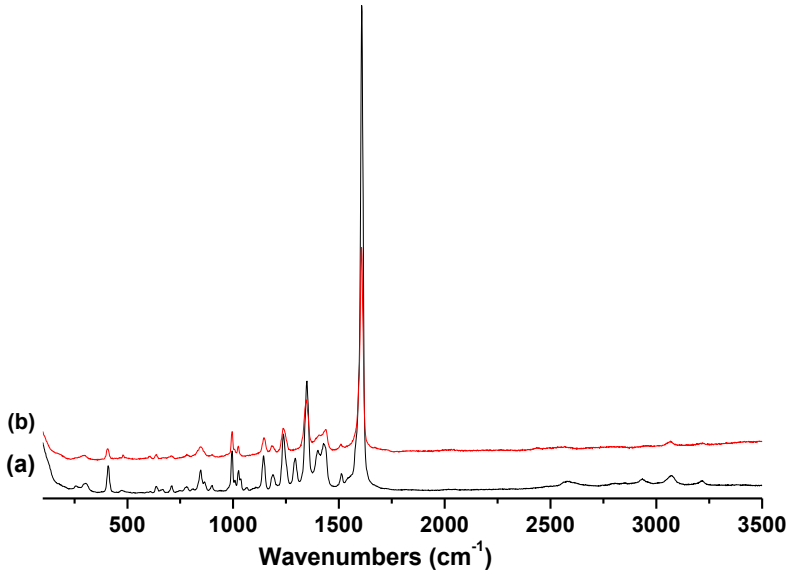

Figure S5-15. Raman spectra of the (a) as-synthesized **CB2**MOF-1⊃**DMF**; (b) **CB2**MOF-1 was immersed in $CHCl_3$ for 24h.

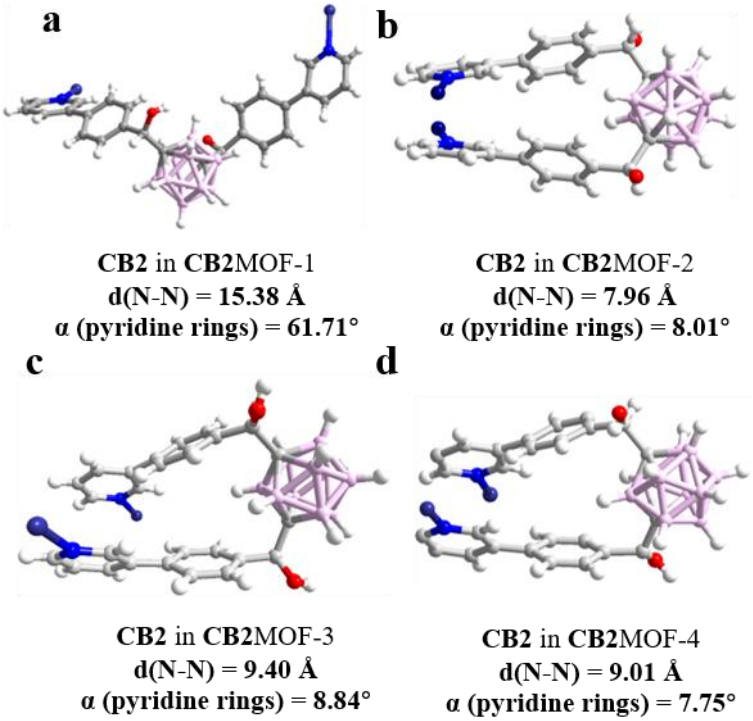

Figure S5-16. CB2 in (a) **CB2**MOF-1, (b) **CB2**MOF-2, (c) **CB2**MOF-3 and (d) **CB2**MOF-4, showing selected structural parameters.

Supporting information for Chapter 6

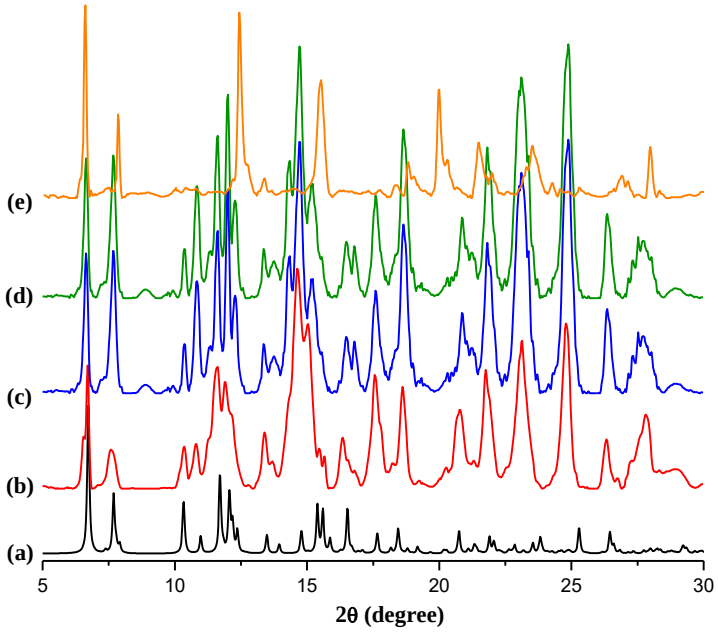

Figure S6-1. (a) calculated PXRD of **CB1**MOF-1´ and experimental PXRD of restacked powder of **CB1**MON-1 nanosheets synthesized from (b) CH_3CN, (c) MeOH (d) $CHCl_3$ and (e) EtOH.

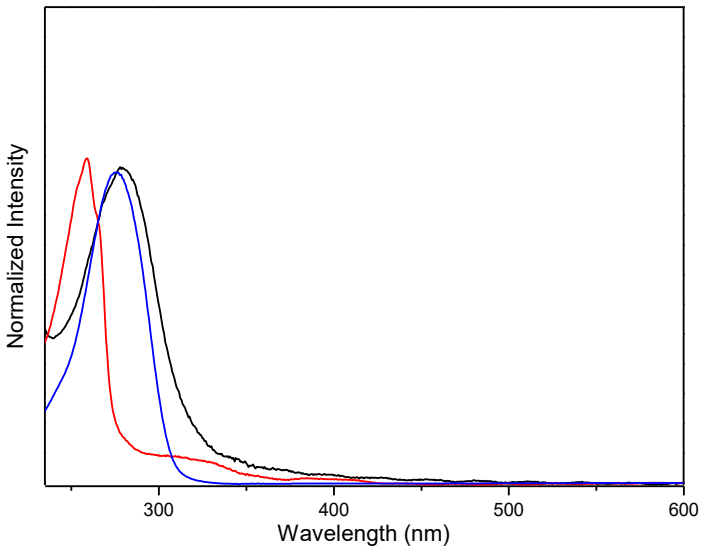

Figure S6-2. UV-vis adsorption of H_3BTB (blue line), **CB1** (red line) and **CB1**MON-1 suspension (black) in EtOH.

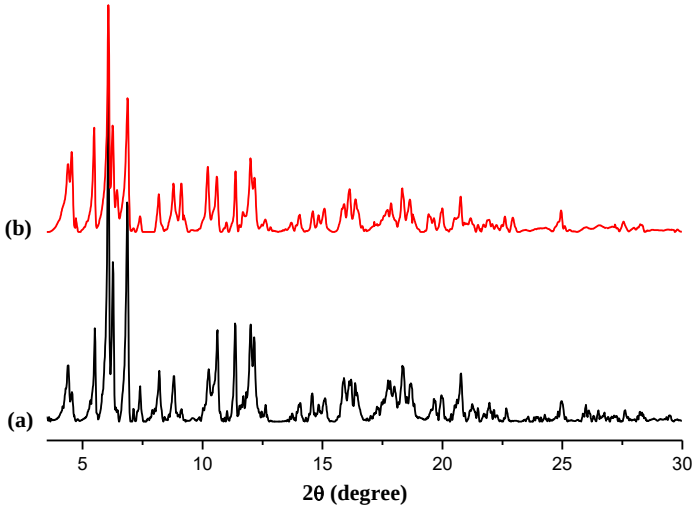

Figure S6-3. (a) PXRD of 2D bulk **CB2**MOF-1 and (b) PXRD of restacked powder of **CB2**MON-1 after immersing into DMF for 30 min.

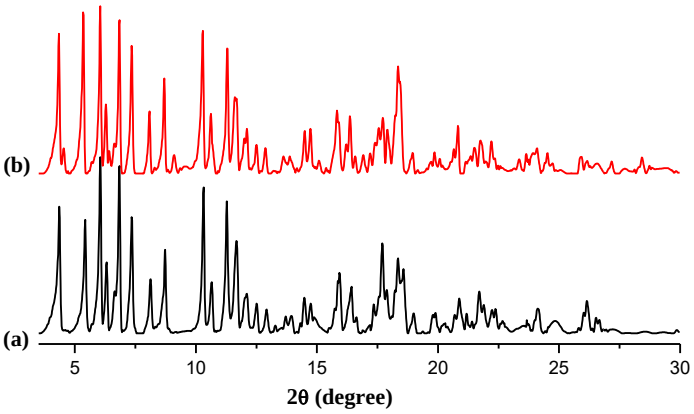

Figure S6-4. (a) PXRD of 2D bulk **I-CB2**MOF-1 and (b) PXRD of restacked powder of **I-CB2**MON-1 after immersing into DMF for 30 min.

General Conclusions

General Conclusions

The results in this Thesis proof that the incorporation of N-disubstituted globular carborane cluster ligands into coordination polymers endows those with unprecedented properties, including structural flexibility, controllable topology and thermal or water stability.

Firstly, it was optimized the synthesis of new coordination polymers constructed by a bis-pyridylacohol carborane ligand (**CB1**), tritopic carboxylic acid 1,3,5-Tris(4-carboxyphenyl)benzene (H_3BTB) or tetratopic carboxylic acid 1,2,4,5-Tetrakis(4-carboxyphenyl)benzene (H_4TCPB) and cobalt or zinc salts by solvothermal conditions. The structures were fully characterized. Due to the high potential solvents accessible volume (33%), **CB1**MOF-1 could act as a crystal sponge for a range of solvents with different polarity whose structures were determined by single-crystal X-ray diffraction. A higher number of interactions between aromatic guest molecules and the **CB1**MOF-1 frameworks were observed. Considering the millimeter scale size of **CB1**MOF-1 crystals, the pillar-layered structure and unchanged geometry of framework after solvent encapsulation, the single crystal nanoindentation was adopted to measure the mechanical properties, elastic modules and hardness values. The crystals encapsulated with aromatic solvents displayed higher elastic and hardness values than with those incorporating non aromatic solvents. The achievement of tunable mechanical properties in **CB1**MOF-1 ⊃ **Guest** is owing to the flexibility of carborane linker and suggest that a higher number of host-guest contacts has also an effect on the hardness and Young's moduli values.

Subsequently, a reversible phase transition from 3D porous **CB1**MOF-1 to 2D non-porous **CB1**MOF-1′ was demonstrated. Notably, this structural transformation was discovered by SXRD. In the 2D final phase **CB1**MOF-1′, the N atoms of the **CB1** carborane ligand coordinated the Co units intralayer, instead of interlayer, as in the initial phase **CB1**MOF-1. The single crystal to single crystal transformation could be accomplished by two-step treatment: exchange of DMF by poor hydrogen acceptor

solvents such as MeOH, $CHCl_3$ or supercritical CO_2; followed by thermal high vacuum evacuation. In addition, heating **CB1**MOF-1′ in the DMF solution would enable the crystal to transform back into **CB1**MOF-1, a process that was confirm by PXRD, SXRD and explained by DFT calculations. To take advantage of this transformation, the inclusion of large fullerene molecules C60 was achieved, providing a new method for encapsulation. A series of characterization techniques have been utilized to analyze the encapsulation, such as PXRD, fluorescence confocal microscopy, raman spectroscopy and TGA. The overall results in this part proved that the incorporation of 3D globular carborane clusters into coordination polymers would provide flexibility and maintain the structure during the coordination bonding reconstruction, something that is not possible when using planar based linkers.

Then a longer bis-pyridylalcohol carborane ligand **CB2** and its B-iodinated derivative I-**CB2** were synthesized and fully characterized. A new family of coordination polymers **CB2**MOF-1 to **CB2**MOF-4 was obtained by the reaction of **CB2** with cobalt nitrate and different tri- or di-topic carboxylic acids (1,3,5-Tris(4-carboxyphenyl)benzene (H_3BTB), 1,4-cyclohexanedicarboxylic acid (H_2CHDA), biphenyl-4,4′-dicarboxylic acid (H_2BPDC) or 4,4′-azobenezenedicarboxylicacid (H_2ADB)). The structures were confirmed by SXRD analysis, which revealed that **CB2**MOF-2 to **CB2**MOF-4 are 3D non-porous crystals where **CB2** coordinated as pillar, in an unusual ice-tweezer shape. On the contrary, **CB2**MOF-1 is a 2D porous structure where **CB2** decorates Co-BTB layers in a similar way to that found in **CB1**MOF-1′. The B-iodinated I-**CB2** seems to form also an isostructural 2D structure (**I-CB2**MOF-1) that has been characterized by PXRD. Both **CB2**MOF-1 and **I-CB2**MOF-1 exhibited a fast phase transformation into crystalline phases **CB2**MOF-1′ and **I-CB2**MOF-1′, respectively, when immersing the compounds in $CHCl_3$. Such transformation is reversible and takes place very fast when immersing the latter into DMF. **CB2**MOF-1′ and **I-CB2**MOF-1′ are non porous to N_2 but porous to CO_2. It is envisioned that the removal of coordinated solvents of **CB2**MOF-1′ and **I-CB2**MOF-1′ will induce large quantity of metal open sites which are much beneficial for its

applications, including adsorption, catalysis or sensing. Detailed studies in these new 2D materials are still being carried out.

Finally, we take advantage of the three 2D bulk crystals **CB1**MOF-1′, **CB2**MOF-1 and **I-CB2**MOF-1 prepared in this Thesis to obtain the corresponding carborane based nanosheets **CB1**MON-1′, **CB2**MON-1 and **I-CB2**MON-1. The latter were obtained by either sonication (30 minutes) or ultrasonication (10-20 seconds) in various organic solvents and fully characterized by UV-vis, Tyndall effect, PXRD, SEM, TEM, AFM and GIWAX measurements. The SEM and TEM images reflected the nanosheets are flat and smooth lamella. The height profile from AFM shows that the high aspect ratio nanosheets possess mono- and bi-layer thickness. Moreover, the intense scattering of q_z from GIWAX measurements indicated the highly anisotropic stacking on the substrates. These findings clearly indicate that most of ultrathin nanosheets were oriented face-on in the substrates and of large aspect/ratio. The latter seems to be due to the weak nature of the intermolecular interactions (mainly dihydrogen bonding) between layers in the bulk 2D material. These studies show the feasibility to prepare ultrathin nanosheets of these carborane capped materials. More studies are still going on and directed toward the study of their properties.

List of Publications

1) Tsang, M. Y.; Rodríguez-Hermida, S.; Stylianou, K. C.; Tan, F.; Negi, D.; Teixidor, F.; Viñas, C.; Choquesillo-Lazarte, D.; Verdugo-Escamilla, C.; Guerrero, M.; Sort, J.; Juanhuix, J.; Maspoch, D.; Giner Planas, J. Carborane Bis-pyridylalcohols as Linkers for Coordination Polymers: Synthesis, Crystal Structures, and Guest-Framework Dependent Mechanical Properties. *Cryst. Growth Des.* **2017**, *17*, 846-857. DOI: 10.1021/acs.cgd.6b01682.

2) Tan, F.; López-Periago, A.; Light, M. E.; Cirera, J.; Ruiz, E.; Borrás, A.; Teixidor, F.; Viñas, C.; Domingo, C.; Planas, J. G. An Unprecedented Stimuli-Controlled Single-Crystal Reversible Phase Transition of a Metal–Organic Framework and Its Application to a Novel Method of Guest Encapsulation. *Advanced Materials* **2018**, *30*, 1800726. DOI: 10.1002/adma.201800726.